University of Windsor

Scholarship at UWindsor

Electronic Theses and Dissertations

Theses, Dissertations, and Major Papers

2010

Turbulent Flow and Combustion in Homogeneous Charge Compression Ignition Engines with Detailed Chemical Kinetics

Srikanth Jonnalagedda
University of Windsor

Follow this and additional works at: https://scholar.uwindsor.ca/etd

Recommended Citation

Jonnalagedda, Srikanth, "Turbulent Flow and Combustion in Homogeneous Charge Compression Ignition Engines with Detailed Chemical Kinetics" (2010). *Electronic Theses and Dissertations*. 8010.
https://scholar.uwindsor.ca/etd/8010

This online database contains the full-text of PhD dissertations and Masters' theses of University of Windsor students from 1954 forward. These documents are made available for personal study and research purposes only, in accordance with the Canadian Copyright Act and the Creative Commons license—CC BY-NC-ND (Attribution, Non-Commercial, No Derivative Works). Under this license, works must always be attributed to the copyright holder (original author), cannot be used for any commercial purposes, and may not be altered. Any other use would require the permission of the copyright holder. Students may inquire about withdrawing their dissertation and/or thesis from this database. For additional inquiries, please contact the repository administrator via email (scholarship@uwindsor.ca) or by telephone at 519-253-3000ext. 3208.

Turbulent Flow and Combustion in Homogeneous Charge Compression Ignition Engines with Detailed Chemical Kinetics

by

Srikanth Jonnalagedda

A Dissertation
Submitted to the Faculty of Graduate Studies
through Mechanical, Automotive and Materials Engineering
in Partial Fulfillment of the Requirements for
the Degree of Doctor of Philosophy at the
University of Windsor

Windsor, Ontario, Canada
2010

© 2010 Srikanth Jonnalagedda

Library and Archives
Canada

Published Heritage
Branch

395 Wellington Street
Ottawa ON K1A 0N4
Canada

Bibliothèque et
Archives Canada

Direction du
Patrimoine de l'édition

395, rue Wellington
Ottawa ON K1A 0N4
Canada

Your file Votre référence
ISBN: 978-0-494-88921-3

Our file Notre référence
ISBN: 978-0-494-88921-3

NOTICE:

The author has granted a non-exclusive license allowing Library and Archives Canada to reproduce, publish, archive, preserve, conserve, communicate to the public by telecommunication or on the Internet, loan, distrbute and sell theses worldwide, for commercial or non-commercial purposes, in microform, paper, electronic and/or any other formats.

The author retains copyright ownership and moral rights in this thesis. Neither the thesis nor substantial extracts from it may be printed or otherwise reproduced without the author's permission.

AVIS:

L'auteur a accordé une licence non exclusive permettant à la Bibliothèque et Archives Canada de reproduire, publier, archiver, sauvegarder, conserver, transmettre au public par télécommunication ou par l'Internet, prêter, distribuer et vendre des thèses partout dans le monde, à des fins commerciales ou autres, sur support microforme, papier, électronique et/ou autres formats.

L'auteur conserve la propriété du droit d'auteur et des droits moraux qui protege cette thèse. Ni la thèse ni des extraits substantiels de celle-ci ne doivent être imprimés ou autrement reproduits sans son autorisation.

In compliance with the Canadian Privacy Act some supporting forms may have been removed from this thesis.

While these forms may be included in the document page count, their removal does not represent any loss of content from the thesis.

Conformément à la loi canadienne sur la protection de la vie privée, quelques formulaires secondaires ont été enlevés de cette thèse.

Bien que ces formulaires aient inclus dans la pagination, il n'y aura aucun contenu manquant.

Canada

Author's Declaration of Originality

I hereby certify that I am the sole author of this thesis and that no part of this thesis has been published or submitted for publication.

I certify that, to the best of my knowledge, my thesis does not infringe upon anyone's copyright nor violate any proprietary rights and that any ideas, techniques, quotations, or any other material from the work of other people included in my thesis, published or otherwise, are fully acknowledged in accordance with the standard referencing practices. Furthermore, to the extent that I have included copyrighted material that surpasses the bounds of fair dealing within the meaning of the Canada Copyright Act, I certify that I have obtained a written permission from the copyright owner(s) to include such material(s) in my thesis and have included copies of such copyright clearances to my appendix.

I declare that this is a true copy of my thesis, including any final revisions, as approved by my thesis committee and the Graduate Studies office, and that this thesis has not been submitted for a higher degree to any other University or Institution.

Abstract

Homogeneous Charge Compression Ignition (HCCI) engines have the potential to achieve higher thermal efficiency and lower emissions compared with conventional Internal Combustion (IC) engines. However, the organization of HCCI engine combustion is extremely critical in order to take advantage of HCCI combustion.

In this dissertation, an integrated numerical solver (named CKL solver) has been developed by integrating the original KIVA-3V solver with CHEMKIN and Large Eddy Simulation. This integrated solver has been validated by comparing the numerical results with the available experimental results, and has been employed to evaluate the combustion performance of the innovative HCCI combustion strategy with the Internal Mixing and Reformation (IMR) chamber that was proposed in the present study.

The results show that:

(1) the CKL solver can provide detailed information on HCCI combustion in terms of turbulent flow structures, temperature fields, concentration fields of all species involved including emissions (NO_x, CO, HC), engine performance (indicated mean effective pressure (IMEP), heat release rate (HRR), thermal efficiency), and spray-flow interactions.

(2) the CKL solver predicts the averaged pressure, IMEP, thermal efficiency, emissions and HRR which are in good agreement with corresponding experimental data, proving that the CKL solver can be applied to practical engineering applications with the accuracy, depending on the intake temperature values, for IMEP of 5-10%, and for peak pressure of 1-7.5%.

(3) the functions of the IMR chamber have been demonstrated and evaluated, showing that the IMR technology is a promising combustion strategy and needs further investigation in the future.

Acknowledgements

It was a wonderful and challenging experience to work at University of Windsor. During my doctoral research, many people helped me directly and indirectly to succeed. I would like to thank them in this way.

First of all, I express my sincere gratitude towards my supervisor Dr. Biao Zhou for his expert guidance, invaluable encouragement and continuous support throughout my graduate research. Working with him led to deeper understanding of fundamentals and simple ways to deal with complex situations.

I am very thankful to my co-supervisor Dr. Andrzej Sobiesiak for his guidance, support, valuable suggestions throughout my studies at the University of Windsor.

I am grateful to Dr. Roydon A. Fraser, Dr. Ronald M Barron, Dr. David Ting, Dr. Paul Henshaw and Dr. Ahmed Azab for spending their precious time reading the manuscript and providing me with valuable suggestions.

I am very thankful and indebted to Dr. Gnanaprakash Gnanam for providing me the experimental data, research advice, valuable comments and help throughout my stay at University of Windsor.

I am especially thankful to my colleague and friend Anh Tuan Nguyen, who always provided me help and support during my research and helped me towards my dissertation completion.

I am thankful to some of my colleagues and friends Jixin Chen, Le Dinh Anh, Ahmad Fadel, Charbel Boutros, Yan Zhang, Chunyi Xia, Michael Johnson, Mwila Clarence Mulenga for their help and support during my stay at university of Windsor.

Finally, I would like to express my sincere gratitude towards my parents and relatives for their patience, love and support over my career. I would like to specially thank my wife Uma and son Adithya for their invaluable support and patience through all these years.

Table of Contents

Author's Declaration of Originality iii

Abstract iv

Acknowledgements v

List of Figures viii

List of Tables xvi

Nomenclature xvii

Abbreviations xxii

Chapter 1 Introduction 1

- 1.1 Background and motivation 1
- 1.2 Literature review 3
  - 1.2.1 HCCI combustion strategies 3
  - 1.2.2 Turbulence modeling of IC engines 5
  - 1.2.3 Combustion modeling of HCCI engines 8
  - 1.2.4 Summary of literature review 13
- 1.3 Objectives 13
- 1.4 Methodology 14
- 1.5 Dissertation overview 14

Chapter 2 Numerical Methodology 15

- 2.1 KIVA-3V solver 15
- 2.2 Governing equations 16
  - 2.2.1 The governing equations of gas phase 16
  - 2.2.2 The LES model 19
- 2.3 Combustion model 23
  - 2.3.1 KIVA combustion model 23
  - 2.3.2 CHEMKIN 24
  - 2.3.3 KIVA-CHEMKIN integration 25
  - 2.3.4 KIVA-CHEMKIN combustion model 26
- 2.4 Iso-octane mechanism – Jia-Xie mechanism 28
- 2.5 Summary 30

Chapter 3 Grid Sensitivity Study and Comparison of RANS and LES Turbulence Models.. 31
3.1 Grid generation 31
3.2 Results and discussion 33
3.2.1 Velocity contours 35
3.2.2 Velocity vectors 38
3.2.3 Streamlines 40
3.2.4 Vorticity 43
3.2.5 Turbulent kinetic energy 45
3.3 Summary 47
Chapter 4 Validation of CKL Solver with Baseline Case 48
4.1 Introduction and boundary conditions 48
4.2 Results and discussion 49
4.3 Summary 60
Chapter 5 Combustion Process in Converted Kubota HCCI Engine 61
5.1 Simulation conditions 62
5.2 Results and discussion 65
5.3 Summary 81
Chapter 6 Effect of Internal Mixing and Reformation Chamber on HCCI Engine Combustion 82
6.1 Simulation conditions 83
6.2 Results and discussions 86
6.3 Summary 152
Chapter 7 Conclusions 154
7.1 Contributions and Conclusions 154
7.2 Recommendations for future work 154
Appendix A Jia-Xie mechanism for iso-octane 156
References 159

List of Figures

Figure 1.1 Compression Ignition (CI), Spark Ignition (SI) and HCCI engine combustion modes. (Gnanam 2008) 2

Figure 2.1 KIVA-3V solution algorithm phases, details and time stepping procedure. 15

Figure 2.2 KIVA-3V and CHEMKIN-II solvers integration 25

Figure 3.1 Vertical valve engine mesh used for computations (a) 3-D mesh and, (b) Different planes in which results are analyzed. 32

Figure 3.2 Grid resolutions for three different meshes (a) Coarse grid, (b) Medium grid, and (c) Fine grid 32

Figure 3.3 Average in-cylinder pressure variations between different grids for LES model. 33

Figure 3.4 Average in-cylinder pressure variations between different grids for RANS model. 33

Figure 3.5 Average sub-grid turbulent kinetic energy variations between three grids using LES model. 34

Figure 3.6 Average turbulent kinetic energy variations between three grids using RANS model 35

Figure 3.7 Velocity contours (m/s) from LES simulations in XY Plane for (a) Coarse grid, (b) Medium grid, and (c) Fine grid. 36

Figure 3.8 Velocity contours (m/s) from RANS simulations in XY Plane for (a) Coarse grid, (b) Medium grid, and (c) Fine grid. 36

Figure 3.9 Velocity contours (m/s) from LES simulations in XZ Plane for (a) Coarse grid, (b) Medium grid, and (c) Fine grid. 36

Figure 3.10 Velocity contours (m/s) from RANS simulations in XZ Plane for (a) Coarse grid, (b) Medium grid, and (c) Fine grid. 37

Figure 3.11 Velocity contours (m/s) from LES simulations in YZ Plane for (a) Coarse grid, (b) Medium grid, and (c) Fine grid. 37

Figure 3.12 Velocity contours (m/s) from RANS simulations in YZ Plane for (a) Coarse grid, (b) Medium grid, and (c) Fine grid. 37

Figure 3.13 Velocity vectors from LES simulations in XY Plane for (a) Coarse grid, (b) Medium grid, and (c) Fine grid. 38

Figure 3.14 Velocity vectors from RANS simulations in XY Plane for (a) Coarse grid, (b) Medium grid, and (c) Fine grid. 39

Figure 3.15 Velocity vectors from LES simulations in XZ Plane for (a) Coarse grid, (b) Medium grid, and (c) Fine grid. 39

Figure 3.16 Velocity vectors from RANS simulations in XZ Plane for (a) Coarse grid, (b) Medium grid, and (c) Fine grid. 39

Figure 3.17 Velocity vectors for from LES simulations in YZ Plane for (a) Coarse grid, (b) Medium grid, and (c) Fine grid. 40

Figure 3.18 Velocity vectors from RANS simulations in YZ Plane for (a) Coarse grid, (b) Medium grid, and (c) Fine grid. 40

Figure 3.19 Streamlines for LES simulations in XY Plane for (a) Coarse grid, (b) Medium grid, and (c) Fine grid. 41

Figure 3.20 Streamlines for RANS simulations in XY Plane for (a) Coarse grid, (b) Medium grid, and (c) Fine grid. 41

Figure 3.21 Streamlines for LES simulations in XZ Plane for (a) Coarse grid, (b) Medium grid, and (c) Fine grid. 41

Figure 3.22 Streamlines for RANS simulations in XZ Plane for (a) Coarse grid, (b) Medium grid, and (c) Fine grid. 42

Figure 3.23 Streamlines for LES simulations in YZ Plane for (a) Coarse grid, (b) Medium grid, and (c) Fine grid. 42

Figure 3.24 Streamlines for RANS simulations in YZ Plane for (a) Coarse grid, (b) Medium grid, and (c) Fine grid. 42

Figure 3.25 Vorticity contours (sec^{-1}) for LES simulations in XY Plane for (a) Coarse grid, (b) Medium grid, and (c) Fine grid. 43

Figure 3.26 Vorticity contours (sec^{-1}) for RANS simulations in XY Plane for (a) Coarse grid, (b) Medium grid, and (c) Fine grid. 43

Figure 3.27 Vorticity contours (sec^{-1}) for LES simulations in XZ Plane for (a) Coarse grid, (b) Medium grid, and (c) Fine grid. 44

Figure 3.28 Vorticity contours (sec^{-1}) for RANS simulations in XZ Plane for (a) Coarse grid, (b) Medium grid, and (c) Fine grid. 44

Figure 3.29 Vorticity contours (sec^{-1}) LES simulations in YZ Plane for (a) Coarse grid, (b) Medium grid, and (c) Fine grid. 44

Figure 3.30 Vorticity contours (sec^{-1}) RANS simulations in YZ Plane for (a) Coarse grid, (b) Medium grid, and (c) Fine grid. 45

Figure 3.31 Sub-grid scale turbulent kinetic energy (m^2/s^2) contours for LES simulations in XY Plane for (a) Coarse grid, (b) Medium grid, and (c) Fine grid. 45

Figure 3.32 Turbulent kinetic energy (m^2/s^2) contours for RANS simulations in XY Plane for (a) Coarse grid, (b) Medium grid, and (c) Fine grid. 46

Figure 3.33 Sub-grid scale turbulent kinetic energy (m^2/s^2) contours for LES simulations in XZ Plane for (a) Coarse grid, (b) Medium grid, and (c) Fine grid. 46

Figure 3.34 Turbulent kinetic energy (m^2/s^2) contours for RANS simulations in XZ Plane for (a) Coarse grid, (b) Medium grid, and (c) Fine grid. 46

Figure 3.35 Sub-grid scale turbulent kinetic energy (m^2/s^2) contours for LES simulations in YZ Plane for (a) Coarse grid, (b) Medium grid, and (c) Fine grid. 47

Figure 3.36 Turbulent kinetic energy (m^2/s^2) contours for RANS simulations in YZ Plane for (a) Coarse grid, (b) Medium grid, and (c) Fine grid. 47

Figure 4.1 Geometry (Dec and Sjöberg, 2003) and 2-D axi-symmetric computational domain when piston is at Top Dead Centre. 49

Figure 4.2 (a) Simulation pressure traces for various equivalence ratios, (b) Experimental data taken from Dec and Sjöberg (2003). 51

Figure 4.3 Comparison of in-cylinder pressure traces with the experimental data for equivalence ratios of 0.26, 0.18 and 0.1 with motoring curve. 51

Figure 4.4 Simulated average in-cylinder temperature variations with respect to equivalence ratios. 52

Figure 4.5 Gross Indicated Mean Effective Pressure (IMEPg) versus equivalence ratios. 53

Figure 4.6 Thermal efficiencies versus equivalence ratios. 53

Figure 4.7 Net heat release rates per crank angle for various equivalence ratios. 54

Figure 4.8 Cumulative heat release curves for various equivalence ratios. 55

Figure 4.9 Heat release durations for various equivalence ratios. 55

Figure 4.10 Heat release crank angle for various equivalence ratios. 56

Figure 4.11 Comparison of emissions with respect to equivalence ratios. 57

Figure 4.12 In-cylinder consumption of fuel (iso-octane). 58

Figure 4.13 In-cylinder production and consumption of CO. 58

Figure 4.14 In-cylinder production of CO_2. 59

Figure 5.1 Kubota D905 engine head. 62

Figure 5.2 Computational domain and grid in isometric view when piston is at Bottom Dead Centre. 63

Figure 5.3 Comparison of pressure trace and pressure rise rate during motoring conditions. 63

Figure 5.4 Comparison of pressure for different intake charge temperatures. 66

Figure 5.5 Comparison of heat release rate for different intake charge temperatures. 66

Figure 5.6 Comparison of 10% heat release crank angle and 10% - 90% heat release duration between experiments and simulations for different intake charge temperatures. 67

Figure 5.7 Comparison of pressure rise rate for different intake charge temperatures. 67

Figure 5.8 Comparison of IMEP for different intake charge temperatures. 68

Figure 5.9 Comparison of thermal efficiency for different intake charge temperatures. 69

Figure 5.10 Comparison of % emissions for different intake charge temperatures. 69

Figure 5.11 Average in-cylinder temperature for different intake charge temperatures. 70

Figure 5.12 Mass fractions of different species for intake charge temperature of 418.5 K. 70

Figure 5.13 Variation of average turbulent kinetic energy for different intake charge temperatures. 71

Figure 5.14 (a) Computational domain at Bottom Dead Centre showing three planes chosen for qualitative analysis, (b) Computational domain shown from top of cylinder. 72

Figure 5.15 Temperature (Kelvin) contours in XY plane at crank angles (a) 345 CA, (b) 350CA, and (c) 355 CA for 418.5K initial temperature. 73

Figure 5.16 Molar fraction contours of fuel in XY plane at crank angles (a) 345 CA, (b) 350CA, and (c) 355 CA for 418.5K initial temperature. 73

Figure 5.17 Equivalence ratio contours in XY plane at crank angles (a) 345 CA, (b) 350CA, and (c) 355 CA for 418.5K initial temperature. 73

Figure 5.18 Temperature (Kelvin) contours in XY plane at crank angles (a) 360 CA, (b) 365 CA, and (c) 370 CAfor 418.5K initial temperature. 74

Figure 5.19 Molar fraction contours of fuel in XY plane at crank angles (a) 360 CA, (b) 365 CA, and (c) 370 CAfor 418.5K initial temperature. 74

Figure 5.20 Equivalence ratio contours in XY plane at crank angles (a) 360 CA, (b) 365 CA, and (c) 370 CA for 418.5K initial temperature. 75

Figure 5.21 Molar fraction contours of O_2 in XY plane at crank angles (a) 360 CA, (b) 365 CA, and (c) 370 CA for 418.5K initial temperature. 75

Figure 5.22 Molar fraction contours of CO_2 in XY plane at crank angles (a) 360 CA, (b) 365 CA, and (c) 370 CA for 418.5K initial temperature. 76

Figure 5.23 Molar fraction contours of H_2O in XY plane at crank angles (a) 360 CA, (b) 365 CA, and (c) 370 CA for 418.5K initial temperature. 76

Figure 5.24 Molar fraction contours of CO in XY plane at crank angles (a) 360 CA, (b) 365 CA, and (c) 370 CA for 418.5K initial temperature. 77

Figure 5.25 Molar fraction contours of H_2 in XY plane at crank angles (a) 360 CA, (b) 365 CA, and (c) 370 CA for 418.5K initial temperature. 77

Figure 5.26 Molar fraction contours of OH in XY plane at crank angles (a) 360 CA, (b) 365 CA, and (c) 370 CA for 418.5K initial temperature. 77

Figure 5.27 Molar fraction contours of N_2 in XY plane at crank angles (a) 360 CA, (b) 365 CA, and (c) 370 CA for 418.5K initial temperature. 78

Figure 5.28 Molar fraction contours of NO in XY plane at crank angles (a) 360 CA, (b) 365 CA, and (c) 370 CA for 418.5K initial temperature. 78

Figure 5.29 Molar fraction contours of NO_2 in XY plane at crank angles (a) 360 CA, (b) 365 CA, and (c) 370 CA for 418.5K initial temperature. 78

Figure 5.30 Streamline plots in XY plane at crank angles (a) 360 CA, (b) 365 CA, and (c) 370 CA for 418.5K initial temperature. 79

Figure 5.31 Sub-grid scale turbulent kinetic energy (m^2/sec) contours in XY plane at crank angles (a) 360 CA, (b) 365 CA, and (c) 370 CA for 418.5K initial temperature. 79

Figure 5.32 Velocity vectors in XY plane at crank angles (a) 360 CA, (b) 365 CA, and (c) 370 CA for 418.5K initial temperature. 79

Figure 5.33 Variation of (a) temperature and (b) velocity vectors within pre-chamber in XZ plane. 80

Figure 6.1 Computational domain of cylinder with internal mixing and reformation chamber. 82

Figure 6.2 IMR chamber valve timings and IMR chamber fuel injection timings for six cases. 85

Figure 6.3 Average in-cylinder pressure traces for cases 1, 2 and 3 after 2 engine cycles. ... 86

Figure 6.4 Average in-cylinder temperature variations for cases 1, 2 and 3 after 2 engine cycles........ 87

Figure 6.5 Heat release rate comparison for cases 1, 2 and 3 after 2 engine cycles.............. 87

Figure 6.6 10% HR crank angle and 10%-90% heat release duration for cases 1, 2 and 3 after 2 engine cycles........ 88

Figure 6.7 Indicated Mean Effective Pressure for cases 1, 2 and 3 after 2 engine cycles...... 89

Figure 6.8 CO and UHC emissions for cases 1, 2 and 3 after 2 engine cycles........ 90

Figure 6.9 Average IMR chamber pressure for cases 2 and 3 after 2 engine cycles............ 91

Figure 6.10 Average IMR chamber pressure for cases 2 and 3........ 91

Figure 6.11 Average IMR chamber temperature for cases 2 and 3 after 2 engine cycles...... 92

Figure 6.12 Average IMR chamber temperature for cases 2 and 3........ 92

Figure 6.13 Mass fraction of fuel in the cylinder and the IMR chamber for cases 2 and 3.... 93

Figure 6.14 Mass fraction of O_2 in the cylinder and the IMR chamber for cases 2 and 3...... 94

Figure 6.15 Mass fraction of N_2 in in-cylinder and IMR chamber for cases 2 and 3............ 94

Figure 6.16 Mass fraction of CO_2 in in-cylinder and IMR chamber for cases 2 and 3. 95

Figure 6.17 Mass fraction of H_2O in the cylinder and the IMR chamber for cases 2 and 3... 95

Figure 6.18 Mass fraction of CO in the cylinder and the IMR chamber for cases 2 and 3..... 96

Figure 6.19 Mass fraction of H_2 in in-cylinder and IMR chamber for cases 2 and 3............ 96

Figure 6.20 Mass fraction of H_2 in IMR chamber for case 3........ 97

Figure 6.21 Mass fraction of OH in in-cylinder and IMR chamber for cases 2 and 3........... 97

Figure 6.22 Average in-cylinder pressures for cases 4, 5 and 6........ 98

Figure 6.23 Average in-cylinder temperatures for cases 4, 5 and 6. 99

Figure 6.24 Heat release rate for cases 4, 5 and 6........ 99

Figure 6.25 10% CA and 10%-90% heat release duration for cases 4, 5 and 6. 100

Figure 6.26 Indicated mean effective pressure for cases 1 to 6........ 100

Figure 6.27 % CO and % UHC emissions for cases 4, 5 and 6........ 101

Figure 6.28 Average in-cylinder and IMR chamber pressure for cases 4, 5 and 6.............. 102

Figure 6.29 Average IMR chamber pressure for cases 4, 5 and 6........ 102

Figure 6.30 Average IMR chamber temperatures for cases 4, 5 and 6. 103

Figure 6.31 Average IMR chamber temperature for cases 4, 5 and 6. 103

Figure 6.32 Mass fractions of fuel within the cylinder and the IMR chamber for cases 4, 5 and 6. 104

Figure 6.33 Mass fractions of O_2 within the cylinder and the IMR chamber for cases 4, 5 and 6 105

Figure 6.34 Mass fractions of N_2 within the cylinder and the IMR chamber for cases 4, 5 and 6 105

Figure 6.35 Mass fractions of CO_2 within the cylinder and the IMR chamber for cases 4, 5 and 6. 106

Figure 6.36 Mass fractions of H_2O within the cylinder and the IMR chamber for cases 4, 5 and 6. 106

Figure 6.37 Mass fractions of CO within the cylinder and the IMR chamber for cases 4, 5 and 6 107

Figure 6.38 Mass fractions of H_2 within the cylinder and the IMR chamber for cases 4, 5 and 6 107

Figure 6.39 Mass fraction of H_2 within cylinder and IMR chamber for case 6. 108

Figure 6.40 Mass fractions of OH within the cylinder and the IMR chamber for cases 4, 5 and 6. 108

Figure 6.41 Indicated Specific Fuel Consumption (ISFC, g/KWh) for all six cases studied. 109

Figure 6.42 3-D computational domain showing three XY planes and XZ plane. 110

Figure 6.43 Computational domain indicating cut-plane locations in XZ plane and XY plane. 110

Figure 6.44 Velocity vectors and spray particles in XZ plane at crank angles (a) 352 CA, (b) 354CA, (c) 356 CA, (d) 358 CA, (e) 360 CA, (f) 362 CA, (g) 364 CA, (h) 366 CA, (i) 368 CA, (j)370 CA, (k) 372 CA, and (l) 374 CA for case 6. 117

Figure 6.45 Temperature contours in XY plane and XZ planes for crank angle (a) 352 CA, (b) 356 CA, (c) 360 CA, (d) 362 CA, (e) 370 CA, and (f) 372 CA. 120

Figure 6.46 Fuel molar fraction contours in XY planes and XZ plane at crank angle (a) 352 CA, (b) 356 CA, (c) 360 CA, (d) 362 CA, (e) 370 CA, and (f) 372 CA. 124

Figure 6.47 O_2 molar fraction contours in XY planes and XZ plane at crank angle (a) 352 CA, (b) 356 CA, (c) 360 CA, (d) 362 CA, (e) 370 CA, and (f) 372 CA. 127

Figure 6.48 N_2 molar fraction contours in XY planes and XZ plane at crank angle (a) 352 CA, (b) 356 CA, (c) 360 CA, (d) 362 CA, (e) 370 CA, and (f) 372 CA. 130

Figure 6.49 CO_2 molar fraction contours in XY planes and XZ plane at crank angle (a) 352 CA, (b) 356 CA, (c) 360 CA, (d) 362 CA, (e) 370 CA, and (f) 372 CA. 133

Figure 6.50 H_2O molar fraction contours in XY planes and XZ plane at crank angle (a) 352 CA, (b) 356 CA, (c) 360 CA, (d) 362 CA, (e) 370 CA, and (f) 372 CA. 136

Figure 6.51 CO molar fraction contours in XY planes and XZ plane at crank angle (a) 352 CA, (b) 356 CA, (c) 360 CA, (d) 362 CA, (e) 370 CA, and (f) 372 CA. 139

Figure 6.52 H_2 molar fraction contours in XY planes and XZ plane at crank angle (a) 352 CA, (b) 356 CA, (c) 360 CA, (d) 362 CA, (e) 370 CA, and (f) 372 CA. 142

Figure 6.53 OH molar fraction contours in XY planes and XZ plane at crank angle (a) 352 CA, (b) 356 CA, (c) 360 CA, (d) 362 CA, (e) 370 CA, and (f) 372 CA. 145

Figure 6.54 NO molar fraction contours in XY planes and XZ plane at crank angle (a) 352 CA, (b) 356 CA, (c) 360 CA, (d) 362 CA, (e) 370 CA, and (f) 372 CA. 148

Figure 6.55 IMEP for cases 3 and 6 with constant IMR valve timing and varied fuel injection timing. 149

Figure 6.56 ISFC for cases 3 and 6 with constant IMR valve timing and varied fuel injection timing. 150

Figure 6.57 Emissions for cases 3 and 6 with constant IMR valve timing and varied fuel injection timing. 150

Figure 6.58 IMEP for cases 3 and 4 with constant IMR fuel injection timing and varied valve timing. 151

Figure 6.59 ISFC for cases 3 and 4 with constant IMR fuel injection timing and varied valve timing. 151

Figure 6.60 Emissions for cases 3 and 4 with constant IMR fuel injection timing and varied valve timing. 152

List of Tables

Table 3.1 Mesh size details of three different meshes used. 32
Table 4.1 Engine specifications from Dec and Sjöberg (2003) for baseline case. 48
Table 5.1 Experimental engine specifications 61
Table 5.2 Experimental conditions for HCCI engine runs. 64
Table 6.1 Initial conditions for simulations. 83
Table 6.2 Simulation conditions for six cases. 83

Nomenclature

Alphabetical order

a	Pressure constant
a_{mr}	Integral stoichiometric coefficient of species
a'_{mr}	Order of reaction
A_{fr}	Forward reaction constant
A_{br}	Backward reaction constant
A_{tkesw}	Parameter indicating whether flow is laminar or turbulence (0 for laminar, 1 for turbulence)
b_{mr}	Integral stoichiometric coefficient of species
C_{ij}	Cross term
c_{pm}	Specific heat at constant pressure of species *m*
C_p	Specific heat at constant pressure
C_{m2}	Turbulence timescale model constant
D	Diffusion coefficient
D^{sgs}	Turbulent dissipation rate
$\tilde{e}$	Specific internal energy
E	Specific total energy
E_{fr}	Forward reaction activation energy
E_{br}	Backward reaction activation energy
F^s	Rate momentum gain per unit volume due to the spray
$\overline{F}_k^s$	Source term due to spray
$\tilde{f}$	Resolved scale
f''	Sub-grid scale
f	Progress variable
g	Gravitational force
G	Filtering function
h_m	Enthalpy of chemical species, *m*

h_j^{sgs}	Sub-grid scale heat flux
I	Specific internal energy
I_m	Specific internal energy of species *m*
J	Heat flux vector
K	Coefficient of heat conduction
k_{fr}	Coefficient of forward reaction
k_{br}	Coefficient of backward reaction
L_{ij}	Leonard term
P	Pressure
P^{sgs}	Production term
Pr	Prandtl number
P_{rt}	Turbulent Prandtl number
$\bar{q}_j$	Heat flux
$\dot{Q}^c$	Heat release per unit time due to chemistry
$\dot{Q}^s$	Heat release per unit time due to spray
Q_r	Negative of enthalpy of reaction
R_m	Species gas constant
R_0	Universal gas constant
R_{ij}	Reynolds term
$\bar{S}_{ij}$	Velocity gradient tensor
S_c	Schmidt number
T	Temperature
t	Time
u	Velocity
V	Volume
x	Cartesian space coordinate
Y_m	Current concentration
Y_m^*	Equilibrium concentration

Y_m'	Species concentration after CHEMKIN model is called
Y_f	Mass fraction of fuel
$\tilde{Y}_m$	Species mass fraction
W_s	Source term due to the interaction with spray
W_m	Molecular weight of species *m*
$\left(\Delta h_f^0\right)_m$	Enthalpy of formation of species *m* at absolute zero

Greek letters

ρ_m	Mass density of species
ρ	Total mass density
$\dot{\rho}_m^c$	Density change of species *m* per unit time due to chemistry
$\dot{\rho}_m^s$	Density change of species *m* per unit time due to spray
$\bar{\dot{\rho}}^s$	Change in total density due to spray
δ	A representative computational cell dimension
$\delta_{m,1}$	Kronecker delta function
σ	Viscous stress tensor
μ	Coefficient of viscosity
λ	Second coefficient of viscosity
ε	Turbulence dissipation rate
ϑ_o	diffusivity
μ_{air}	Dynamic viscosity of air
Ξ	Filter domain
$\bar{\Delta}$	Computational cell
τ_{turb}	Kinetic timescale
$\tau_{kin,m}$	Turbulent timescale ~ k / ε
$\bar{\tau}_{ij}$	Viscous stress tensor
τ_{ij}^{sgs}	Sub-grid scale stress tensor

υ_t	Eddy viscosity
δ_{ij}	Kronecker delta
Θ^{sgs}	Sub-grid viscous work
Π^{sgs}	Pressure gradient correlation term
$\phi^{sgs}_{j,m}$	Sub-grid species mass flux
$\theta^{sgs}_{j,m}$	Diffusive mass flux term
$\overline{\omega}_{kin.m}$	Kinetics-controlled reaction rate
$\dot{\omega}_r$	The rate of kinetic reaction r
ξ_{fr}	Forward reaction constant
ξ_{br}	Backward reaction constant

Subscript

m	Species
$tkesw$	Turbulent kinetic energy switch
k	Turbulent kinetic energy
ε	Dissipation rate
μ	Dynamic viscosity
sgs	Sub-grid scale
υ	Kinematic viscosity
r	Reaction
fr	Forward reaction
br	Backward reaction
$kin.m$	Kinetic
$turb$	Turbulence
f	Progress variable

Superscript

c	Chemistry
s	spray
sgs	Sub-grid scale

T	Transpose

Abbreviations

1-D	One Dimensional
3-D	Three Dimensional
ALE	Arbitrary Lagrangian-Eulerian
ATAC	Active Thermo-Atmosphere Combustion
CEPA	Canadian Environmental Protection Act
CFD	Computational Fluid Dynamics
CI	Compression Ignition
CIHC	Compression-Ignited Homogenous Charge
CO	Carbon Monoxide
DNS	Direct Numerical Simulation
EGR	Exhaust Gas Recirculation
ER	Equivalence Ratio
EVC	Exhaust Valve Close
EVO	Exhaust Valve Open
HC	Hydro Carbons
HCCI	Homogeneous Charge Compression Ignition
HRR	Heat Release Rate
IMEP	Indicated Mean Effective Pressure
IMR	Internal Mixing and Reformation
IVC	Intake Valve Close
IVO	Intake Valve Open
LES	Large Eddy Simulation
NO_x	Nitrogen Oxides
NTC	Negative Temperature Coefficient

PGS	Pressure Gradient Scale
PM	Particulate Matter
RANS	Reynolds Averaged Navier-Stokes
SI	Spark Ignition
TDC	Top Dead Centre
VVA	Variable Value Activation
VVT	Variable Valve Train

Chapter 1
Introduction

1.1 Background and motivation

There are two types of Internal Combustion (IC) engines, Spark Ignition (SI) and Compression Ignition (CI). The conventional SI engine combustion is characterized by a flame propagation process. The fuel-air mixture is pre-mixed and typically stoichiometric. The onset of combustion in SI engines is controlled by the ignition timing of the spark discharge. The major disadvantage of SI engines is its low efficiency at partial loads due to the pumping losses and low thermal efficiency. The compression ratio in SI engines is usually limited to 8 to 12 in order to avoid knocks and this low compression ratio results in a low efficiency. On the other hand, the CI engines usually have a high compression ratio in the range of 18 to 24, thus giving high thermal efficiency. In conventional CI engines, fuel is directly introduced into the cylinder as spray at the end of compression stroke and the fuel-air mixture auto-ignites when the temperature reaches the auto-ignition temperature. The onset of combustion in a CI engine is controlled by the fuel injection timing. The main concerns for conventional CI engines are high NO_x emissions due to high temperature (above 2700 K) created by the high compression ratio and high particulate matter (PM) emissions due to poor fuel-air mixing created by direct injection of fuel to the cylinder. In CI engines, a trade-off between the NO_x and PM emissions must be balanced in order to have an optimum emission performance. In order to meet the high standard of emission regulations proposed by CEPA (1999), innovative technologies such as Homogeneous Charge Compression Ignition (HCCI) have been attracting more attention from engineers and scientists in the last three decades.

HCCI combustion was first proposed as an alternative combustion mode for two-stroke engines by Onishi et al. (1979), and significant reductions in emissions and improvement in fuel economy were achieved by using a high level of internal residuals of exhaust gases and high initial charge temperature that provide the conditions for auto-ignition. An HCCI engine is characterized by the auto-ignition of the lean pre-mixed homogeneous charge by the heat released from compression of the mixture. Unlike the traditional SI combustion that relies on the flame propagation and the diesel combustion that heavily depends on the fuel-air mixing, HCCI combustion is mostly a chemical kinetic combustion process controlled by the pressure, temperature and in-cylinder fuel-air mixture composition. Figure 1.1 shows the difference between CI engine, SI engine and HCCI engine combustion. In CI engines, fuel spray evaporates and mixes with air to form a combustible mixture and then auto-ignites when temperature reaches the ignition temperature. In SI engines, combustion happens within a thin reaction zone which propagates through the combustion chamber. This reaction zone starts from the spark plug and propagates to the cylinder walls. For HCCI engine combustion, the entire mixture in the cylinder reacts almost at the same instant, but at a lower reaction rate due to lower temperature as compared to CI ignition.

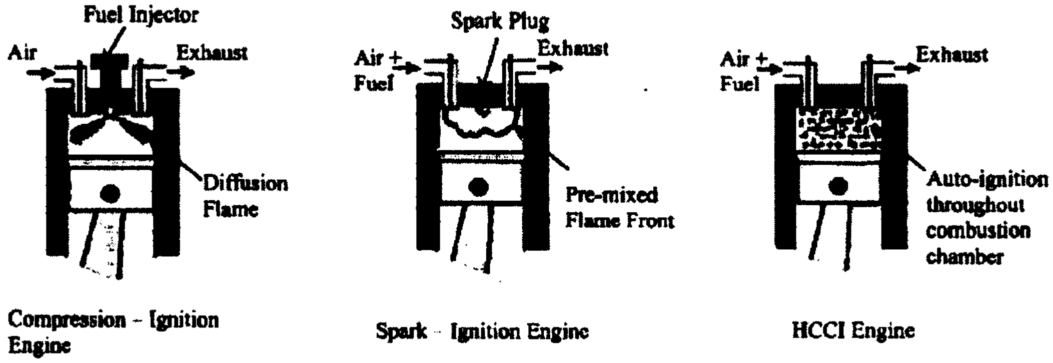
Fuel Injector
Air
Exhaust
Diffusion Flame
Compression - Ignition Engine
Spark Plug
Air + Fuel
Exhaust
Pre-mixed Flame Front
Spark - Ignition Engine
Air + Fuel
Exhaust
Auto-ignition throughout combustion chamber
HCCI Engine

Figure 1.1 Compression Ignition (CI), Spark Ignition (SI) and HCCI engine combustion modes. (Gnanam 2008)

Najt and Foster (1983) extended the work of Onishi et al. (1979) to four-stroke engines. The results showed that HCCI auto-ignition is controlled by the same low-temperature (below 1000K) chemistry leading to knock in SI engines, and that the bulk heat release is controlled by the high-temperature (above 1000K) chemistry dominated by CO oxidation. They termed the combustion mode as Compression-Ignited Homogeneous Charge (CIHC). Thring (1989) extended the work of Najt and Foster (1983) in four-stroke engines. He proposed integration of the HCCI combustion mode into the engine operating strategy by running the engine at part-loads on HCCI combustion and conventional SI operation mode at high loads. Recently, interest in HCCI engine control strategies has increased due to challenges to meet emission standards. Good comprehensive reviews of HCCI engine development and control strategies were compiled by Zhao et al. (2003), and recently by Yao et al. (2009).

For HCCI combustion techniques, some critical challenges still remain unresolved; for example, it is difficult to control the onset of combustion due to auto-ignition, the pressure rise rates due to the fast heat release, and the emissions of unburned hydrocarbons (UHC) and carbon monoxide (CO) during incomplete combustion. These drawbacks limit the operating range of HCCI engines.

High performance computational techniques with proper numerical schemes and physical models can provide sufficient details on fluid flow, heat transfer and the combustion process to help engineers diagnose the performance of HCCI engine combustion with lower cost than engine testing. Therefore, a sophisticated numerical study is proposed for this dissertation.

1.2 Literature review

The HCCI technique, as one type of combustion mode for IC engines, has many common features of SI and CI engines. It also involves many different physical and chemical processes. The performance of HCCI combustion strongly depends on the strategies for organizing combustion processes that are significantly affected by the details of turbulent flow structures, chemical reaction rates of different species, and the valve and injection timings, as well as combustion chamber designs.

1.2.1 HCCI combustion strategies

The main advantages of HCCI combustion technology that could be obtained are the high fuel efficiency and low emissions, but there exist many critical challenges on the road to bringing HCCI to the market. For example, how does one control the onset of combustion, completely burn fuel with high efficiency, and produce low emissions as well as no knocks?

For the last three decades, scientists and engineers have been working on HCCI combustion and have developed some combustion strategies to meet these challenges, for example, fuel injection technologies, charge boost technologies, Exhaust Gas

Recirculation (EGR) technologies, variable compression ratio, multi-mode ignition, fuel modification etc. (Yao et al. 2009). Detailed review of different strategies can be found in this reference. In this dissertation, only some related strategies, which are relevant to this work, will be reviewed.

The fuel injection strategies deal with when, where and how to inject fuel. Some researchers (Marriott and Reitz, 2002, Gnanam 2008) have done significant work on these strategies such as port or direct injection, late or early injection, multiple injections, etc.

The goal of EGR technology is to reduce the NO_x emission and control the auto-ignition time by controlling the temperature of the mixture inside the cylinder. EGR technologies concern bringing exhaust gases back to the engine cylinder (referred to as external EGR) or retaining some of the exhaust gases inside the engine cylinder by closing the exhaust valve early (referred to as internal EGR). These technologies have been practiced by many researchers (Law 2000, Kaahaaina et al. 2001, Shen et al. 2006, Gnanam 2008).

The purpose of variable compression ratio technologies is to properly arrange the required temperature and pressure for auto-ignition by changing the compression ratio. This is relatively new technology (Christensen and Johansson 2002, Haraldsson et al. 2003).

Besides these technologies reviewed in Yao et al. (2009), Gnanam (2008) proposed a new strategy where a fuel reformation chamber was introduced to control the start of combustion. The proposed strategy was to vary the compression ratio during the compression stroke to control combustion onset, in addition to the effects of fuel reformation. The experimental engine used was a four-stroke, three cylinder indirect injection type compression ignition engine which was converted to single cylinder operation for HCCI combustion. It was concluded that a temporary change in compression ratio that results from utilizing the proposed pre-chamber methodology has a stronger influence in controlling the onset of HCCI combustion compared to the effects of fuel reformation products alone.

Although each technology mentioned above can solve some of the challenges, they also bring some new problems. Behind all these different technologies, the key issue actually remains the same, i.e., how to organize the reactants (fuel and air) in such a way so that they can be burned at the right time, right place, with the right rate and produce the power required with an acceptable level of emissions. The performance for different strategies to organize the reactants fundamentally depends on how to organize the flow, usually turbulent flow, and how to control the detailed reaction processes. Therefore a fundamental understanding of turbulent structures and detailed chemical kinetics within the HCCI engines still remains as the major challenge for HCCI technologies.

1.2.2 Turbulence modeling of IC engines

Turbulence is a common flow phenomena which exists in IC engines and plays a fundamental role in the combustion performance. The numerical methods used to solve the turbulence governing equations can be classified as Reynolds Averaged Navier-Stokes (RANS) based method, Direct Numerical Simulation, and Large Eddy Simulation.

In RANS, all quantities are decomposed into a mean (averaged) value and a fluctuation. In RANS-based methods the entire spectrum of turbulence is represented by a statistical turbulence model. A wide range of models are available ranging from simple algebraic models to Reynolds stress closure models. The most commonly used turbulence models in engine simulations so far have been RANS-based. An example is KIVA-3V, a general-purpose Computational Fluid Dynamics (CFD) solver for unsteady fluid flow, heat transfer and combustion developed by Los Alamos National Laboratory (Amsden et al. 1989). The KIVA family of codes (KIVA-II, KIVA-III, KIVA-3V, and KIVA-3V Release 2) is based on the Arbitrary Lagrangian-Eulerian (ALE) method (Amsden et al. 1989). These are time marching block-structured Navier-Stokes solvers for simulation of transient, two and three dimensional, reactive fluid flows with sprays. The gas flow is modeled by an Eulerian method and the liquid phase is modeled by a Lagrangian method. A stochastic particle method is used to calculate evaporation in liquid sprays, including the droplet collisions and aerodynamic breakups. A standard k-ε model is incorporated in the KIVA-3V solver for turbulence modeling. In RANS models, the governing equations are ensemble averaged. This removes unsteadiness from the flow field and smears out flow structures. These results can only be compared with the averaged flow field over time. The actual engine performance depends on the cycle-to-cycle variability, which cannot be captured by using RANS turbulence models.

Direct Numerical Simulation (DNS) is an approach in which direct solution of the governing equations are obtained numerically. The mesh must be fine enough to resolve the smallest scales. The size of the smallest eddy is governed by the rate of dissipation of the turbulent kinetic energy (ε) and the coefficient of viscosity (ν). The smallest length scale (η_d) is called the Kolmogorov scale. To resolve the Kolmogorov scales a grid size of the order of $R_L^{9/4}$ is needed, where R_L is LV_t/ν, L and V_t are the length scale and velocity scale of large eddies. For example, if R_L is 10000, the number of grid points would be 10^9. The time step also has to be very small. Thus the DNS method is very time-consuming and requires high computational power.

Large Eddy Simulation (LES) is an intermediate approach between RANS and DNS where large-scale unsteady motions are resolved and small-scale turbulent motions are modeled. To differentiate between large-scale and small-scale eddies a filter size has to be determined. Scales larger than the filter size are known as large scales and smaller than the filter size are known as Sub-Grid Scales (SGS). In LES simulations, the small grid size is considered as the filter size. The governing equations obtained after applying the filter are known as filtered governing equations. The sub-grid scale models were developed to represent small-scale turbulence motions (Sagaut 2002).

The typical sub-grid scale models used to date are as follows:

1. Smagorinsky model.

2. One-equation eddy viscosity model.

3. Dynamic Smagorinsky model.

4. Dynamic structure model.

The Smagorinsky model (Smagorinsky 1963) used for sub-grid scale modeling is a zero-equation eddy viscosity model, in which a sub-grid stress tensor is calculated based on the eddy viscosity and rate of strain tensor. The eddy viscosity is calculated from the magnitude of the rate of strain tensor, Smagorinsky constant and filter width. The Smagorinsky constant is flow dependent and is a fixed constant in this model. Several researchers applied the Smagorinsky model to IC engine applications (Haworth 1999, Celik et al. 2001, Thobois et al. 2005, Jhavar and Rutland 2006). Haworth (1999) showed that the LES predictions for a two-valve pancake type combustion chamber motored four-stroke cycle engine were in better agreement with the experimental results compared to RANS results. The LES results predicted flow structures similar to instantaneous Particle Image Velocimetry (PIV) flow fields. Thobois et al. (2005) simulated flow in an axisymmetric sudden expansion valve with LES and RANS models and compared the simulation results with experimental results obtained using Doppler Global Velocimetry (DGV). The results indicated that the LES model was able to predict swirl with an error of 1%, whereas RANS predicts it with an error of 31%. The disadvantage of using the Smagorinsky method is that it is dissipative in nature and the Smagorinsky model constant is an unknown constant prior to simulations.

The Dynamic Smagorinsky model (Germano et al. 1991) is a modified version of the Smagorinsky model in which the Smagorinsky model constant is calculated from the flow field parameters instead of specifying a constant value. This method involves applying a test filter over the sub-grid scale filter to obtain the rate of strain values. Haworth (1999) and Jhavar and Rutland (2006) implemented the Dynamic Smagorinsky model and compared results obtained with the Smagorinsky model. Although this model gives better prediction of flow fields compared to the Smagorinsky model, the methodology caused numerical instability due to the negative model constant.

The one-equation eddy viscosity model (Sone et al. 2001), also known as the k-Δ model, where k is sub-grid scale turbulent kinetic energy and Δ is filter width, consists of an additional transport equation for sub-grid scale turbulent kinetic energy. The eddy viscosity is calculated from the sub-grid scale turbulent kinetic energy, filter width and rate of strain tensor. This model is suitable for coarse grids since the kinetic energy budget has been considered. This model has been widely used by several researchers for engine flows (Sone and 2001, Lee et al. 2002, Sone and Menon 2003, Jhavar and Rutland 2006, Kamata et al. 2007). Sone et al. (2001) used this model to study fuel-air mixing in a direct injection IC engine. This model was validated with benchmark cases of shear layer and backward facing step before applying to engine simulations. The results indicate that the LES model was able to capture unsteady features of fuel-air mixing. Lee et al. (2002) used this model to simulate a direct-injection diesel engine combustion process. Results indicate that LES prediction of pressure traces matched well with experimental results and also indicate that LES resolves large kinetic energy scales which give realistic turbulent viscosity predictions. Jhavar and Rutland (2006) compared various LES models and also showed the differences with RANS models. These model results were compared with RNG k-ε model results for the Caterpillar 3401 single cylinder direct injection diesel engine. The LES model results showed very good agreement with the experimental data compared to RANS results. Kamata et al. (2007) used this model to investigate instantaneous and statistical spray structures of diesel spray. The simulation predictions were validated by experimental visualizations of diesel spray. The results indicated that the LES model was able to capture instantaneous spray structures and heterogeneity at the periphery of the spray.

The one-equation, non-viscosity dynamic model, also known as the Dynamic Structure model, was developed by Pomraning and Rutland (2002). An additional transport equation for the sub-grid scale turbulent kinetic energy is added to the dynamic model. A test filter is applied over a sub-grid scale filter. The sub-grid stress term is calculated from the sub-grid scale filter and test filter, and sub-grid scale turbulent kinetic energies using a tensor coefficient based on the Leonard stress term. Jhavar and Rutland (2006) used this model for fuel-air mixing and combustion simulations in a direct injection diesel engine.

In engine flow simulations, it is important to capture the unsteady cycle-to-cycle differences of the flow fields. LES is suitable for engine flow simulations because it resolves the instantaneous flow fields within the engine and thus the details of local flow structures can be simulated efficiently and effectively.

1.2.3 Combustion modeling of HCCI engines

Yao et al. (2009) discussed five types of models applied to HCCI engine combustion modeling which are summarized as follows:

1. Zero-dimensional single-zone models with detailed chemistry

2. Quasi-dimensional multi-zone model with detailed chemistry
3. One-dimensional engine cycle model with detailed chemistry
4. Multi-dimensional CFD model with multi-zone detailed chemistry
5. Multi-dimensional CFD model with detailed chemistry

Zero-dimensional single-zone models with detailed chemistry (Dec and Sjöberg 2003)**:** In these models, the in-cylinder temperature and mixture concentration are assumed to be homogeneous. These models are single zone in the sense that the simulations were carried out on a single point in space marching in the time direction. There is no physical domain and geometry. The detailed chemical kinetic processes of hydrocarbon fuels in HCCI combustion have been studied by this approach (Curran et al. 2002). This method can give a good prediction of the onset of combustion and the combustion mechanism, but cannot predict rate of heat release, the combustion duration and emissions due to the absence of geometry information and flow effects.

Quasi-dimensional multi-zone with detailed chemistry (Fiveland and Assanis 2001, Kongsereeparp and Checkel 2007)**:** In this model, the temperature inhomogeneity of the combustion is taken into account by considering a number of zones with varying temperatures. Here the computational domain contains a number of zones and each zone interacts with the surroundings for heat transfer, mass transfer and pressure work. Fiveland and Assanis (2001) used a comprehensive multi-zone model to predict performance and emissions under turbo-charge conditions. The model is based on a full cycle simulation code and includes an adiabatic zone, boundary layer zone and a crevice zone. Recently, a modified multi-zone chemical kinetic model was developed by Kongsereeparp and Checkel (2007) to describe the effects of base fuel/reformed fuel blends on HCCI engine combustion. Their model includes imperfectly stirred mixture effects via the virtual enthalpy exchange between hotter internal residual and cooler intake mixtures. No mass transfer was considered in their model.

This type of quasi-dimensional multi-zone model with detailed chemistry considers the effect of temperature inhomogeneities by the number of zones. These models can predict the start of combustion, heat release and emissions, but they do not take into consideration the geometry effects and residual gas effects on combustion.

One-dimensional engine cycle with detailed chemistry (Fiveland and Assanis 2000, Ogink 2003, Narayanaswamy and Rutland 2004): In these models, a commercial 1-D cycle simulation software is coupled with a chemical kinetic solver e.g., CHEMKIN (Kee et al. 1996). By using cycle simulation codes, the initial temperature and species compositions are calculated. These parameters are taken as inputs to the chemical kinetic solvers to simulate combustion. Fiveland and Assanis (2000) simulated a full engine cycle using a 1-D cycle simulation model and CHEMKIN. Xu et al. (2003) developed a model combining the CHEMKIN-based single-zone chemical kinetic model with the Ricardo 1-D gas dynamics and engine simulation code WAVE. Ogink (2003) developed a BOOST-CHEMKIN single-zone model to accurately predict the moment of auto-ignition and the rate of heat release in a gasoline HCCI engine. Narayanaswamy and Rutland (2004) coupled GT-Power, a commercial 1-D engine cycle code with external cylinder model which incorporates sub-models for fuel injection, vaporization, multi-zone detailed chemistry calculations, heat transfer, energy conservation and species conservation.

The advantages of these models is that they can simulate complete engine cycle by using inputs from experimental data at the intake as the initial conditions and they can calculate engine-out emissions. These models can give faster estimation of the engine-out emissions than multi-dimensional modeling and help in engine designs, but the temperature inhomogeneity and geometry effects are not considered.

Multi-dimensional CFD with multi-zone detailed chemistry (Aceves et al. 2001, Babajimopoulos et al. 2002, Aceves et al. 2004): In these models multi-dimensional CFD solvers are coupled with multi-zone combustion solvers. The CFD solver gives the flow field at the start of the combustion and the flow field is segregated into several zones based on temperature. The multi-zone chemical kinetics code is initialized by different initial temperature and other needed parameters e.g., species mass fractions, obtained from the CFD code. The multi-zone chemical kinetics code simulates the combustion process and returns back parameters to the flow solver. This solution methodology takes into account the effect of temperature distributions in the cylinder. These models are able to predict satisfactorily the cylinder pressure traces and emissions. Babajimopoulos et al. (2002) developed the model to simulate a full engine cycle to study the effects of valve movement and gas exchange processes. Results obtained by this model showed large variations in temperature, and significant inhomogeneities in residual gases within the combustion chamber at the start of combustion. Aceves et al. (2004) used this model to investigate HC and CO emissions in a HCCI engine under low-load conditions. The results showed good agreement with experiments.

These types of models take the advantage of using CFD solvers to determine the temperature in-homogeneities within the cylinder. However, the formation of zones based on temperature would have effects on heat release rate and combustion duration. These models indicate that multi-dimensional modeling of the flow field and integration of chemical kinetic codes are necessary to predict the HCCI combustion performance and emissions.

Multi-dimensional CFD with detailed chemistry:

Agarwal and Assanis (1998) integrated CHEMKIN with KIVA-3 to study auto-ignition of natural gas injected under compression ignition conditions. A detailed chemical kinetic mechanism consisting of 22 species and 104 elementary reactions was used. The results showed that both flow and ignition modeling are needed to get quantitative predictions of ignition delay under compression ignition conditions. It was shown that coupling of multi-dimensional flow and multi-step chemistry are essential to reveal detailed features of the ignition process.

Kong et al. (2001) integrated KIVA and CHEMKIN to study HCCI engine combustion with detailed chemical kinetics. Effects of turbulent mixing on the reaction rates were also considered. The results showed good agreement with experimental data for a wide range of engine conditions, including various fuels, injection systems, engine speeds and EGR levels. Ignition timings were predicted well. It was found that the presence of residual radicals could enhance the mixture reactivity and hence shorten the ignition delay time. The model was applied to simulate two different heavy-duty diesel engines operating in the HCCI mode (Volvo engine and Caterpillar engine). The computations used a 2-D mesh and started from intake valve closure. A reduced reaction mechanism for iso-octane, which contains 79 species and 398 reactions, was used.

Kong and Reitz (2002) studied the turbulence mixing effects using detailed chemical kinetics and showed that the KIVA/CHEMKIN coupling was able to simulate the ignition and combustion process in three different HCCI engines including a Cooperative Fuel Research (CFR) engine and two modified heavy-duty diesel engines. The results showed that the ignition timings were predicted correctly using the detailed chemistry without the need to adjust kinetic constants in the reaction mechanism. However, the kinetics-controlled reaction rates resulted in too high heat release rates, and the effects of turbulent mixing needed to be considered to give a better agreement in the combustion phasing with the experiments. The computations started at intake valve closure and assumed a uniform distribution of mixture properties.

Kong et al. (2003) numerically investigated the pre-mixed iso-octane HCCI engine combustion and its sensitivity to computational mesh. The KIVA/CHEMKIN coupling developed by Kong et al. (2001) was used. The method is able to simulate accurately the ignition timing and combustion phasing for various engine conditions. The CO emission was under-predicted by this method. The results show that most of HC and CO emissions are initiated in the crevice region and in the vicinity of cylinder walls. A sensitivity study of the computational grid resolution indicated that the combustion predictions were relatively insensitive to the grid density. The computations also show that HCCI combustion and emissions are extremely sensitive to the initial mixture temperature. The computations were started at the time of intake valve closure and a 2-D sector mesh was used. The initial mixture temperature was estimated by using a 1-D engine cycle analysis program.

Jhavar (2007) studied a direct injection HCCI diesel engine using LES for turbulence and CHEMKIN for detailed chemistry. He studied different LES models and showed that LES is able to capture large scale flow structures. Multiple engine cycles were simulated to identify sources of cycle-to-cycle variations. The results show that simulations from intake to exhaust using CHEMKIN-LES match better with experimental data than using CHEMKIN-RANS. This was attributed to the capability of LES in representing fuel-air mixing and flow structures better than RANS. LES simulations were also used to evaluate variable valve actuation strategies. It was concluded that the LES approach allows simulating the complete engine cycle with detailed information on the flow, mixing and combustion of an HCCI engine.

This kind of multi-dimensional CFD method with detailed chemistry is the state-of–the-art in HCCI engine modeling. It can provide necessary information regarding combustion process although it is time consuming and requires high computational power.

1.2.4 Summary of literature review

As an alternative for CI and SI engines, HCCI combustion technologies can play a significant role in reducing emissions and improving combustion efficiency. But, the current available HCCI technologies are still not mature enough to be commercialized. All the challenges related to HCCI technologies can always be tracked back to the fundamental understanding of the combustion process that involves turbulent flow, turbulent combustion with hundreds, if not thousands, of species and multi-step chemical reactions.

Therefore, the following are needed to meet these challenges:

(1) a fundamental understanding of turbulent flow structures and their effects on the combustion performance;

(2) a fundamental understanding of fuel reaction mechanism with detailed chemistry and their effect on the combustion performance;

(3) an innovative HCCI combustion strategy that can provide better control on the combustion process.

1.3 Objectives

The long term objective for HCCI combustion research is to develop an effective combustion strategy to reach the idealized goal of HCCI, i.e., better fuel economy and lower emissions than that of the existing conventional engines.

The short term objectives, i.e., the objectives for this dissertation, are as follows:

(1) to develop an effective numerical solver that can deal with detailed turbulent flow structures with detailed chemical kinetics in HCCI combustion;

(2) to propose an innovative HCCI combustion strategy and evaluate its performance by using the solver developed in (1).

1.4 Methodology

In this dissertation, a numerical method will be developed by integrating the original KIVA-3V solver with CHEMKIN and Large Eddy Simulation, and validated by comparing the numerical results with the available experimental results, and employed to evaluate the combustion performance of an innovative HCCI combustion strategy that will be proposed through this dissertation.

The Large Eddy Simulation sub-grid scale model developed by Sone et al. (2001) and the CHEMKIN solver with iso-octane multi-step reaction mechanism developed by Jia and Xie (2006) will be implemented in the original KIVA-3V solver. Hereafter, this integrated solver will be called CKL (CHEMKIN-KIVA-LES) solver for convenience.

This CKL solver will be validated by using the experimental results from Dec and Sjöberg. (2003) for Cummins B-series production diesel engine with a 2-D axi-symmetric domain, and results from Gnanam (2008) indirect injection type Kubota D905 diesel engine with a 3-D domain.

An innovative HCCI combustion strategy with Internal Mixing and Reformation (IMR) chamber will be proposed and evaluated by using the CKL solver.

1.5 Dissertation overview

The governing equations, algorithm, and solution methodology are explained in Chapter 2; the grid sensitivity and the comparison of RANS and LES turbulence models for a vertical valve engine case are discussed in Chapter 3; the CKL solver is validated with a Cummins B-series production diesel engine in Chapter 4; the CKL solver is further validated with an indirect injection type compression ignition engine in Chapter 5 with a discussion of the combustion process of this engine; the function of a IMR chamber is discussed and evaluated in Chapter 6.

Chapter 2

Numerical Methodology

2.1 KIVA-3V solver

KIVA-3V uses a time-marching, finite volume scheme which solves the equations of mass, momentum, energy and turbulence using a combined Lagrangian and Eulerian technique in three solution phases.

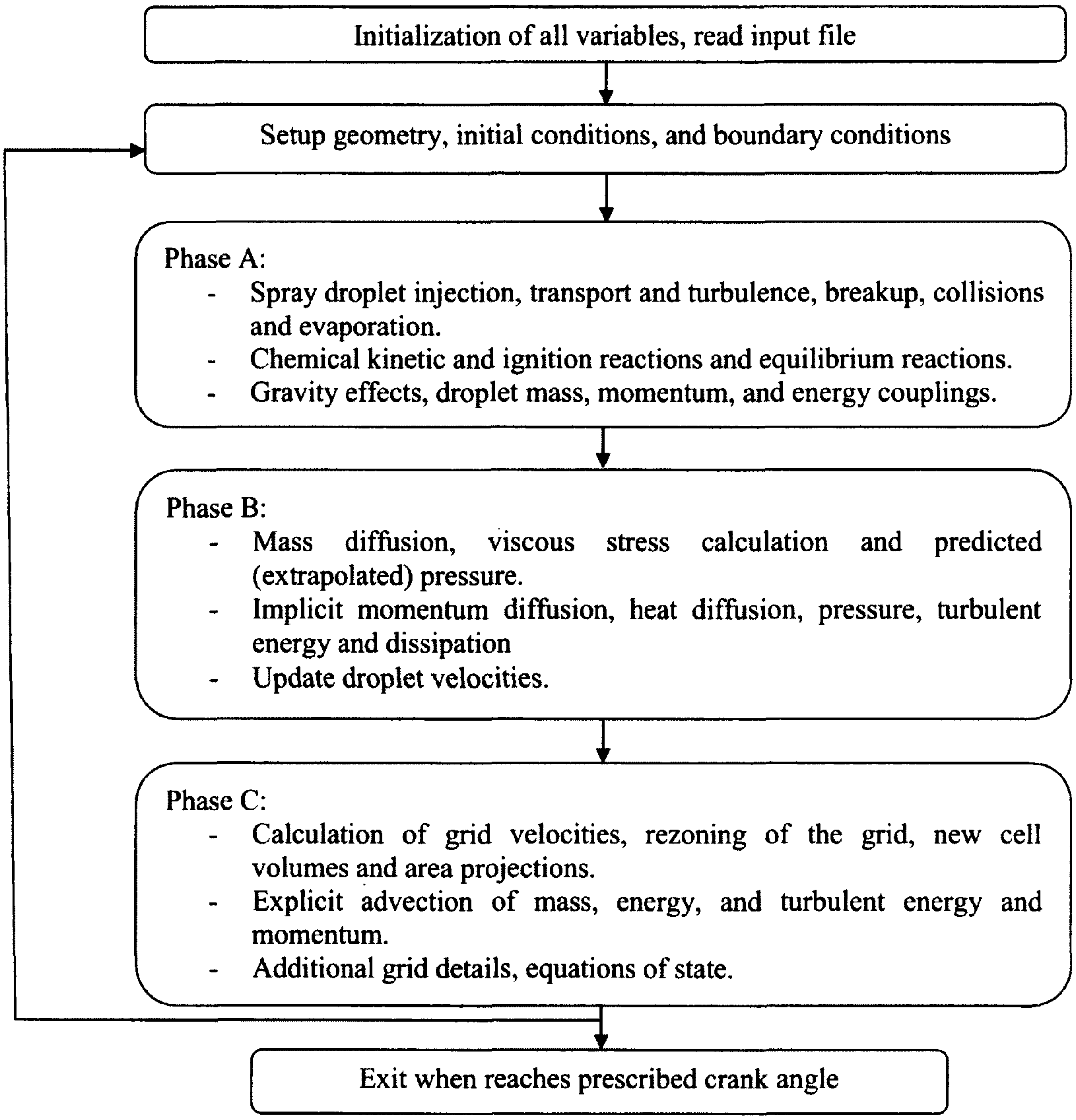

Initialization of all variables, read input file
Setup geometry, initial conditions, and boundary conditions
Phase A:
- Spray droplet injection, transport and turbulence, breakup, collisions and evaporation.
- Chemical kinetic and ignition reactions and equilibrium reactions.
- Gravity effects, droplet mass, momentum, and energy couplings.
Phase B:
- Mass diffusion, viscous stress calculation and predicted (extrapolated) pressure.
- Implicit momentum diffusion, heat diffusion, pressure, turbulent energy and dissipation
- Update droplet velocities.
Phase C:
- Calculation of grid velocities, rezoning of the grid, new cell volumes and area projections.
- Explicit advection of mass, energy, and turbulent energy and momentum.
- Additional grid details, equations of state.
Exit when reaches prescribed crank angle

Figure 2.1 KIVA-3V solution algorithm phases, details and time stepping procedure.

The governing equations in KIVA-3V and the modified LES equations are given in the next section.

The finite volume procedure is second order accurate in space and first order accurate in time. The arbitrary Lagrangian-Eulerian (ALE) method is used in KIVA-3V for temporal differencing. In KIVA-3V, each time step is broken into three separate phases as shown in Figure 2.1.

2.2 Governing equations

2.2.1 The governing equations of gas phase

The KIVA-3V code can be used to solve both laminar and turbulent flows. The mass, momentum, and energy equations for the two cases differ primarily in the form and magnitude of the transport coefficients.

The continuity equation for species *m* is given as follows:

$$\frac{\partial \rho_m}{\partial t}+\nabla\cdot\left(\rho_m u\right)=\nabla\left[\rho D\nabla\left(\frac{\rho_m}{\rho}\right)\right]+\dot{\rho}_m^c+\dot{\rho}_m{}^s\delta_{m,1} \tag{2.1}$$

where ρ_m is the mass density of species *m*, ρ is the total mass density, and u is the fluid velocity. Fick's diffusion law is assumed with a single diffusion coefficient D. The final two terms $\dot{\rho}_m^c$ and $\dot{\rho}_m^s$ are density change per unit time due to chemistry and spray respectively. $\delta_{m,1}$ is the Kronecker delta function, which is equal to 1 when m=1, and 0 otherwise. By summing Eq. (2.1) over all species, the total fluid density equation becomes:

$$\frac{\partial \rho}{\partial t}+\nabla\cdot\left(\rho u\right)=\dot{\rho}^s \tag{2.2}$$

where $\dot{\rho}^s$ is source term due to spray.

The momentum equation for the fluid mixture is:

$$\frac{\partial(\rho u)}{\partial t}+\nabla\cdot\left(\rho u u\right)=-\frac{1}{a^2}\nabla P-A_{tkesw}\nabla\left(\frac{2}{3}\rho k\right)+\nabla\cdot\sigma+F^s+\rho g \tag{2.3}$$

where P is the fluid pressure. The dimensionless quantity, a, is used in conjunction with the Pressure Gradient Scaling (PGS) Method. This is a method for enhancing computational efficiency in low Mach number flows, where the pressure is nearly uniform. The PGS method lowers the courant number to improve the computational efficiency. A_{tkesw} indicates whether the flow is laminar or turbulent (0 for laminar, 1 for turbulence). σ is the viscous stress tensor, which is given with μ and λ being the first and second coefficients of viscosity, respectively.

$$\sigma = \mu\left[\nabla u + (\nabla u)^T\right] + \lambda \nabla \cdot u E \tag{2.4}$$

The superscript T denotes transpose, and E is the unit matrix. μ and λ are the coefficients of viscosity and are defined in equations (2.14) and (2.15). F^s in the momentum equation (2.3) is the rate of momentum gain per unit volume due to the spray. The specific body force g is assumed to be constant. k is the turbulent kinetic energy.

The internal energy equation is given as follows:

$$\frac{\partial(\rho I)}{\partial t} + \nabla \cdot (\rho u I) = -P\nabla \cdot u + (1 - A_{tkesw})\sigma : \nabla u - \nabla \cdot J + A_{tkesw}\rho\varepsilon + \dot{Q}^c + \dot{Q}^s \tag{2.5}$$

where I is the specific internal energy, exclusive of chemical energy, ε is the dissipation rate of turbulent kinetic energy, and J is the heat flux vector, which is the sum of contributions due to heat conduction and enthalpy diffusion, i.e.,

$$J = -K\nabla T - \rho D \sum_m h_m \nabla\left(\rho_m / \rho\right) \tag{2.6}$$

where T is the fluid temperature, h_m is the specific enthalpy of species m, and K is the coefficient of heat conduction. The final two terms in the internal energy equation (2.5), $\dot{Q}^c$ and $\dot{Q}^s$, are source terms due to chemical heat release and spray interaction.

The turbulence quantities (k and ε) that appear in the conservation equation are given by their own transport equation (standard k-ε equations with some added terms cf., Launder and Spalding 1972):

$$\frac{\partial(\rho k)}{\partial t} + \nabla \cdot (\rho u k) = -\frac{2}{3}\rho k(\nabla \cdot u) + \sigma : \nabla \cdot u + \nabla \cdot \left(\frac{\mu}{\mathrm{Pr}_k}\nabla k\right) - \rho\varepsilon + W^s \tag{2.7}$$

$$\frac{\partial(\rho\varepsilon)}{\partial t}+\nabla\cdot(\rho u\varepsilon)=-\left(\frac{2}{3}c_1-c_3\right)\rho\varepsilon(\nabla\cdot u)+\nabla\cdot\left(\frac{\mu}{\mathrm{Pr}_\varepsilon}\nabla\varepsilon\right)+\frac{\varepsilon}{k}\left[c_1\sigma:\nabla u-c_2\rho\varepsilon+c_s W^s\right] \tag{2.8}$$

where W^s is the source term due to the interaction with spray, and the standard values of some constants often used in engine calculation are c_1 =1.44, c_2=1.92, c_3 =-1.0, c_s=1.5, Pr_k =1.0, Pr_ε =1.3.

In addition, the state equations are assumed to be those of an ideal gas mixture and corresponding thermodynamic properties are taken from the JANAF tables, cf,. Stull and Prophet (1974). Therefore,

$$p=R_o T\sum_m\left(\rho_m/W_m\right) \tag{2.9}$$

$$I(T)=\sum_m\left(\rho_m/\rho\right)I_m T \tag{2.10}$$

$$c_p(T)=\sum_m\left(\rho_m/\rho\right)c_{pm}(T) \tag{2.11}$$

$$h_m(T)=I_m(T)+R_o T/W_m \tag{2.12}$$

where R_o is the universal gas constant, W_m is the molecular weight of species m, I_m is the specific internal energy of species m, and c_{pm} is the specific heat at constant pressure of species m. The values of h_m and c_{pm} are taken from the JANAF table (Stull and Prophet 1974). The thermodynamic data of species properties also can be calculated by the NASA polynomial coefficients. The transport coefficients in KIVA-3V are taken to be:

$$\mu=(1-A_o)\rho\upsilon_o+\mu_{air}+A_o c_\mu k^2/\varepsilon \tag{2.13}$$

$$\lambda=A_3\mu \tag{2.14}$$

$$K=\frac{\mu c_p}{\mathrm{Pr}} \tag{2.15}$$

$$D=\frac{\mu}{\rho S_c} \tag{2.16}$$

$$\mu_{air} = \frac{A_1 T^{0.5}}{T + A_2} \tag{2.17}$$

where diffusivity υ_o is an input constant, and A_1, A_2 and c_μ are constants. A_3 is taken to be -2/3 for turbulent flow but can be arbitrarily specified in laminar flows. Pr (Prandtl number) and S_c (Schmidt number) are input constants.

The detailed information about the spray model and the governing equations of the liquid phase is described in Appendix D (Amsden et al. 1989).

2.2.2 The LES model

In LES, the flow field is decomposed into a resolved scale component, which is solved directly, and a sub-grid scale component, which is modeled. To achieve this, a filtering operation is required which is in physical space the local spacial average of the flow field. The decomposition of turbulent scales into large scale motions and small scale motions can be given as:

$$f = \bar{f} + f'' \tag{2.18}$$

where f is the instantaneous quantity, $\bar{f}$ is the resolved quantity, and f'' is the unresolved quantity. The resolved quantity is given by,

$$\bar{f}(x) = \int_V G(x, y) f(y) dy \tag{2.19}$$

where G is a spatial filter function and V is the filter domain. The spatial filter G is a function of space having characteristic filter width Δ. In this study, the characteristic filter width is taken to be the characteristic length scale of each computational cell, that is, the cubic root of local computational cell volume $V^{1/3}$.

Following Erlebacher et al. (1992), Favre spatial filtering is adopted for compressible flow applications:

$$\tilde{f} = \frac{\overline{\rho f}}{\bar{\rho}}, \tag{2.20}$$

then the flow field is decomposed into a Favre filtered resolved part denoted by (~) and a sub-grid (unresolved) part denoted by (") such as

$$f = \tilde{f} + f'' \tag{2.21}$$

Filtering the Navier-Stokes equations yields the following LES equations:

The continuity equation is given as:

$$\frac{\partial \bar{\rho}}{\partial t} + \frac{\partial \bar{\rho}\tilde{u}_j}{\partial x_j} = \bar{\dot{\rho}}^s \tag{2.22}$$

This continuity equation is similar to the RANS equation.

The momentum equation is given as:

$$\frac{\partial \bar{\rho}\tilde{u}_t}{\partial t} + \frac{\partial}{\partial x_j}\left(\bar{\rho}\tilde{u}_i\tilde{u}_j - \bar{\tau}_{ij} + \tau_{ij}^{sgs}\right) = \bar{F}_i^s \tag{2.23}$$

$\bar{\tau}_{ij}$ is viscous stress tensor,

τ_{ij}^{sgs} is sub-grid stress tensor,

$\bar{F}_i^S$ is source term due to spray drag.

Where $\bar{\tau}_{ij}$ is obtained by filtering the stress tensor and neglecting contribution from unresolved field,

$$\bar{\tau}_{ij} = -\bar{p}\delta_{ij} + 2\bar{\rho}\bar{\nu}\left(\bar{S}_{ij} - \frac{1}{3}\bar{S}_{kk}\delta_{ij}\right) \tag{2.24}$$

where the pressure is determined by the equation of state and δ_{ij} is Kronecker delta.

$$\bar{p} = \bar{\rho}\tilde{T}\sum_{m=1}^{N} R_m\tilde{Y}_m \tag{2.25}$$

where R_m and $\tilde{Y}_m$ are the m^{th} species gas constant and mass fraction, and the sub-grid scale stress tensor is given by

$$\tau_{ij}^{sgs} = \bar{\rho}\left[\widetilde{u_i u_j} - \tilde{u}_i\tilde{u}_j\right] \tag{2.26}$$

The sub-grid scale (SGS) stress tensor is conventionally decomposed into three terms as shown:

$$\begin{aligned}\tau_{ij}^{sgs} &= \widetilde{u_i u_j} - \tilde{u}_i \tilde{u}_j \\ &= \widetilde{\tilde{u}_i \tilde{u}_j} - \tilde{u}_i \tilde{u}_j + \widetilde{\tilde{u}_i u''_j} + \widetilde{u''_i \tilde{u}_j} + \widetilde{u''_i u''_j} \\ &= L_{ij} + C_{ij} + R_{ij}\end{aligned} \qquad (2.27)$$

The L_{ij} term is known as Leonard term, C_{ij} is known as cross term and R_{ij} is known as Reynolds term.

In the present study, SGS stress is modeled with the eddy viscosity hypothesis by employing the sub-grid turbulent kinetic energy, thus,

$$\tau_{ij}^{sgs} = -2\bar{\rho}\nu_t\left(\tilde{S}_{ij} - \frac{1}{3}\tilde{S}_{kk}\delta_{ij}\right) + \frac{2}{3}\bar{\rho}k^{sgs}\delta_{ij} \qquad (2.28)$$

where eddy viscosity is defined by $\nu_t = C_\nu k^{sgs1/2}\overline{\Delta}$.

Sub-grid turbulent kinetic energy is obtained by solving the following equation proposed by Sone et al. (2001),

$$\frac{\partial \bar{\rho} k^{sgs}}{\partial t} + \frac{\partial \bar{\rho}\tilde{u}_j k^{sgs}}{\partial x_j} = P^{sgs} - D^{sgs} + \frac{\partial}{\partial x_j}\left(\bar{\rho}\frac{\nu_t}{\mathrm{Pr}_t}\frac{\partial k^{sgs}}{\partial x_j}\right) + \bar{\dot{W}}^s \qquad (2.29)$$

where the production term P^{sgs} is given by

$$P^{sgs} = -\tau_{ij}^{sgs}\frac{\partial \tilde{u}_i}{\partial x_j} \qquad (2.30)$$

and the sub-grid energy dissipation rate term D^{sgs} is closed by

$$D^{sgs} = C_\varepsilon \bar{\rho} k^{sgs3/2} / \Delta \qquad (2.31)$$

For C_ν and C_ε, 0.067 and 0.916 are used.

KIVA-3V employs the internal energy equation instead of total energy equation, so the filtered energy equation for LES in terms of specific internal energy ($\tilde{e}$) is given as

$$\frac{\partial \bar{\rho}\tilde{e}}{\partial t}+\frac{\partial \bar{\rho}\tilde{u}_j\tilde{e}}{\partial x_j}+\bar{p}\frac{\partial \tilde{u}_j}{\partial x_j}+\frac{\partial h_j^{sgs}}{\partial x_j}+\frac{\partial \bar{q}_j}{\partial x_j}-\bar{\sigma}_{ij}\frac{\partial \tilde{u}_i}{\partial x_j}-\Theta^{sgs}-\Pi^{sgs}=\bar{\dot{Q}}^c+\bar{\dot{Q}}^s \tag{2.32}$$

where $\bar{q}_j$, the filtered heat flux, is given by $\bar{q}_j=-\bar{K}\frac{\partial \tilde{T}}{\partial x_j}-\bar{\rho}\sum_{m=1}^{N}\tilde{h}_m\tilde{D}_m\frac{\partial \tilde{Y}_m}{\partial x_j}$ (2.33)

unresolved viscous work $\sigma_i^{sgs}=[\overline{u_j\tau_{ij}}-\tilde{u}_j\bar{\tau}_{ij}]$, (2.34)

$\bar{\dot{Q}}^c$ = heat release per unit time due to chemistry

$\bar{\dot{Q}}^s$ = heat release per unit time due to spray

In the above equation (2.32) the unknown terms, Π^{sgs}, Θ^{sgs} and h_j^{sgs} are unclosed. The pressure gradient correlation term Π^{sgs} is ignored and h_j^{sgs} term is modeled by gradient diffusion as

$$h_j^{sgs}=-\bar{\rho}\frac{\nu_t C_p}{\Pr_t}\frac{\partial \tilde{T}}{\partial x_j} \tag{2.35}$$

Θ^{sgs} stands for sub-grid viscous work modeled by turbulent dissipation rate

$$\Theta^{sgs}=C_\varepsilon\bar{\rho}k^{sgs3/2}/\Delta \tag{2.36}$$

The filtered species equation is given as

$$\frac{\partial \bar{\rho}\tilde{Y}_m}{\partial t}+\frac{\partial}{\partial x_j}\left(\bar{\rho}\tilde{u}_j\tilde{Y}_m-\bar{\rho}\bar{D}_m\frac{\partial \tilde{Y}_m}{\partial x_j}+\Phi_{j,m}^{sgs}+\theta_{j,m}^{sgs}\right)=\bar{\rho}^c+\bar{\rho}^s \tag{2.37}$$

where sub-grid species mass flux is modeled by $\Phi_{i,m}^{sgs}=-\bar{\rho}\frac{\nu_t}{Sc_t}\frac{\partial \tilde{Y}_m}{\partial x_i}$ (2.38)

and diffusive mass flux term is ignored since this term is small compared to sub-grid species mass flux term.

In the present work the one-equation sub-grid scale eddy viscosity model, known as the k-Δ model, was used (Sone et al. 2001). This model has been validated with benchmark cases of shear layer and backward facing step simulations.

2.3 Combustion model

2.3.1 KIVA combustion model

In KIVA-3V the chemical reactions are divided into two types based on rate of reaction; kinetic (slow) and/or equilibrium (fast) reactions, respectively. In this dissertation, kinetic reactions are considered. Details about equilibrium reactions are given in Amsden et al. (1989).

An elementary chemical reaction can be generally symbolized by

$$\sum_m a_{mr} x_m \Leftrightarrow \sum_m b_{mr} x_m \tag{2.39}$$

where x_m represents one mole of species m, while a_{mr} and b_{mr} are the integral stoichimetric coefficients of species on the left and right hand sides of the reaction r and must satisfy the following mass conservation of the chemical reactions:

$$\sum_m (a_{mr} - b_{mr}) W_m = 0 \tag{2.40}$$

where W_m is the molecular weight. The rate of kinetic reaction r is given by

$$\dot{\omega}_r = \kappa_{fr} \prod_m \left(\rho_m / W_m \right)^{a'_{mr}} - \kappa_{br} \prod_m \left(\rho_m / W_m \right)^{b'_{mr}} \tag{2.41}$$

where the exponents a'_{mr} and b'_{mr} specify order of the reaction, ρ_m is the mass density of species m, κ_{fr} and κ_{br} are the coefficients of the forward and backward reactions and are assumed to be of a generalized Arrhenius form:

$$\kappa_{fr} = A_{fr} T^{\xi_{fr}} \exp\left\{ - E_{fr} / T \right\} \tag{2.42}$$

and

$$\kappa_{br} = A_{br} T^{\xi_{br}} \exp\left\{ - E_{br} / T \right\} \tag{2.43}$$

where A_{fr}, A_{br}, ξ_{fr}, and ξ_{br} are constants and E_{fr} and E_{br} are equivalent activation temperatures.The source term due to chemical reactions in the continuity equation is given by

$$\dot{\rho}_m^c = W_m \sum_r (b_{mr} - a_{mr})\dot{\omega}_r \tag{2.44}$$

and the chemical energy release term is given by

$$\dot{Q}^c = \sum_r Q_r \dot{\omega}_r \tag{2.45}$$

where Q_r is the negative of the enthalpy of reaction at absolute zero, i.e.,

$$Q_r = \sum_m (a_{mr} - b_{mr})(\Delta h_f^0)_m \tag{2.46}$$

and $(\Delta h^0_f)_m$ is the enthalpy of formation of species m at absolute zero.

In KIVA-3V combustion model, the one step global reaction is solved along with NO_x mechanism. This model is simple so it does not give any detailed information about the combustion process and emissions. In the HCCI engine combustion process, the detailed chemical kinetics plays an important role in combustion and emissions. To obtain detailed information of the combustion process and emissions, a combustion model with detailed chemical kinetics, e.g., CHEMKIN, is required.

2.3.2 CHEMKIN

CHEMKIN is a highly structured and modular package that requires the manipulation of a number of programs, subroutines, and data files. The general structure of the CHEMKIN-II package is shown in Figure 2.2. The interpreter is a program that reads a symbolic description of a reaction mechanism and then extracts the needed thermodynamic data for each species involved from the thermodynamic database. The input file *chem.inp* contains details of the number of species involved in the kinetic reactions and description of reactions. The thermodynamic database is opened as *thermo.dat*. This file contains thermodynamic data related to each species. The primary output from the interpreter is a binary file called the linking file. This file contains all required information about the elements, species, and reactions in the user's mechanism. The linking file is a binary file called *chem.bin*. This file must be opened in the user's code. Once the interpreter has been executed and the linking file created, the user is ready to use the gas-phase subroutine library. Subroutines from this library are called from the user's FORTRAN code. Selection of CHEMKIN subroutines for any problem begins by finding the appropriate equations in the CHEMKIN manual. Normally, only a few of the subroutines in the package would be called for any one problem (Kee et al. 1996).

2.3.3 KIVA-CHEMKIN integration

KIVA-3V provides information related to fluid and species for each computational cell for each computational time instant. CHEMKIN solves the details chemistry of reaction mechanism.

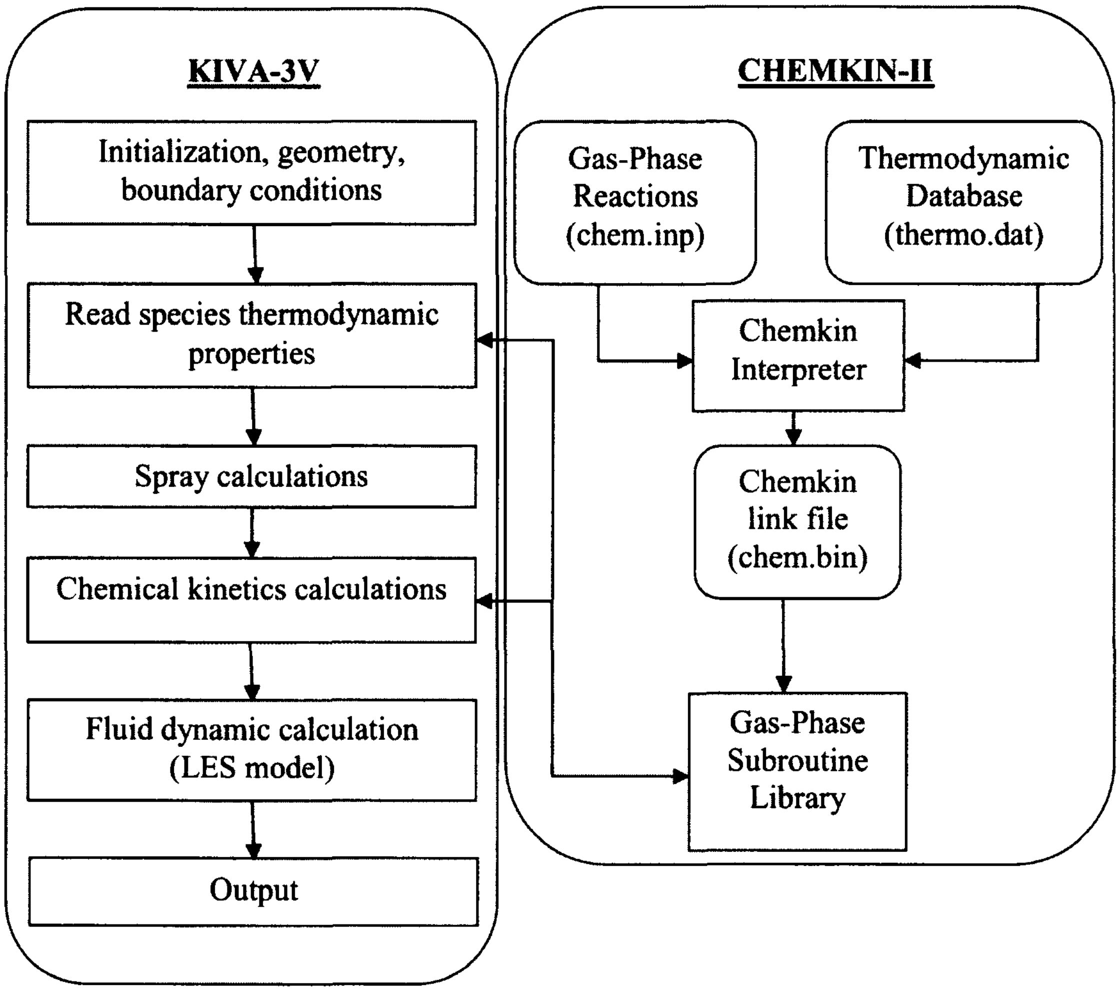
KIVA-3V
Initialization, geometry, boundary conditions
Read species thermodynamic properties
Spray calculations
Chemical kinetics calculations
Fluid dynamic calculation (LES model)
Output
CHEMKIN-II
Gas-Phase Reactions (chem.inp)
Thermodynamic Database (thermo.dat)
Chemkin Interpreter
Chemkin link file (chem.bin)
Gas-Phase Subroutine Library

Figure 2.2 KIVA-3V and CHEMKIN-II solvers integration

As shown in Figure 2.2 for the schematic of the integrated solver, CHEMKIN gas-phase library subroutines are called to read species into KIVA-3V, and to update the species parameters and calculate enthalpies during initial setup. Once the chemical kinetic calculations start, KIVA-3V transfers information on the temperature, pressure and compositions of each cell to CHEMKIN, in which each cell is treated as a single constant volume reactor. CHEMKIN solves the chemical reactions with an ordinary differential equation solver and returns the heat release rate and new compositions to KIVA-3V.

2.3.4 KIVA-CHEMKIN combustion model

The KIVA-CHEMKIN combustion model (Kong et al. 2001) was used to calculate the heat release rate and change in species density, given by

$$\bar{\dot{Q}}^{c} = -\sum_{m=1}^{M} \bar{\dot{\omega}}_m \left(\Delta h_f^o\right)_m W_m \tag{2.47}$$

$$\bar{\dot{\rho}}_m = \bar{\dot{\omega}}_m W_m,\ m = 1, \cdots M \tag{2.48}$$

where ρ_m is density of species *m*, M is total number of species and ω_m and W_m are molar production rate and molecular weight of species *m,* respectively.

The molar production rate is expressed as:

$$\bar{\dot{\omega}}_m = \frac{\bar{Y}_m^* - \bar{Y}_m}{\tau_{kin,m} + \chi\tau_{turb}} \begin{cases} \bar{Y}_m : current\ concentration \\ \bar{Y}_m^* : equilibrium\ concentration \\ \tau_{kin,m} : kinetic\ timescale \\ \tau_{turb} : turbulent\ timescale \sim k/\varepsilon \end{cases} \tag{2.49}$$

The kinetic timescale is the time needed for a species to reach its equilibrium state under perfectly mixed conditions. The turbulent timescale is the time of eddy breakup given by

$$\tau_{turb} = \frac{C_{m2} k^{sgs}}{D^{sgs}} \tag{2.50}$$

The kinetic timescale is different for each species while the turbulent timescale is the same for all the species. The unknowns include the equilibrium concentration and the kinetic timescale of each species. If turbulent effects on the reaction rate are excluded, the equation (2.49) can be simplified to a kinetics-controlled reaction rate, $\omega_{kin,m}$, as

$$\bar{\omega}_{kin,m} = \frac{\bar{Y}_m^* - \bar{Y}_m}{\bar{\tau}_{kin,m}} \qquad (2.51)$$

The kinetics-controlled reaction rate can be rewritten in terms of the CHEMKIN solutions as

$$\bar{\omega}_{kin,m} = \frac{\bar{Y}'_m - \bar{Y}_m}{dt} = \frac{\Delta \bar{Y}_m}{dt} \qquad (2.52)$$

where dt is the numerical time-step, and Y_m and Y'_m are the species concentrations before and after the CHEMKIN model is called, respectively. A relation between the kinetic timescale and the equilibrium concentration of each species is then obtained by equations (2.51) and (2.52):

$$\bar{\tau}_{kin,m} = \frac{\bar{Y}_m^* - \bar{Y}_m}{\Delta \bar{Y}_m} dt \qquad (2.53)$$

However, it is impractical to solve the equilibrium concentration and the kinetic timescale for each individual species, considering that the reaction mechanism may involve hundreds of species and reactions. Two assumptions were made to help solve the equation. First, the kinetic timescale for all the species was assumed to be equal to that of the fuel. Second, the equilibrium concentration of the fuel was assumed to be zero since the fuel is likely to react into intermediate species soon after the reaction has started, even in rich conditions. Therefore, the kinetic timescale and equilibrium concentration of each species can be derived in terms of the CHEMKIN solution as

$$\left.\begin{array}{r} \bar{\tau}_{kin,m} = \bar{\tau}_{kin,fuel} \\ \bar{Y}_f^* \rightarrow 0 \end{array}\right\} \Rightarrow \left\{\begin{array}{l} \bar{\tau}_{kin} = (-\bar{Y}_f / \Delta \bar{Y}_f) dt \\ \bar{Y}_m^* - \bar{Y}_m \doteq (-\bar{Y}_f / \Delta \bar{Y}_f) \Delta \bar{Y}_m \end{array}\right. \qquad (2.54)$$

Notice that the terms $\Delta \bar{Y}_m$ and $\Delta \bar{Y}_f$ are the concentration changes of the fuel and species *m*, respectively, obtained from CHEMKIN calculations. However, in case of fuel concentration approaching zero, the kinetic timescale of CO is used as the rate limiting kinetic time since CO is transformed to CO_2 and contributes significantly to energy release after fuel consumption is completed. In terms of model formulation, the maximum of the kinetic timescales of fuel or CO is taken as the resulting kinetic timescale.

By combining equations (2.53) and (2.54), a new formula to compute the new species at the current time-step, Y_i^{n+1}, can be obtained as

$$\bar{Y}_m^{n+1} - \bar{Y}_m^n = \bar{\dot{\omega}}_m dt = \frac{\left(-\bar{Y}_f / \Delta\bar{Y}_f\right)\Delta\bar{Y}_m}{\bar{\tau}_{kin} + \tau_{turb}} dt = \frac{\bar{\tau}_{kin}}{\bar{\tau}_{kin} + \chi\tau_{turb}} \Delta\bar{Y}_m \tag{2.55}$$

This formula includes the effects of both chemical kinetics and flow turbulence on the reaction rate. The model is also formulated such that the turbulence starts to have effects after ignition has occurred. Ignition occurs at molecular level and the turbulence will not have effects on the combustion until the reaction zones grow to a size comparable to that of the turbulent eddies. From equation (2.55), if the turbulent timescale is neglected, the solution remains kinetics-controlled. The model is also formulated such that the turbulence starts to have an effect after ignition has occurred through the use of the progress variable, χ:

$$\chi = \frac{1-e^{-r}}{1-e^{-1}} = \frac{1-e^{-r}}{0.632} \tag{2.56}$$

where r is the ratio of the current amount of products to the amount of products assuming the combustion has completed, i.e., r denotes the extent of completeness of combustion in a particular region. Therefore, r is equal to zero at the beginning of combustion and approaches 1.0 as combustion progresses. Consequently the value of χ also changes from 0.0 to 1.0 exponentially.

2.4 Iso-octane mechanism – Jia-Xie mechanism

The most comprehensive detailed chemical kinetic mechanism for iso-octane (analogous to gasoline fuel) which is widely used in the scientific community is Curran's mechanism (Curran et al. 2002). It consists of 857 species and 3606 reactions. This mechanism can be used for a wide range of temperatures, pressures and equivalence ratio, but it is impractical to couple this sophisticated mechanism with multi-dimensional simulations with HCCI engine applications.

A skeletal iso-octane oxidation mechanism developed by Jia and Xie (2006) for HCCI combustion has been used to simulate the chemistry for all the combustion cases in this dissertation. Hereafter this mechanism is referred to the "Jia-Xie Mechanism". This reaction mechanism consists of 38 species and 69 reactions, which could predict satisfactorily the ignition timing, the burn rate, and emissions of HC, CO and NO_x for HCCI combustion. Jia and Xie (2006) showed that this mechanism performs well over wide ranges of temperatures, pressures, and equivalence ratios, especially at high pressures and lean equivalence ratio conditions. The low temperature mechanisms are taken from the skeletal mechanism of Tanaka et al. (2003), including the following reactions:

$C_8H_{18} + O_2 \Leftrightarrow C_8H_{17} + HO_2$ (R1)

$C_8H_{17} + O_2 \Leftrightarrow C_8H_{17}OO$ (R2)

$C_8H_{17}OO \Leftrightarrow C_8H_{16}OOH$ (R3)

$C_8H_{16}OOH + O_2 \Leftrightarrow OOC_8H_{16}OOH$ (R4)

$OOC_8H_{16}OOH \Rightarrow OC_8H_{15}OOH + OH$ (R5)

$C_8H_{18} + OH \Rightarrow C_8H_{17} + H_2O$ (R6)

$OC_8H_{15}OOH \Rightarrow OC_8H_{15}O + OH$ (R7)

The (R1) reaction shows the oxidation of fuel molecule and formation of alkyl radical and HO_2. Reactions (R2)-(R7) show the decomposition of alkyl radicals and formation of OH radicals.

$C_8H_{17} + O_2 \Leftrightarrow C_8H_{16} + HO_2$ (R8)

$HO_2 + HO_2 \Rightarrow H_2O_2 + O_2$ (R9)

The negative temperature coefficient region in the heat release curve is due to reactions (R8) and (R9) leading to lower reactivity.

$H_2O_2 + M = OH + OH + M$ (R10)

The temperature rise slowly initiates the (R10) reaction, which is an important reaction for thermal explosion. The products of the reactions (R1)-(R8) decomposed as follows:

$OC_8H_{15}O + O_2 \Rightarrow C_2H_3 + 2CH_2O + C_3H_4 + CH_3 + HO_2$ (R11)

$C_8H_{17} \Rightarrow C_4H_8 + C_3H_6 + CH_3$ (R12)

$C_8H_{16} \Rightarrow C_4H_8 + C_3H_5 + CH_3$ (R13)

The products of reactions (R11)-(R13) are decomposed based on oxidation mechanism developed by Patel et al. (2004). The reaction mechanism output from CHEMKIN is given in Appendix A. This mechanism was tested with several experimental cases; shock tube, rapid compression machine, jet stirred reactor and HCCI engine. Results showed that the mechanism performs satisfactorily under HCCI conditions over a wide range of temperatures, pressures and equivalence ratios (Jia and Xie 2006).

2.5 Summary

In this chapter, the governing equations, algorithm, numerical solution procedure for the original KIVA-3V code, KIVA-LES version of the code, the CHEMKIN solution procedure, KIVA-3V combustion model, KIVA-CHEMKIN integration and reduced detailed chemical kinetic scheme for iso-octane mechanism have been introduced. In this dissertation, the one equation k-Δ LES sub-grid model has been implemented into the original KIVA-3V solver together with the Jia–Xie Mechanism with detailed chemical kinetics using the CHEMKIN solver.

Chapter 3

Grid Sensitivity Study and Comparison of RANS and LES Turbulence Models

Computations have been performed to compare the results obtained from RANS and LES turbulence models for different the grid resolutions. Three different meshes were used for the simulations. The computations were carried out without combustion and fuel injection. The RANS turbulence model results become grid independent after reaching a certain grid resolution. In the case of the LES model, since the LES filter size depends on the size of the grid, the results obtained will capture the smallest scales. As the grid size is refined, the results from LES converge to DNS results, where all the scales in the flow field are resolved. The objective of this study is to examine the results obtained by refining the grid size and to compare between RANS and LES model predictions.

3.1 Grid generation

The grids used for simulations are generated using K3PREP, the KIVA grid generator. The vertical valve engine example case in the KIVA manual (Amsden 1997) is taken as the testing case. It consists of one intake manifold and one exhaust manifold. The piston is flat. It has the bore of 0.08255 m and stroke of 0.092075 m. The engine runs at a speed of 1500 rpm. The intake pressure and temperature are 1.0 bar and 350 K, respectively. The intake valve opens at 705 degrees ATDC and closes at 200 degrees ATDC. The exhaust valve opens at 500 degrees ATDC and closes at 5 degrees ATDC. The computations have been carried out from 15 degrees BTDC to 720 degrees ATDC.

Figure 3.1 shows the vertical valve engine mesh in 3-D and the domain with three planes (XY, XZ and YZ planes) in which the results are examined. XY plane crosses the Z axis near the top dead centre at 0.092 m from bottom. XZ plane crosses the Y axis at 0.0 m and YZ plane crosses X axis at 0.0 m.

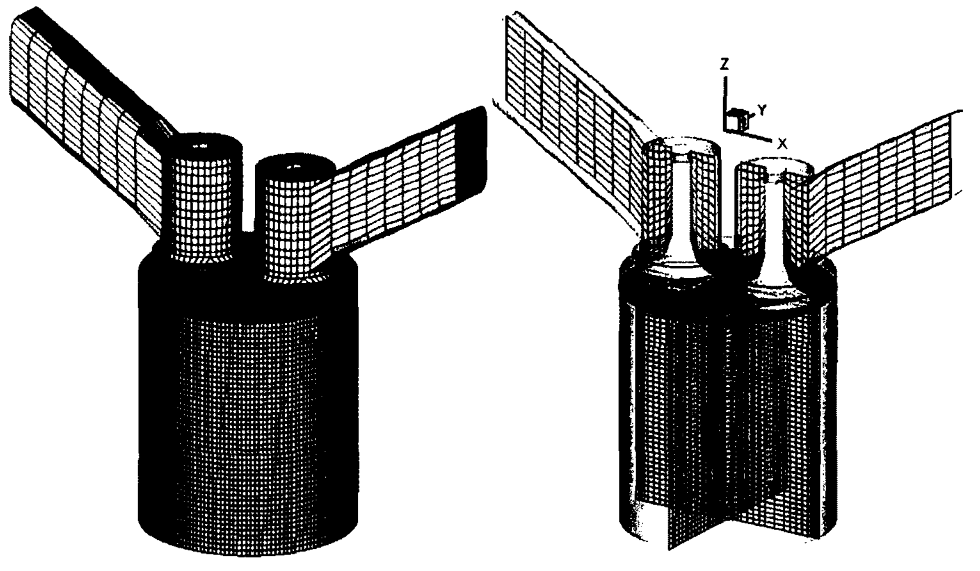

(a) (b)

Figure 3.1 Vertical valve engine mesh used for computations (a) 3-D mesh and, (b) Different planes in which results are analyzed.

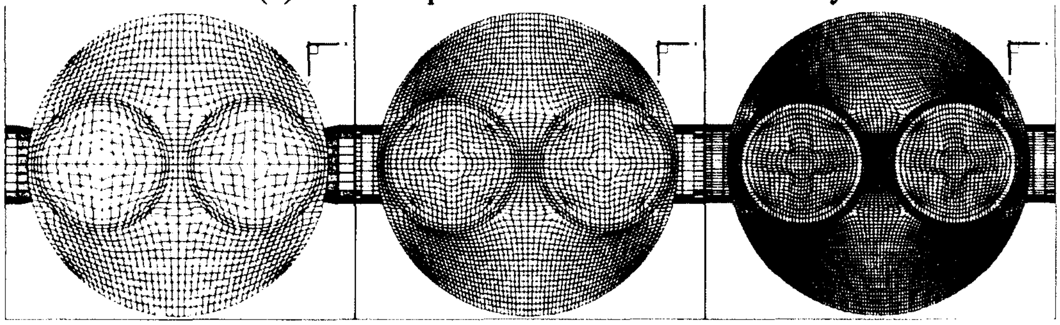

(a) (b) (c)

Figure 3.2 Grid resolutions for three different meshes (a) Coarse grid, (b) Medium grid, and (c) Fine grid.

Details of three different grids generated are shown in Table 3.1.

Mesh type	No. of cells in X, Y and Z directions respectively.	Total no. of cells
Coarse mesh	40 x 40 x 46	99,961 cells
Medium mesh	60 x 60 x 60	289,425 cells
Fine mesh	86 x 86 x 86	771,256 cells

Table 3.1 Mesh size details of three different meshes used.

3.2 Results and discussion

Figures 3.3 and 3.4 show the variation of volume averaged in-cylinder pressure with respect to crank angle between different meshes for RANS and LES models, respectively.

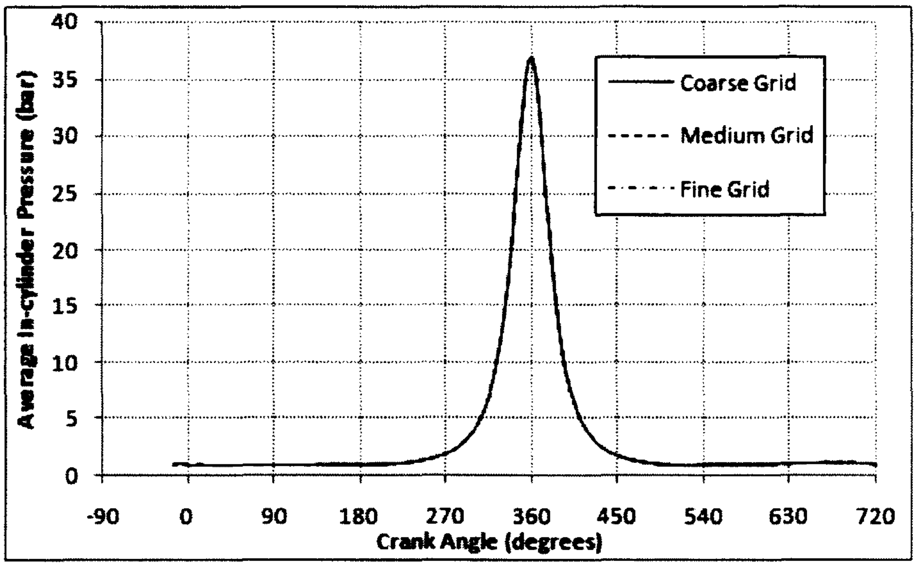

Figure 3.3 Average in-cylinder pressure variations between different grids for LES model.

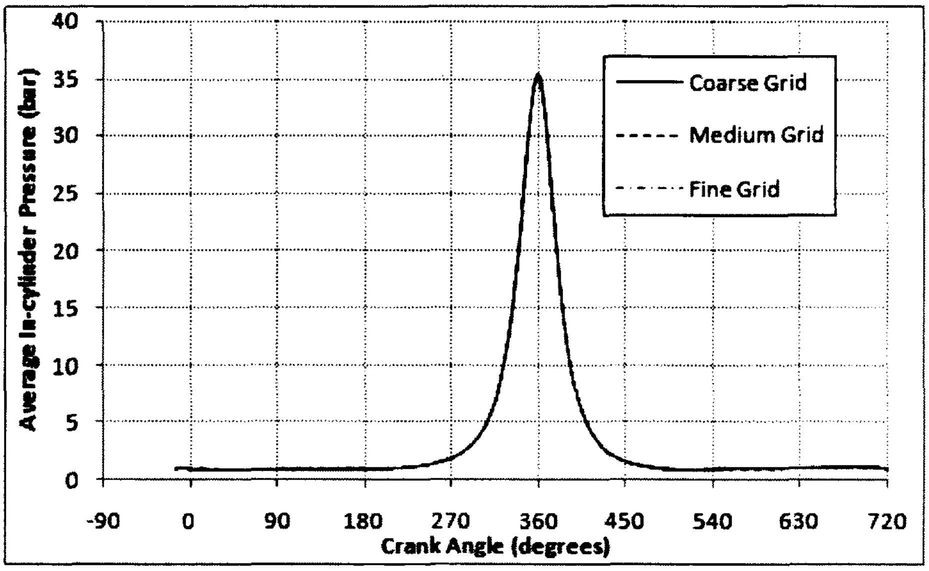

Figure 3.4 Average in-cylinder pressure variations between different grids for RANS model.

From Figures 3.3 and 3.4, it can be said that the volume averaged in-cylinder pressures does not vary with change in grid size for this case. If RANS and LES pressure traces are compared, the LES model predicts slightly higher peak pressure compared to the RANS model.

To understand the effect of grid size on turbulent quantities, Figures 3.5 and 3.6 are plotted to show volume averaged turbulence kinetic energy with respect to crank angle. Figure 3.5 shows volume averaged sub-grid turbulent kinetic energy for the LES model. The variations in the peaks of sub-grid kinetic energy are due to cell size. Coarse grid predicts higher peak compared to the fine grid. As the cell size decreases, the amount of sub-grid turbulent kinetic energy present within that cell decreases and the LES model retains energy within the flow field. Figure 3.6 shows volume averaged turbulent kinetic energy obtained from the RANS model. In this case, the coarse grid predicts less peak turbulent kinetic energy compared to the fine grid. If we compare Figures 3.5 and 3.6, it shows that the amount of turbulent kinetic energy presented in the RANS case is four times that predicted by the LES model. RANS models all turbulence scales, whereas LES resolves large scales and models small scales. In LES all the scales smaller than the filter size are modeled. Therefore, the turbulent kinetic energy in RANS is larger than that in sub-grid scale turbulent kinetic energy in LES. In order to understand the flow field better, qualitative results were presented.

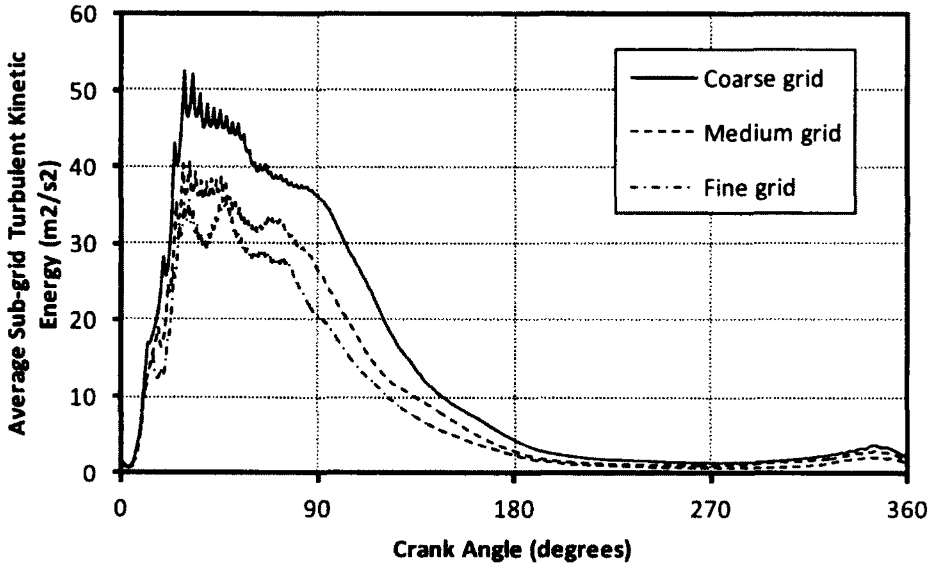

Figure 3.5 Average sub-grid turbulent kinetic energy variations between three grids using LES model.

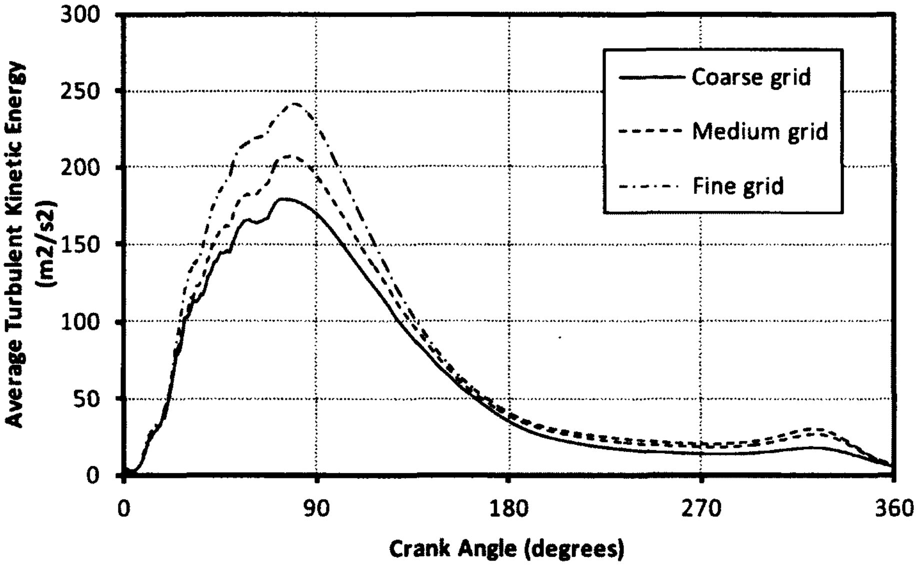

Figure 3.6 Average turbulent kinetic energy variations between three grids using RANS model.

Figures 3.7 to 3.36 show snapshots of various parameters at 200 degrees ATDC in three different planes. Crank angle 200 degrees ATDC is chosen since the intake valve closes at 200 degrees ATDC and the flow field contains the largest eddy structures within the cylinder volume. The parameters selected for comparison between the RANS and LES models are velocity magnitude contours, velocity vectors, streamlines, vorticity magnitude contours and turbulent kinetic energy contours. We need to understand the flow structures since the temperature and concentration inhomogenities within the engine cylinder depend on the large scale flow structures and small scale mixing.

3.2.1 Velocity contours

Figure 3.7 to 3.12 shows the instantaneous velocity contours in three grids using RANS and LES models. The velocity magnitude is in the range of 2 m/sec to 24 m/sec. From the velocity contours it can be seen that the LES model is able to capture the unsteady flow structures, whereas the RANS model captured only the large scale structures. If we compare the velocity contours between the medium grid and fine grid for RANS model, it can be said that the results are grid independent, since the medium grid has captured the flow structures and shows similar flow structures as the fine grid. In the LES case, it can be said that the fine grid shows more detailed small scale structures compared to the medium case. In the coarse grid case, both RANS and LES models show symmetric structures with respect to the Y plane and LES shows more complex flow structures compared to RANS results.

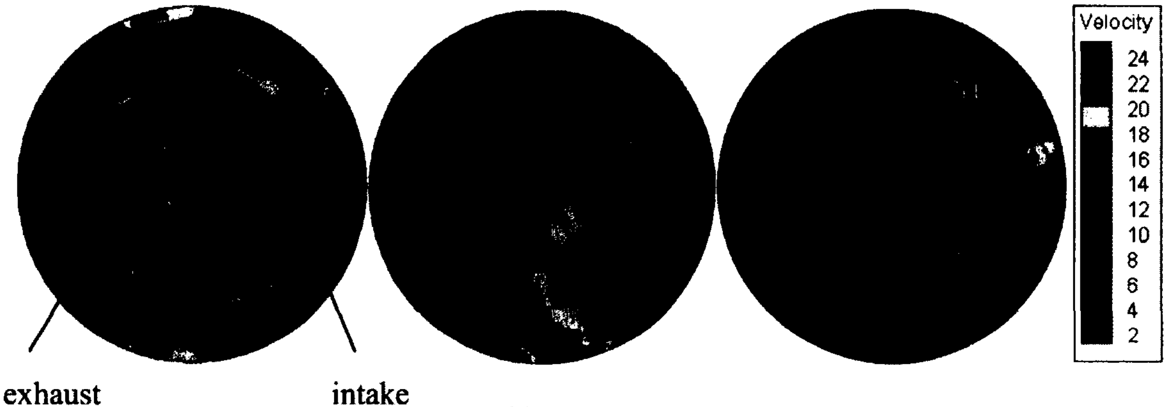

(a) (b) (c)

Figure 3.7 Velocity contours (m/s) from LES simulations in XY Plane for (a) Coarse grid, (b) Medium grid, and (c) Fine grid.

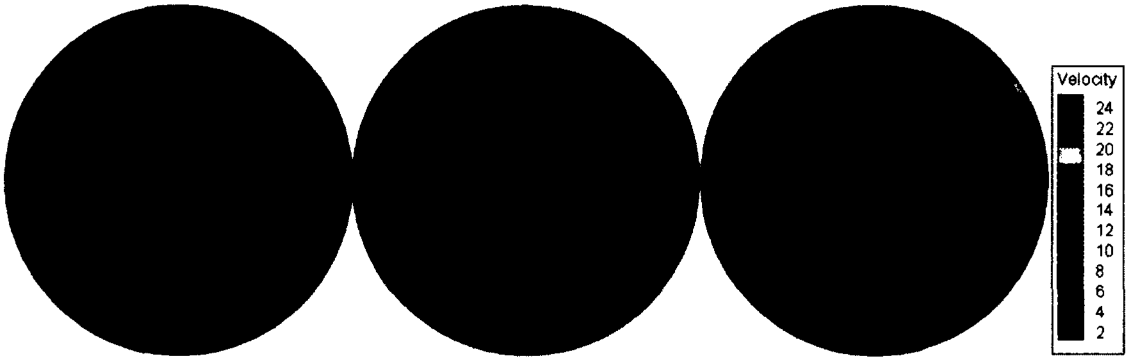

(a) (b) (c)

Figure 3.8 Velocity contours (m/s) from RANS simulations in XY Plane for (a) Coarse grid, (b) Medium grid, and (c) Fine grid.

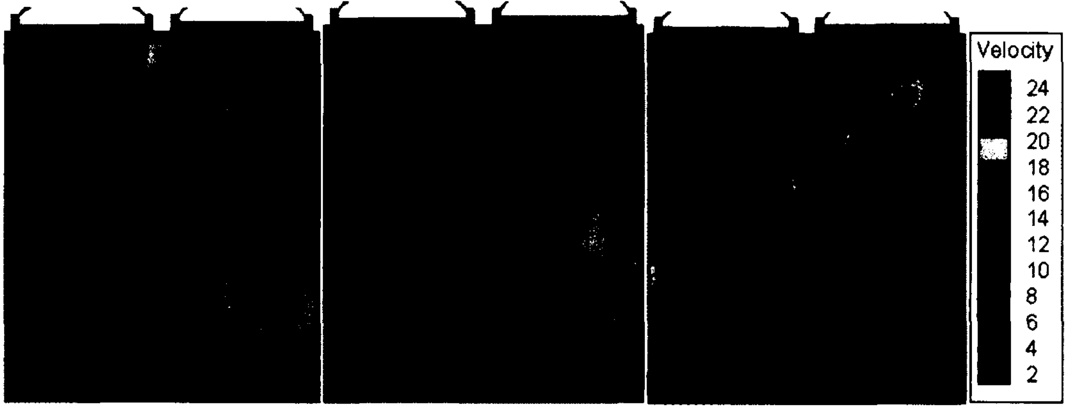

(a) (b) (c)

Figure 3.9 Velocity contours (m/s) from LES simulations in XZ Plane for (a) Coarse grid, (b) Medium grid, and (c) Fine grid.

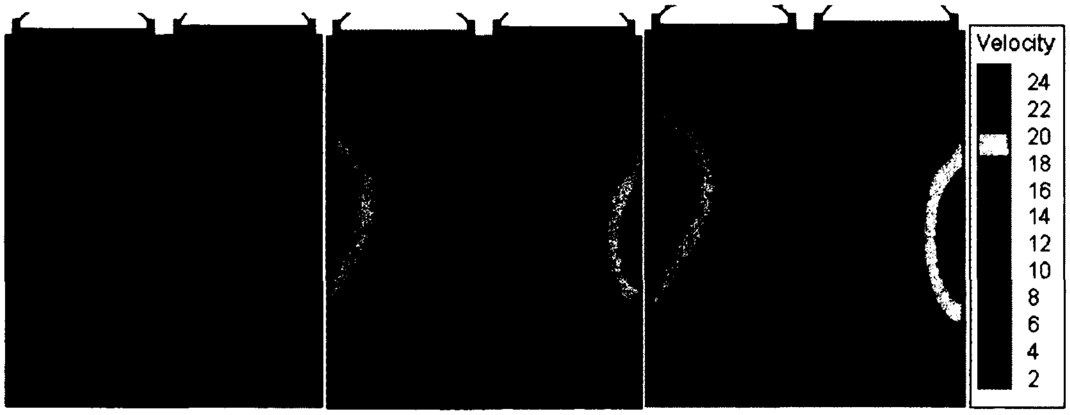

(a) (b) (c)

Figure 3.10 Velocity contours (m/s) from RANS simulations in XZ Plane for (a) Coarse grid, (b) Medium grid, and (c) Fine grid.

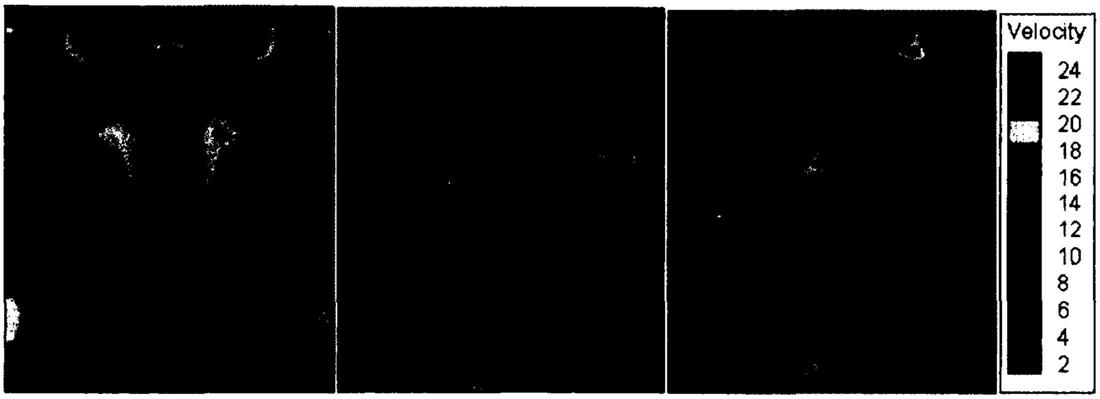

(a) (b) (c)

Figure 3.11 Velocity contours (m/s) from LES simulations in YZ Plane for (a) Coarse grid, (b) Medium grid, and (c) Fine grid.

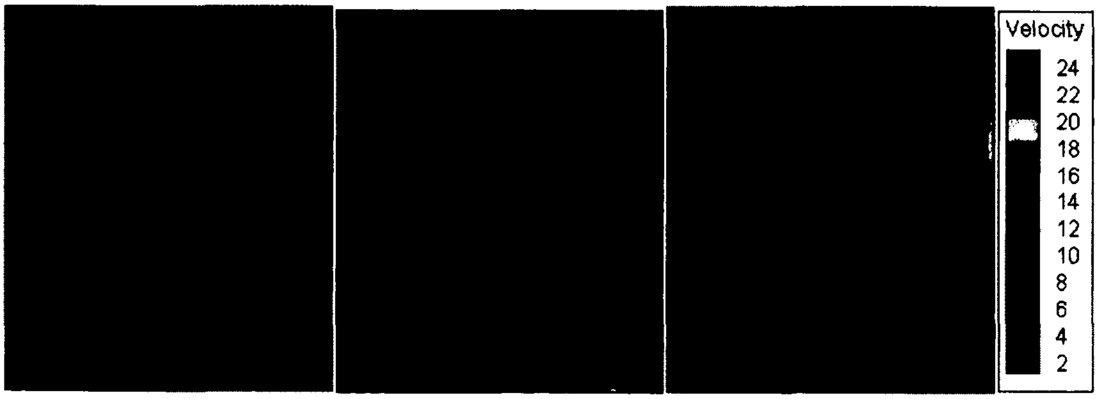

(a) (b) (c)

Figure 3.12 Velocity contours (m/s) from RANS simulations in YZ Plane for (a) Coarse grid, (b) Medium grid, and (c) Fine grid.

3.2.2 Velocity vectors

Figures 3.13 to 3.18 show velocity vectors for three different grids in three planes for RANS and LES models. Figure 3.13 and 3.14 show velocity vectors in the XY plane near to the top dead centre. The velocity vectors show flow structures formed due to the intake valve closing, which is on the right hand side in XY plane. LES model results show unsteady structures due to valve closing at the valve tip. RANS model results show the overall flow structure, but smoothens the small scale structures. Figure 3.15 and 3.16 show velocity vectors in the XZ plane for RANS and LES models. The XZ plane passes through the centre of the valves and it clearly shows the tumbling flow due to valve closing. The coarse grid results for both RANS and LES models show the large scale flow structure due to tumbling flow. This is formed due to valve closing and movement of the piston in an upward direction. As the grid size is increased, the RANS model results do not vary the overall structure but maintain the same flow field. But, in the case of LES model results, the small scale flow structures are captured as the grid size is refined. Figures 3.17 and 3.18 show velocity vectors in the YZ plane. The results show similar behavior as in the XZ plane.

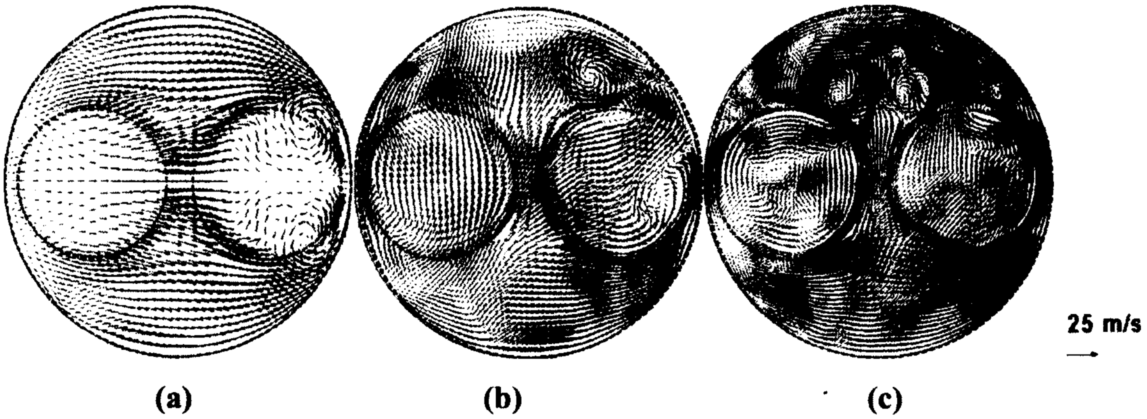

(a) (b) (c)

Figure 3.13 Velocity vectors from LES simulations in XY Plane for (a) Coarse grid, (b) Medium grid, and (c) Fine grid.

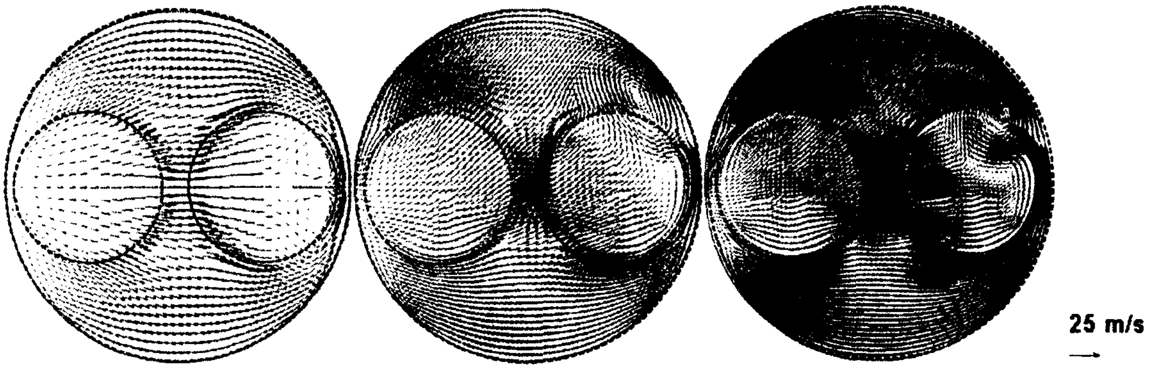

(a) (b) (c)

Figure 3.14 Velocity vectors from RANS simulations in XY Plane for (a) Coarse grid, (b) Medium grid, and (c) Fine grid.

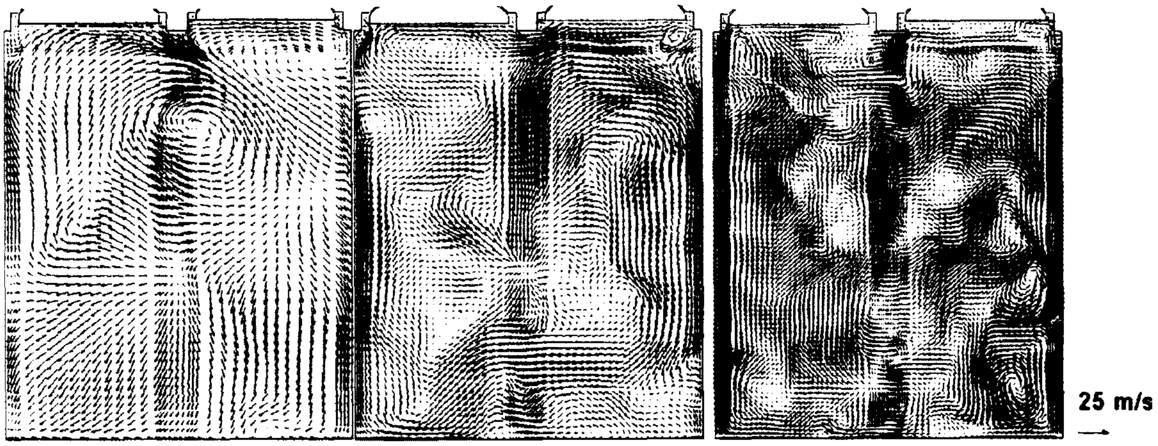

(a) (b) (c)

Figure 3.15 Velocity vectors from LES simulations in XZ Plane for (a) Coarse grid, (b) Medium grid, and (c) Fine grid.

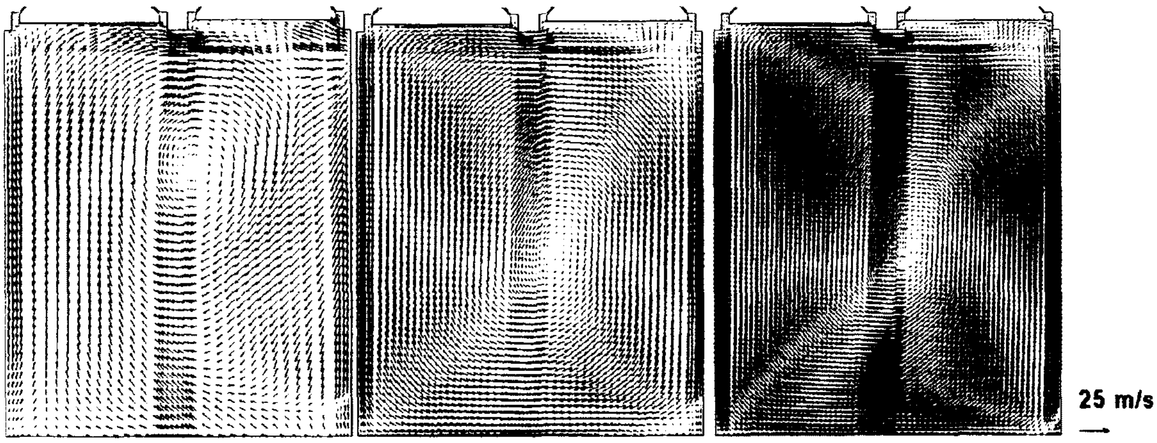

(a) (b) (c)

Figure 3.16 Velocity vectors from RANS simulations in XZ Plane for (a) Coarse grid, (b) Medium grid, and (c) Fine grid.

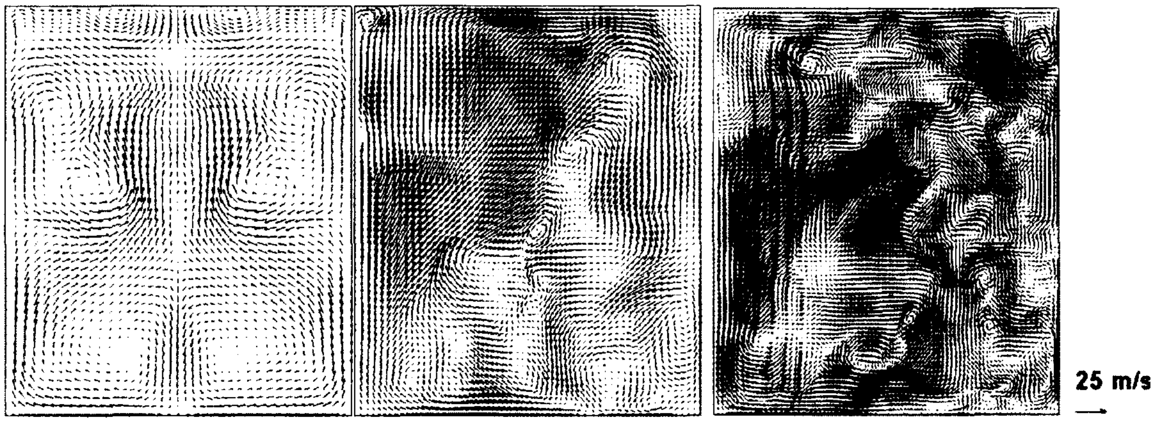

(a) (b) (c)

Figure 3.17 Velocity vectors for from LES simulations in YZ Plane for (a) Coarse grid, (b) Medium grid, and (c) Fine grid.

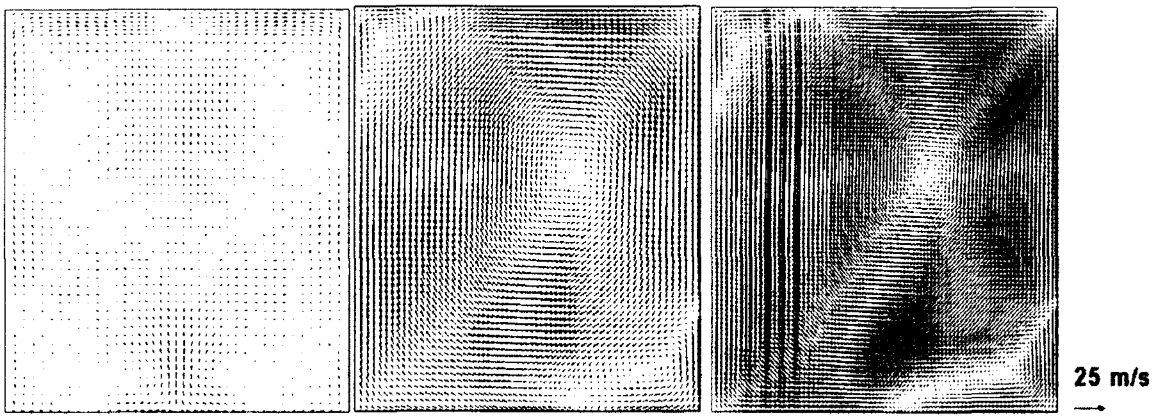

(a) (b) (c)

Figure 3.18 Velocity vectors from RANS simulations in YZ Plane for (a) Coarse grid, (b) Medium grid, and (c) Fine grid.

3.2.3 Streamlines

Figures 3.19 to 3.24 shows streamlines for three different grids in three planes for RANS and LES models. Figures 3.19 and 3.20 show streamlines in the XY plane for LES and RANS models, respectively. These streamline plots indicate the flow direction. The intake valve is symmetric to the XZ plane. But, the streamlines indicate asymmetric flow structures as the grid is refined. LES results indicate the vortex location asymmetric to the axis and as the grid is refined, small scale flow structures are resolved. In the case of RANS results, as the grid is refined, the asymmetric vortex occurring in the right top corner can be seen. Further grid refinement in RANS does not vary the flow structures. Figures 3.21 and 3.22 show the clock-wise rotation of the flow field with the centre of rotation in the middle of the cylinder. The results from RANS are somewhat smoother than those of LES, this is because the fundamental differences between these two methods in terms of the way to calculate the mean values and fluctuations.

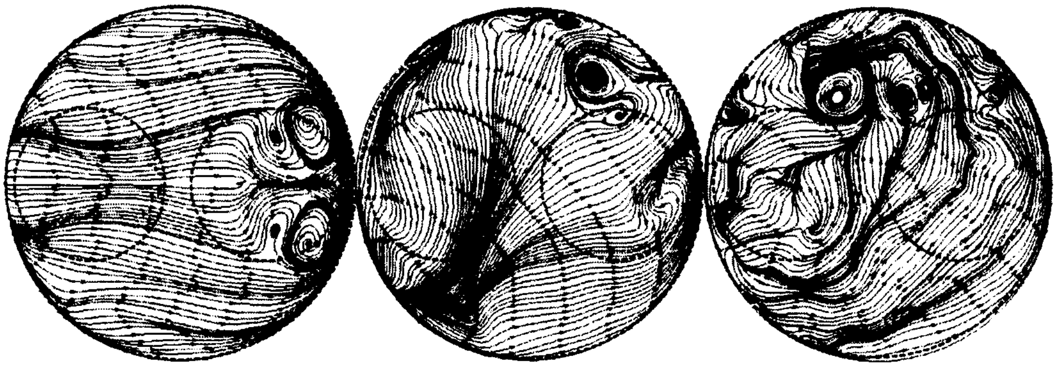

(a) (b) (c)

Figure 3.19 Streamlines for LES simulations in XY Plane for (a) Coarse grid, (b) Medium grid, and (c) Fine grid.

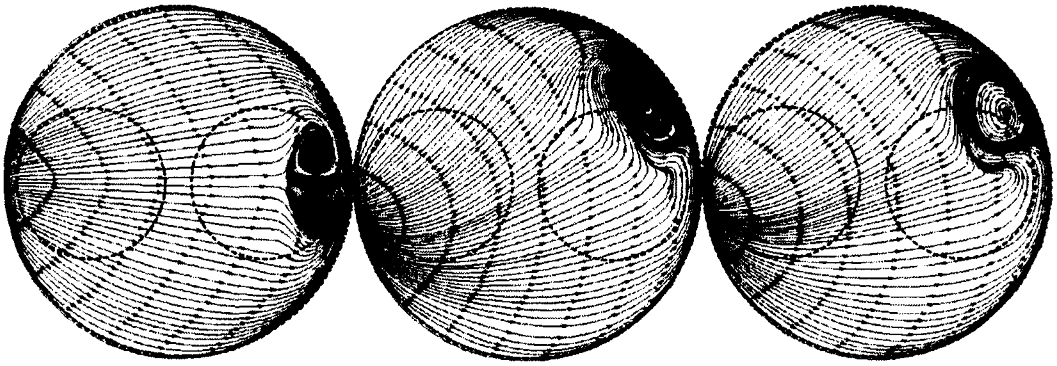

(a) (b) (c)

Figure 3.20 Streamlines for RANS simulations in XY Plane for (a) Coarse grid, (b) Medium grid, and (c) Fine grid.

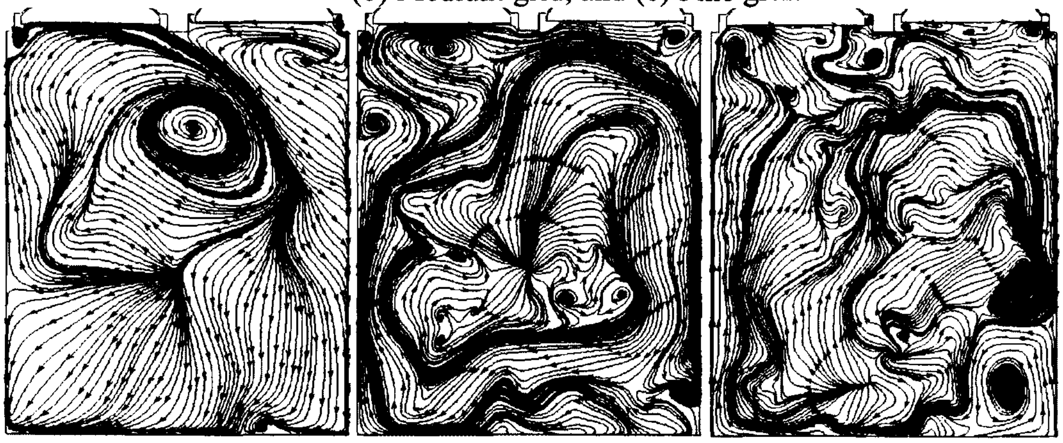

(a) (b) (c)

Figure 3.21 Streamlines for LES simulations in XZ Plane for (a) Coarse grid, (b) Medium grid, and (c) Fine grid.

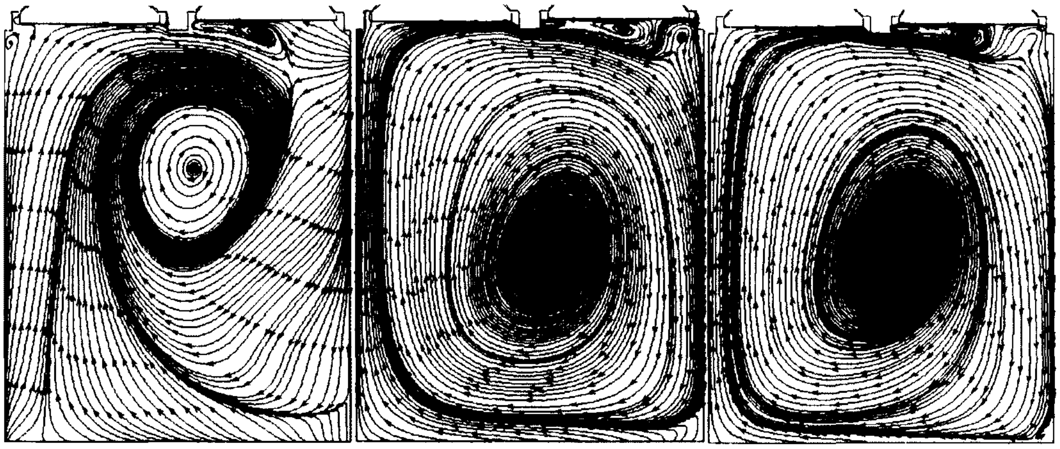

(a) (b) (c)

Figure 3.22 Streamlines for RANS simulations in XZ Plane for (a) Coarse grid, (b) Medium grid, and (c) Fine grid.

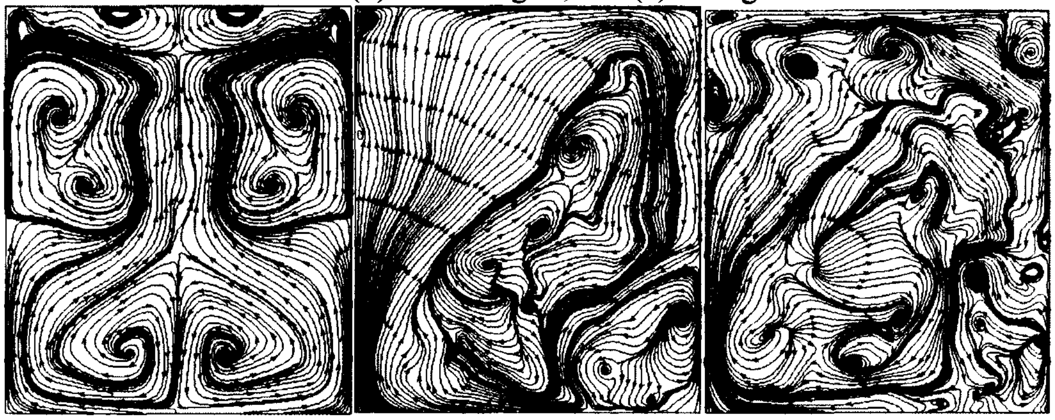

(a) (b) (c)

Figure 3.23 Streamlines for LES simulations in YZ Plane for (a) Coarse grid, (b) Medium grid, and (c) Fine grid.

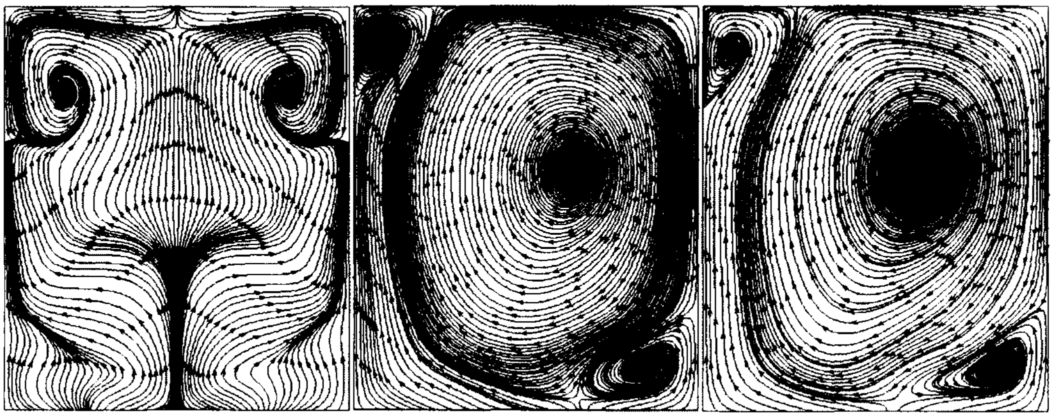

(a) (b) (c)

Figure 3.24 Streamlines for RANS simulations in YZ Plane for (a) Coarse grid, (b) Medium grid, and (c) Fine grid.

3.2.4 Vorticity

Figures 3.25 to 3.30 show vorticity contours for three different grids in three planes for LES and RANS models. Vorticity contours show the small scale structures. These small scale structures show the local mixing within the cylinder. In an engine case with direct injection of fuel into the cylinder, these flow structures play an important role in dispersion of the fuel and proper mixing of fuel with air in the cylinder. The higher the magnitude of vorticity, higher would be the strength of mixing. The amount of heat transfer from the fluid to the walls and surroundings depends on the strength and location of the vortex structures. The magnitude of local vorticity is a good indicator to tell the engineers how the flow inside the engine will affect the combustion and heat transfer processes. More details of this information can be obtained from the LES model, thus from this point of view, LES is more suitable for these type of applications.

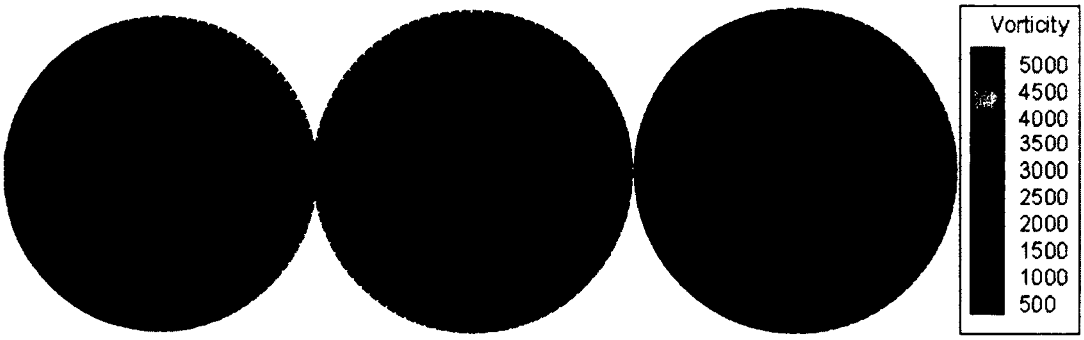

(a) (b) (c)

Figure 3.25 Vorticity contours (sec^{-1}) for LES simulations in XY Plane for (a) Coarse grid, (b) Medium grid, and (c) Fine grid.

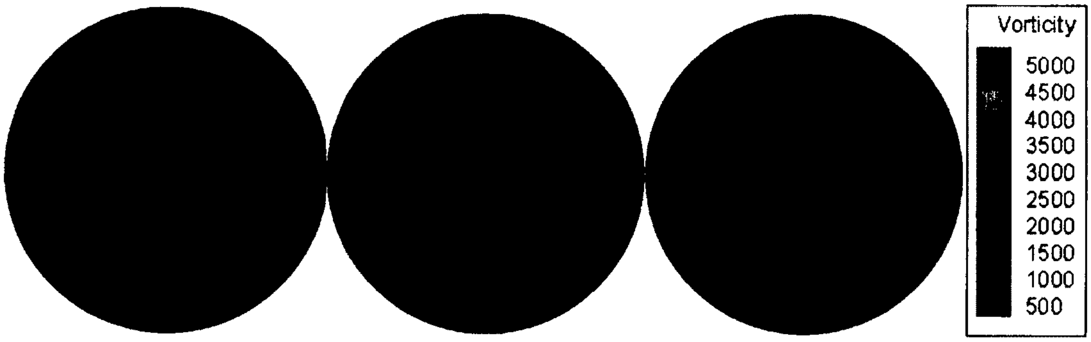

(a) (b) (c)

Figure 3.26 Vorticity contours (sec^{-1}) for RANS simulations in XY Plane for (a) Coarse grid, (b) Medium grid, and (c) Fine grid.

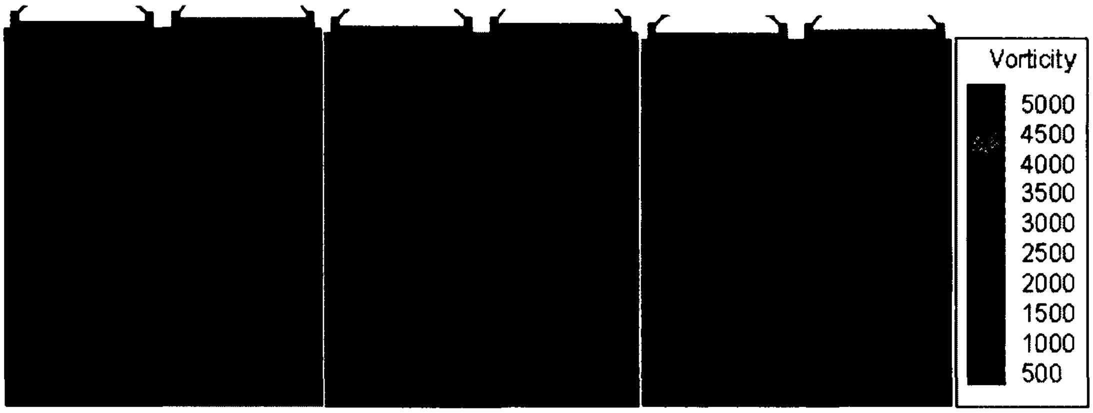

(a) (b) (c)

Figure 3.27 Vorticity contours (sec^{-1}) for LES simulations in XZ Plane for (a) Coarse grid, (b) Medium grid, and (c) Fine grid.

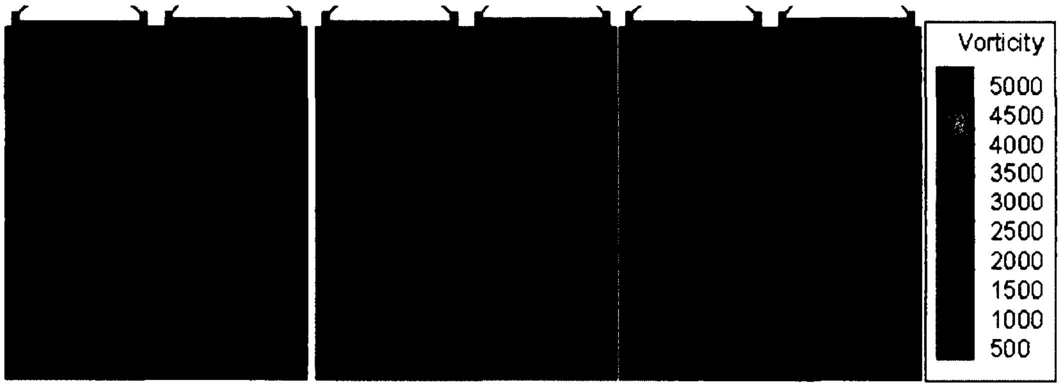

(a) (b) (c)

Figure 3.28 Vorticity contours (sec^{-1}) for RANS simulations in XZ Plane for (a) Coarse grid, (b) Medium grid, and (c) Fine grid.

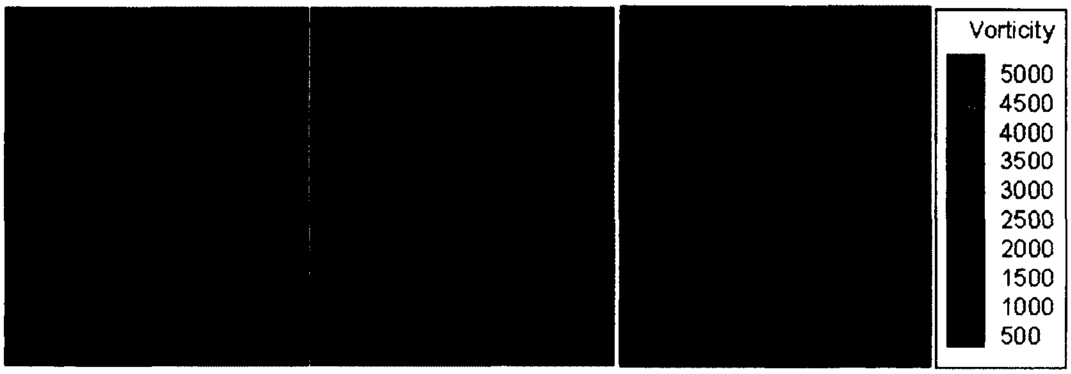

(a) (b) (c)

Figure 3.29 Vorticity contours (sec^{-1}) LES simulations in YZ Plane for (a) Coarse grid, (b) Medium grid, and (c) Fine grid.

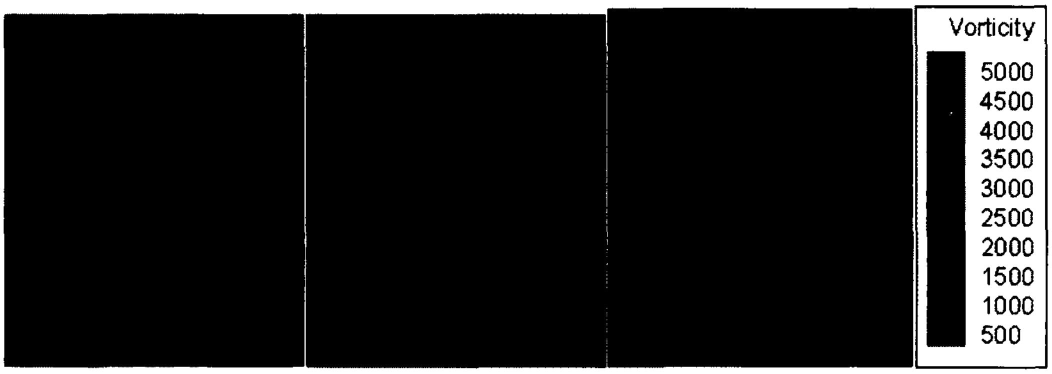

(a) (b) (c)

Figure 3.30 Vorticity contours (sec^{-1}) RANS simulations in YZ Plane for (a) Coarse grid, (b) Medium grid, and (c) Fine grid.

3.2.5 Turbulent kinetic energy

Figures 3.31 to 3.36 show variation of sub-grid scale turbulent kinetic energy and mean turbulent kinetic energy contours for three different grids in three planes for LES and RANS. Plots show significant differences between LES and RANS turbulent kinetic energy locations and contours. The turbulent kinetic energy from LES is usually smaller than that from RANS, and this is due to the fundamental difference between these two different methods in terms of how to describe the turbulence, i.e., in RANS one single value is used to describe the mean value while a varied mean value is used in LES. Therefore for the same physical instantaneous flow, the fluctuations predicted by RANS would be bigger than that by LES.

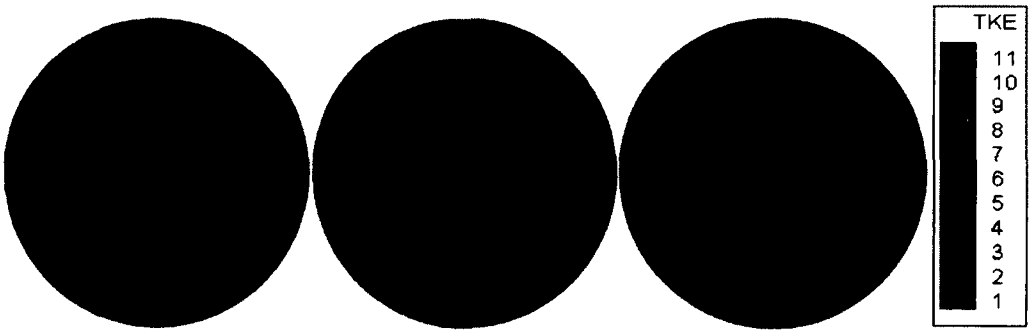

(a) (b) (c)

Figure 3.31 Sub-grid scale turbulent kinetic energy (m^2/s^2) contours for LES simulations in XY Plane for (a) Coarse grid, (b) Medium grid, and (c) Fine grid.

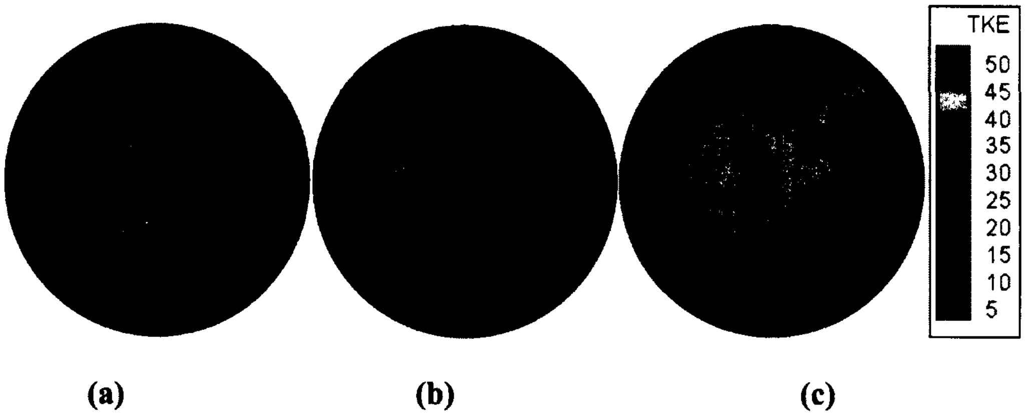

Figure 3.32 Turbulent kinetic energy (m^2/s^2) contours for RANS simulations in XY Plane for (a) Coarse grid, (b) Medium grid, and (c) Fine grid.

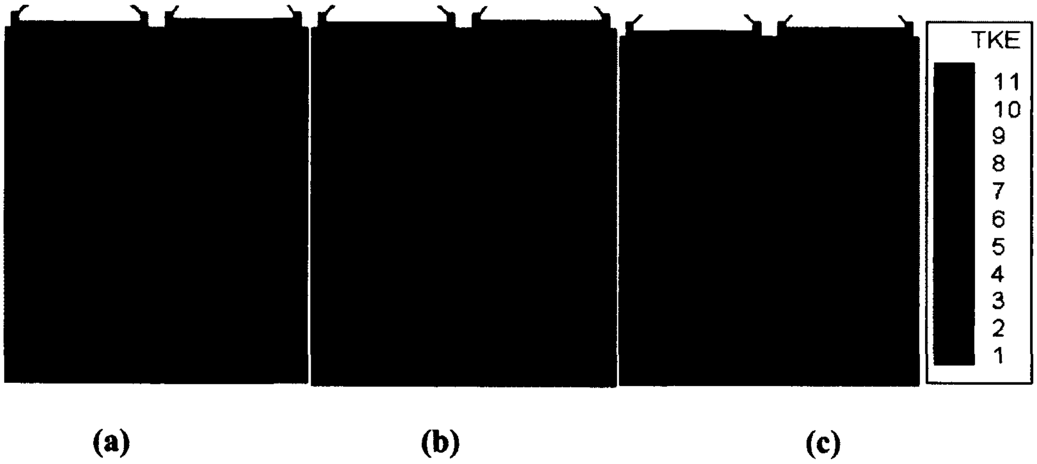

Figure 3.33 Sub-grid scale turbulent kinetic energy (m^2/s^2) contours for LES simulations in XZ Plane for (a) Coarse grid, (b) Medium grid, and (c) Fine grid.

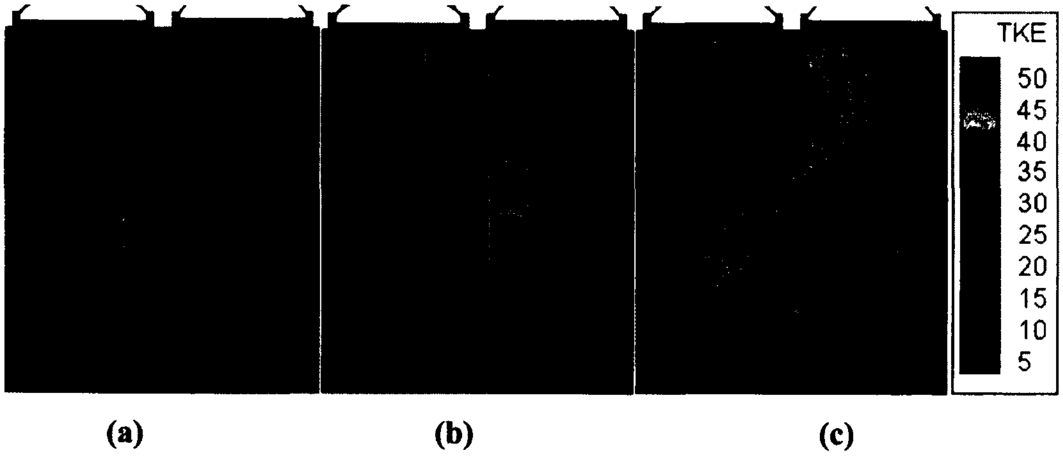

Figure 3.34 Turbulent kinetic energy (m^2/s^2) contours for RANS simulations in XZ Plane for (a) Coarse grid, (b) Medium grid, and (c) Fine grid.

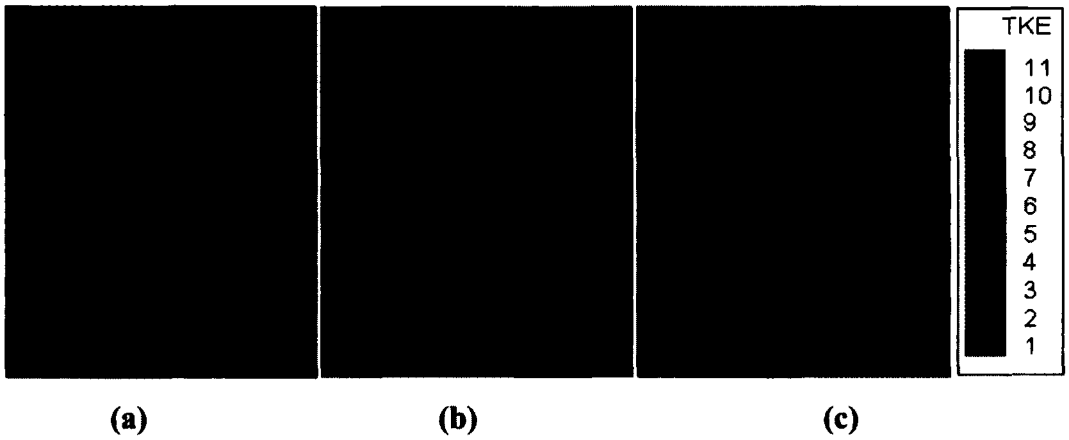

Figure 3.35 Sub-grid scale turbulent kinetic energy (m^2/s^2) contours for LES simulations in YZ Plane for (a) Coarse grid, (b) Medium grid, and (c) Fine grid.

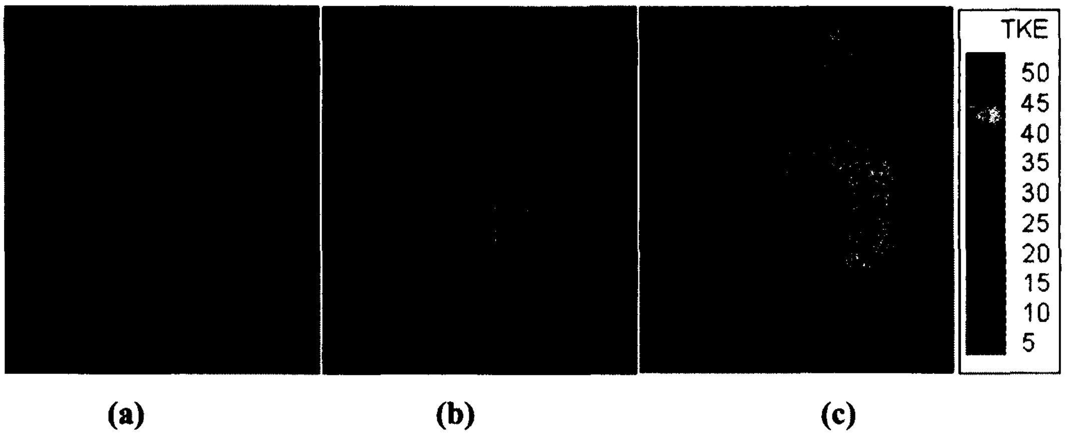

Figure 3.36 Turbulent kinetic energy (m^2/s^2) contours for RANS simulations in YZ Plane for (a) Coarse grid, (b) Medium grid, and (c) Fine grid.

3.3 Summary

Grid sensitivity analysis and flow field comparisons have been carried out for a test case with RANS and LES turbulence models. It can be concluded that LES is able of capturing more details of the local flow structures. LES results are more close to the instantaneous flow fields with respect to time and space. Several researchers (Haworth1999, Celik et al. 2001, Thobois et al. 2005, Jhavar and Rutland 2006) have compared the LES and RANS model results with experimental flow structures and showed that LES predicts the realistic flow structures compared to RANS models. Therefore, LES is more suitable for modeling HCCI engine combustion where the local flow structures, local temperatures, local air-fuel ratio are directly related to the HCCI combustion process.

Chapter 4

Validation of CKL Solver with Baseline Case

4.1 Introduction and boundary conditions

Simulations have been performed to validate the combustion model with detailed chemical kinetics. The primary goal of these simulations was to check whether the solver and the chemical kinetic mechanism were able to capture the HCCI engine combustion trends as given in the literature. The Jia-Xie skeletal iso-octane oxidation mechanism discussed in Chapter 2 was used. Experimental results for HCCI engine with iso-octane fuel were taken from Dec and Sjöberg. (2003) as the baseline case. The test engine used in the experiments was a Cummins B-series production diesel engine. Detailed specifications of the engine and initial conditions are shown in Table 4.1.

Displacement (cc)	981
Bore (m)	0.10
Stroke (m)	0.12
Connecting rod length (m)	0.192
Geometric compression ratio	18:1
Speed (rpm)	1200
Intake valve open	717^{0} ATDC
Intake valve close	205^{0} ATDC
Exhaust valve open	480^{0} ATDC
Exhaust valve close	8^{0} ATDC
Fuel	Iso-octane
Intake pressure (bar)	1.07
Intake temperature (K)	413
Wall temperature (K)	371

Table 4.1 Engine specifications from Dec and Sjöberg (2003) for baseline case.

Simulations start from the intake valve closing to the exhaust valve opening (compression stroke and power stroke). The intake pressure was adjusted from 1.2 bar given in experiments to 1.07 bar in simulations to match the pressure from the motoring curve. Simulations were carried out for equivalence ratios (ER) starting from 0.06 to 0.26 with increments of 0.04. These equivalence ratios were chosen to cover the range from the idle fueling condition to the onset of knocking. In the experiments, the initial conditions were adjusted such that the 50% burn point for a equivalence ratio of 0.14 occurs at 360 CA. The simulations were conducted on a 2-D axi-symmetric grid and periodic boundary conditions are applied on the front and rear surfaces. The computational domain is as shown in Figure 4.1. The domain was simplified to include the crevice as in the case of real engine geometry. The computational domain contains approximately 13515 cells and grids are clustered near the piston region.

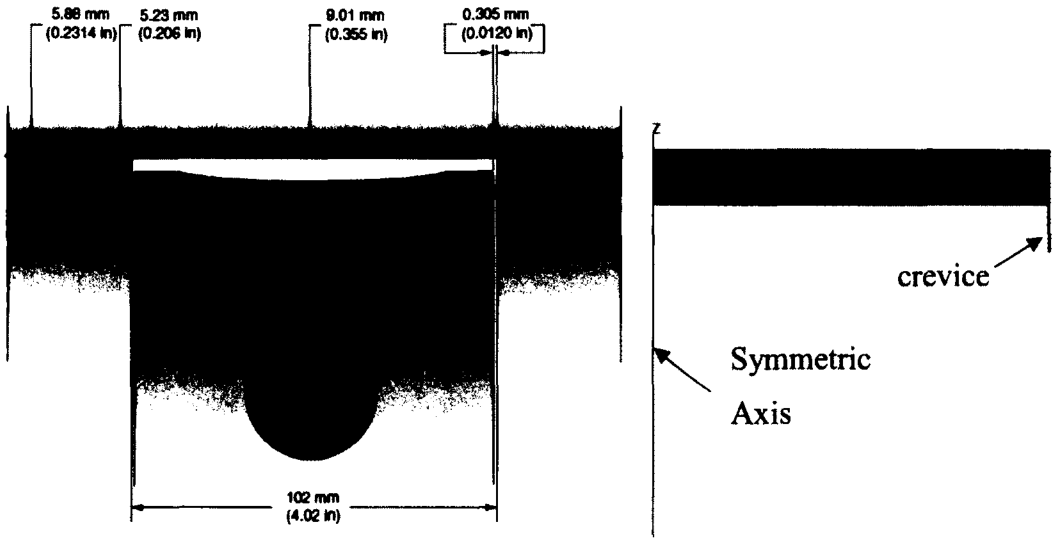

Figure 4.1 Geometry (Dec and Sjöberg, 2003) and 2-D axi-symmetric computational domain when piston is at Top Dead Centre.

4.2 Results and discussion

Figure 4.2(a) show the pressure traces for equivalence ratios starting from 0.06 to 0.26 from simulation and Figure 4.2(b) shows experimental data taken from Dec and Sjöberg (2003).

The assumptions under which the simulations are carried out are discussed as follows:

(a) Experimental results are obtained by averaging the pressure traces over 100 cycles while the simulations are carried from IVC to EVO.

(b) Experiments were carried on a Cummins B-series diesel engine with the intake and exhaust valves, while simulations are carried on 2-D axi-symmetric pan-cake type combustion chamber without valves.

(c) In the experiments, fuel-air mixture is brought into the cylinder and the mixture is assumed to be homogeneous, while in simulations it is homogeneous mixture of fuel-air mixture at fixed equivalence ratio within the cylinder.

(d) In the experiments, the heat transfer to the cylinder walls varies with time, while in simulations the wall temperature is kept constant.

(e) In experiments at lower equivalence ratios (<0.14), the heat loss to the cylinder walls, residual gases from previous cycle and crevices have predominant effects on the combustion process (Dec and Sjöberg, 2003), while in the simulations, only fuel and air mixture is assumed to be present in the cylinder.

The simulated pressure traces show similar trends as in the experiments. The peak pressure locations are slightly rounded in the simulations and do not appear to be varying with equivalence ratio. These differences are due to the domain considered and swirl ratio. As mentioned in Dec and Sjöberg (2003), the simulation results show that the kinetic rates leading to ignition are almost unaffected by the fuel loading as indicated by onset of combustion for a single stage ignition fuel, like iso-octane.

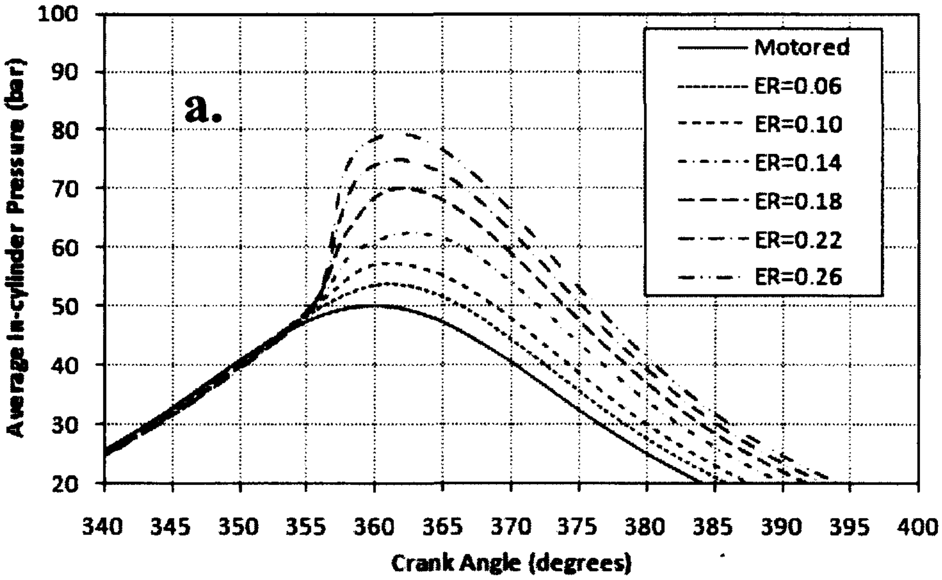

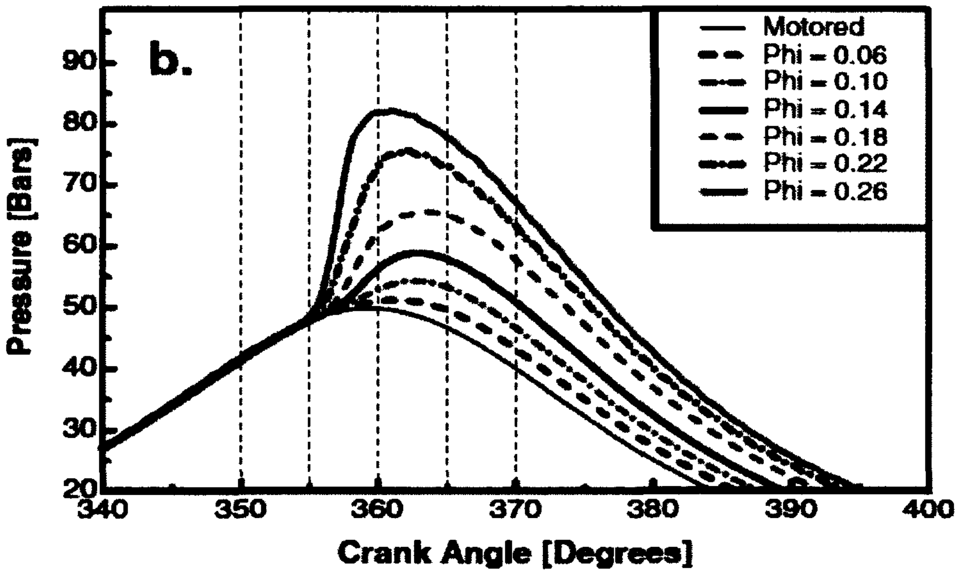

Figure 4.2 (a) Simulation pressure traces for various equivalence ratios, (b) Experimental data taken from Dec and Sjöberg (2003).

To know specifically how well the simulation results compared with the experimental data, pressure traces from three different equivalence ratios are plotted on the same graph along with experimental data. The plots also include the motoring curve for simulation and experiments. The in-cylinder pressure was adjusted to 1.07 bar compared to experimental data given as 1.2 bar to match the motoring curve.

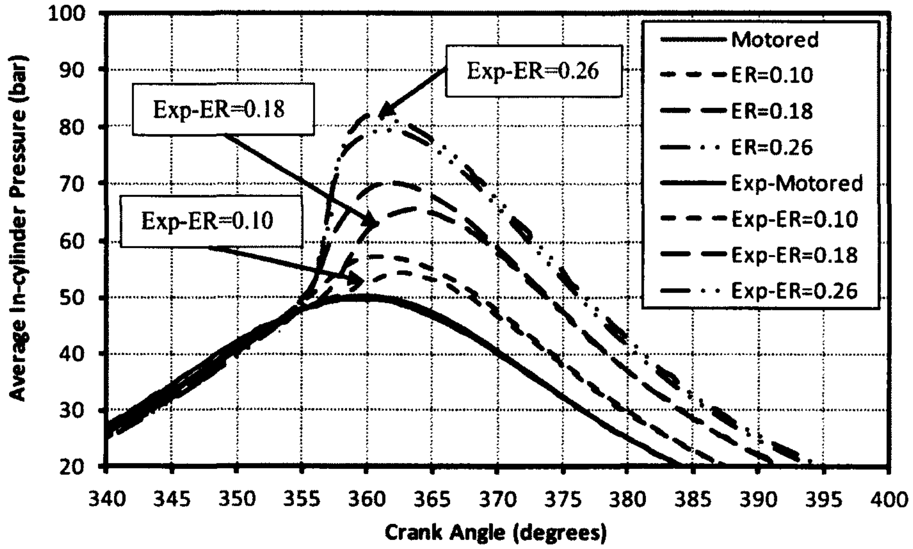

Figure 4.3 Comparison of in-cylinder pressure traces with the experimental data for equivalence ratios of 0.26, 0.18 and 0.1 with motoring curve.

The pressure traces in Figure 4.3 indicate that for equivalence ratio of 0.26, the simulation result is slightly lower than that from the experimental data. The pressure traces for equivalence ratios of 0.18 and 0.10 indicate that simulations reach peak pressure earlier than experiments. In the case of experiments, the pressure rise is shifted between different equivalence ratios. This shift in pressure traces gives higher IMEP compared to simulations.

Figure 4.4 shows the variation of simulated average in-cylinder temperature with respect to equivalence ratio. The peak temperature was reached around 360 CA. The trends indicate that the exhaust temperature differs by approximately 40 K between adjacent equivalence ratios. This would affect the species in the residual gas and fresh charge coming into the cylinder. From Figure 4.2(a) we see that the average in-cylinder pressure would be relatively low at exhaust valve opening time for lower equivalence ratios. This will allow the engine to retain some of the residual gas within the cylinder.

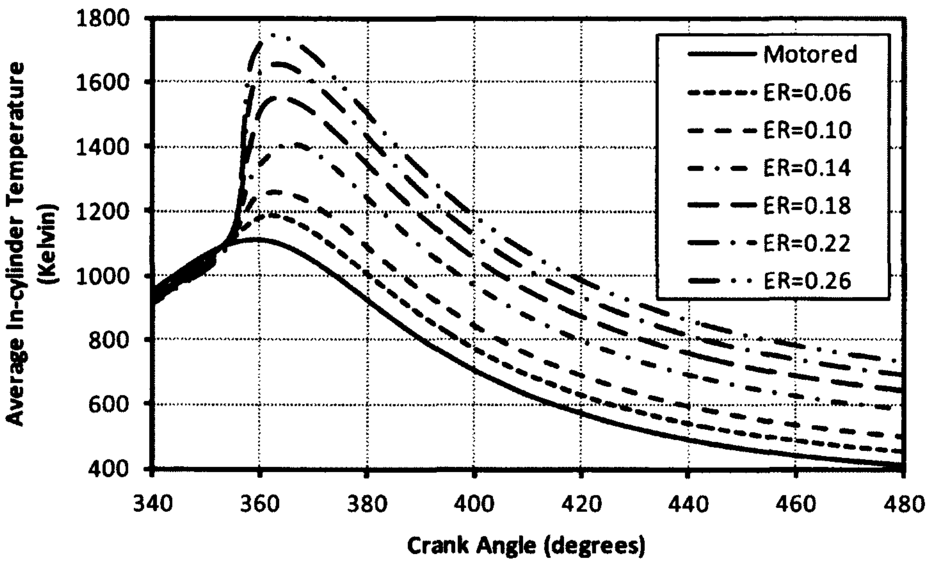

Figure 4.4 Simulated average in-cylinder temperature variations with respect to equivalence ratios.

The simulation pressure and temperature traces give an idea where the start of combustion is located and the crank angle at which peak pressure and temperatures are obtained. Figure 4.5 shows the variation of gross indicated mean effective pressure (IMEPg). The IMEPg is defined as follows:

$IMEPg = \frac{\int_{IVC}^{EVO} pdV}{V_d}$, where Intake Valve Close (IVC) is at crank angle 205 CA, the Exhaust Valve Open (EVO) is at 480 CA, V_d is the displacement volume, p is the in-cylinder pressure and dV is the change in volume. The differences of IMEPg between experiments and simulation can be explained as follows: the higher pressure before TBC gives negative work which subsequently reduces IMEPg.

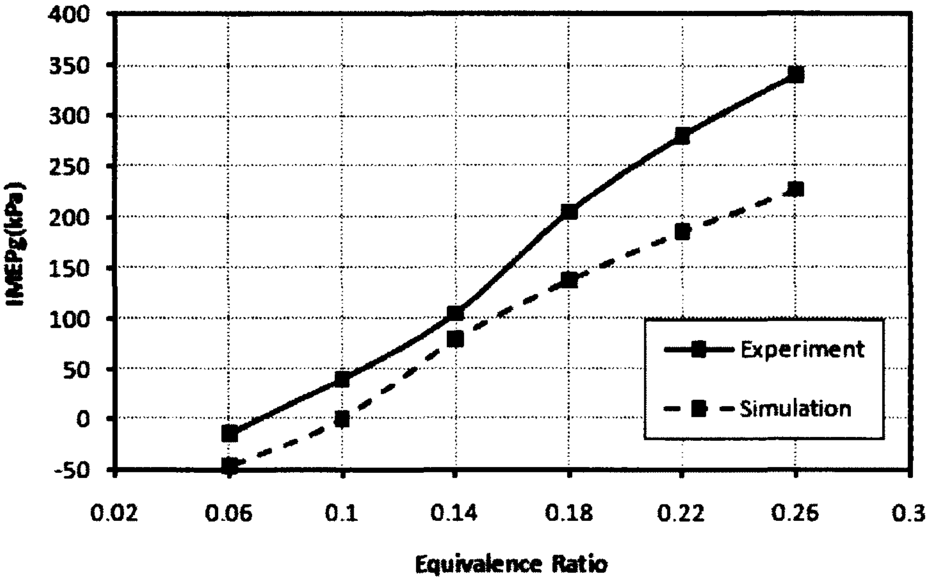

Figure 4.5 Gross Indicated Mean Effective Pressure (IMEPg) versus equivalence ratios.

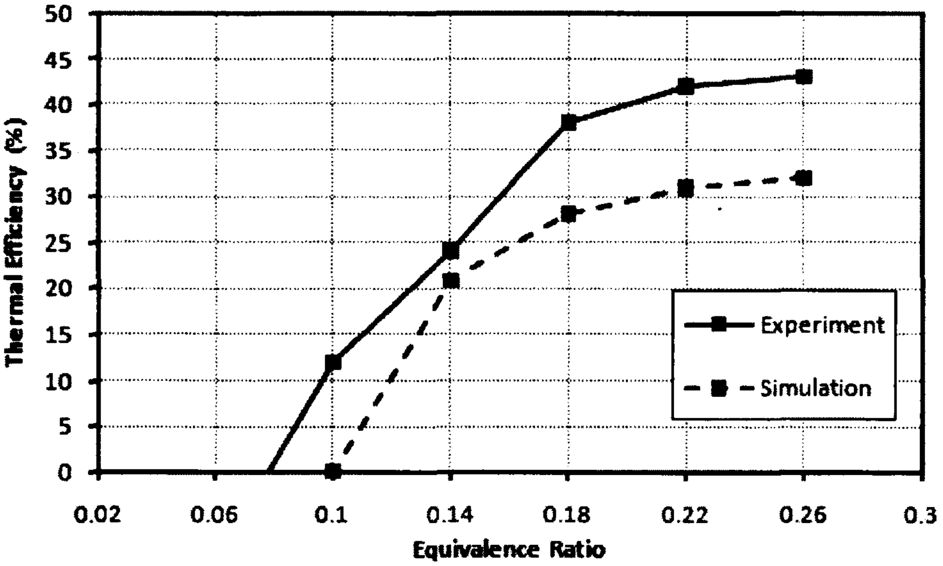

Figure 4.6 Thermal efficiencies versus equivalence ratios.

As the equivalence ratio goes below 0.14, the thermal efficiency of the engine decreases. Thermal efficiencies for various equivalence ratios were shown in Figure 4.6. Since the work done is lower, thermal efficiency would be lower. Thermal efficiency is given by

$\eta_{th} = \dfrac{\int pdV}{m_f * CV}$, where m_f is the mass of fuel in the cylinder and CV is high heating value of the fuel. To understand the trends given by IMEPg and thermal efficiency, the combustion characteristics need to be taken into account. The heat release rate curve gives the amount of heat released per crank angle. Figure 4.7 shows the net heat release rate within the cylinder for different equivalence ratios. The heat release rate curves show that regardless of the amount of fuel present in the cylinder, the start of combustion remains the same, since it depends on the initial conditions. For a particular fuel, in this case iso-octane, the in-cylinder conditions at 345CA are sufficient for it to initiate fuel oxidation reaction. As the equivalence ratio is decreased, the amount of heat released per crank angle reduces as shown in Figure 4.7. The peak heat release rate crank angle remains almost in the same range for all the equivalence ratios.

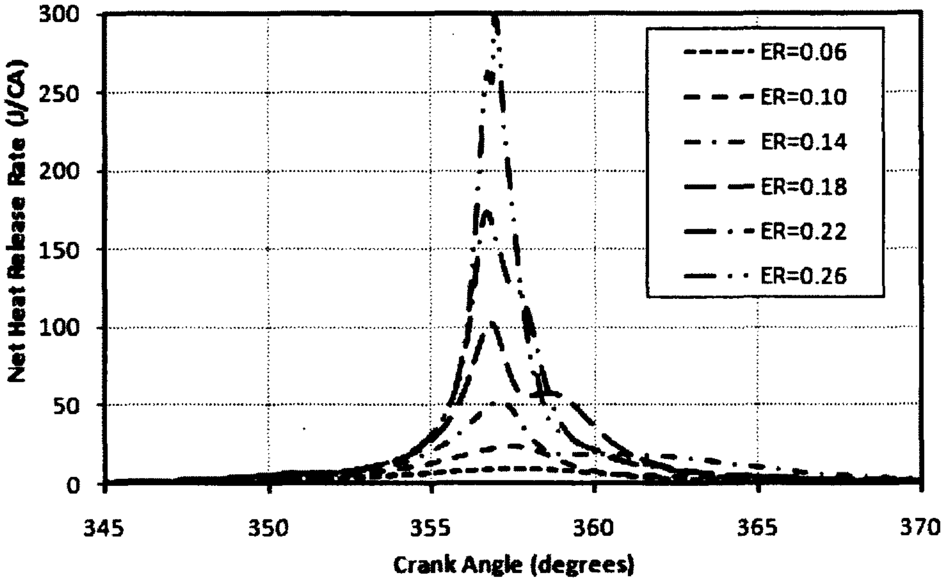

Figure 4.7 Net heat release rates per crank angle for various equivalence ratios.

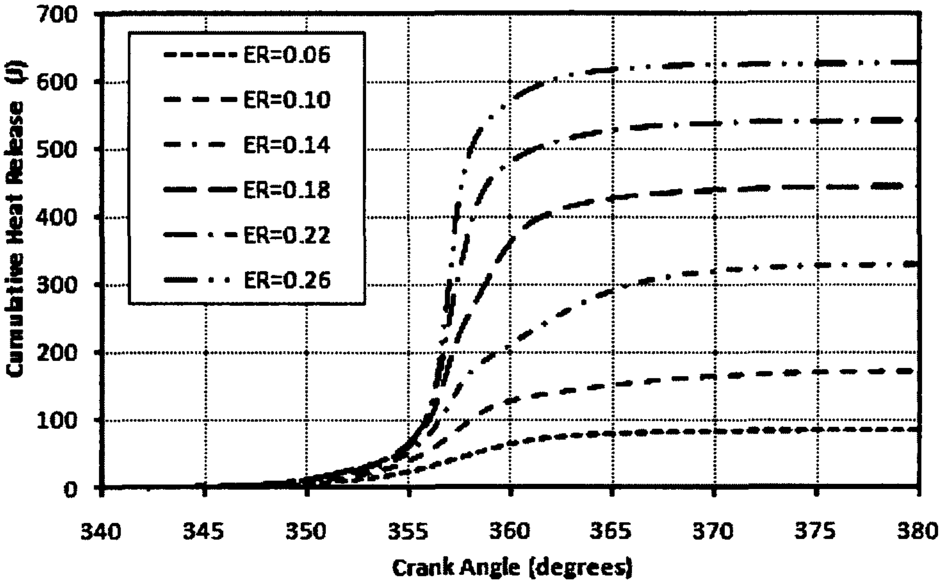

Figure 4.8 Cumulative heat release curves for various equivalence ratios.

The cumulative heat release curves for different equivalence ratios were shown in Figure 4.8. The cumulative heat release curves indicate that for equivalence ratios below 0.18, the heat release is prolonged. The amount of total heat released for equivalence ratio of 0.18 reduces to 50 % of heat released for ER of 0.26. The heat release duration can be divided into two parts: 10% to 50% heat release and 50% to 90% heat release.

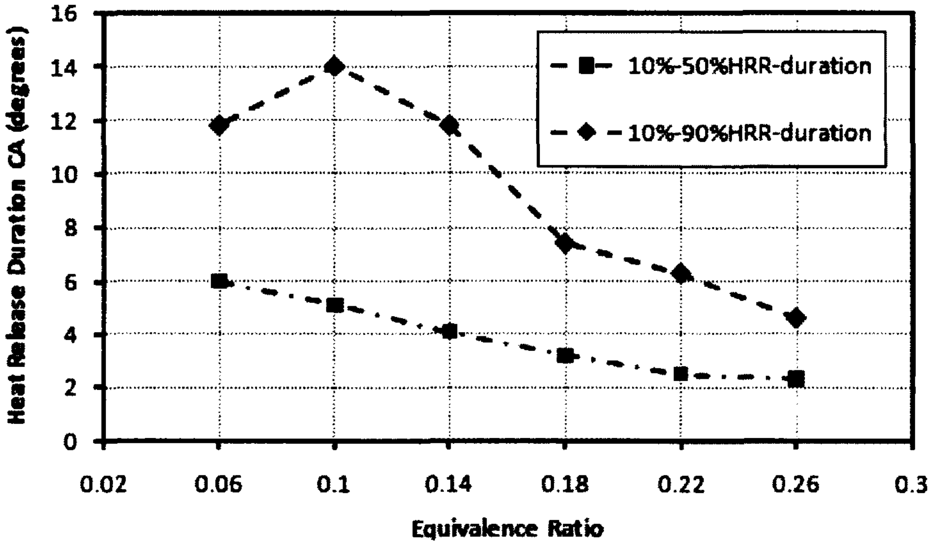

Figure 4.9 Heat release durations for various equivalence ratios.

The duration of heat release for different equivalence ratios are plotted in Figure 4.9. The 10% to 50% heat release duration varies linearly with equivalence ratio. There are large deviations in the 50% to 90% heat release duration. This was due to the in-cylinder temperature, which is not high enough for conversion of CO to CO_2 at low equivalence ratios. These results indicate that as the equivalence ratio is reduced, the combustion duration increases. In the case of 10% to 90% heat release duration, the equivalence ratios 0.14, 0.10 and 0.06 have longer duration compared to other equivalence ratios. This difference in durations can be attributed to the absence of high temperature combustion reactions. The in-cylinder temperatures in these cases are not high enough for complete conversion of CO to CO_2.

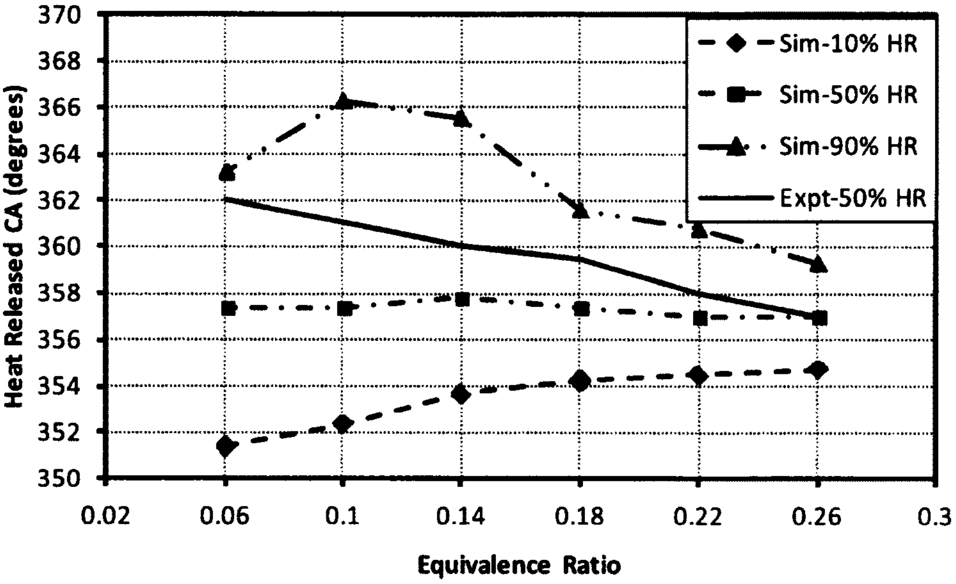

Figure 4.10 Heat release crank angle for various equivalence ratios.

Figure 4.10 indicates the crank angle at which the simulations complete 10% heat release, 50% heat release and 90% heat release. The experimental data is available for only 50% heat release crank angle. The simulation trends indicate that as the equivalence ratios decreases, the 50% heat release crank angle remains almost unchanged. The deviation between experiments and simulations for 50% heat release can be explained from the conditions under which the data were obtained. In the experiments the data was ensemble averaged over 100 cycles, while the simulation data was for a single cycle from intake valve close to exhaust valve open. If we consider the 0.06 equivalence ratio case, the combustion is incomplete and it has large amounts of residual gas containing CO and HC at relatively lower temperatures and pressures. These gases would stay within the cylinder and have an effect on the start of combustion and subsequent combustion duration. The residual gas dilution with the fresh charge coming into the cylinder significantly changes the combustion timing and duration.

Figure 4.11 shows the CO_2, CO and HC emissions from experiments and simulations. The simulations have the same trends as the experiments with the biggest difference for the equivalence ratio of 0.14. For the equivalence ratio of 0.14, the experiments show a higher amount of CO and lower amount of CO_2 due to the engine has higher heat loss. The simulation predicts more complete combustion in these leaner mixtures due to the higher predicted temperature from the fixed wall temperature boundary conditions that give lower heat losses from the numerical simulation than that in the experiments.

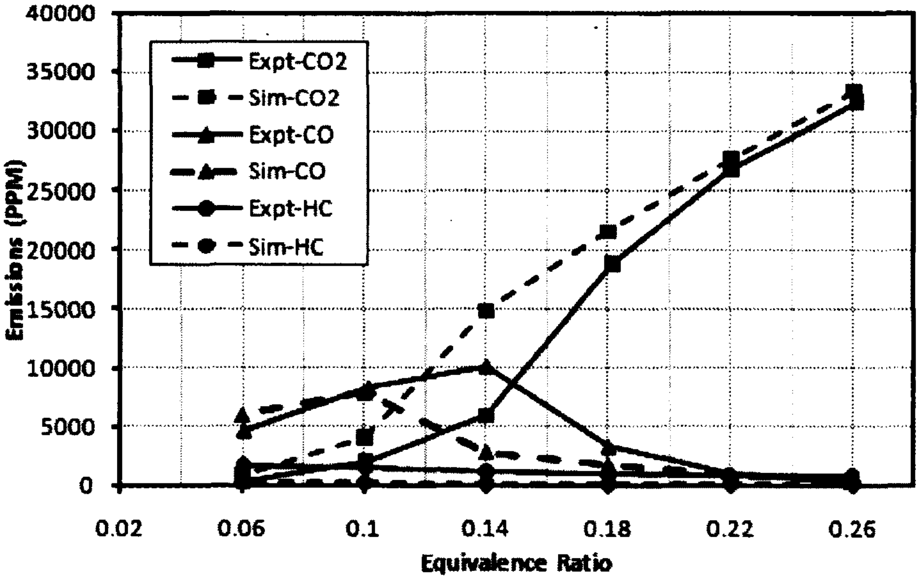

Figure 4.11 Comparison of emissions with respect to equivalence ratios.

Figure 4.12 shows the remaining unburnt fuel with respect to crank angle. The results indicate that the fuel consumption starts at 345 CA and decreases rapidly to a very low amount when the piston reaches top dead centre. It seems that the fuel consumption does not depend on the equivalence ratio as long as the conditions for fuel auto-ignition are present. In all these cases there would be some amount of fuel left within the cylinder as there are crevices in the cylinder. The amount of fuel residing in the cylinder crevices varies with respect to equivalence ratio. The fuel consumption plots indicate that the fuel oxidation reactions start at 345 CA, when the in-cylinder temperature reaches auto-ignition temperature of the fuel. The temperature rise due to compression stroke and oxidation reactions initiate high temperature reactions. The fuel oxidizes completely except for the fuel left in the crevices at 360 CA.

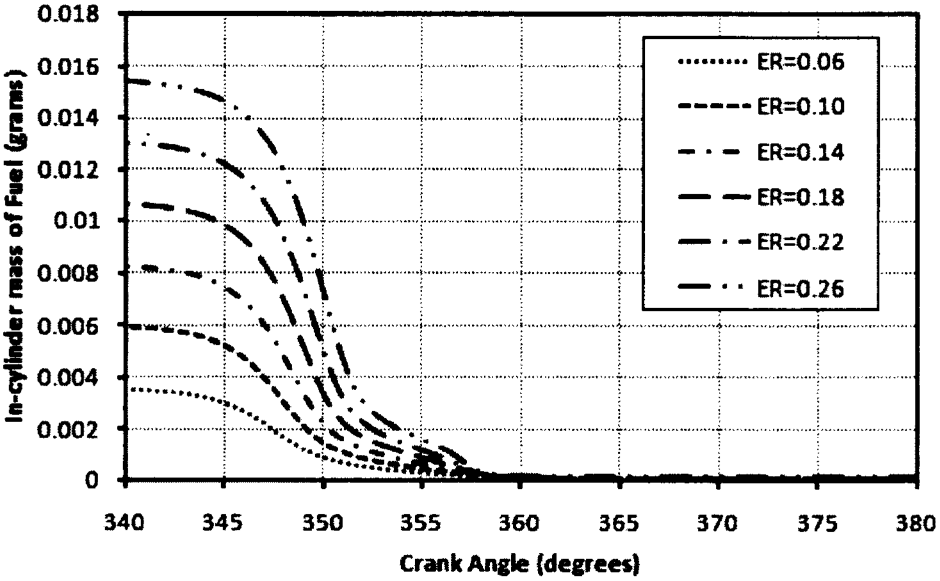

Figure 4.12 In-cylinder consumption of fuel (iso-octane).

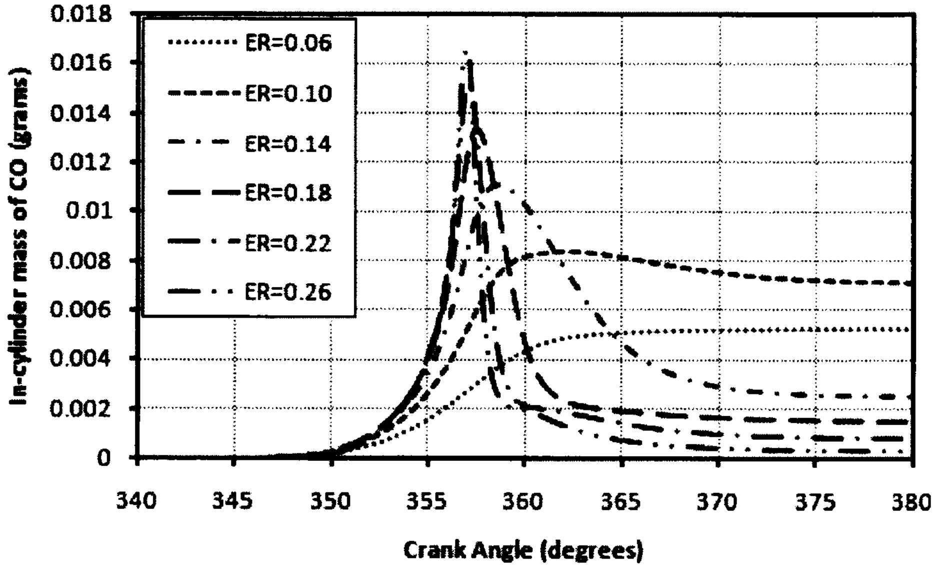

Figure 4.13 In-cylinder production and consumption of CO.

Figure 4.13 shows that the production of CO starts at 350 CA for all the equivalence ratios and the concentration increases rapidly for higher equivalence ratios. As the equivalence ratio decreases the rate of CO production decreases and subsequently consumption slows down. For the case of 0.06 and 0.10 equivalence ratios, the CO remains within the cylinder and it does not oxidize to CO_2. The trends shown in emissions (Figure 4.10) can be understood from these curves. The CO oxidation process can also be explained from the average in-cylinder temperature traces plotted in Figure 4.3. The average peak temperature for equivalence ratio of 0.14 was 1400 K. At this temperature, CO oxidizes to CO_2. For the equivalence ratios below 0.14, the average in-cylinder temperature is less than 1400 K, which would not allow oxidation of CO. Figure 4.14 shows the variation of CO_2 with respect to crank angle for different equivalence ratios.

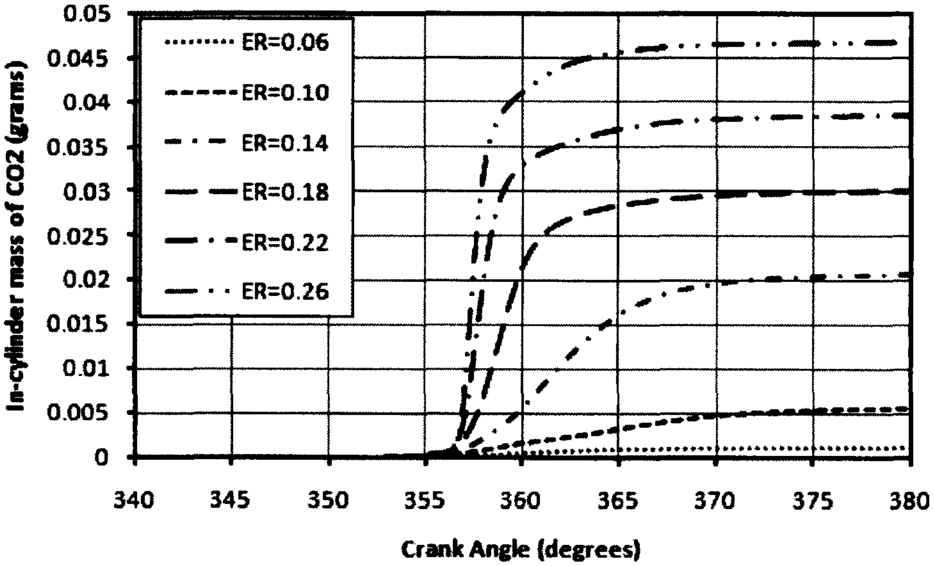

Figure 4.14 In-cylinder production of CO_2.

4.3 Summary

Numerical simulations have been conducted for a Cummins B-series production diesel engine running in HCCI mode to validate the detailed chemical reaction mechanism of iso-octane (Jia-Xie Mechanism) together with KIVA-3V coupled with the LES turbulence model described in Chapter 2. The results show that this solution methodology for HCCI combustion is suitable for application to iso-octane HCCI combustion engines. The application of this solution methodology with different types of HCCI engines will be discussed in Chapters 5 and 6.

Chapter 5

Combustion Process in Converted Kubota HCCI Engine

Numerical simulations have been carried on an Indirect Injection (IDI) type diesel engine converted to an HCCI engine. The experimental results used to validate the computational results were taken from Gnanam (2008). The stock engine was a Kubota D905 with a pre-chamber. The specifications of the engine are given in Table 5.1.

Engine type	Vertical 4-stroke liquid cooled diesel
Number of cylinders	3
Compression ratio	21:1
Total displacement	898 cc
Bore x Stroke (cm)	7.2 x 7.36
Intake valve open	14^0 before TDC
Intake valve close	210^0 after TDC
Exhaust valve open	485^0 after TDC
Exhaust valve open	17^0 after TDC
Pre-chamber volume	9 cc

Table 5.1 Experimental engine specifications

The experimental engine has a pre-chamber for mixing of fuel and capturing combustion products. The pre-chamber is located in the engine head. The pre-chamber passage was modified for HCCI engine operations. HCCI engine experiments were carried out by Gnanam (2008) for a single cylinder of three-cylinder engine. The head can be seen in Figure 5.1. The original pre-chamber passage and the modified pre-chamber passage are shown in Figure 5.1. In the original engine, diesel fuel was directly injected into the pre-chamber. In the converted engine, the fuel injector was replaced with a secondary piston allowing for compression ratio changes. The compression ratio of the cylinder was adjusted by varying the secondary piston position. The pre-chamber in the stock engine was spherical shaped and connected to the main cylinder through a small passage. In the modified engine, the passage to the cylinder was enlarged as shown in Figure 5.1. The pre-chamber shape was also modified from spherical to cylindrical form. A pressure sensor was mounted through the glow plug passage in the pre-chamber.

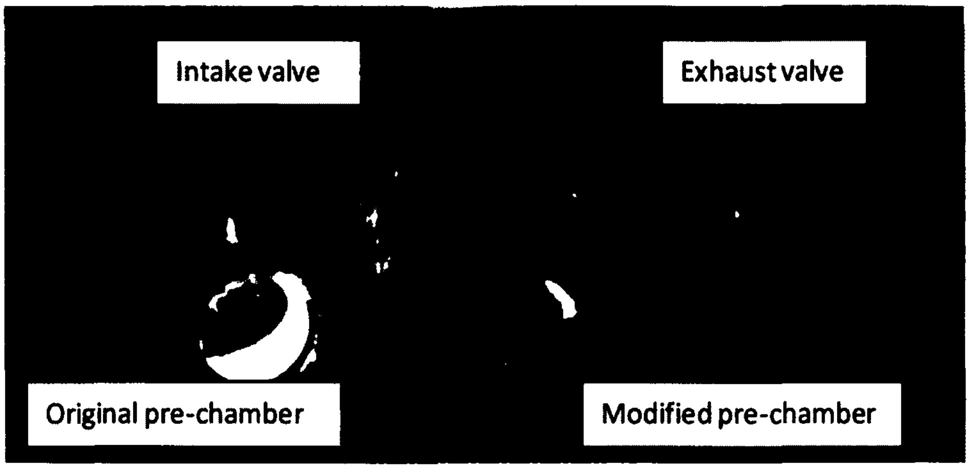

Figure 5.1 Kubota D905 engine head.

Experimental Variations:

Form the statistical analysis carried out by Gnanam (2008) on his experimetnal data, the peak pressure showed cycle-to-cycle variation of 4.76%. The Coefficient Of Variation (COV) for IMEP was confirmed to be about 5% for temperatures of 420 K and 410 K and about 28% for 400K. The in-cylinder pressure sensor used in the experiments has about 0.5 % accuracy of the measured value at 423 K. The intake charge temperature has an accuracy of 1.5 K and the coolant temperature variation was found to be about 1.46% (about 2 K). The results obtained were averaged over 125 cycles.

5.1 Simulation conditions

The computational geometry used in the simulations is a simplified version of the actual engine. The computational domain and the mesh used are shown in Figure 5.2. The K3PREP grid generation program was used for the mesh generation. K3PREP is based on a multi-block grid generation algorithm. For the engine geometry considered, 115 blocks were patched together to generate the domain. The grid spacing can be defined separately in each individual block. The intake port and exhaust port shapes were simplified to generate the engine domain. The port shapes in the computational studies are cylinders with a 90 degree bend while they are cylinders with a smooth turn in between. The pre-chamber origin was located at the same place as in the experimental geometry. The shape of the pre-chamber was considered to be cylindrical in the numerical studies while in the experiments it is with a spherical-like shape. The intake and exhaust ports were slightly offset from the central axis as in the real geometry. Grids are clustered near the top of the cylinder and in the pre-chamber region. There are 56,480 cells at TDC and 278,640 cells when the piston is at the BDC. The simulations were carried out on an Intel Quad-core Q9550 processor machine and it took approximately 200 hours of CPU time for one cycle (intake to exhaust). Most of the CPU time was spent on chemical kinetic calculations.

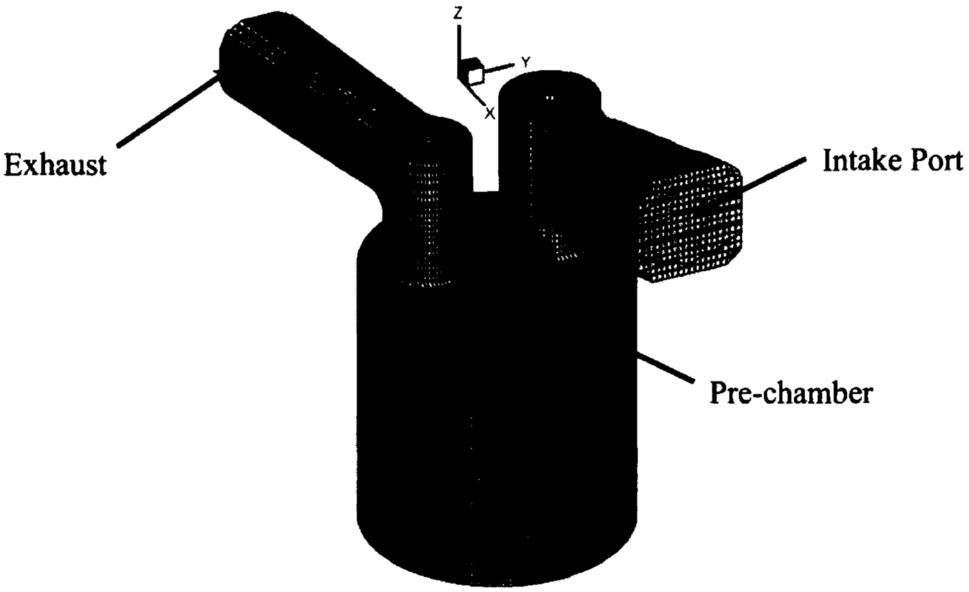

Figure 5.2 Computational domain and grid in isometric view when piston is at Bottom Dead Centre.

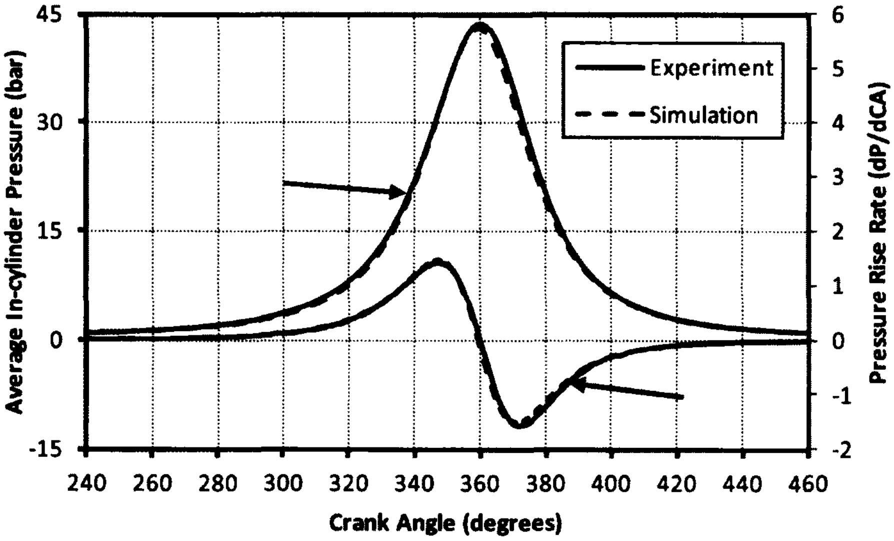

Figure 5.3 Comparison of pressure trace and pressure rise rate during motoring conditions.

Initially, computations are carried out for a single complete engine cycle without combustion to compare pressure traces and pressure rise rates. Figure 5.3 shows the comparison between experimental data and computational results obtained for the motoring case. The wall temperature in the simulations is assumed to be constant and equal to the coolant temperature, it may not be the case in experiments.

The experimental conditions given in Table 5.2 at intake charge temperature of 420 K were taken as initial conditions for the motoring simulations. The simulation pressure was adjusted to match the experimental pressure trace by varying the intake pressure. The simulation was carried out for one engine cycle. Results indicate that the simulation had a similar pressure rise rate as that of the experiments. The motoring trace still shows some minor differences .in the pressure traces and pressure rise rate, which is due to the differences of the geometry of the engine between the experimental and the numerical studies as mentioned before. After calibrating the numerical simulation results with engine experimental data for motoring conditions, simulations were carried out with combustion. Computations have been carried out for two engine cycles and the results obtained from the second cycle are compared with the experimental results. The first cycle results are used only to set the initial conditions discussed here. The simulation conditions were taken from the experimental conditions as shown in Table 5.2.

Engine	Single-Cylinder HCCI engine
Engine speed (rpm)	1035
Equivalence ratio	0.3
Coolant Temperature	348K (± 2)
Intake charge Temperature	420K, 410K, 400K (± 1.5)
Compression ratio	21:1
Volumetric efficiency	80%
Fuel	100% Iso-octane

Table 5.2 Experimental conditions for HCCI engine runs.

The experimental investigations were carried out for different fuels with varying intake charge temperature and EGR conditions (Gnanam 2008). In the numerical studies, the effect of intake charge temperature on HCCI engine combustion was studied and all other conditions were held constant, as listed in Table 5.2.The experimental results used for comparison are obtained by averaging over 125 individual cycles. The fuel was injected into preheated intake air ahead of the intake port. The fuel-air mixture was assumed to be homogeneous by the time it reached the intake port. The experimental results include HRR, IMEP, thermal efficiency and engine out emissions.

Simulations were carried out for three cases with different intake charge temperatures, 418.5K, 408.5K, and 398.5K respectively. The intake temperature and equivalence ratio were adjusted to match the peak pressure and onset of combustion. For the first case, with experimental intake charge temperature of the 420K, the simulation intake temperature was adjusted to 418.5K (which is within the temperature range of experimental data, 420K±1.5) to get the right onset of combustion and the equivalence ratio was increased to 0.35 to give the correct pressure rise compared to experiments. The other two cases were carried out with same initial conditions except for intake temperature. The objective of this study is to check the sensitivity of HCCI engine combustion to intake charge temperature in terms of onset of combustion and also to validate the combustion solver in predicting the combustion performance parameters for a full engine cycle.

5.2 Results and discussion

Figures 5.4 and 5.5 shows the comparison of pressure traces and heat release rates for different intake charge temperatures from simulations and experimental data (Gnanam 2008). The simulations results indicate similar trends as those of the experiments shown in Figure 5.4. The peak pressure locations for intake temperatures of 418.5 K and 408.5 K are at the same crank angle as that of experiments. For the higher temperature case, the experimental pressure trace shows a higher peak pressure than the simulations. The difference in the peak pressures is likely due to a higher than actual heat loss in simulation from the engine cylinder at a given crank angle. In the simulations we are assuming constant wall temperature, which may not be the case in the real experiments. In the computational domain, it can be shown that at the end of compression, the surface area to volume ratio would be highest. The experimental peak pressure is usually obtained by averaging the peak pressure from certain number of experiments with a range of variation about 4.76% (about 3.57 bar for a peak pressure of 75 bar) that has been marked in Figure 5.4 by an error bar as shown. From this figure, it can be seen that the simulation pressure traces are in good agreement with the experimental data.

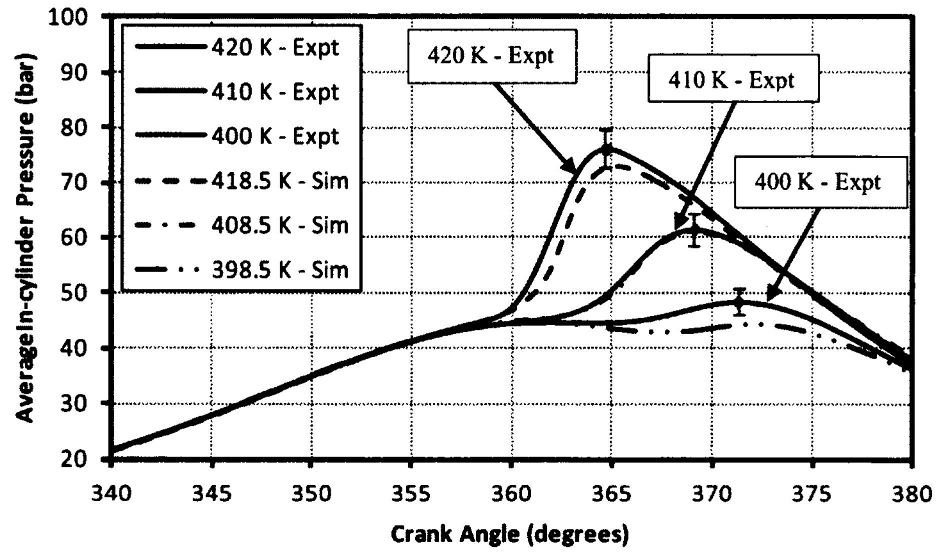

Figure 5.4 Comparison of pressure for different intake charge temperatures.

The heat release rates also follow the same trend as the experiments. The peak heat release rate for intake temperature of 418.5 K is higher than in the experiments but the onset of combustion and duration remain the same. The peak heat release rate locations are slightly shifted for intake temperature of 418.5 K.

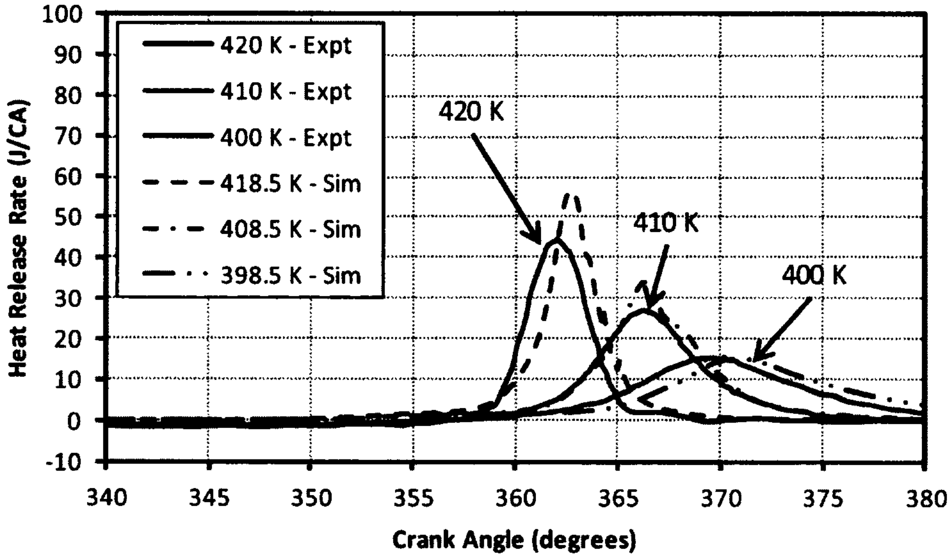

Figure 5.5 Comparison of heat release rate for different intake charge temperatures.

In order to further analyze the heat release, the 10% heat release crank angles and 10% to 90% heat release durations are plotted in Figure 5.6. Simulation results indicate the same trend as experiments. The 90% heat release durations indicate the simulation takes slightly longer compared to experiments.

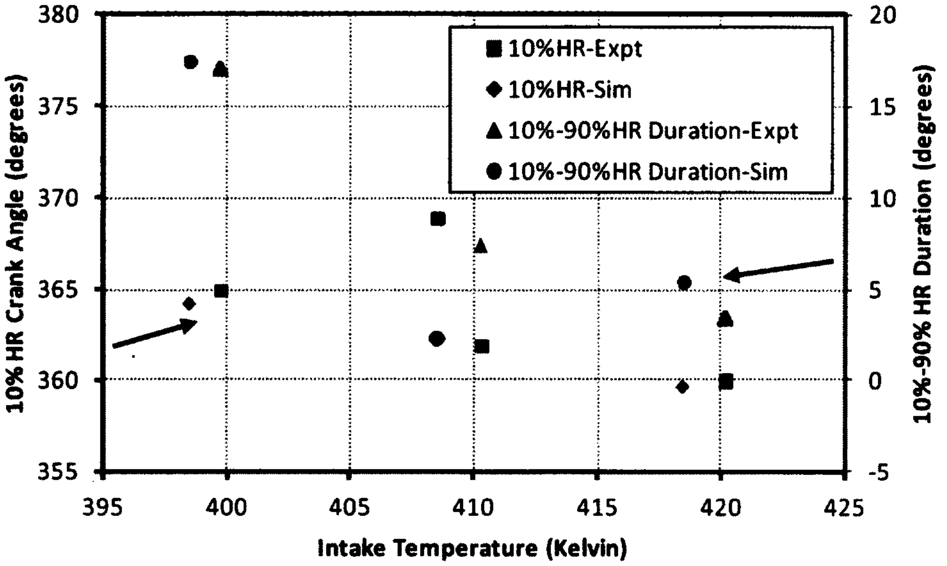

Figure 5.6 Comparison of 10% heat release crank angle and 10% - 90% heat release duration between experiments and simulations for different intake charge temperatures.

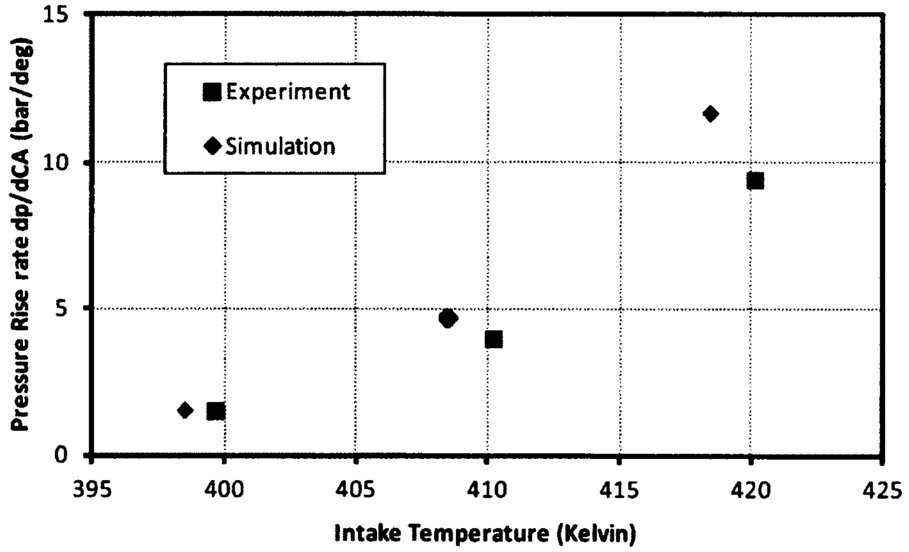

Figure 5.7 Comparison of pressure rise rate for different intake charge temperatures.

One of the important engine parameters is the pressure rise rate. This parameter differentiates between the engine knock and low temperature combustion. In order to run an engine smoothly, the pressure rise rate should be less than 15 bar per crank angle

(Gnanam 2008). Figure 5.7 shows the comparison of pressure rise rates between the experiments and simulations for different intake charge temperatures. As the intake charge temperature increases, the pressure rise rate also increases. Therefore, for a particular equivalence ratio, there is a limit on the maximum intake charge temperature. The differences between the simulation and experiment results are due to geometry and heat transfer losses. In the simulations the throat to the chamber was simplified into a circular hole, while in the experiments it is an oval shape and causes throttling effect.

Figure 5.8 shows the work done by the cylinder in terms of IMEP. Simulation results show a higher IMEP compared to experiments but follow the same trend. As the intake charge temperature increases, the engine reaches a higher IMEP until around 410 K and then the IMEP slightly reduces. Figure 5.8 indicates that an increase in intake charge temperature will not increase power produced and there is an optimum intake charge temperature of 410K. Figure 5.9 shows the thermal efficiency of the engine. Simulation results show higher thermal efficiency compared to experiments. Since the IMEP was higher for simulations, it shows the same trend in thermal efficiency.

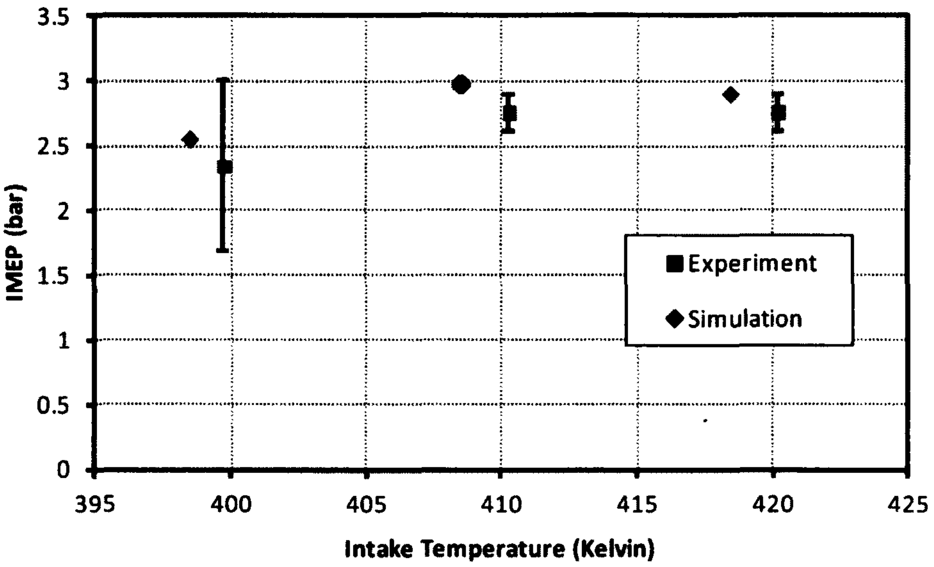

Figure 5.8 Comparison of IMEP for different intake charge temperatures.

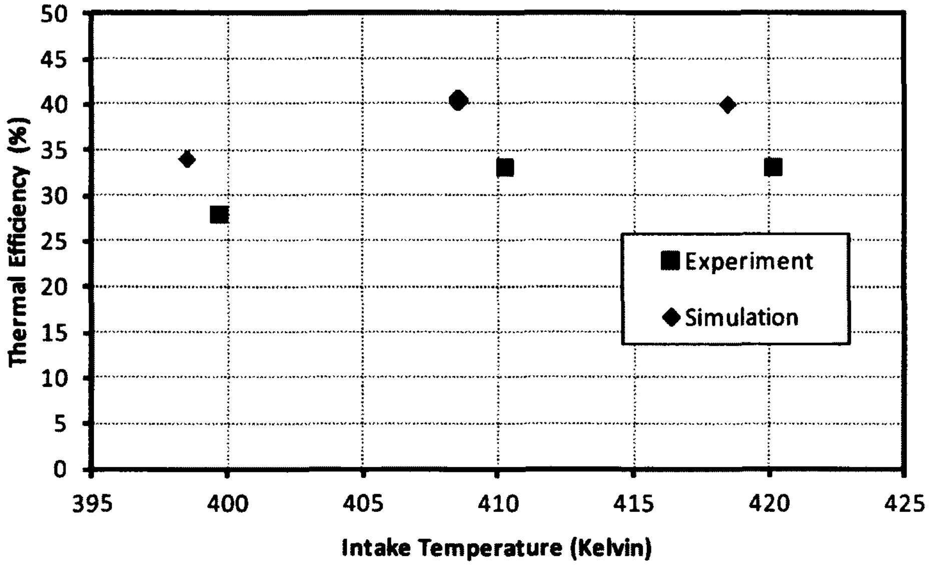

Figure 5.9 Comparison of thermal efficiency for different intake charge temperatures.

Figure 5.10 shows the comparison of CO and UHC emissions for different intake charge temperatures. Results indicate that as the intake temperature decreases below 408 K, the amount of CO and UHC emissions increases drastically. This indicates that the intake charge temperature has to be kept above 408 K to reduce the amount of CO and UHC emissions.

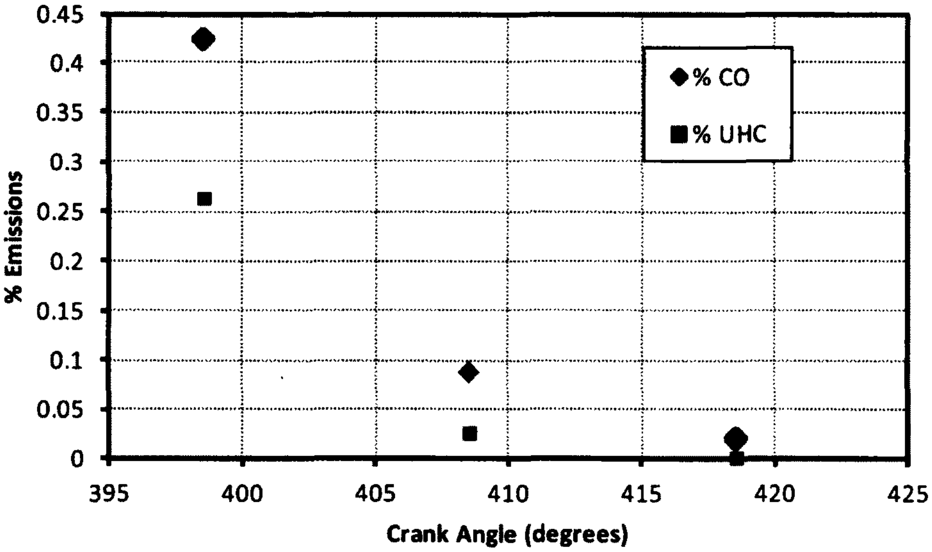

Figure 5.10 Comparison of % emissions for different intake charge temperatures.

Figure 5.11 shows the variation of average in-cylinder temperature for different intake charge temperatures. The temperature trends indicate that the 10 K difference in intake charge temperature makes significant difference in peak temperatures. Although the NO_x emissions are negligible for all the cases, the UHC and CO emissions increase considerably at lower temperatures due to partial oxidation of fuel and CO.

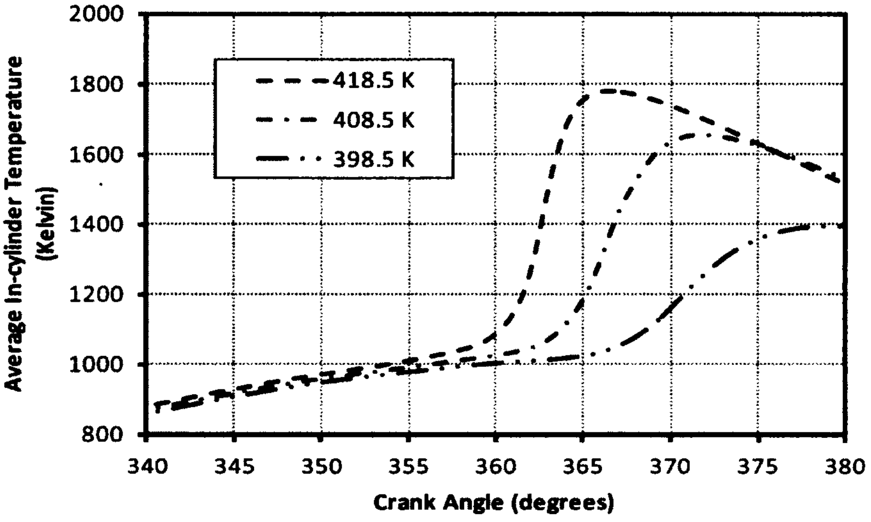

Figure 5.11 Average in-cylinder temperature for different intake charge temperatures.

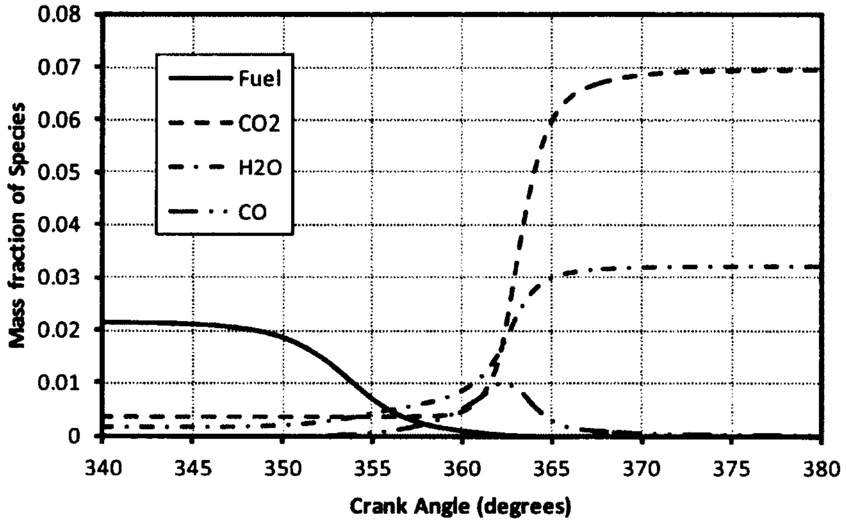

Figure 5.12 Mass fractions of different species for intake charge temperature of 418.5 K.

Mass fractions of species were shown in Figure 5.12. The fuel mass fraction starts to decrease significantly above 350 CA, when the temperature due to compression reaches the auto-ignition temperature of iso-octane . The formation of CO species starts from 355

CA, reaches peak around 362 CA and then drops down. This species shows the same trend as heat release. The peak heat release happens at 362 CA. Figure 5.12 also shows the mass fraction of CO_2 and H_2O. The combustion products CO_2 and H_2O indicate that the combustion process is complete and the oxidation of CO to CO_2 completes by 370 CA.

Figure 5.13 shows the variation of average turbulent kinetic energy for different intake charge temperatures. These data show an increase in the turbulent kinetic energy due to combustion. The qualitative results indicate that, when the combustion happens in the pre-chamber, fluid within the pre-chamber is forced to enter the cylinder, which causes a sudden raise in the turbulent kinetic energy of the flow field. The results also show the same trend for all the cases, but as the intake charge temperature is decreased, the increase in turbulent kinetic energy was delayed and prolonged compared to higher intake charge temperatures.

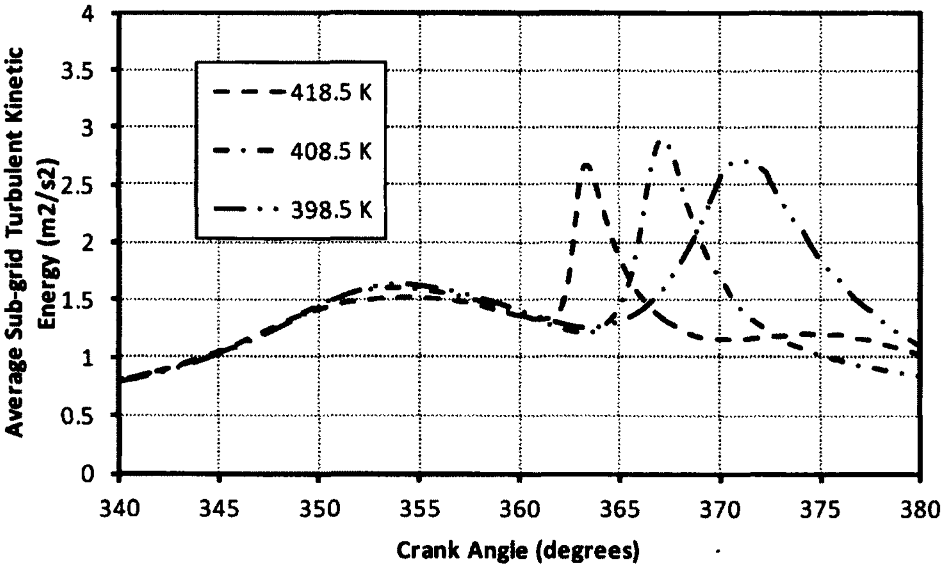

Figure 5.13 Variation of average turbulent kinetic energy for different intake charge temperatures.

To study flow field and combustion characteristics within the cylinder, qualitative results were analyzed. The results were plotted in three planes (XY, XZ and YZ) passing through the computational domain as shown in Figure 5.14. The three planes shown in Figure 5.14 (a) are chosen such that the planes pass through the centerline of main components. The YZ plane is chosen such that it passes through the centre of the intake and exhaust valves as shown in Figure 5.14 (b). The XZ plane is chosen such that it passes through the centre of the pre-chamber. The XY plane is chosen near to the top dead centre at 0.0011 m from the top dead centre. Several flow parameters and concentration parameters have been plotted to understand the flow field and combustion phenomena.

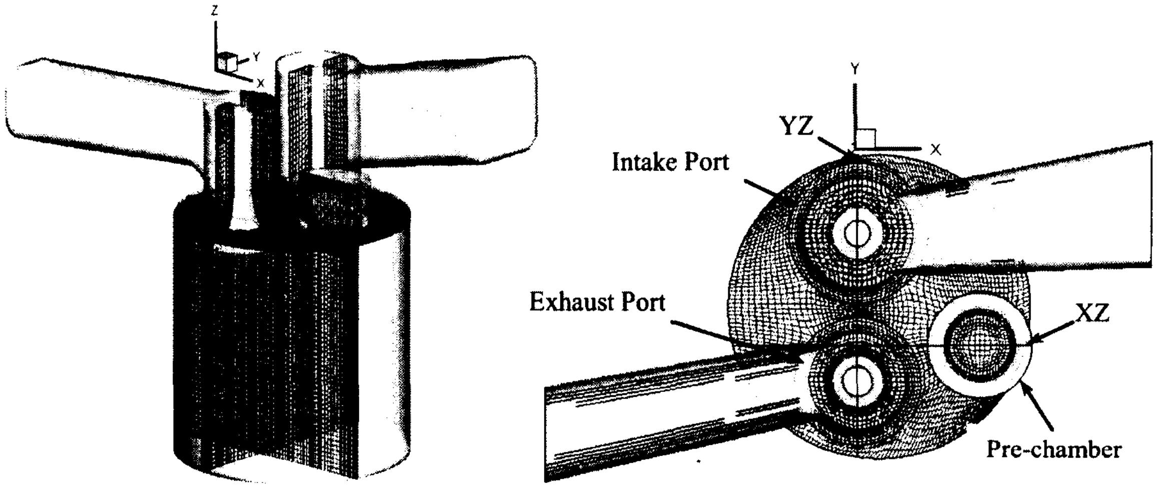

Figure 5.14 (a) Computational domain at Bottom Dead Centre showing three planes chosen for qualitative analysis, (b) Computational domain shown from top of cylinder.

In the numerical simulations, it was assumed that the intake port contains homogeneous charge of fuel-air mixture at an equivalence ratio of 0.35. The qualitative analysis was carried out for intake charge temperature of 418.5 K.

The combustion process in the cylinder starts during the compression stroke, when the in-cylinder temperature reaches a sufficient value to auto-ignite the iso-octane . The fuel consumption starts around 345 CA and it is completely consumed by 365 CA. Figures 5.15-5.17 show variation of temperature, molar fraction of fuel and equivalence ratio distributions within the cylinder from crank angle 345 CA to 355 CA. The equivalence ratio contours and molar fraction of fuel contours indicate that the fuel consumption starts at 345 CA. The plots also show the “islands” of fuel consumption and the paths towards the pre-chamber, which indicate that the fluid is forced into the pre-chamber. The temperature distributions illustrated in Figure 5.15 do not show any considerable variation but the overall temperature was increasing steadily. This period can be considered as the fuel oxidation time where the fuel converts into intermediate species.

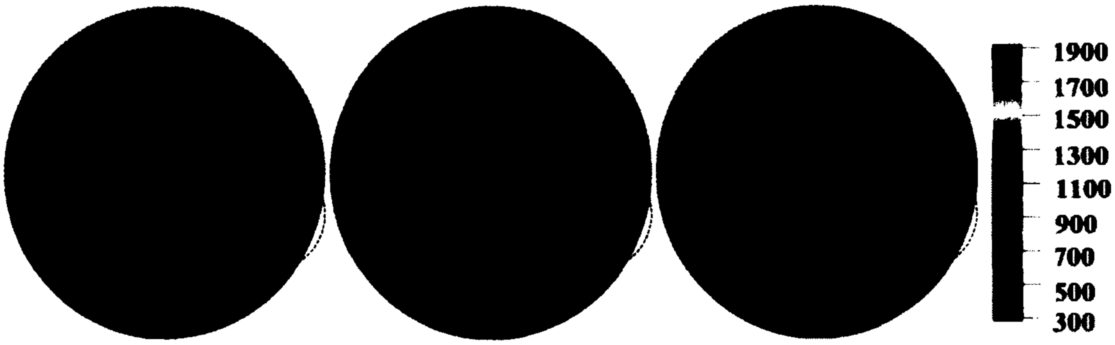

(a) (b) (c)

Figure 5.15 Temperature (Kelvin) contours in XY plane at crank angles (a) 345 CA, (b) 350CA, and (c) 355 CA for 418.5K initial temperature.

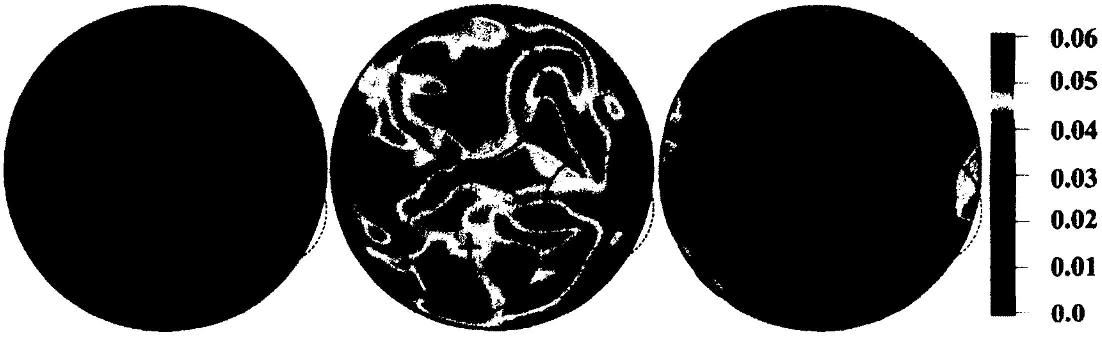

(a) (b) (c)

Figure 5.16 Molar fraction contours of fuel in XY plane at crank angles (a) 345 CA, (b) 350CA, and (c) 355 CA for 418.5K initial temperature.

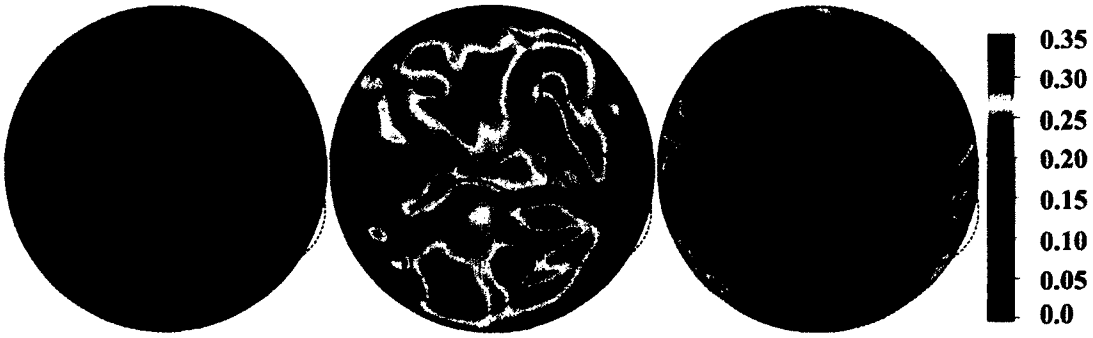

(a) (b) (c)

Figure 5.17 Equivalence ratio contours in XY plane at crank angles (a) 345 CA, (b) 350CA, and (c) 355 CA for 418.5K initial temperature.

Figures 5.18 to 5.20 show the variation of temperature, molar fraction of fuel and equivalence ratio distributions for crank angles 360, 365 and 370 respectively. Molar fractions of fuel and equivalence ratio distributions indicate complete consumption of fuel by 366 CA. The in-cylinder temperature reaches peak temperature around 365 CA. It can be seen that there are several high temperature zones within the cylinder. Figure 5.18(a) shows the temperature distribution within the cylinder at 360 CA. It can be seen that there are multiple sites of high temperature under the intake valve and clearance areas between the valves. The combustion phenomena can be considered as HCCI combustion, since multiple ignition points can be seen within the cylinder. The slight temperature variation within the cylinder due to valve locations, wall temperatures, pre-chamber location and flow within the cylinder determine the ignition zones.

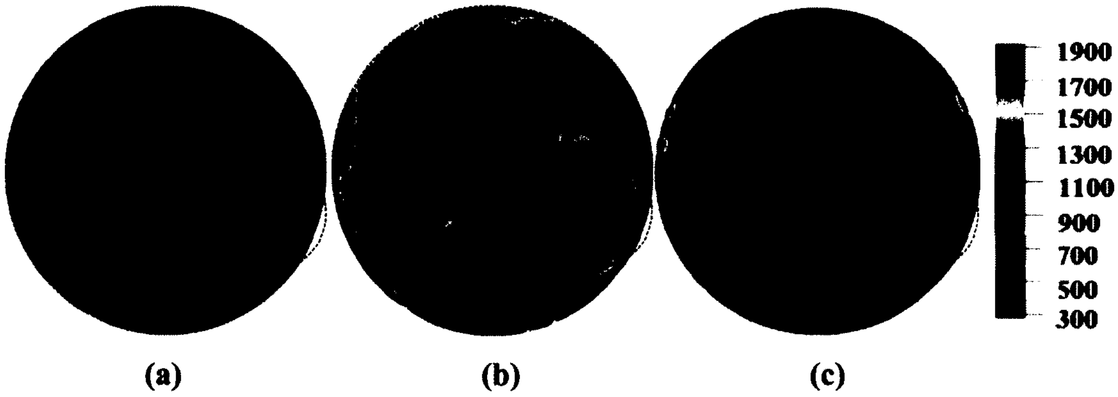

Figure 5.18 Temperature (Kelvin) contours in XY plane at crank angles (a) 360 CA, (b) 365 CA, and (c) 370 CAfor 418.5K initial temperature.

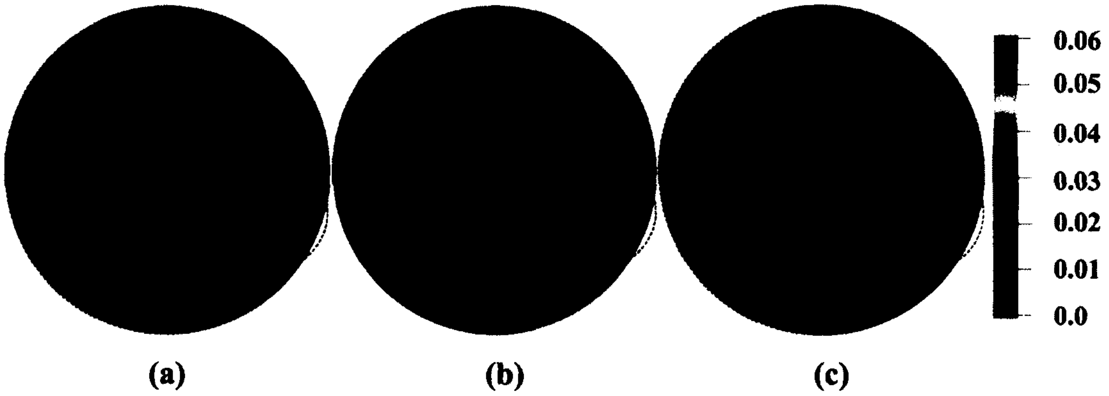

Figure 5.19 Molar fraction contours of fuel in XY plane at crank angles (a) 360 CA, (b) 365 CA, and (c) 370 CAfor 418.5K initial temperature.

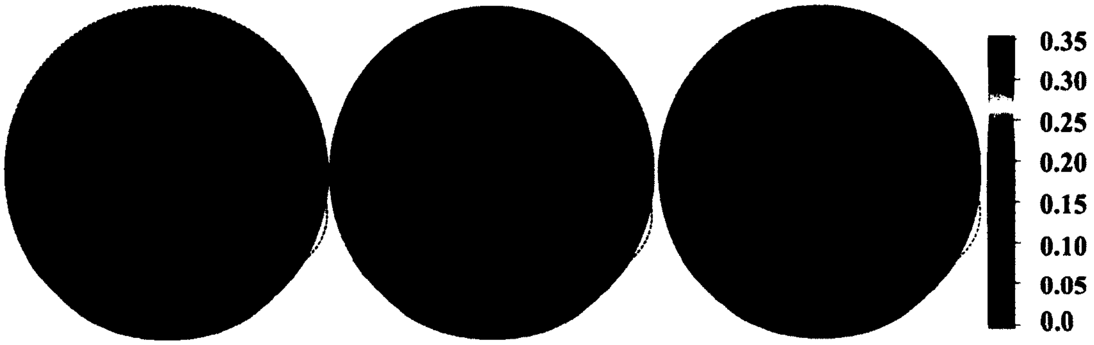

(a) (b) (c)

Figure 5.20 Equivalence ratio contours in XY plane at crank angles (a) 360 CA, (b) 365 CA, and (c) 370 CA for 418.5K initial temperature.

Figures 5.21 to 5.23 show molar fraction distributions of O_2, CO_2 and H_2O respectively. The O_2 molar fraction contours show the O_2 consumption within the cylinder starts at 360 CA and continues to spread towards the walls. At 370 CA, the in-cylinder has uniform O_2 distribution. Figures 5.22 and 5.23 show distributions indicating the production of CO_2 and H_2O.

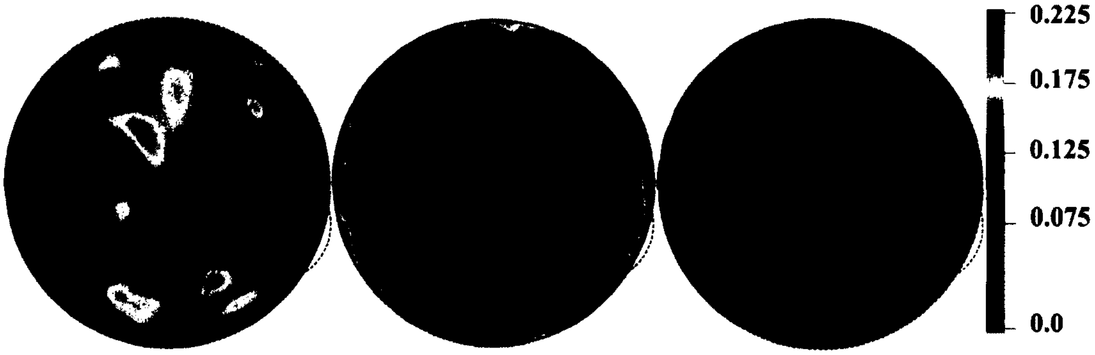

(a) (b) (c)

Figure 5.21 Molar fraction contours of O_2 in XY plane at crank angles (a) 360 CA, (b) 365 CA, and (c) 370 CA for 418.5K initial temperature.

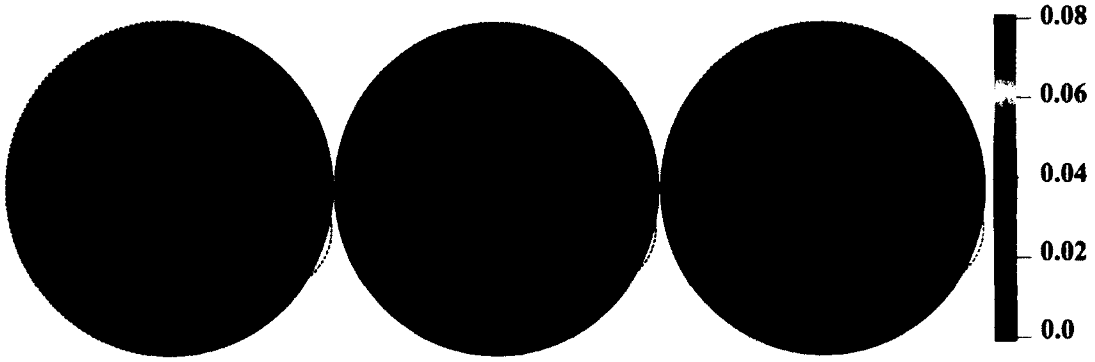

(a) (b) (c)

Figure 5.22 Molar fraction contours of CO_2 in XY plane at crank angles (a) 360 CA, (b) 365 CA, and (c) 370 CA for 418.5K initial temperature.

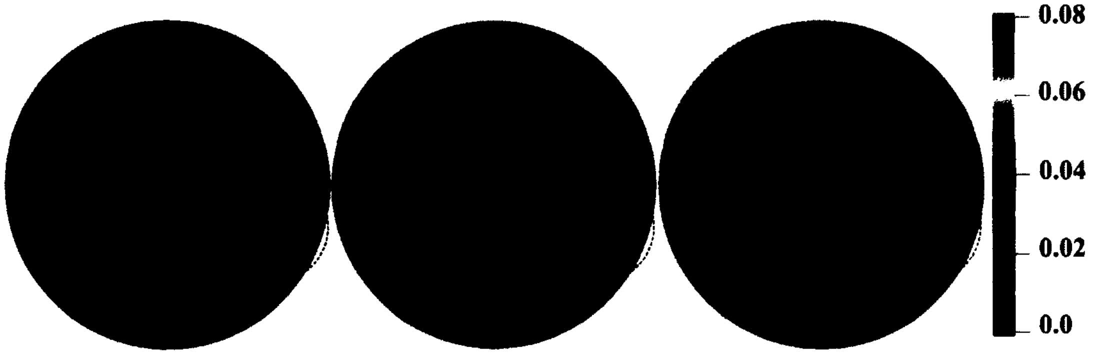

(a) (b) (c)

Figure 5.23 Molar fraction contours of H_2O in XY plane at crank angles (a) 360 CA, (b) 365 CA, and (c) 370 CA for 418.5K initial temperature.

Figures 5.24-5.26 show the variation of molar fractions for CO, H_2 and OH respectively. These plots identify that the local zones where the consumption of species are higher. At 370 CA, the CO produced is almost consumed and there are only traces of H_2. The OH concentration remains within the cylinder.

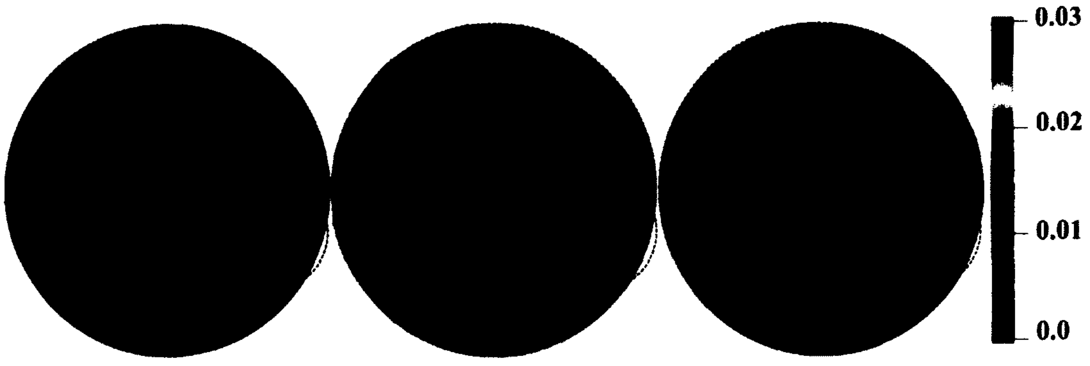

(a) (b) (c)

Figure 5.24 Molar fraction contours of CO in XY plane at crank angles (a) 360 CA, (b) 365 CA, and (c) 370 CA for 418.5K initial temperature.

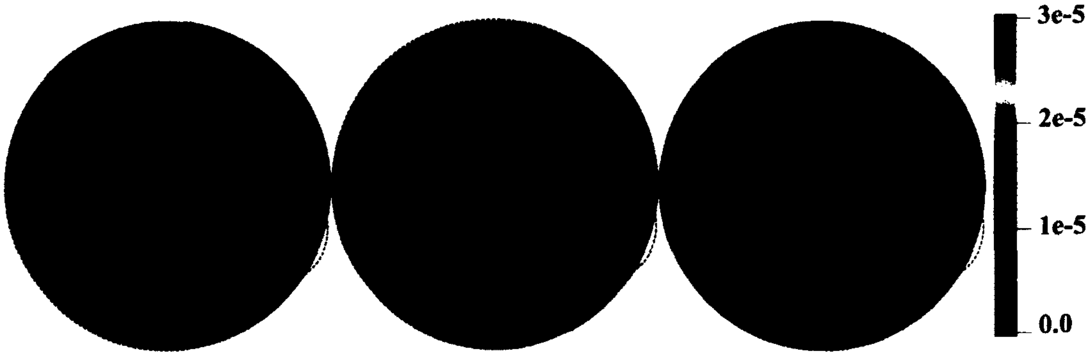

(a) (b) (c)

Figure 5.25 Molar fraction contours of H_2 in XY plane at crank angles (a) 360 CA, (b) 365 CA, and (c) 370 CA for 418.5K initial temperature.

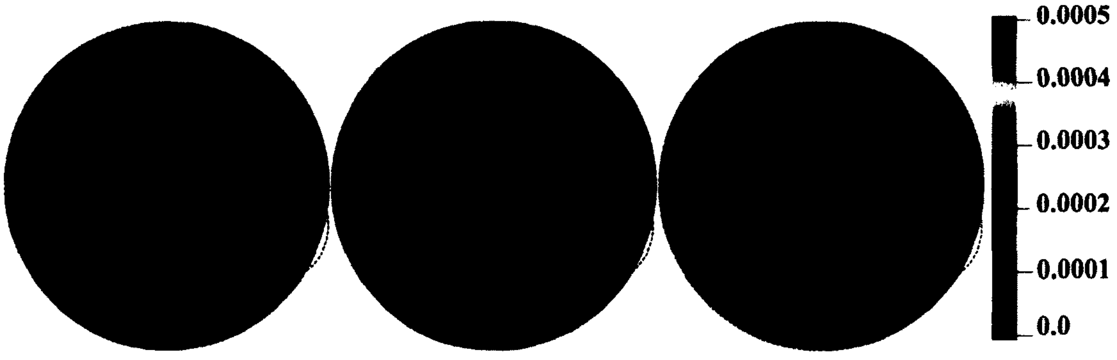

(a) (b) (c)

Figure 5.26 Molar fraction contours of OH in XY plane at crank angles (a) 360 CA, (b) 365 CA, and (c) 370 CA for 418.5K initial temperature.

Figures 5.27 to 5.29 show the molar fractions of N_2, NO and NO_2 respectively. These plots show the production of NO_x at high temperature zones within the cylinder.

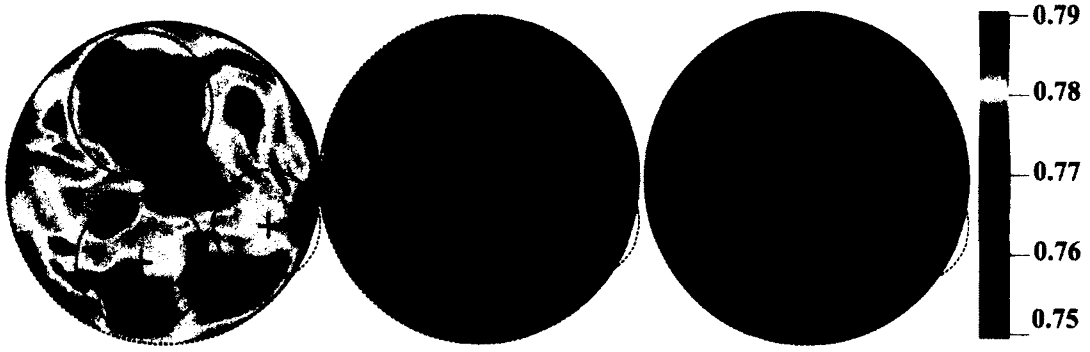

(a) (b) (c)

Figure 5.27 Molar fraction contours of N_2 in XY plane at crank angles (a) 360 CA, (b) 365 CA, and (c) 370 CA for 418.5K initial temperature.

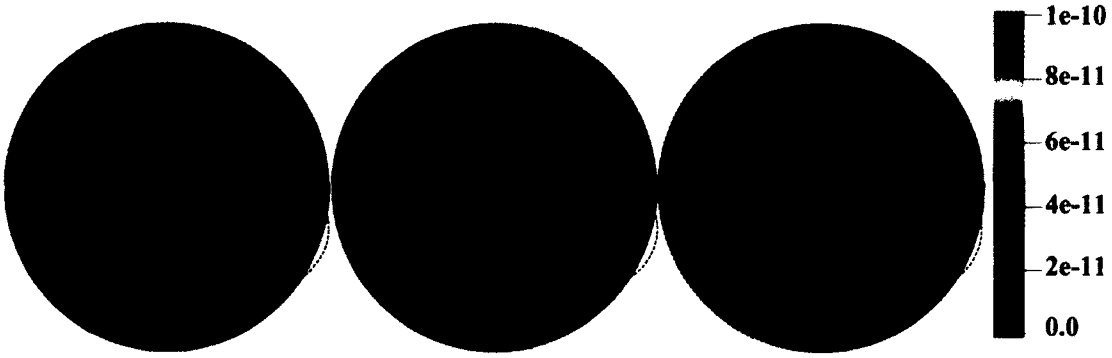

(a) (b) (c)

Figure 5.28 Molar fraction contours of NO in XY plane at crank angles (a) 360 CA, (b) 365 CA, and (c) 370 CA for 418.5K initial temperature.

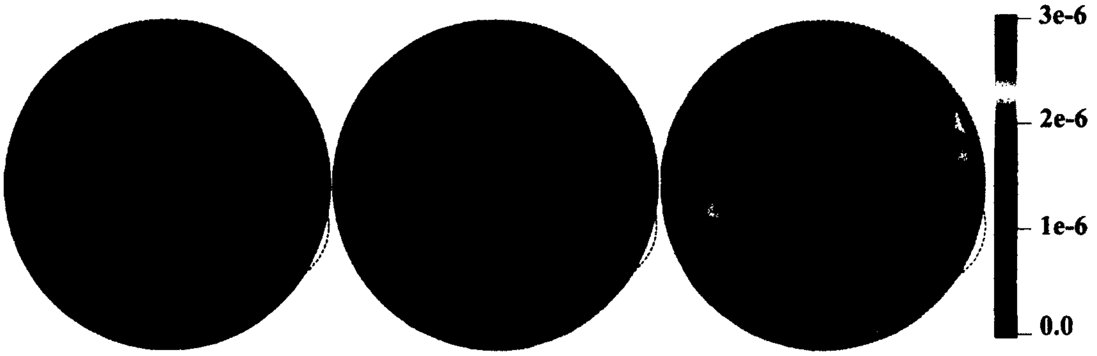

(a) (b) (c)

Figure 5.29 Molar fraction contours of NO_2 in XY plane at crank angles (a) 360 CA, (b) 365 CA, and (c) 370 CA for 418.5K initial temperature.

Figures 5.30 to 5.32 shows streamlines, sub-grid scale turbulent kinetic energy and velocity vectors, respectively. These plots illustrate the flow direction and the flow structures. At 365 CA, it can be seen that there is a sudden increase in the turbulent kinetic energy. This is due to combustion within the pre-chamber which forces the fluid into the cylinder.

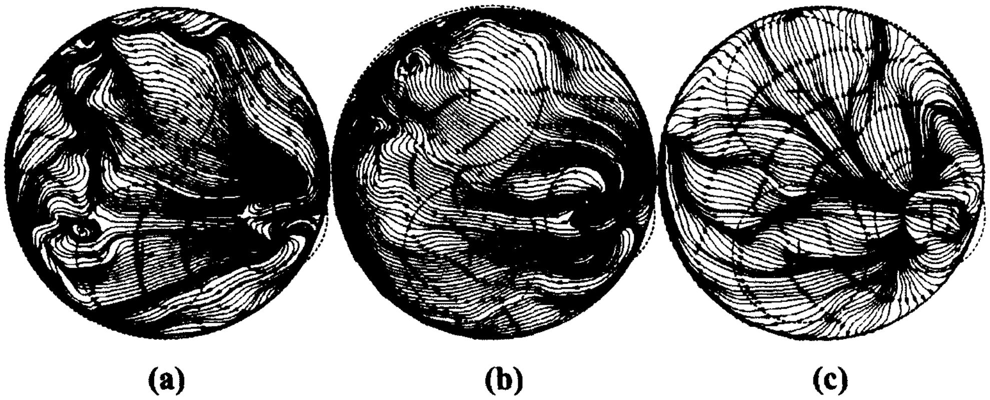
(a) (b) (c)

Figure 5.30 Streamline plots in XY plane at crank angles (a) 360 CA, (b) 365 CA, and (c) 370 CA for 418.5K initial temperature.

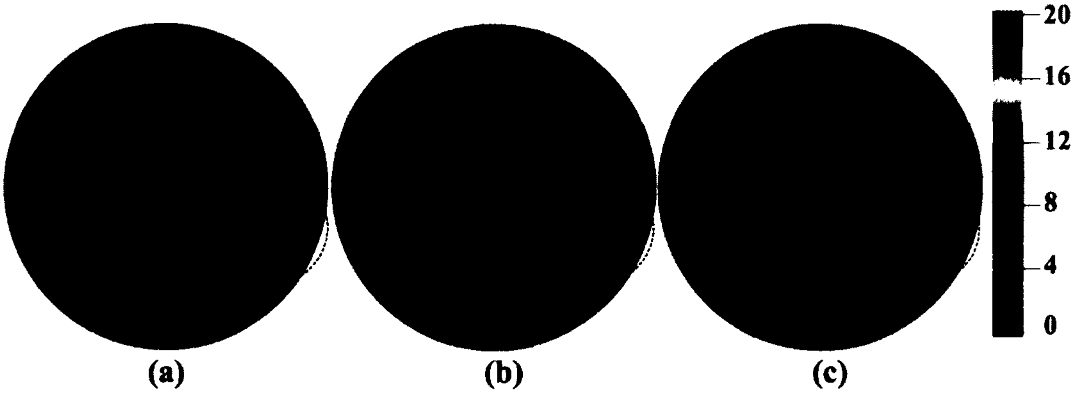

(a) (b) (c)

Figure 5.31 Sub-grid scale turbulent kinetic energy (m^2/sec) contours in XY plane at crank angles (a) 360 CA, (b) 365 CA, and (c) 370 CA for 418.5K initial temperature.

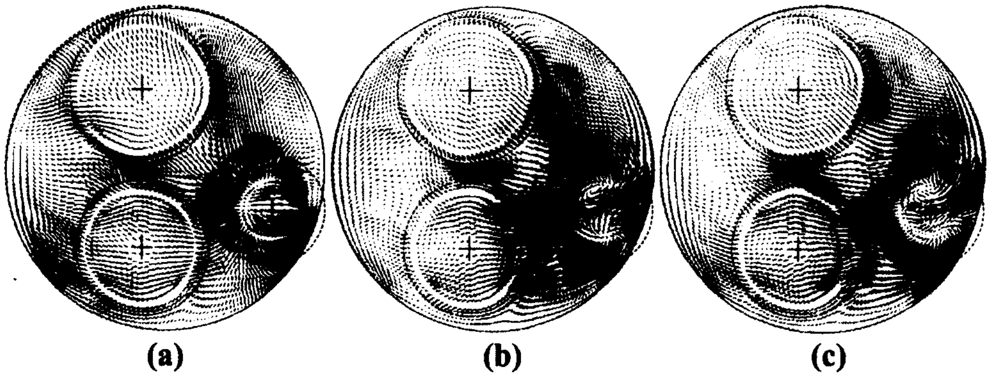
(a) (b) (c)

Figure 5.32 Velocity vectors in XY plane at crank angles (a) 360 CA, (b) 365 CA, and (c) 370 CA for 418.5K initial temperature.

Figure 5.33 shows the temperature contours and velocity vectors in the pre-chamber. The temperature contours show the high temperature core region within the pre-chamber. The corresponding vector plot shows the vortex flow structure within the pre-chamber. The combustion process within the pre-chamber forces the flow into the cylinder, which is shown by velocity vectors pointing downwards at 362 CA. At 364 CA, peak temperature within the pre-chamber reaches 2000 K in the centre. The high temperature zone within the pre-chamber gradually reduces and temperature distributes uniformly throughout the pre-chamber.

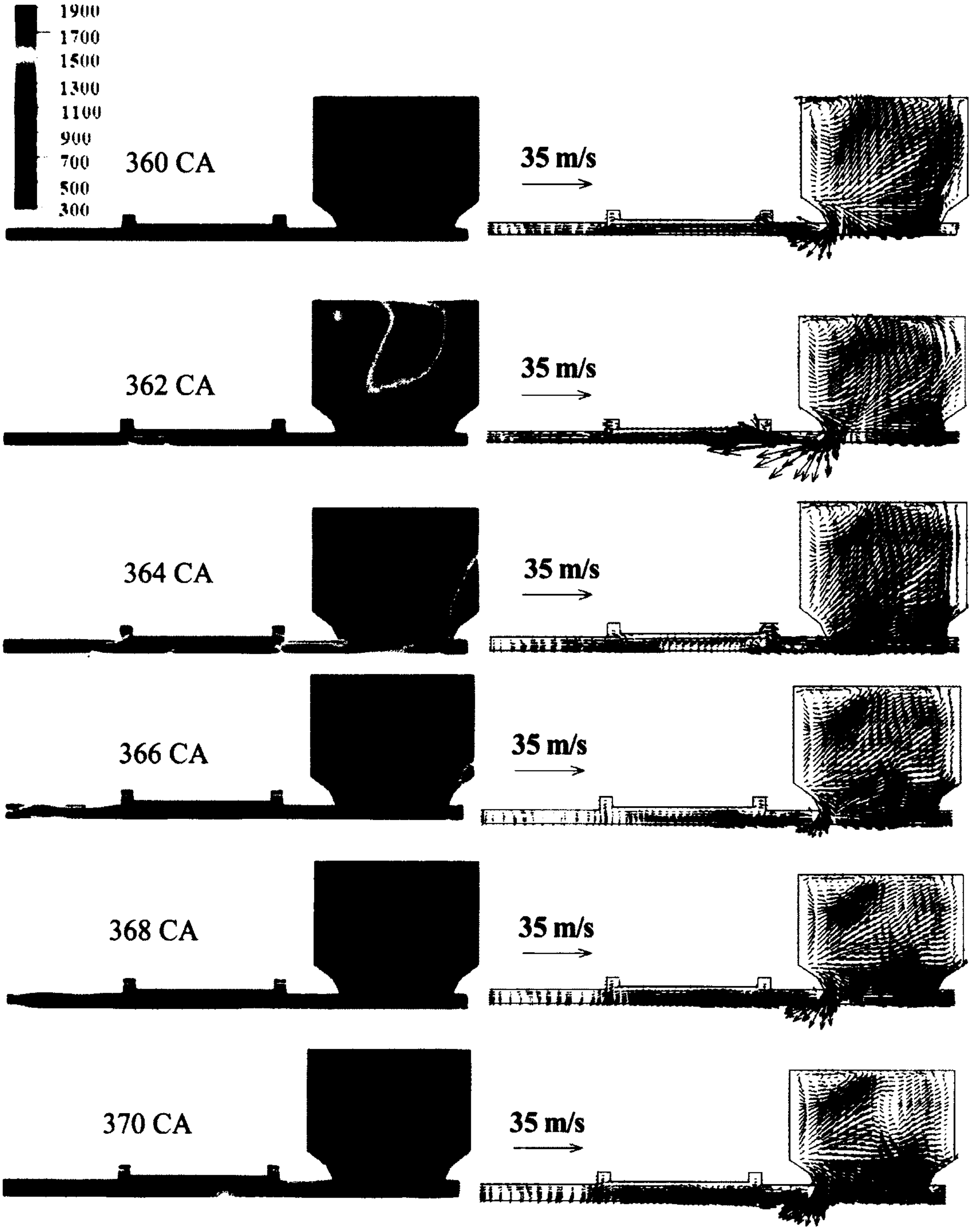
1900
1700
1500
1300
1100
900
700
500
300
360 CA
362 CA
364 CA
366 CA
368 CA
370 CA
35 m/s
35 m/s
35 m/s
35 m/s
35 m/s
35 m/s

(a) (b)

Figure 5.33 Variation of (a) temperature and (b) velocity vectors within pre-chamber in XZ plane.

5.3 Summary

Three dimensional numerical investigations with a Large Eddy Simulation and detailed chemical kinetic mechanism for the combustion of iso-octane have been conducted in a HCCI engine that was converted from Indirect Injection type diesel engine (Kubota D905). By comparing the numerical simulation results with the corresponding experimental results, it can be concluded that the numerical simulations can provide reliable sophisticated information regarding HCCI combustion that is in good agreement with experimental results.

The accuracy of the CKL solver in predicting HCCI engine performance parameters are as follows:

1. The simulations predicted IMEP is within 5% variation for high intake temperature cases and within 10% variation for lower intake temperature, which is consistent with the experimental Coefficient of Variation (COV) (cf., Gnanam 2008).

2. The peak pressures from simulations show 4% deviation from the experimental data for intake temperature of 418.5 K, less than 1% for 408.5 K and 7.5% for lower intake temperature of 398.5 K.

3. The pressure rise rates show 4% deviation from the experimental data for intake temperature of 398.5 K and 20% deviation for intake temperature of 408.5 K and 25% variation for 418.5 K.

In order to calibrate the CKL solver, temperature and pressure traces within the cylinder and intake pressure and temperature are required from the experiments.

The details of the parametric studies with different intake temperatures show that the intake temperature is one of the most important parameters to control the start of HCCI combustion and the emissions. Most importantly, these types of parametric studies using the methodology developed in this dissertation, detailed turbulent flow structures, combustion startup process and emissions generation mechanisms, can be used to optimize engineering design of HCCI engines.

Chapter 6

Effect of Internal Mixing and Reformation Chamber on HCCI Engine Combustion

The effect of an internal mixing and reformation (IMR) chamber on the HCCI engine combustion is studied numerically in this chapter. The design of the chamber was based on the concept of using an additional independent valve to control the duration of HCCI combustion and reduce the pressure rise rate to subsequently decrease the peak temperature. Fuel reformation is a partial oxidation process in which the fuel is converted into H_2 and CO. These products, due to their partial oxidation state, can be used to advance combustion timing and have control over the combustion process.

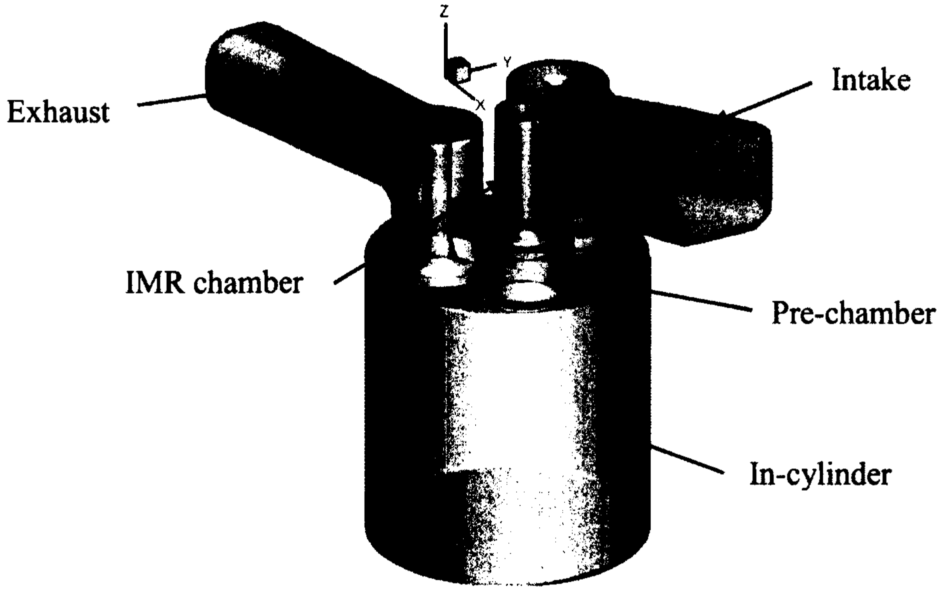

Figure 6.1 Computational domain of cylinder with internal mixing and reformation chamber.

The IMR chamber valve opens outwards and can be managed independently. The IMR chamber volume is 5 cc. The simulation initial conditions are taken to be the same as the conditions from Chapter 5 with an intake charge temperature of 418.5 K. The computations were carried out for the following two scenarios: 1) additional fuel injection into the IMR chamber and 2) without fuel injection into the IMR chamber.

Table 6.1 shows the initial conditions taken from Chapter 5 and condition with the IMR chamber.

Engine speed	1035 rpm
Compression ratio without IMR chamber	21:1
Compression ratio with IMR chamber open	16:1
Additional amount of fuel injected into IMR chamber	20% of the fuel in the cylinder.
Wall temperature	350 K
Intake charge temperature	418.5 K
Equivalence ratio	0.35
Fuel	Iso-octane

Table 6.1 Initial conditions for simulations.

The initial intake temperature, pressure and equivalence ratio are kept constant. In the cases where fuel is directly injected into the IMR chamber, the amount of fuel injected was calculated based on the amount of air within the chamber and equivalence ratio of 0.35.

6.1 Simulation conditions

Simulation conditions for cases studied are given in Table 6.2.

Cases	**Engine Cycle**	**IMR Chamber**	**Fuel Injection into IMR Chamber**		**IMR chamber Valve Timing**	
			Start	**End**	**Open**	**Close**
Case 1	2	No	N/A	N/A	N/A	N/A
Case 2	2	Yes	N/A	N/A	360 CA	372 CA
Case 3	2	Yes	360 CA	370 CA	360 CA	372 CA
Case 4	3	Yes	360 CA	370 CA	360 CA	405 CA
Case 5	3	Yes	360 CA	390 CA	360 CA	405 CA
Case 6	3	Yes	350 CA	360 CA	360 CA	372 CA

Table 6.2 Simulation conditions for six cases.

The cases shown in Table 6.2 are divided based on the engine cycle and conditions of the IMR chamber. The results from cases 1, 2 and 3 were analyzed after two engine cycles. The IMR chamber valve opening and closing crank angle were decided based on the results from case 1. The function of the IMR chamber is to capture the high temperature combustion products and potentially to reduce the pressure rise rate and lower the peak temperature. The IMR chamber valve opening time was chosen at the crank angle at which 10% of the heat is released for case 1, without the IMR chamber. The average in-cylinder temperature for case 1 without IMR chamber increased above 1000 K just before 360 CA, reached a peak temperature of 1800 K around 365 CA and then dropped down gradually. By opening the valve from 360 CA to 372 CA, the peak temperature is reduced and combustion products at a high temperature enough for fuel reformation (1500 K) are captured. The fuel injection timing was decided based on the mixing within the IMR chamber. By injecting the fuel at the same time as the valve opening crank angle (360 CA), the fuel mixes well with the in-cylinder charge. The additional amount of fuel injected into the IMR chamber was determined based on the amount of air residing in the IMR chamber. The amount of fuel injected was equal to 20% of fuel entering through the intake valve, and is calculated to keep an equivalence ratio of 0.35 within the chamber. The fuel injection follows a half-sine wave form. The fuel injector was located near top wall of the IMR chamber and injection was directed downwards into the chamber.

Results obtained at the end of the 2nd cycle for IMR chamber cases 1, 2 and 3 reveal some effects of IMR chamber valve timing and fuel injection into the IMR chamber. Three new cases 4, 5 and 6 given in Table 6.2 were defined based on the results obtained from case 3. The initial conditions for cases 4, 5 and 6 were taken from the end of cycle results of case 3. Compared with case 3, cases 4 and 5 have prolonged valve timing with different fuel injection durations. Case 6 has advanced fuel injection timing and the same valve timing as case 3. For all cases with injection into the IMR chamber (Cases 3, 4, 5 and 6), the amount of fuel injected remains the same.

Details of valve timing and fuel injection timing for six cases discussed in Table 6.2 are shown in Figure 6.2. The IMR chamber valve timings are shown on top of the scale and IMR chamber fuel injection timing on bottom of the scale.

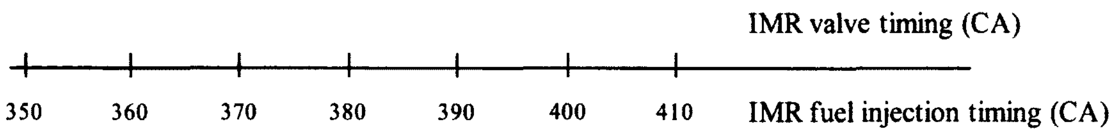
IMR valve timing (CA)
350
360
370
380
390
400
410
IMR fuel injection timing (CA)

(a) Case 1

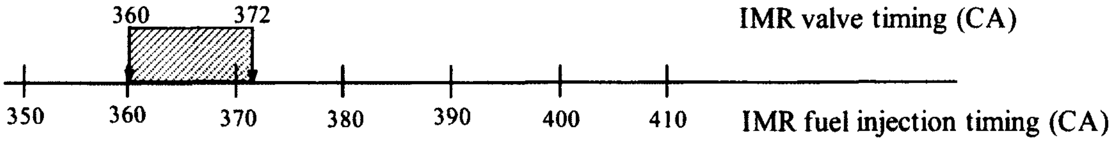
360
372
IMR valve timing (CA)
350
360
370
380
390
400
410
IMR fuel injection timing (CA)

(b) Case 2

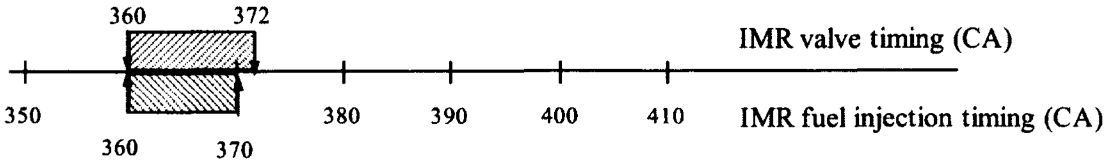
360
372
IMR valve timing (CA)
350
380
390
400
410
IMR fuel injection timing (CA)
360
370

(c) Case 3

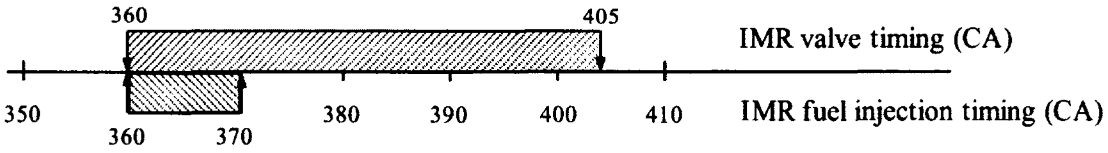
360
405
IMR valve timing (CA)
350
380
390
400
410
IMR fuel injection timing (CA)
360
370

(d) Case 4

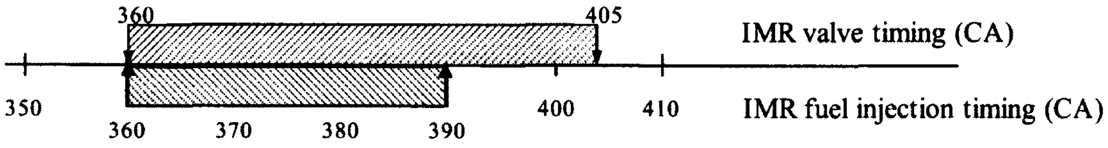
360
405
IMR valve timing (CA)
350
400
410
IMR fuel injection timing (CA)
360
370
380
390

(e) Case 5

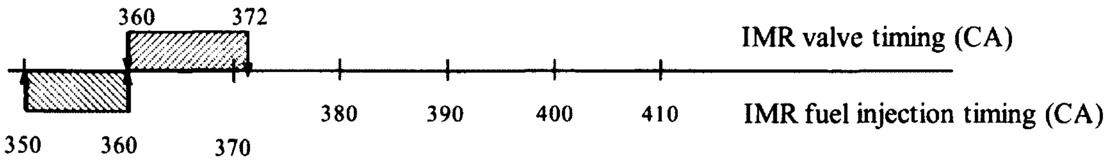
360
372
IMR valve timing (CA)
380
390
400
410
IMR fuel injection timing (CA)
350
360
370

(f) Case 6

Figure 6.2 IMR chamber valve timings and IMR chamber fuel injection timings for six cases.

6.2 Results and discussions

Figure 6.3 shows the average in-cylinder pressure trace for cases 1, 2 and 3 mentioned in Table 6.2. The in-cylinder pressure traces for cases 2 and 3 show lower peak pressure due to valve opening at 360 CA and the adjustment in pressure due to movement of the valve. The peak pressure locations for the IMR chamber cases are slightly shifted to 367 CA, while the peak pressure location without the IMR chamber is at 365 CA. The maximum in-cylinder pressure for case 2 is low compared to cases 1 and 3. This was due to the IMR chamber trapping the combustable products. The in-cylinder pressure trace from case 2 shows the drop in pressure due to the IMR chamber valve opening at 362 CA and after 363 CA, in-cylinder pressure starts to increase until it reaches a peak pressure of 57 bar at 366 CA due to the combustion process happening in-cylinder. In case 3, the in-cylinder pressure rises at the same rate until it reaches a peak pressure of 60 bar. The in-cylinder pressure traces indicate that pressure rise rates are lower for IMR chamber cases 2 and 3 compared with case 1.

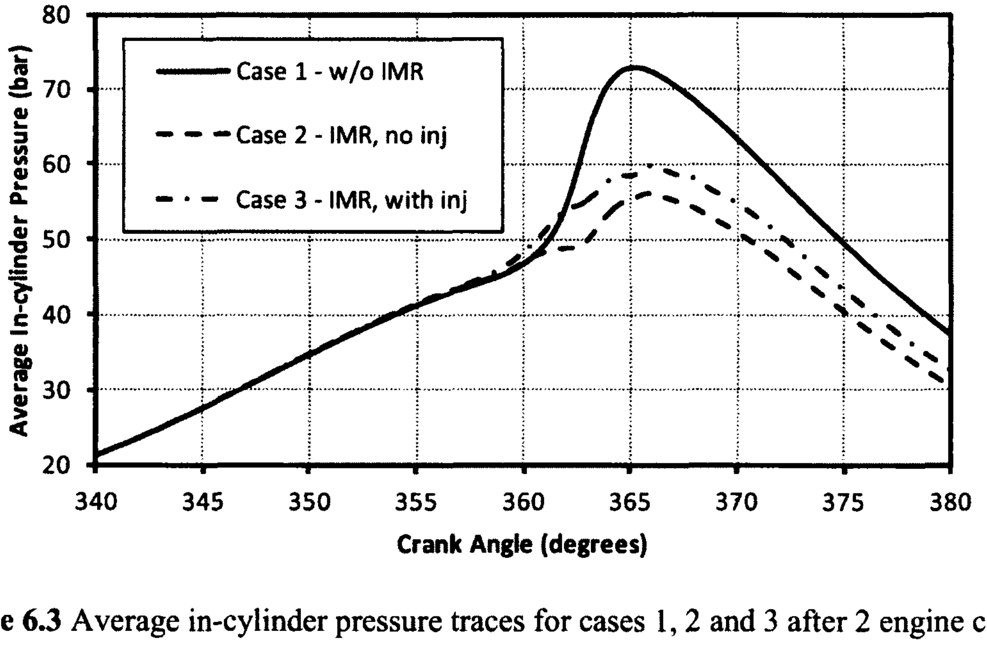

Figure 6.3 Average in-cylinder pressure traces for cases 1, 2 and 3 after 2 engine cycles.

Figure 6.4 shows the average in-cylinder temperature for cases 1, 2 and 3 mentioned in Table 6.2. The in-cylinder temperature trends indicate that cases 2 and 3, with IMR chamber, have lower in-cylinder temperatures compared to case 1 and the peak temperature for case 2 and 3 are 50 K lower compared to case 1. The difference in the peak temperature can make significant differences in the amount of NO_x emissions.

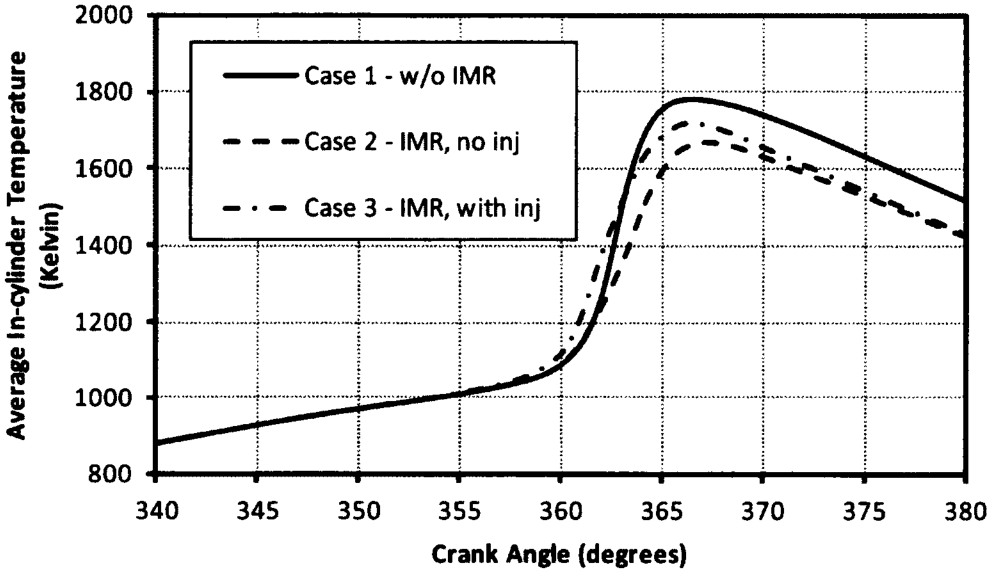

Figure 6.4 Average in-cylinder temperature variations for cases 1, 2 and 3 after 2 engine cycles.

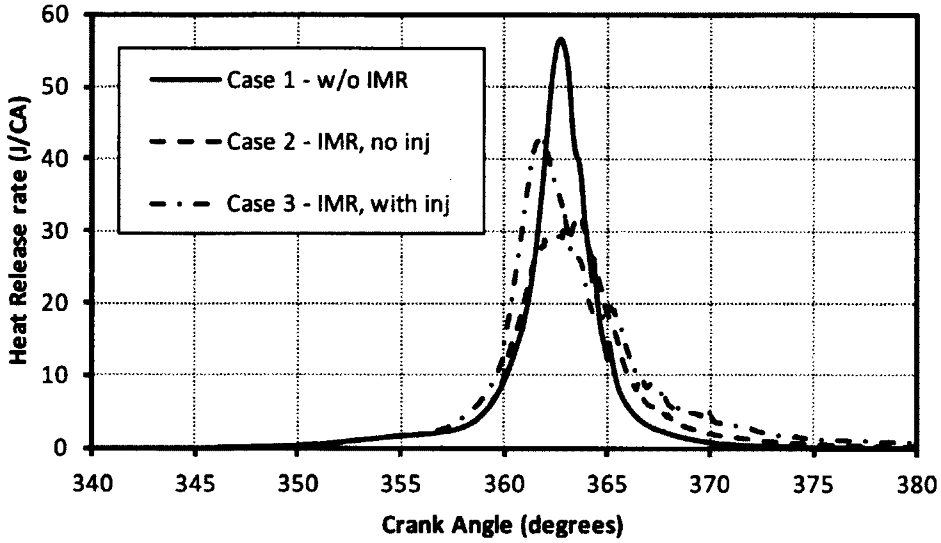

Figure 6.5 Heat release rate comparison for cases 1, 2 and 3 after 2 engine cycles.

Figure 6.5 shows the heat release rate for cases 1, 2 and 3 mentioned in Table 6.2. The heat release rate curves show that the heat release lasts longer for IMR chamber cases 2 and 3 compared to without the IMR chamber (Case 1). For the case with fuel injection in the IMR chamber (Case 3), the heat release rate reaches peak of 43 J/CA and then drops down slowly compared to other cases. The peak heat release rate location for the case with fuel injection into IMR chamber (Case 3) is slightly advanced compared to the case without IMR chamber (Case 1) due to presence of residual gases from the previous cycle within the cylinder.

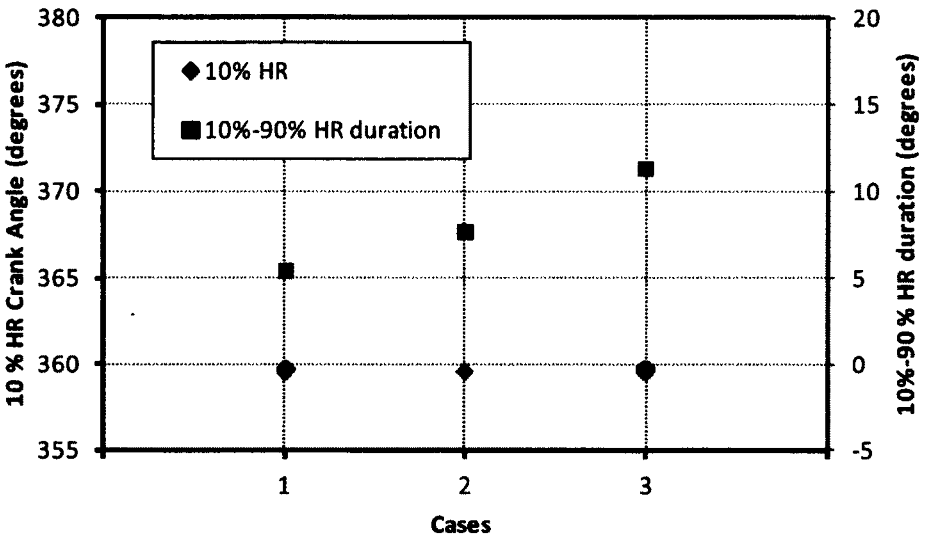

Figure 6.6 10% HR crank angle and 10%-90% heat release duration for cases 1, 2 and 3 after 2 engine cycles.

Figure 6.6 shows the 10% heat release crank angle and 10% to 90% heat release duration for cases 1, 2 and 3. For all three cases, 10% HR occurred at approximately at the same crank angle, around 359 CA. This indicates that the IMR chamber valve opening at 360 CA was as expected at 10% heat release. 10% to 90% HR duration shows variations between the cases 1, 2 and 3. The case with fuel injection into the IMR chamber (Case 3) shows the largest duration compared to the other cases. Both cases 2 and 3, with the IMR chamber, show prolonged heat release.

Figure 6.7 shows IMEP for cases 1, 2 and 3 respectively. The values obtained indicate that the IMEP of the engine drops down due to opening of the IMR chamber valve, but the case with fuel injection into the IMR chamber (Case 3) indicates higher IMEP compared to the case without fuel injection into the IMR chamber. Although the amount of work obtained is less compared to the case without IMR chamber, the IMR chamber valve timing and fuel injection could be manipulated to obtain the required IMEP.

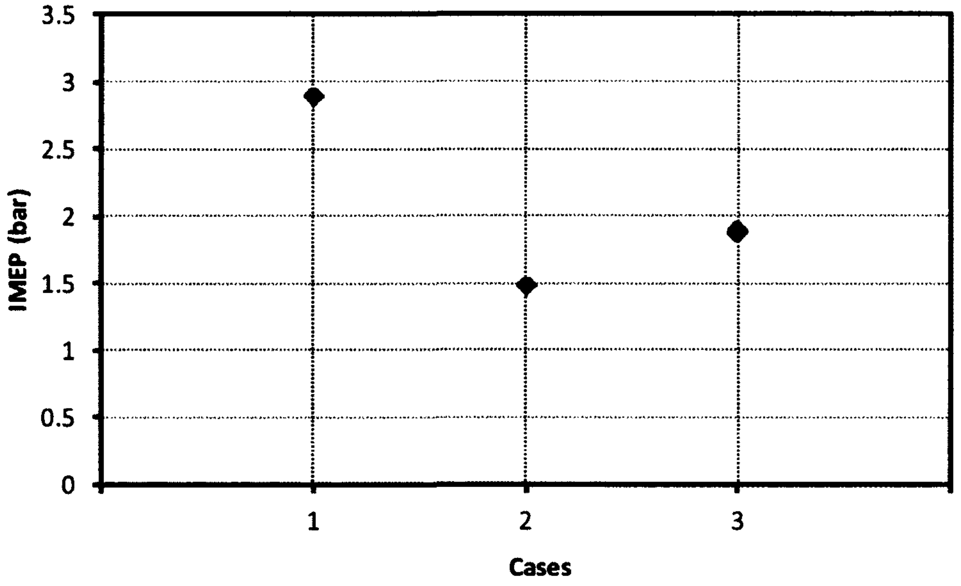

Figure 6.7 Indicated Mean Effective Pressure for cases 1, 2 and 3 after 2 engine cycles.

Figure 6.8 shows CO and UHC emissions obtained for cases 1, 2 and 3. The CO emission is high in cases 2 and 3. These cases would require after-treatment. The NO_x emissions are negligible (less than 1 ppm) in cases 1, 2 and 3 since the average peak temperature was below 1800 K. The trends indicate that the fuel injection into the IMR chamber (Case 3) gives higher CO emissions than the case without the IMR chamber (Case 1). This can be attributed to not having an optimal fuel injection time and IMR chamber valve timing. The UHC emissions show that the case with no fuel injection into the IMR chamber (Case 2) is high compared with fuel injection into the IMR chamber (Case 3). This is due to lower temperature and pressure in the cylinder in case 2.

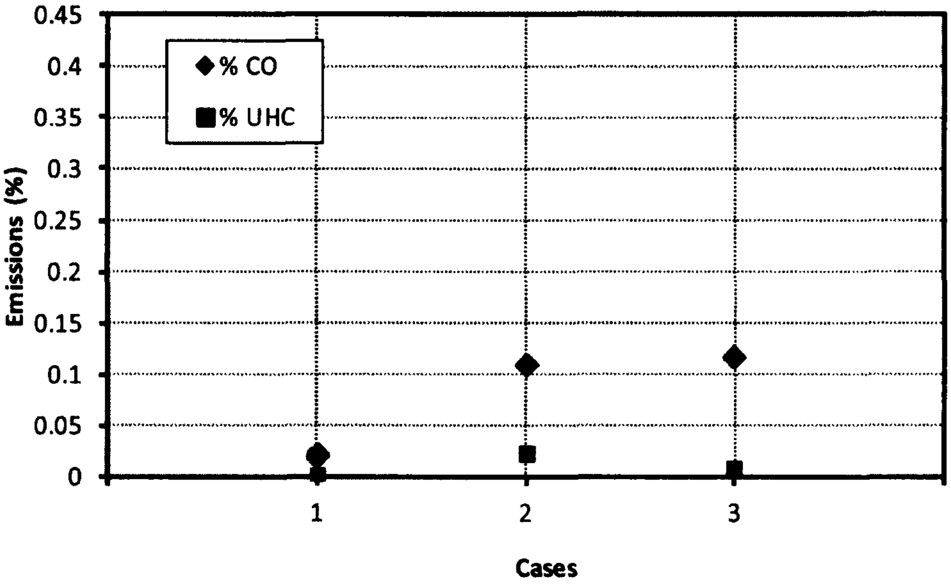

Figure 6.8 CO and UHC emissions for cases 1, 2 and 3 after 2 engine cycles.

To understand the effect of the IMR chamber, average pressure within the in-cylinder and the IMR chamber is plotted in Figure 6.9. Figure 6.10 shows the variation of average pressure within the IMR chamber for cases 2 and 3. Pressure trace for the case with fuel injection into the IMR chamber (Case 3) indicates that the average pressure within the IMR chamber increases to 55 bar after the IMR chamber valve closes. This suggests that the high temperatures due to reactions happening within the IMR chamber cause a pressure rise and the combustion process continues after the IMR chamber valve is closed. Figure 6.11 show average in-cylinder and IMR chamber temperature. Figure 6.12 shows the temperature variation in IMR chamber for cases 2 and 3. The temperature traces show that the IMR chamber temperature reaches a peak of 1370 K in the case of fuel injection into IMR chamber. The thermal energy produced within the IMR chamber due to fuel injection was not utilized due to early closure of IMR chamber valve. The fuel injected into the IMR chamber vaporizes and mixes with the high temperature combustion products, thus producing partial oxidation products CO and H_2. These products further oxidize into CO_2 and H_2O producing thermal energy. The temperature traces for case 3 indicate that the temperature within the IMR chamber before the valve opened was around 810 K. This temperature would be sufficient for fuel reformation, i.e., breaking up of the fuel into intermediate species and formation of radicals. This indicates that fuel can be injected into the IMR chamber before the IMR chamber valve opens to begin the fuel reformation process.

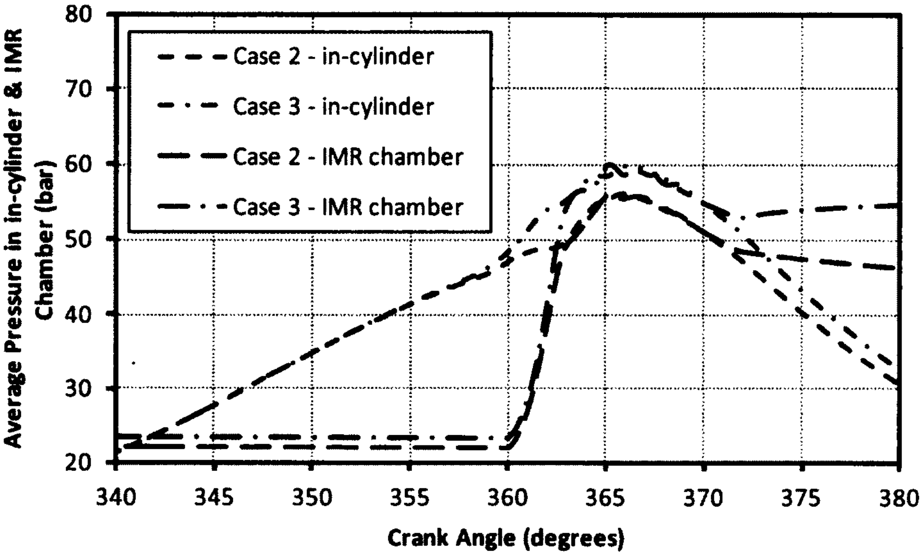

Figure 6.9 Average IMR chamber pressure for cases 2 and 3 after 2 engine cycles.

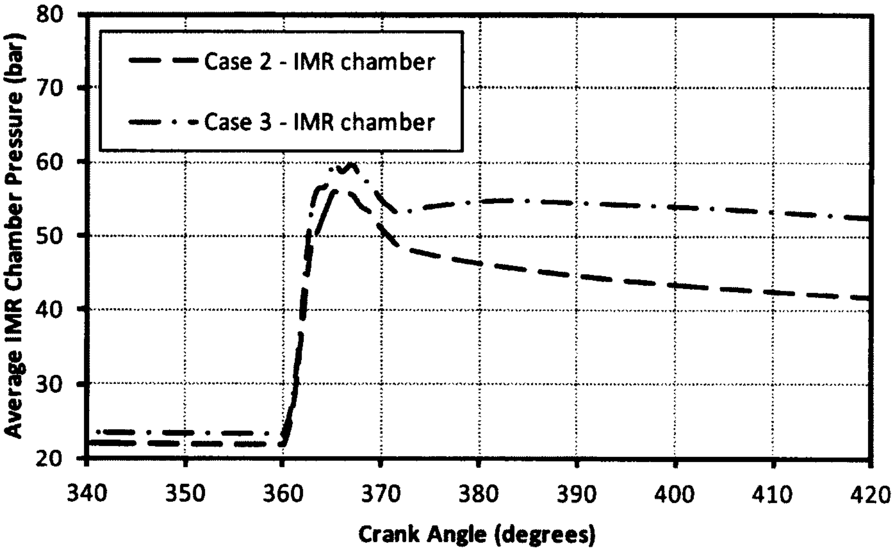

Figure 6.10 Average IMR chamber pressure for cases 2 and 3.

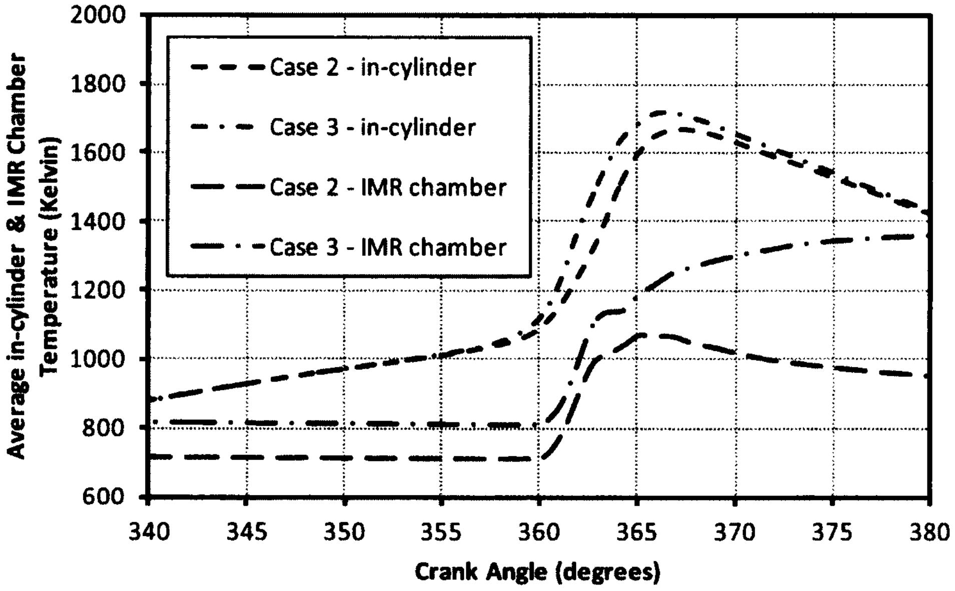

Figure 6.11 Average IMR chamber temperature for cases 2 and 3 after 2 engine cycles.

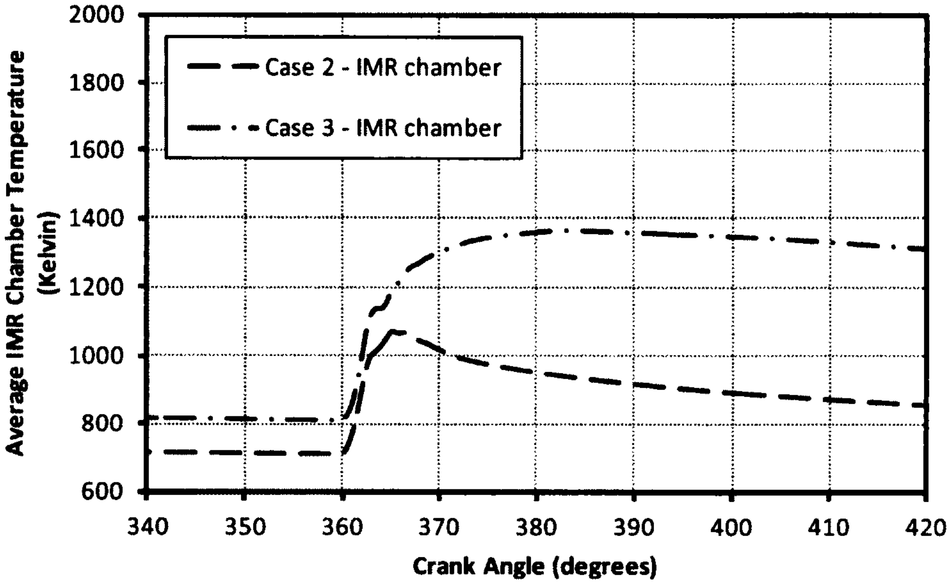

Figure 6.12 Average IMR chamber temperature for cases 2 and 3.

To understand the combustion process within the in-cylinder and IMR chamber, concentration plots of species with respect to crank angle are shown. These plots show the consumption of fuel, production of some of the intermediate species and final products. Figure 6.13 shows the mass fraction of gaseous fuel within the cylinder and the IMR chamber for cases 2 and 3. These plots indicate that the original fuel within the cylinder is consumed at 362 CA. In the case of an IMR chamber without fuel injection

(Case 2), a small amount of fuel from the cylinder enters the IMR chamber at 360 CA and is immediately consumed. In the case of IMR chamber with fuel injection (Case 3) it can be seen that vaporized fuel inside the IMR chamber starts to increase from 363 CA and continues to stay until 375 CA. The fuel injection starts at 360 CA and it takes about 3 degrees duration to vaporize and form mixture. This can be seen in Figure 6.13. The increase in the mass fraction of fuel at 363 CA indicates that the vaporized liquid fuel is mixing with the IMR chamber gaseous mixture.

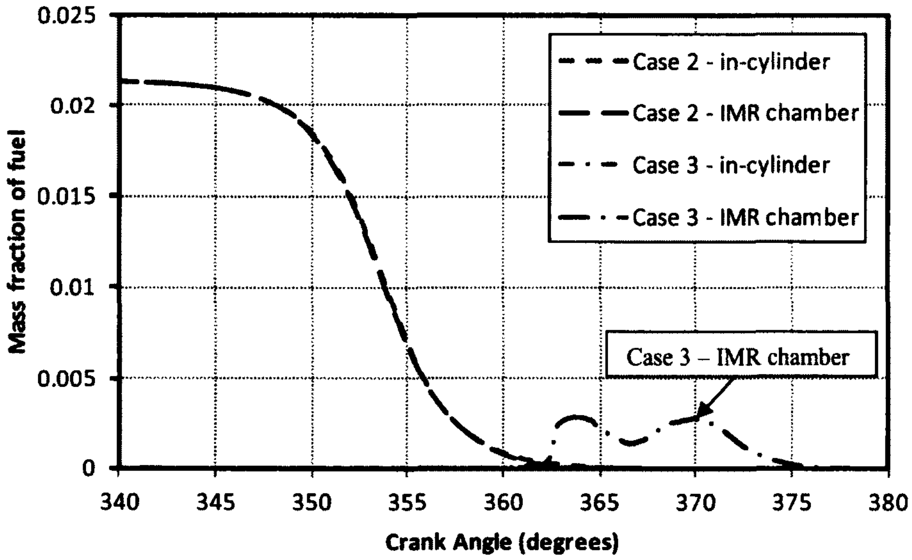

Figure 6.13 Mass fraction of fuel in the cylinder and the IMR chamber for cases 2 and 3.

Figure 6.14 shows the variation of O_2 mass fraction for cases 2 and 3. The trends show the O_2 consumption in-cylinder and within the IMR chamber. The O_2 content in the IMR chamber increases when the IMR chamber valve was opened because mass fraction of O_2 in fresh charge is higher than in combustion products from the previous cycle and this is an effect of internal mixing. In the case of the IMR chamber with fuel injection, the amount of O_2 content in the IMR chamber reduces gradually due to the combustion process.

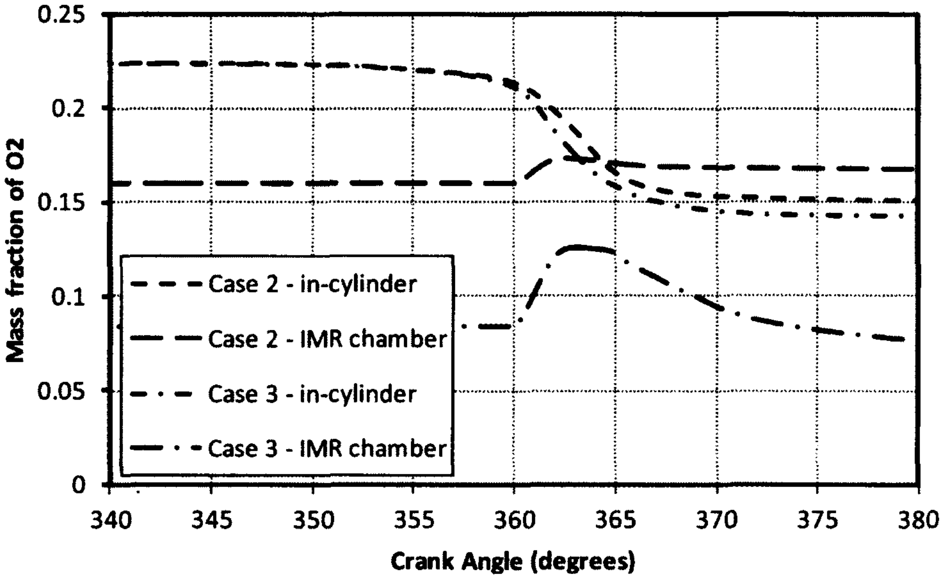

Figure 6.14 Mass fraction of O_2 in the cylinder and the IMR chamber for cases 2 and 3.

Figures 6.15 to 6.21 show some of the species production and consumption for cases 2 and 3. The trends demonstrate the combustion process is happening in the IMR chamber and production of H_2, OH and CO within the IMR chamber. Case 3 with fuel injection into the IMR chamber shows large variations in species concentrations compared to case 2 without fuel injection.

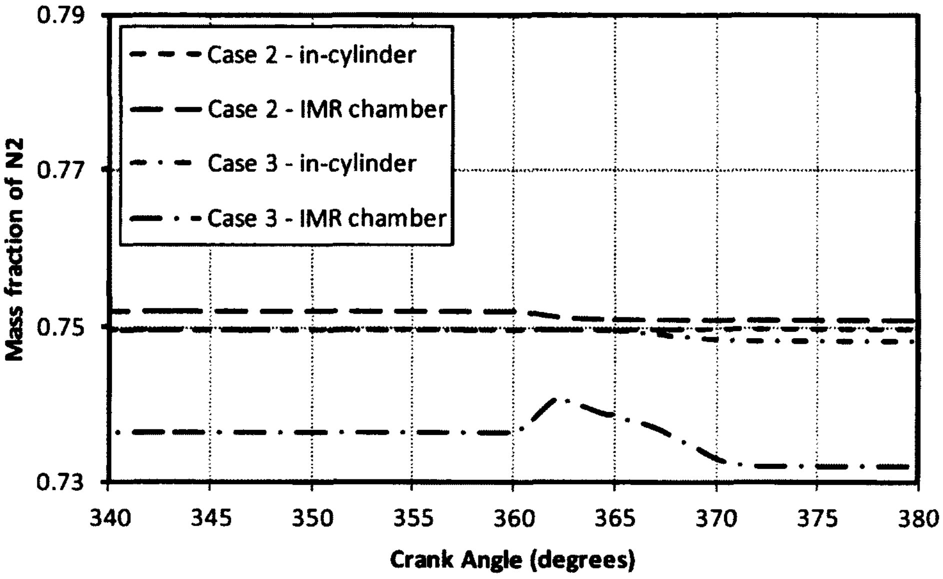

Figure 6.15 Mass fraction of N_2 in in-cylinder and IMR chamber for cases 2 and 3.

Figures 6.16 and 6.17 indicate the formation of combustion products CO_2 and H_2O within the cylinder and IMR chamber. The plots illustrate the combustion process carried in the IMR chamber and production of CO_2 and H_2O.

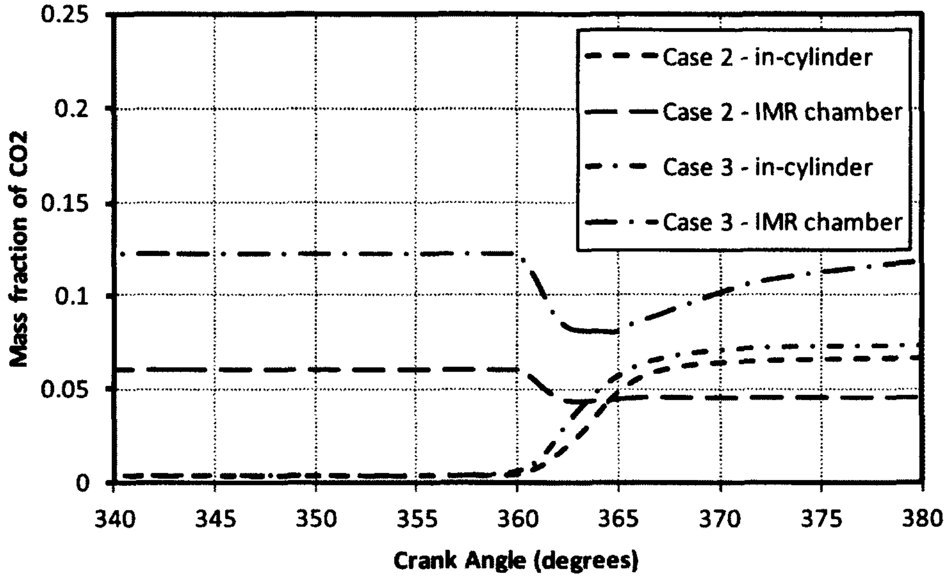

Figure 6.16 Mass fraction of CO_2 in in-cylinder and IMR chamber for cases 2 and 3.

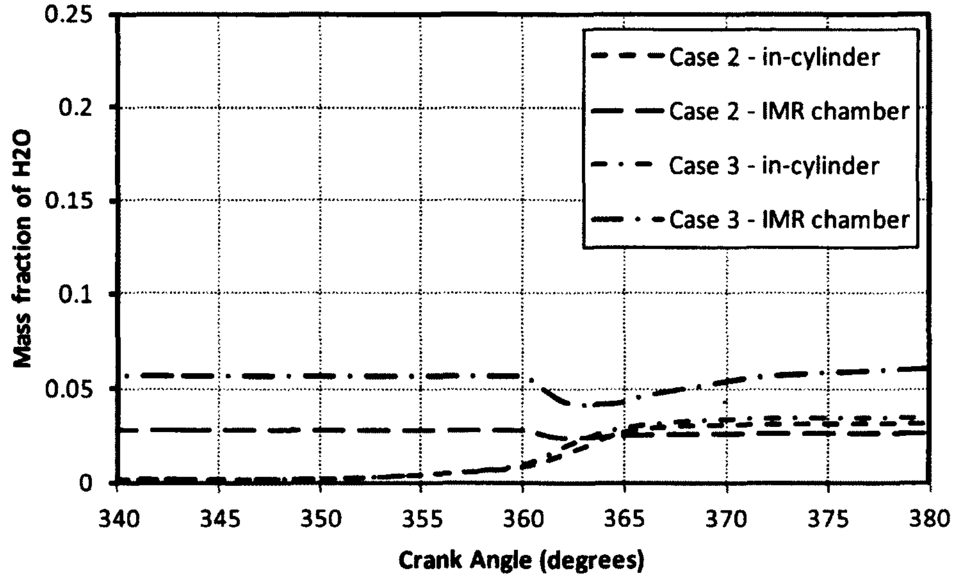

Figure 6.17 Mass fraction of H_2O in the cylinder and the IMR chamber for cases 2 and 3.

Figure 6.18 shows the mass fraction of CO within the cylinder and IMR chamber. The results show that the CO reaches peak value at a crank angle of 374 CA. This indicates the combustion process due to fuel injected carried in the IMR chamber.

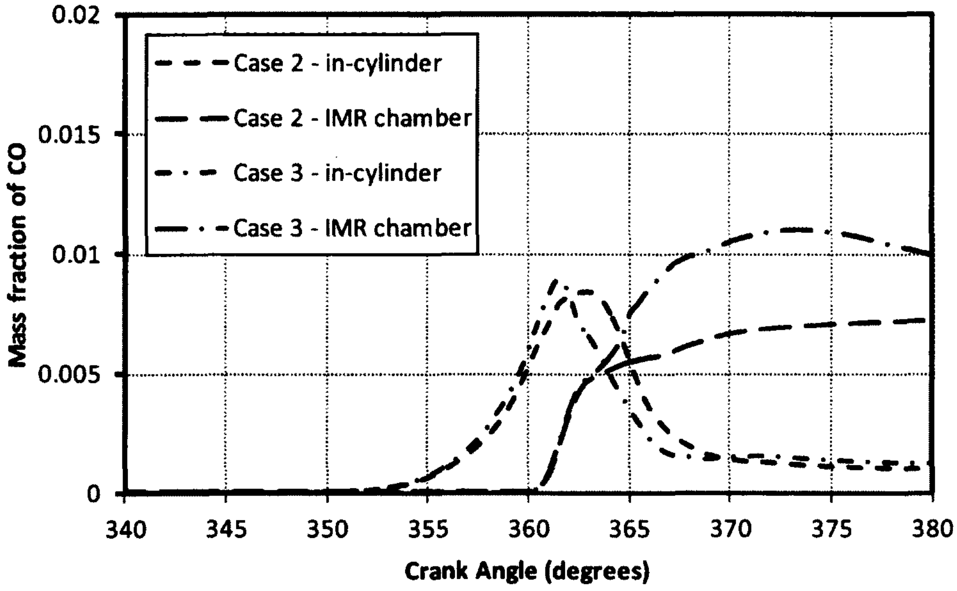

Figure 6.18 Mass fraction of CO in the cylinder and the IMR chamber for cases 2 and 3.

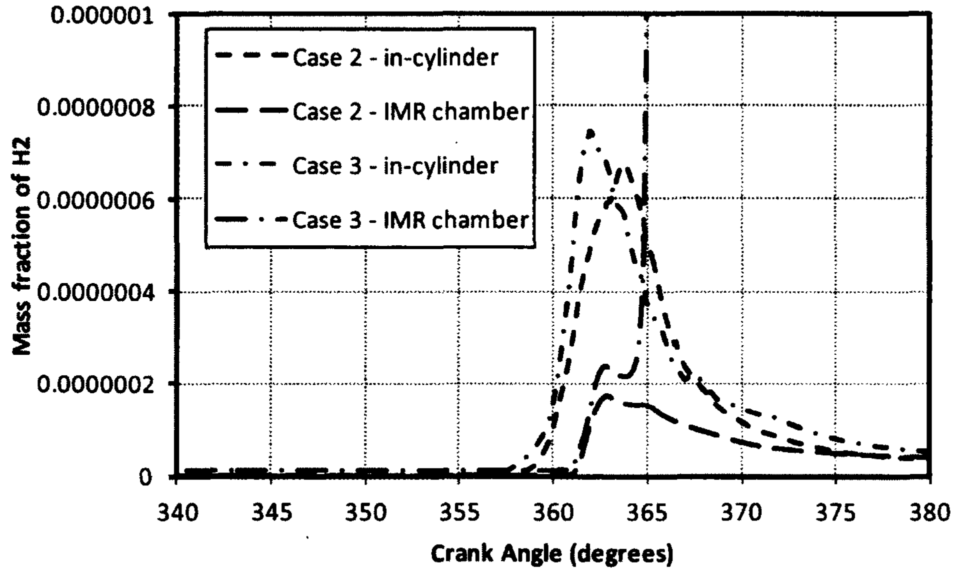

Figure 6.19 Mass fraction of H_2 in in-cylinder and IMR chamber for cases 2 and 3.

Figure 6.19 shows the production and consumption of H_2 within the cylinder and IMR chamber. Due to lack of oxygen content within the IMR chamber and due to presence of H_2O and CO_2, the H_2 mass fraction increases to a peak of 0.00012 at 375 CA and gradually reduces until 460 CA. This indicates the function of the IMR chamber in reforming the fuel injected. The OH radical mass fraction shown in Figure 6.21 indicates the initiation of high temperature reactions and subsequent heat release.

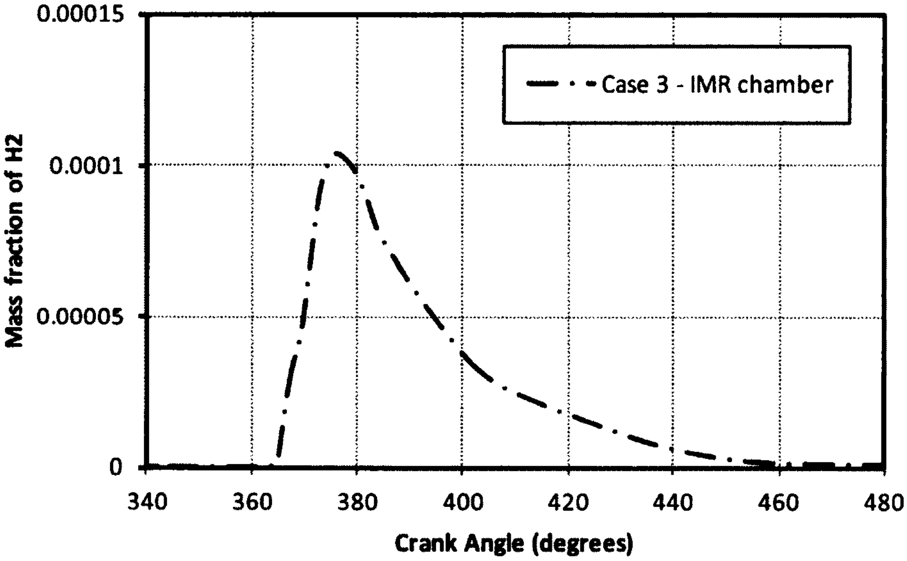

Figure 6.20 Mass fraction of H_2 in IMR chamber for case 3.

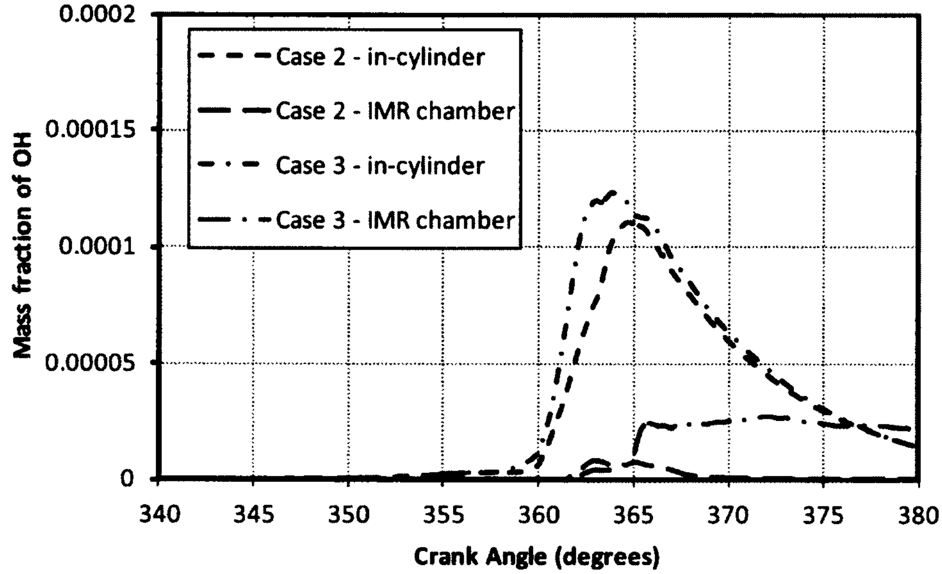

Figure 6.21 Mass fraction of OH in in-cylinder and IMR chamber for cases 2 and 3.

The results from cycle 2 for case 3 show the function of the IMR chamber in reducing the pressure rise rate, forming of intermediate species, decreasing in overall temperature and extending the heat release rate.

From case 3 results, it can be inferred that:

1) by closing the IMR chamber valve early there is less thermal energy converted to useful work.

2) the fuel injected into the IMR chamber takes several crank angle degrees to evaporate, react with surrounding combustion products and form reformation products and subsequently burn.

To demonstrate the effect of IMR chamber fuel injection timing and IMR chamber valve timing on the combustion process, three cases are defined and referred to as case 4, 5 and 6 respectively. The details of cases are given in Table 6.2. Case 4 has extended IMR chamber valve duration compared to case 3. Case 5 has extended IMR chamber valve duration and extended injection timing. Case 6 has advanced fuel injection timing. The flow field and compositions within the in-cylinder and IMR chamber at the end of cycle 2 for case 3 were taken as the initial conditions for cases 4, 5 and 6. The amount of fuel injected into the IMR chamber was kept constant in all the cases. The simulations were carried out for one engine cycle.

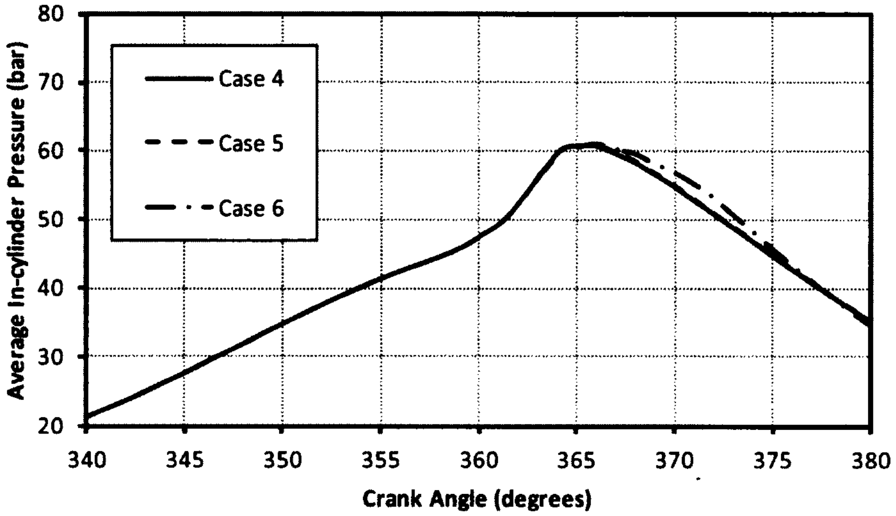

Figure 6.22 Average in-cylinder pressures for cases 4, 5 and 6.

Figure 6.22 shows the average in-cylinder pressure for case 4, 5 and 6. The trends indicate that cases 4 and 5 do not show any difference in pressure trace, while case 6 shows an increase in pressure after 365 CA until 375 CA. Figure 6.23 shows the average in-cylinder temperature for cases 4, 5 and 6. The trends indicate that the peak temperature remains the same for all cases and case 6 has higher temperature after 372 CA, since the IMR chamber valve was closed earlier compared to cases 4 and 5.

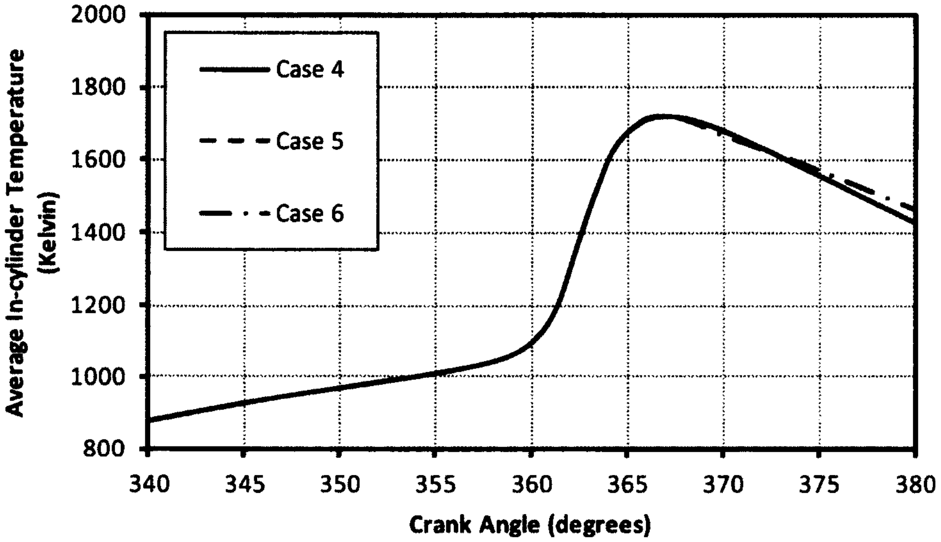

Figure 6.23 Average in-cylinder temperatures for cases 4, 5 and 6.

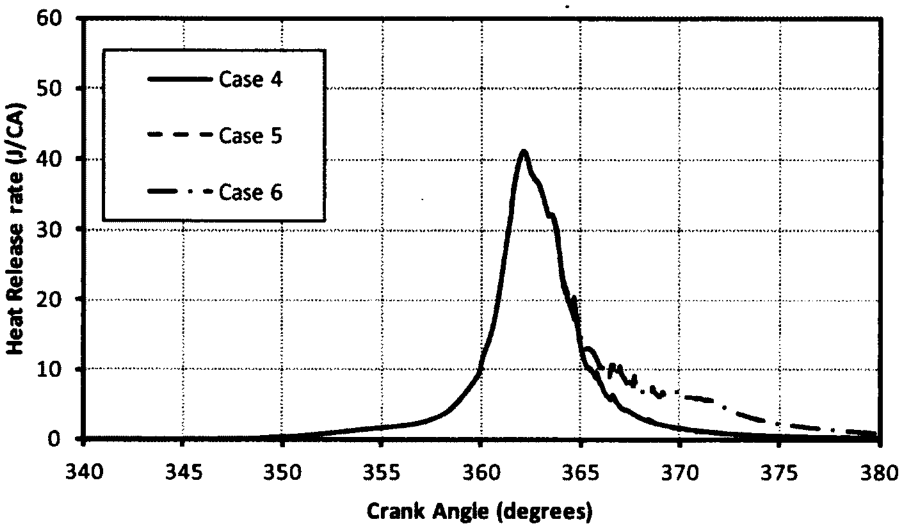

Figure 6.24 Heat release rate for cases 4, 5 and 6.

Figure 6.24 shows the variation of heat release rate between cases 4, 5 and 6. The heat release rate does not vary between cases 4 and 5 but, for case 6, it shows heat release until 380 CA. Figure 6.25 shows the 10% heat release crank angle and 10% to 90% heat release duration. The results indicate that for cases 4 and 5 there are no significant differences in the values, whereas in the case 6, the heat release duration was prolonged to 13 degrees duration. This shows that the fuel injected into the IMR chamber had sufficient time to convert to the intermediate species and subsequently convert to final products.

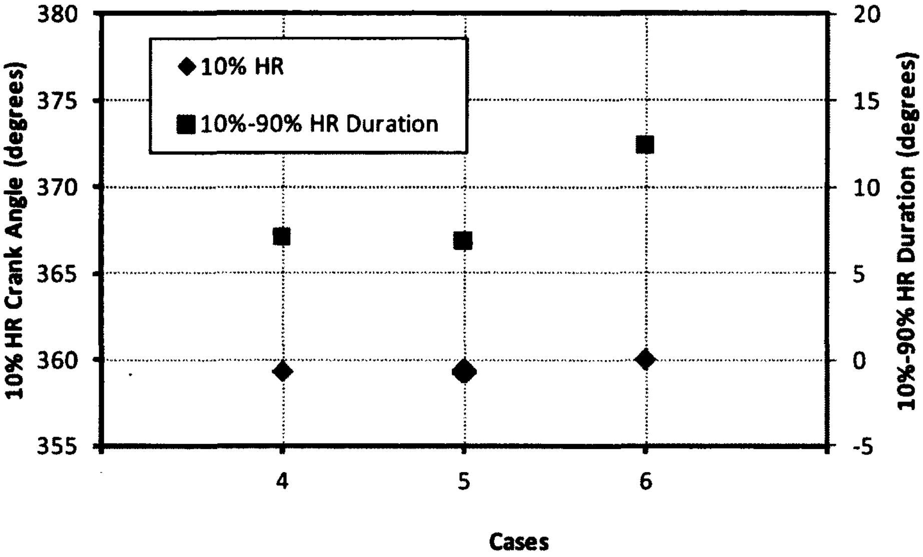

Figure 6.25 10% CA and 10%-90% heat release duration for cases 4, 5 and 6.

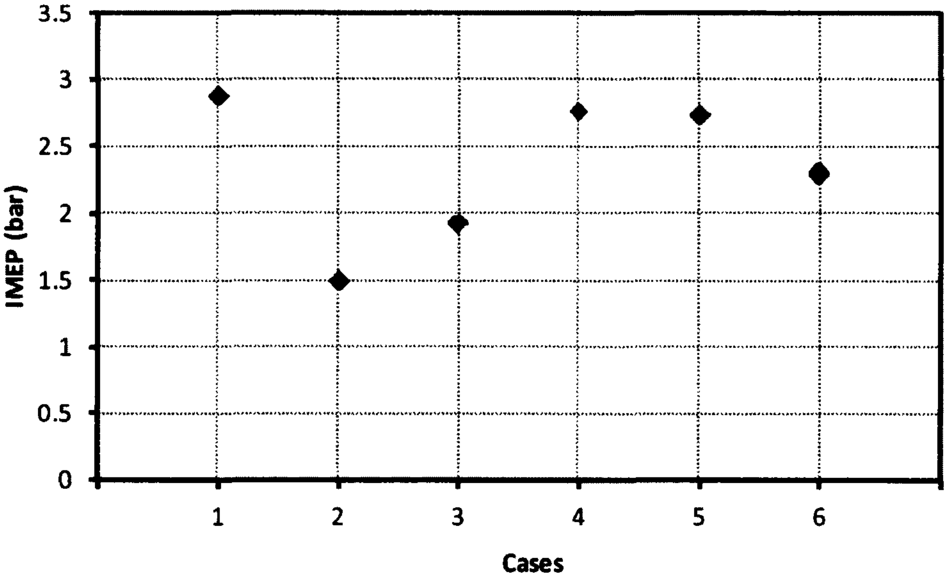

Figure 6.26 Indicated mean effective pressure for cases 1 to 6.

Figure 6.26 shows the IMEP obtained for cases 4, 5 and 6. The IMEP for cases 4 and 5 indicate significant improvement in IMEP compared to case 3. The IMEP obtained from cases 4 and 5 was in the range of 2.75 bar and for case 6, the IMEP was 2.3 bar.

Figure 6.27 shows emissions obtained from cases 4, 5 and 6.

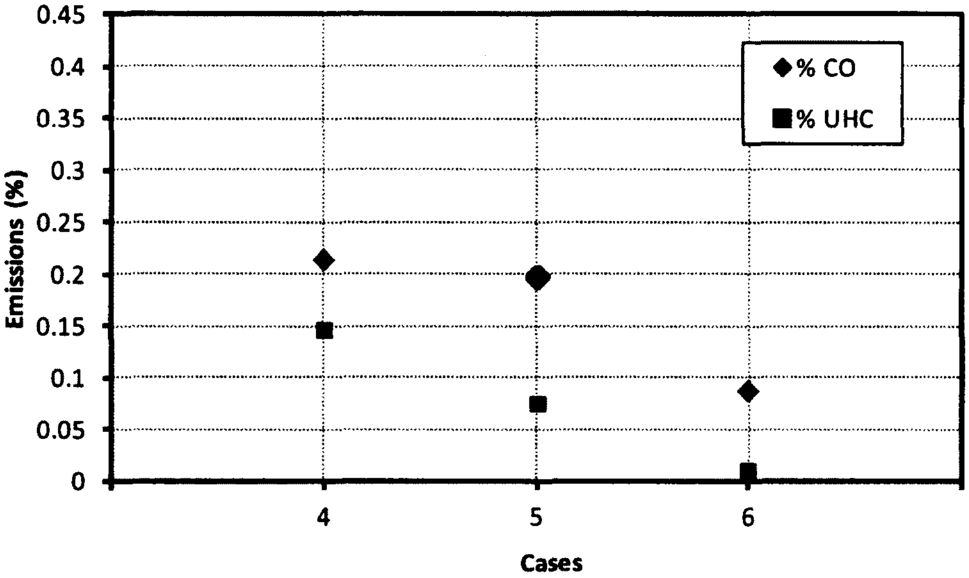

Figure 6.27 % CO and % UHC emissions for cases 4, 5 and 6.

The emissions are calculated in-cylinder just before the exhaust valve opens. From the emissions, it can be said that although cases 4 and 5 give a higher amount of IMEP, they produce 0.2% CO emissions and 0.15% UHC emissions for case 4 and 0.075% UHC for case 5. Case 6 produces significantly less emissions compared to cases 4 and 5. This suggests that there is an optimum for fuel injection timing and valve opening duration to achieve higher IMEP and lower emissions.

Figures 6.28 and 6.29 show average in-cylinder and IMR chamber pressure for cases 4, 5 and 6 respectively. The trends indicate that the IMR chamber pressure and in-cylinder pressure do not show any differences for cases 4 and 5 due to the IMR chamber valve timing. In case 6, the IMR chamber valve was closed at 372 CA, which causes the deviation in the IMR chamber pressure and allows an increase in the pressure within the IMR chamber to 60 bar due to the combustion process, as shown in Figure 6.29. The temperature curves shown in Figures 6.30 and 6.31 follow the same trend and the average peak temperature in the IMR chamber for case 6 shows approximately 1300 K. In case 6, the temperature increase starts at 366 CA, when the IMR chamber valve was still open and the piston moving down. This shows the combustion process is happening within the IMR chamber. In cases 4 and 5, the peak temperature within the IMR chamber was at

1100 K. This indicates that the complete combustion process did not take place within the IMR chamber for cases 4 and 5.

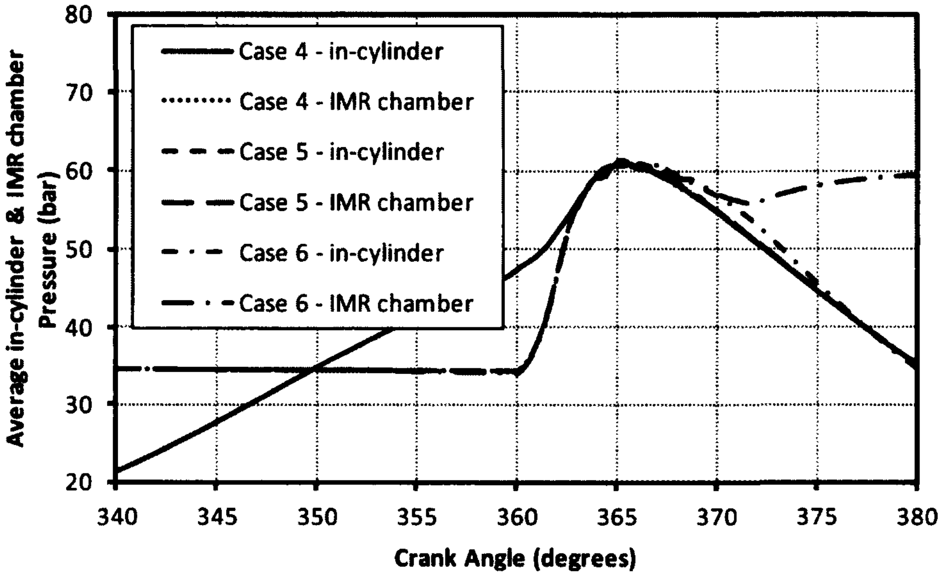

Figure 6.28 Average in-cylinder and IMR chamber pressure for cases 4, 5 and 6.

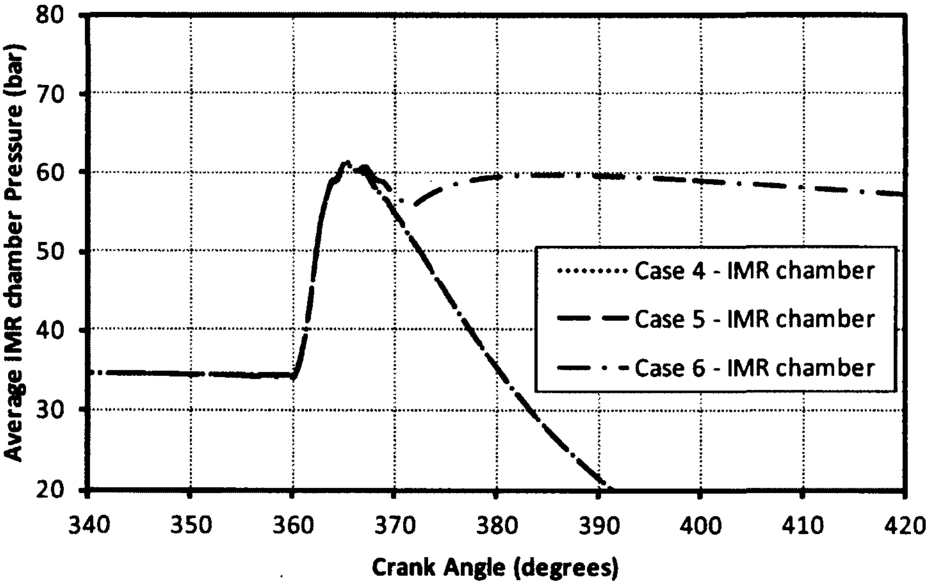

Figure 6.29 Average IMR chamber pressure for cases 4, 5 and 6.

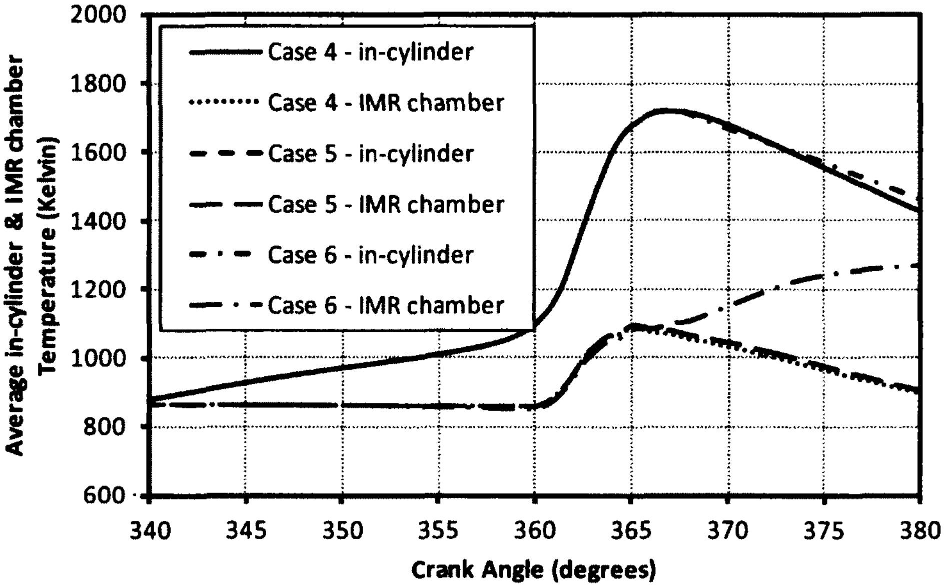

Figure 6.30 Average IMR chamber temperatures for cases 4, 5 and 6.

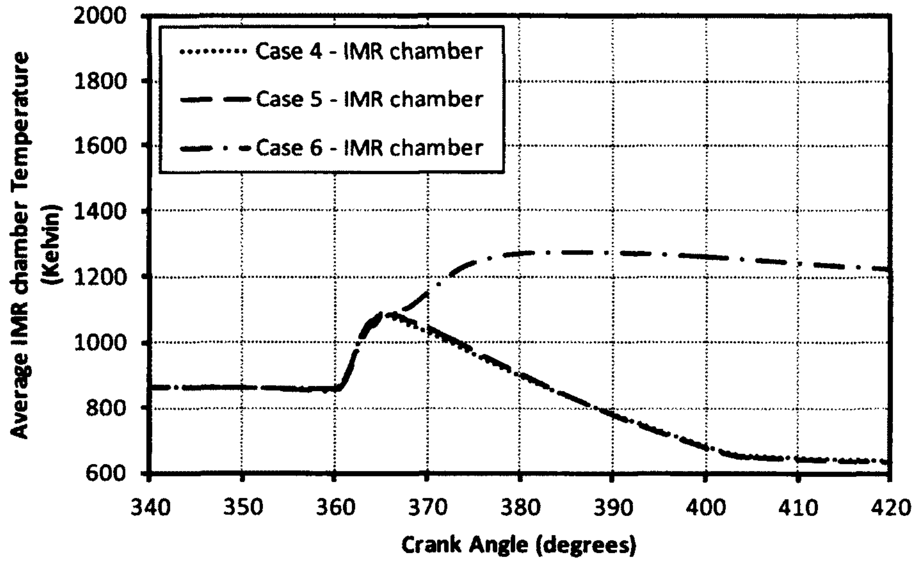

Figure 6.31 Average IMR chamber temperature for cases 4, 5 and 6.

Figures 6.32 to 6.40 show the in-cylinder and IMR chamber species concentrations. The concentration plots show the mass fractions of species and their changes with respect to crank angle. Figure 6.32 shows the mass fraction of fuel for cases 4, 5 and 6. Case 4 results indicate that the fuel was added starting at the crank angle 360 CA and rises sharply due to injection. In case 5, fuel was added gradually and reaches a peak around 395 CA. In case 6, fuel mass fraction starts to increase from 350 CA, reaches a peak at

364 CA and drops down. In the case of in-cylinder fuel mass fractions for cases 4 and 5, it can be seen that the fuel within the cylinder was consumed by 365 CA and after 385 CA it starts to slowly increase. This increase in fuel mass fraction in-cylinder was due to fuel added into the IMR chamber. The prolonged IMR chamber valve timing in cases 4 and 5 causes the fuel injected into the IMR chamber to pass into the cylinder.

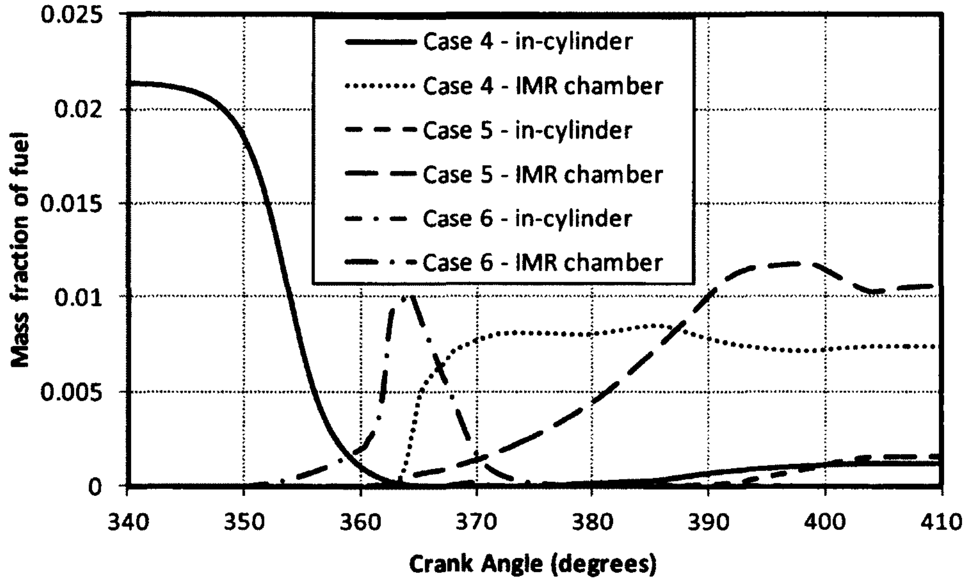

Figure 6.32 Mass fractions of fuel within the cylinder and the IMR chamber for cases 4, 5 and 6.

Figure 6.33 shows mass fraction of O_2 within in-cylinder and IMR chamber for cases 4, 5 and 6. The trends indicate that for case 6, the O_2 content in IMR chamber decreases from 365 CA. The O_2 content in IMR chamber for cases 4 and 5 does not vary after 375 CA. The piston movement pulls the fluid within the IMR chamber into the main cylinder. This will reduce the temperature and does not allow the combustion process to carry within the IMR chamber. For case 6, the closing of the IMR chamber valve at 372 CA, retains sufficient temperature to continue combustion process. The O_2 mass fraction in Figure 6.33 indicates the consumption within the IMR chamber for case 6. The N_2 mass fractions in Figure 6.34 indicate the consumption of N_2 due to high temperature zones within the IMR chamber.

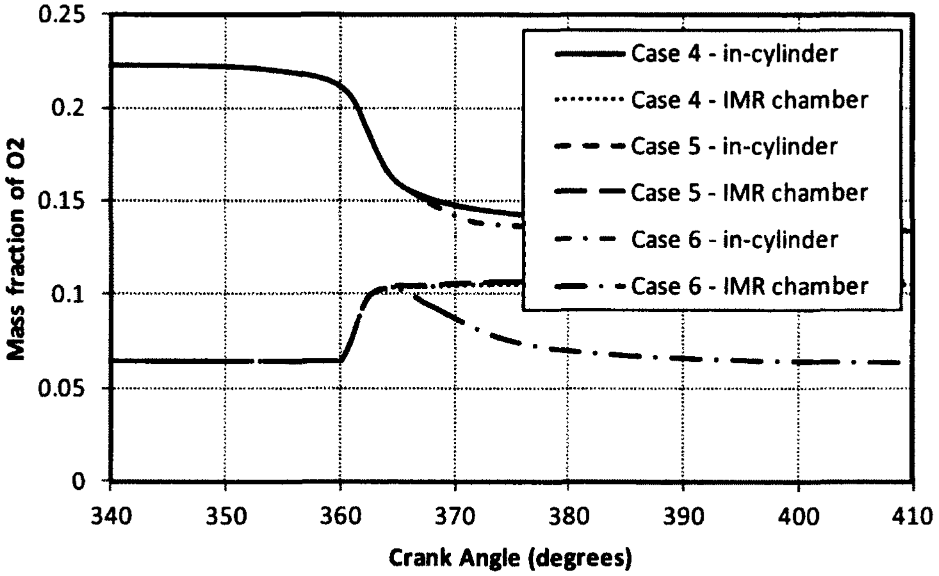

Figure 6.33 Mass fractions of O_2 within the cylinder and the IMR chamber for cases 4, 5 and 6.

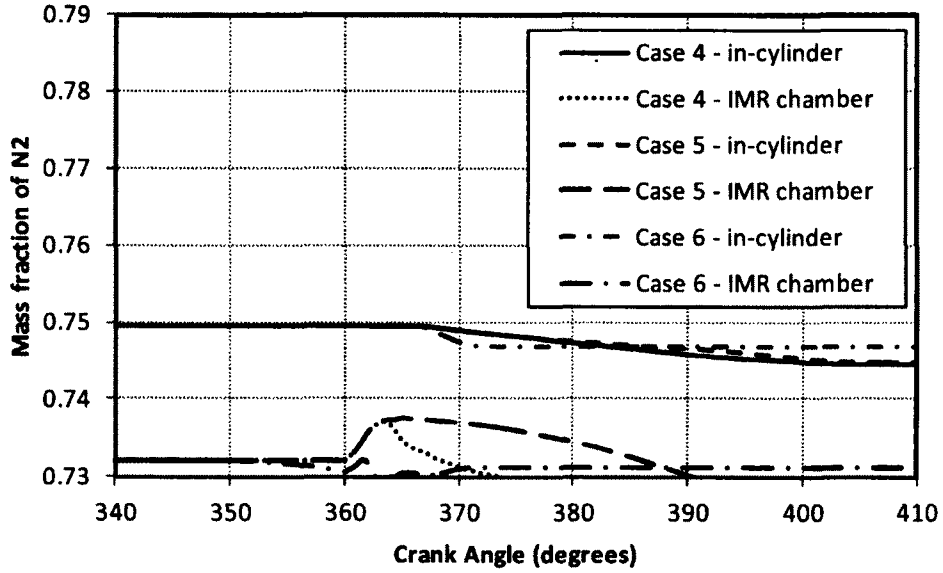

Figure 6.34 Mass fractions of N_2 within the cylinder and the IMR chamber for cases 4, 5 and 6.

Figures 6.35 and 6.36 show the complete combustion products production in-cylinder and in the IMR chamber.

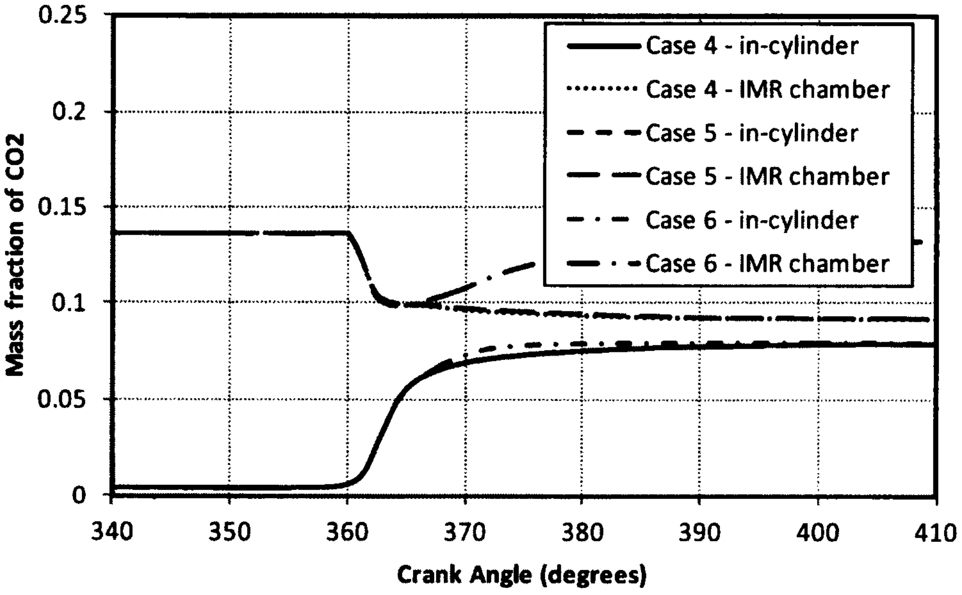

Figure 6.35 Mass fractions of CO_2 within the cylinder and the IMR chamber for cases 4, 5 and 6.

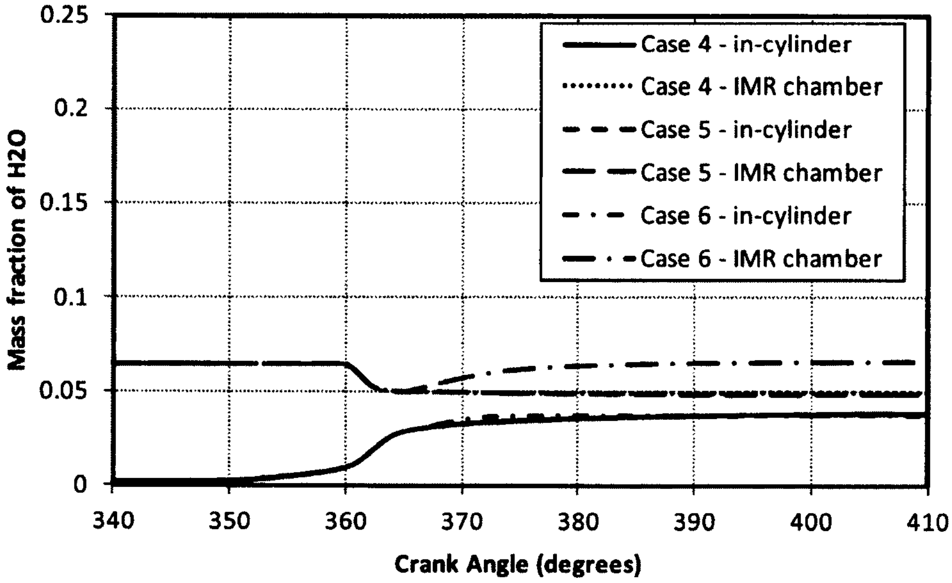

Figure 6.36 Mass fractions of H_2O within the cylinder and the IMR chamber for cases 4, 5 and 6.

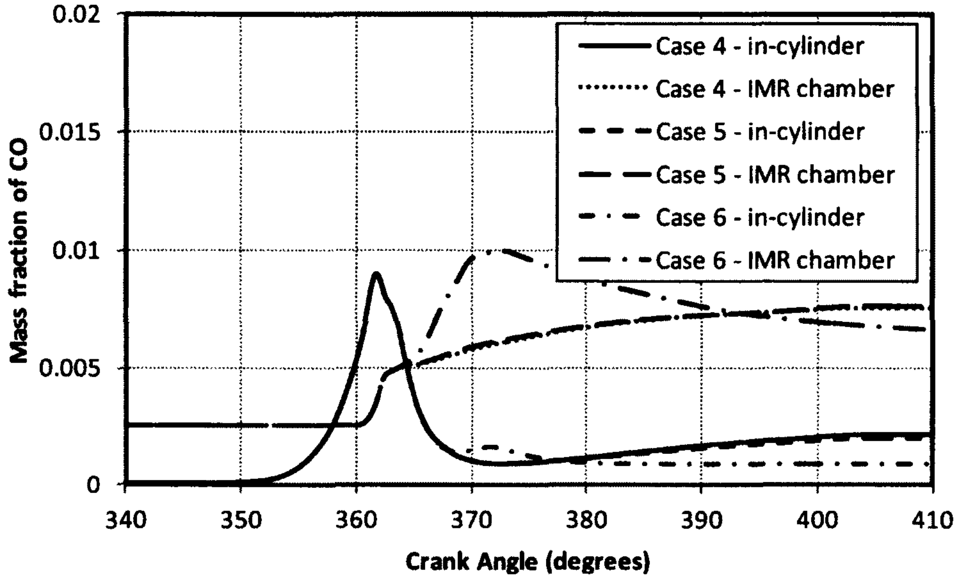

Figure 6.37 Mass fractions of CO within the cylinder and the IMR chamber for cases 4, 5 and 6.

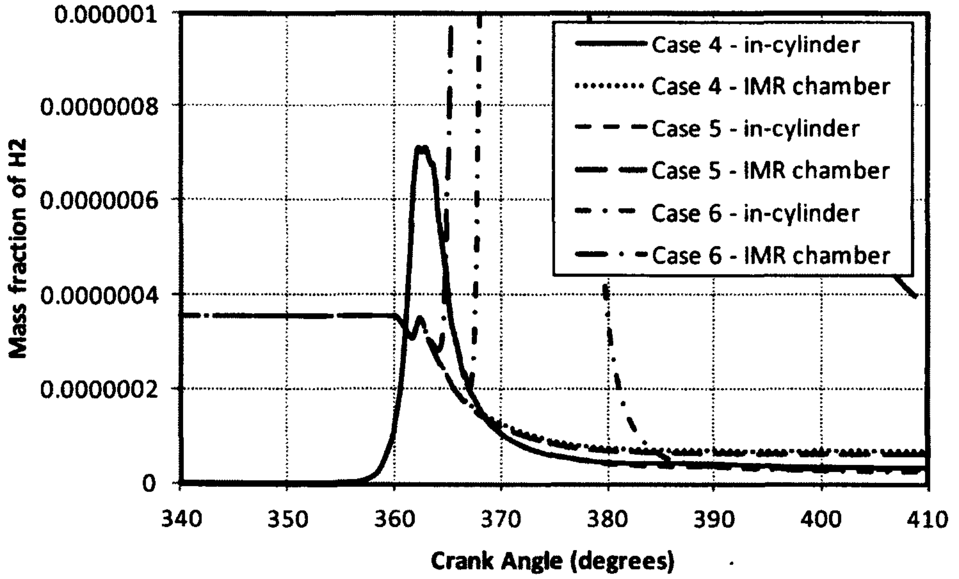

Figure 6.38 Mass fractions of H_2 within the cylinder and the IMR chamber for cases 4, 5 and 6.

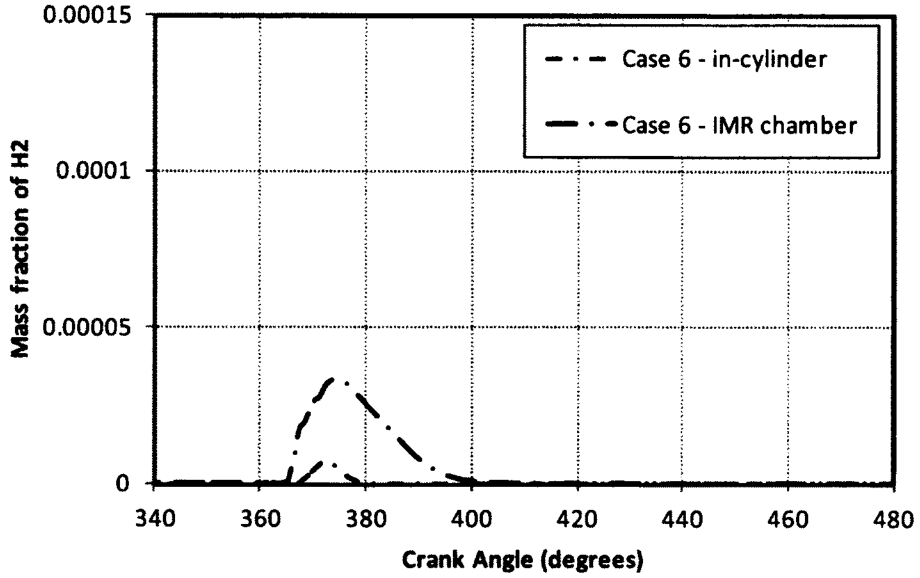

Figure 6.39 Mass fraction of H_2 within cylinder and IMR chamber for case 6.

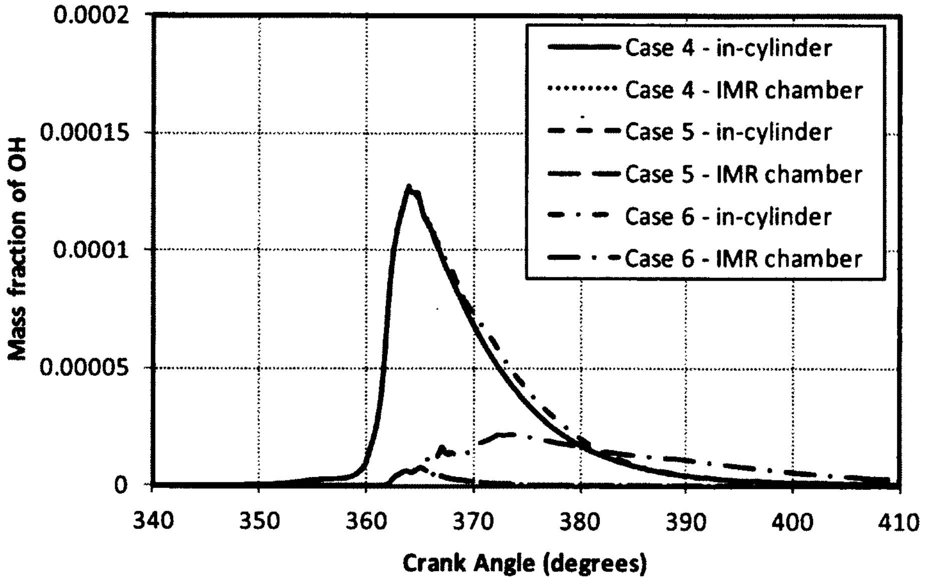

Figure 6.40 Mass fractions of OH within the cylinder and the IMR chamber for cases 4, 5 and 6.

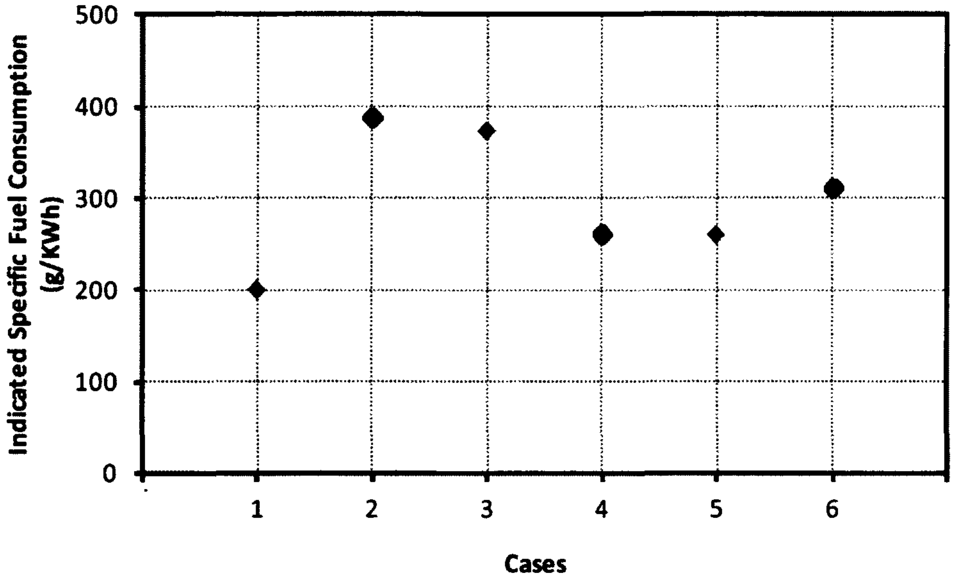

Figure 6.41 Indicated Specific Fuel Consumption (ISFC, g/KWh) for all six cases studied.

Figure 6.41 shows the Indicated Specific Fuel Consumption (ISFC) for all the six cases studied as mentioned in Table 6.2. These values indicate the amount of fuel consumed for unit power produced. Case 1 shows the lowest amount of fuel consumed per unit power. Cases 4, 5 produce more power compared to cases 3 and 6, but produce more CO and UHC emissions. Case 6 produces less emissions and slightly better fuel consumption than case 3. These trends indicate that there is a need for more runs to find optimum conditions and a need to run several cycles with different fuel injection and valve timing to get optimum power with lower fuel consumption and lower emissions.

To understand and possibly link flow features with combustion process, flow fields are plotted for case 6 at various important crank angles after injection (352 CA, 356 CA, 360 CA) and IMR chamber valve timings (362 CA, 370 CA, 372 CA). The four cut planes are shown in Figure 6.42.

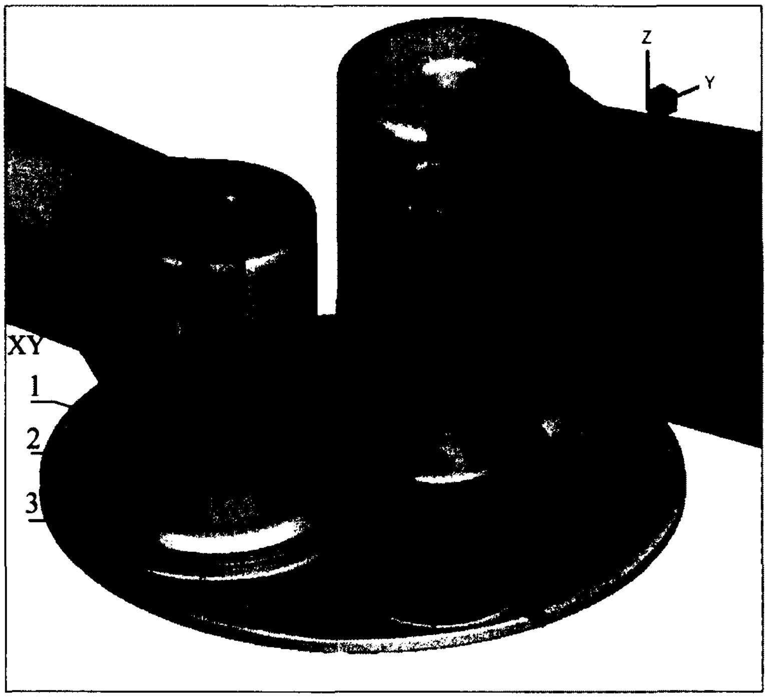

Figure 6.42 3-D computational domain showing three XY planes and XZ plane.

The cut-planes are shown with temperature contours in Figure 6.42 to indicate the plane locations. The planes are also shown in Figure 6.43 in the XZ plane and the XY plane to indicate the plane locations. The XY planes are located at the top where the IMR chamber valve opens, in the centre of the pre-chamber and at the neck region between the in-cylinder and pre-chamber.

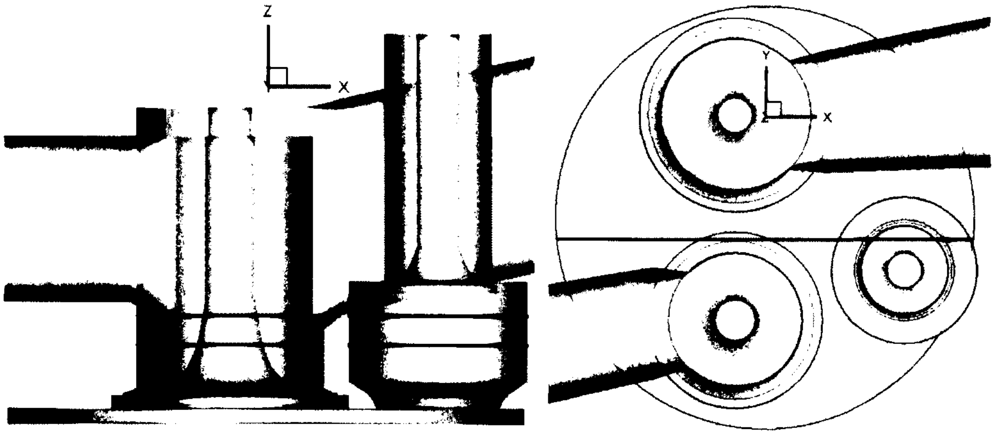

(a) XZ plane (b) XY plane

Figure 6.43 Computational domain indicating cut-plane locations in XZ plane and XY plane.

Figure 6.44 show velocity vectors with fuel spray in the IMR chamber in different cut-planes. These plots indicate the spray penetration and interaction between flow and spray when the valve is opened. The vectors show the direction of the flow field and the crank angle at which the flow reverses from the IMR chamber to the pre-chamber. The flow field demonstrates the function of the IMR chamber in mixing the previous cycle's combustion products with the fresh charge; and the flow reversal. The XY plane flow fields (cut-planes AA, BB and CC) indicate the flow rotation within the pre-chamber during combustion process and during the valve movement.

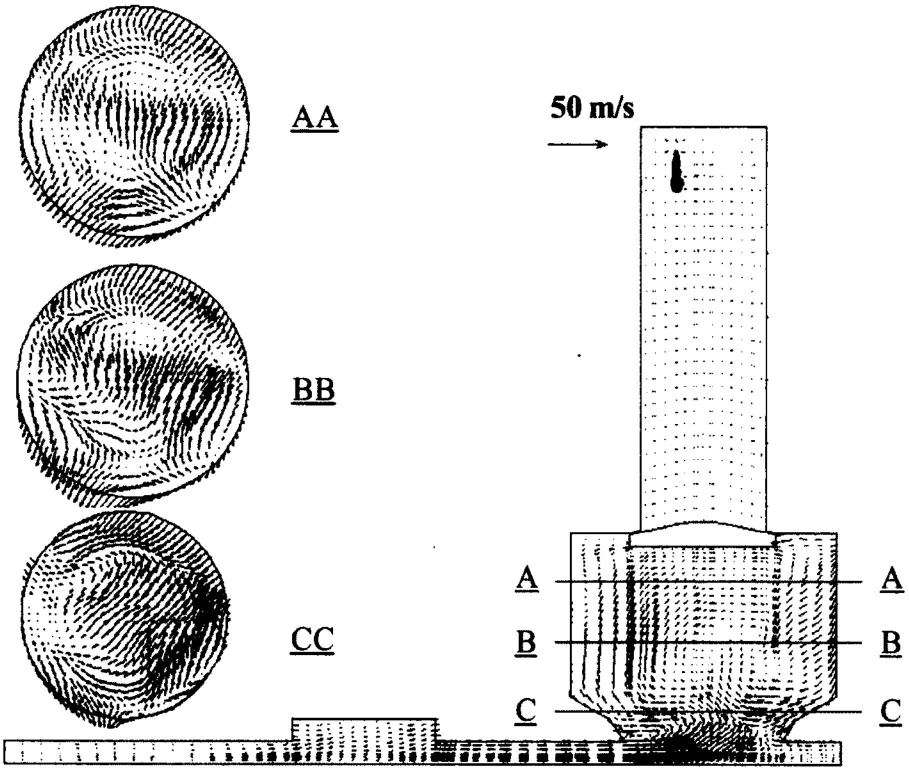

Figure 6.44 (a) 352 CA

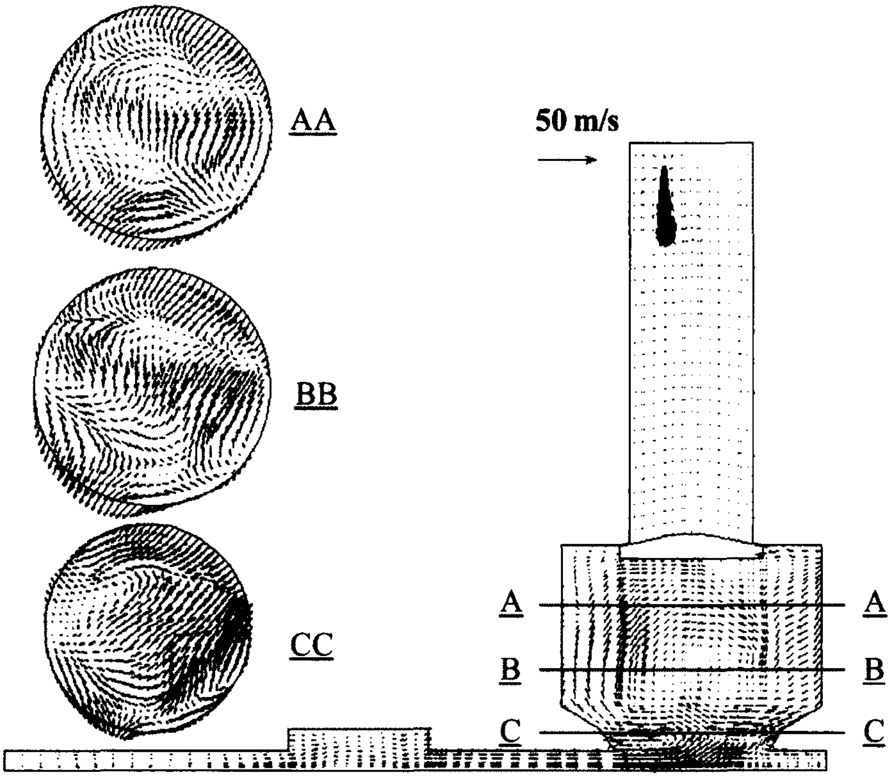
AA
BB
CC
50 m/s
A
A
B
B
C
C

Figure 6.44 (b) 354 CA

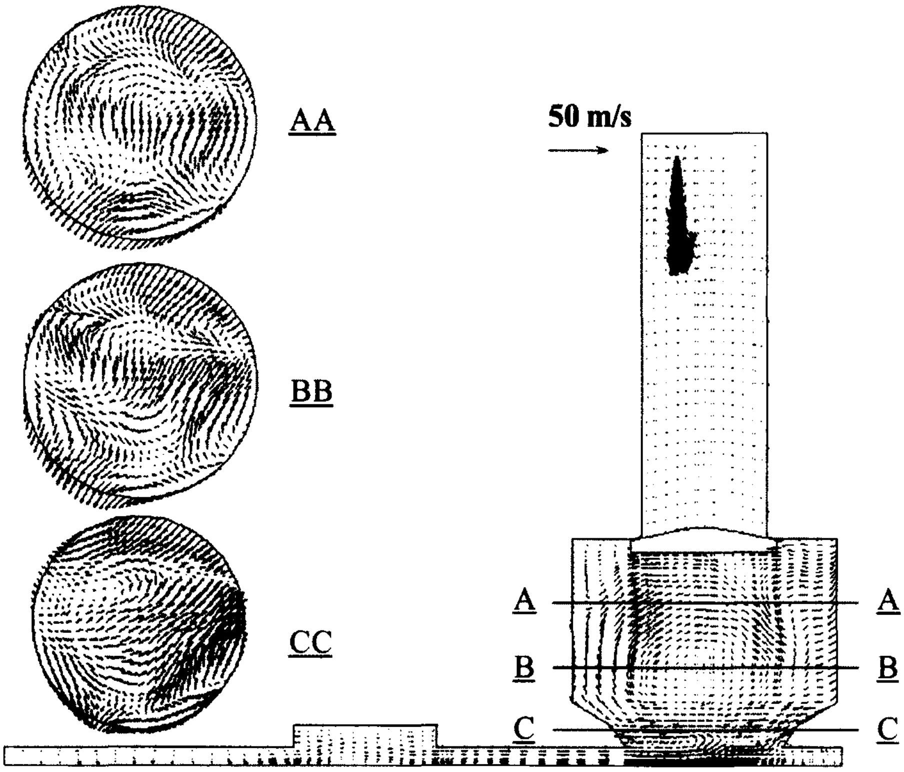
AA
BB
CC
50 m/s
A
A
B
B
C
C

Figure 6.44 (c) 356 CA

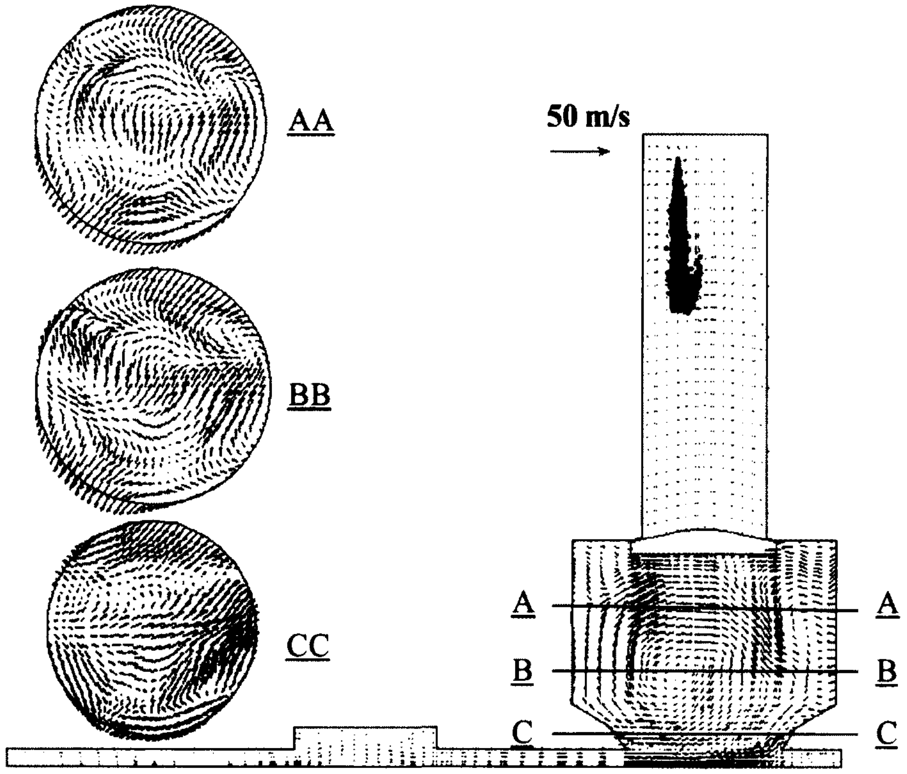

Figure 6.44 (d) 358 CA

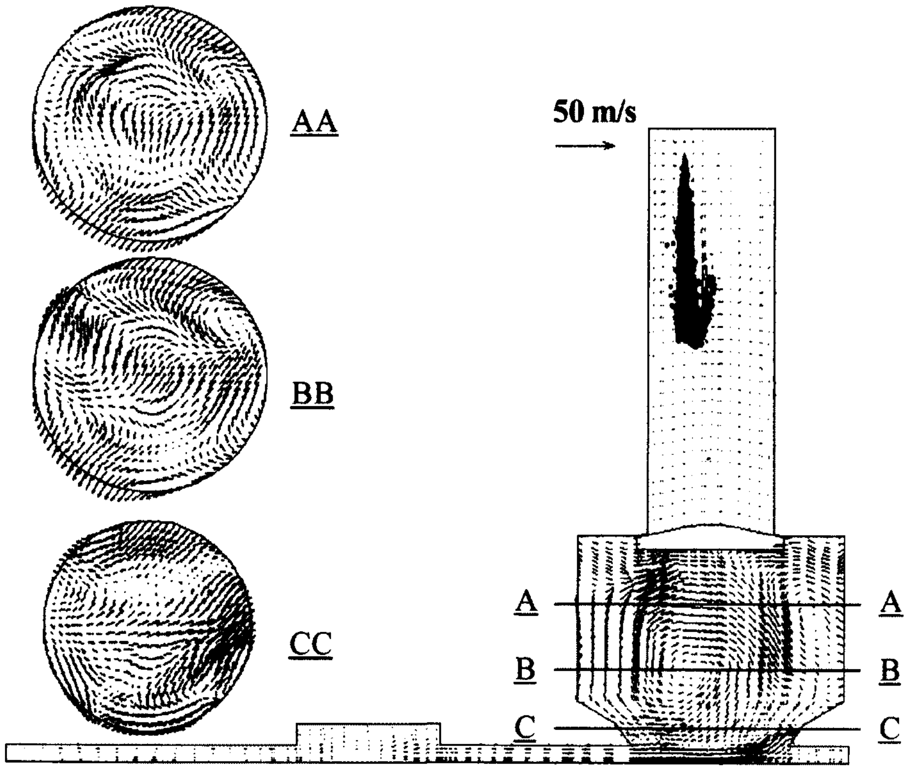

Figure 6.44 (e) 360 CA

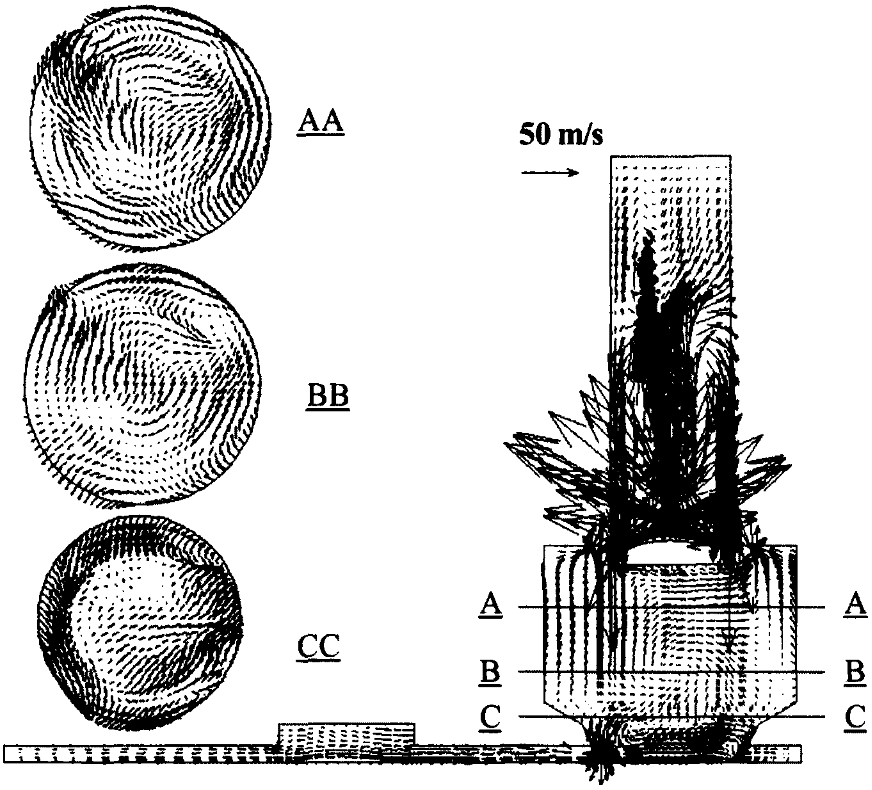

Figure 6.44 (f) 362 CA

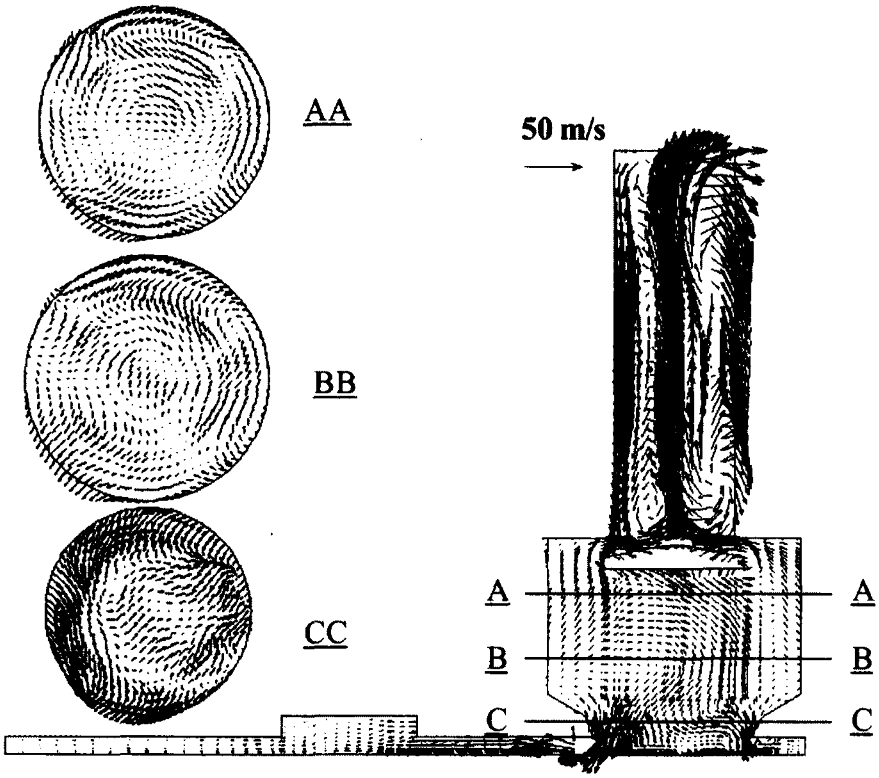

Figure 6.44 (g) 364 CA

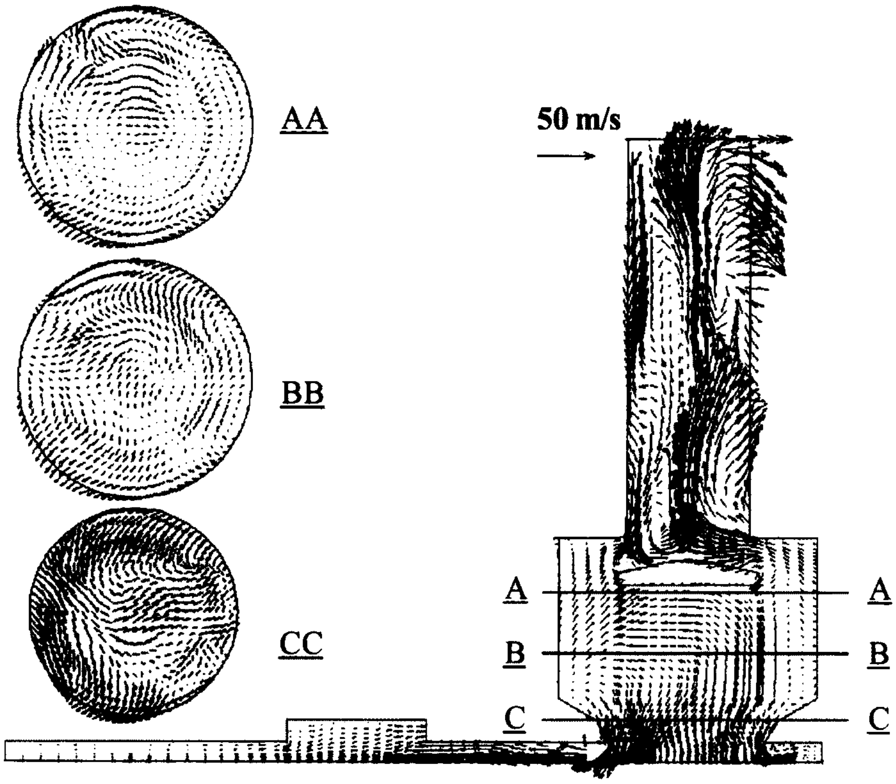
AA
BB
CC
50 m/s
A
A
B
B
C
C

Figure 6.44 (h) 366 CA

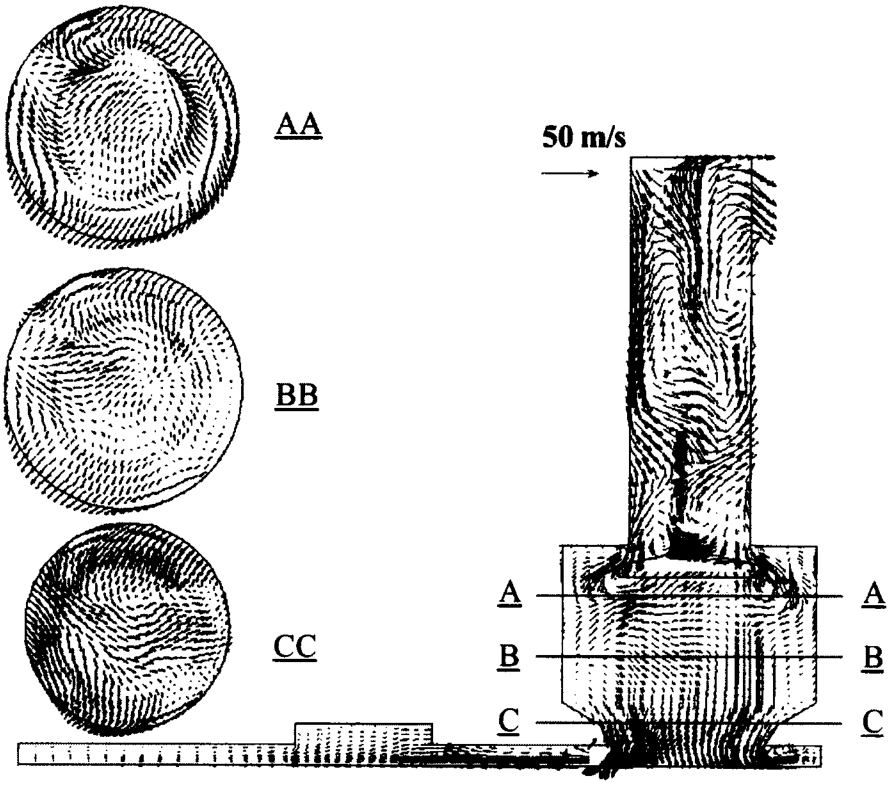
AA
BB
CC
50 m/s
A
A
B
B
C
C

Figure 6.44 (i) 368 CA

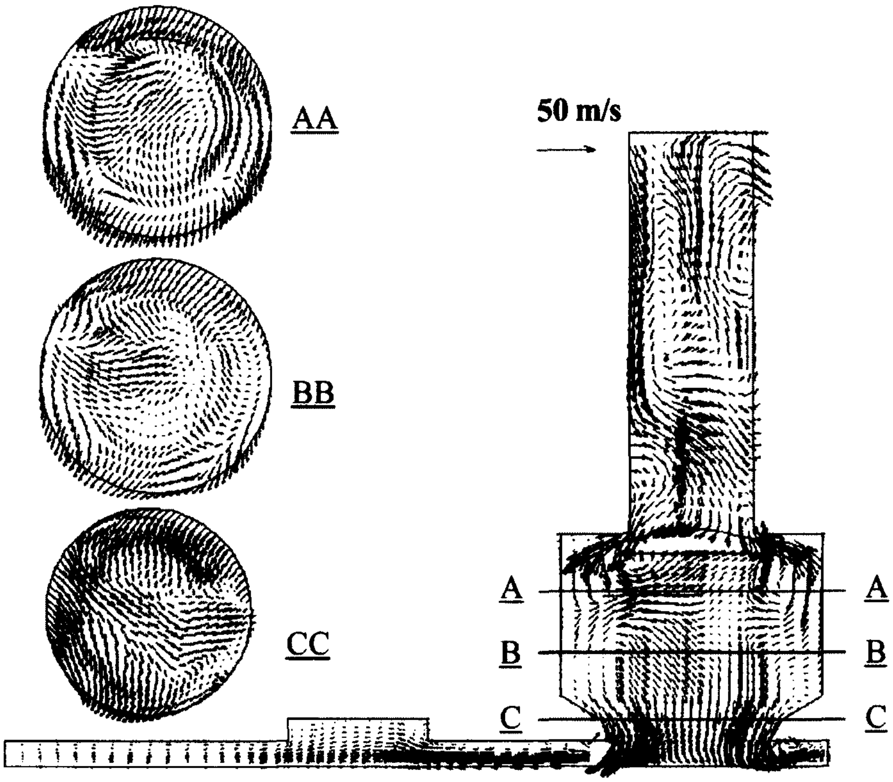
AA
BB
CC
50 m/s
A
A
B
B
C
C

Figure 6.44 (j) 370 CA

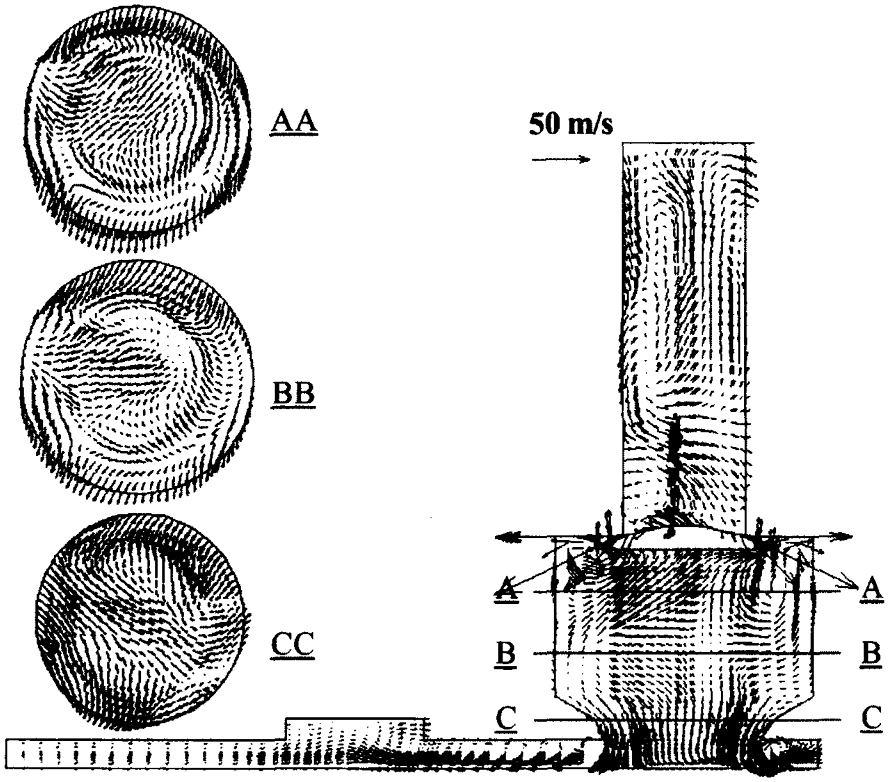
AA
BB
CC
50 m/s
A
A
B
B
C
C

Figure 6.44 (k) 372 CA

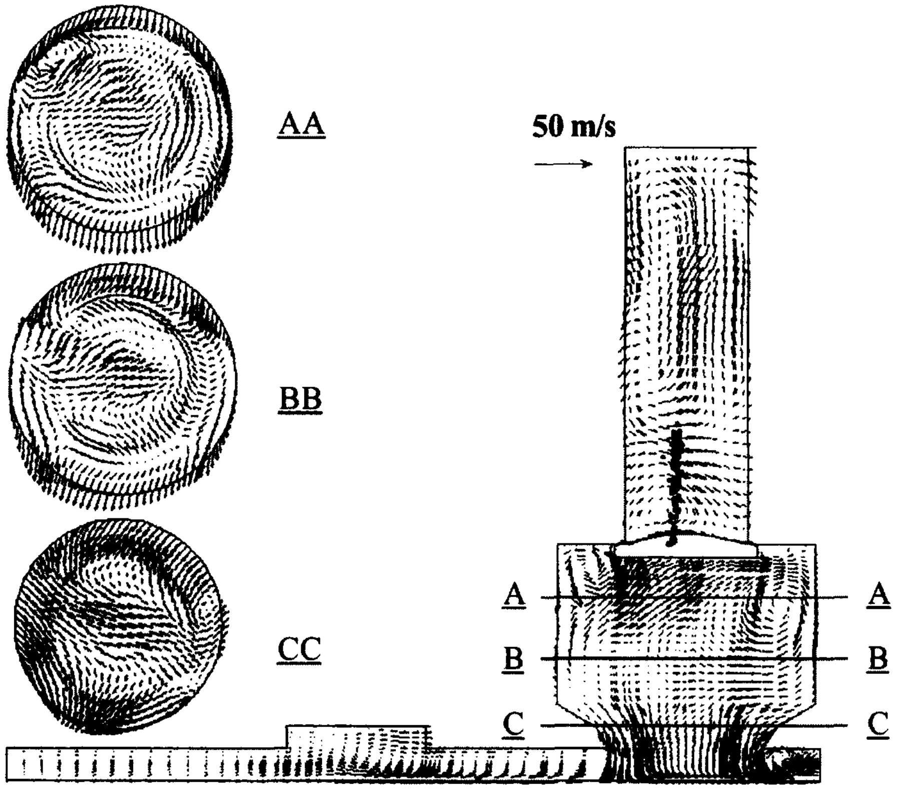

Figure 6.44 (l) 374 CA

Figure 6.44 Velocity vectors and spray particles in XZ plane at crank angles (a) 352 CA, (b) 354CA, (c) 356 CA, (d) 358 CA, (e) 360 CA, (f) 362 CA, (g) 364 CA, (h) 366 CA, (i) 368 CA, (j)370 CA, (k) 372 CA, and (l) 374 CA for case 6.

Figure 6.45 shows the temperature contours in various cut-planes. The temperature plots indicate that high temperature zones appear within the pre-chamber and IMR chamber. The plots show high temperature core regions due to flow structures. When the IMR chamber valve is opened, high temperature gases passes into the IMR chamber and combustion process starts at the top region of the IMR chamber due to vaporized fuel. The plots show local high temperature zones which reach a peak temperature of 2000 K due to vaporized fuel concentration at particular zones. This can be seen from the molar fraction contours of fuel plotted in Figure 6.46.

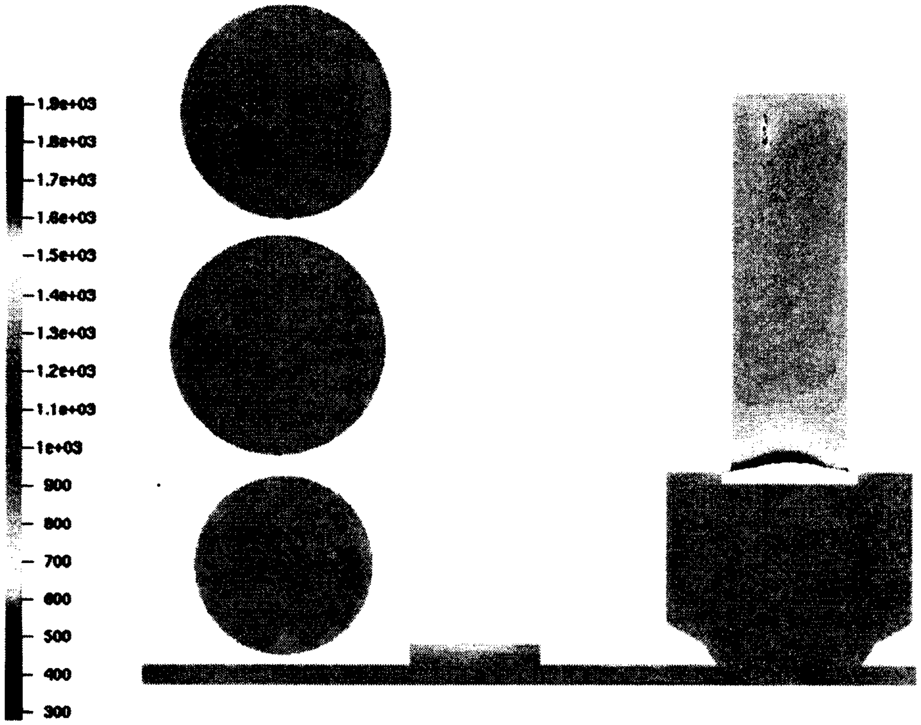

Figure 6.45 (a) 352 CA

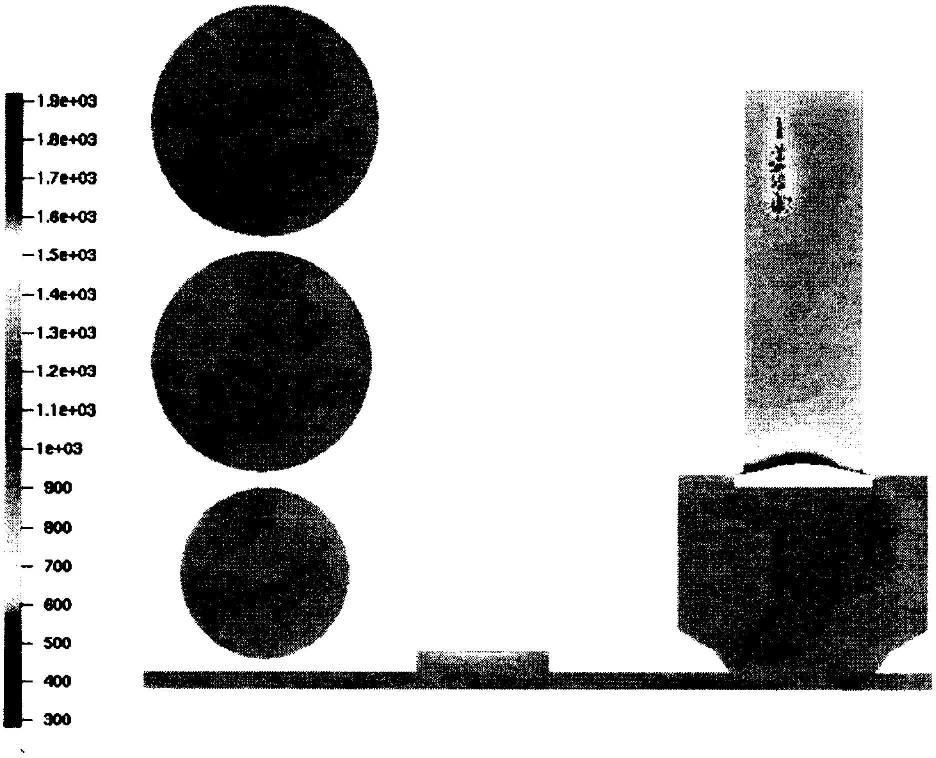

Figure 6.45 (b) 356 CA

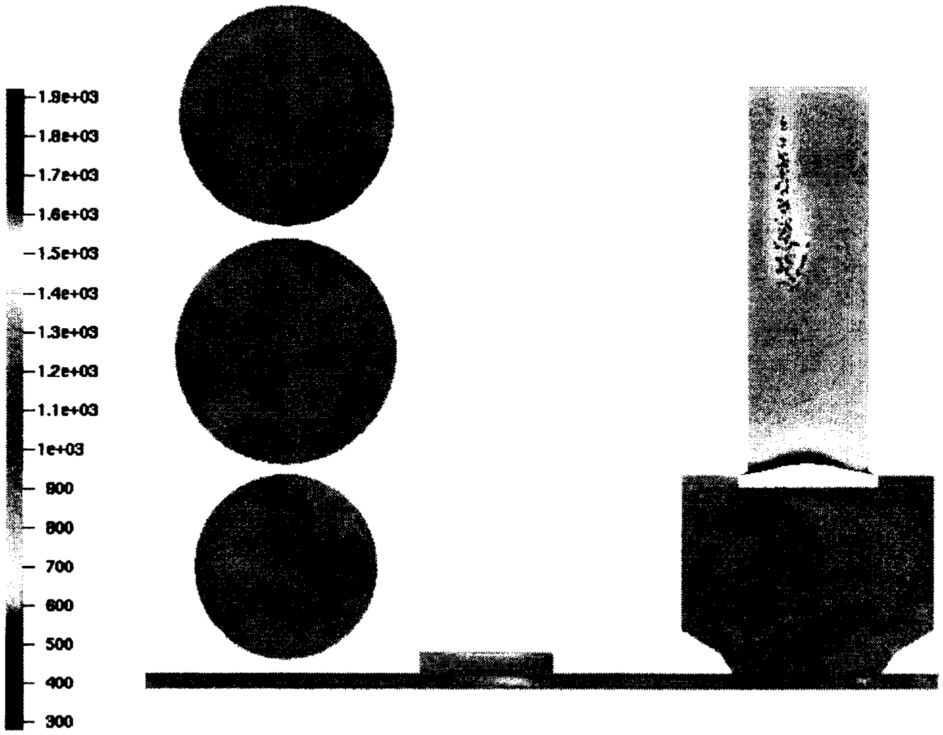

Figure 6.45 (c) 360 CA

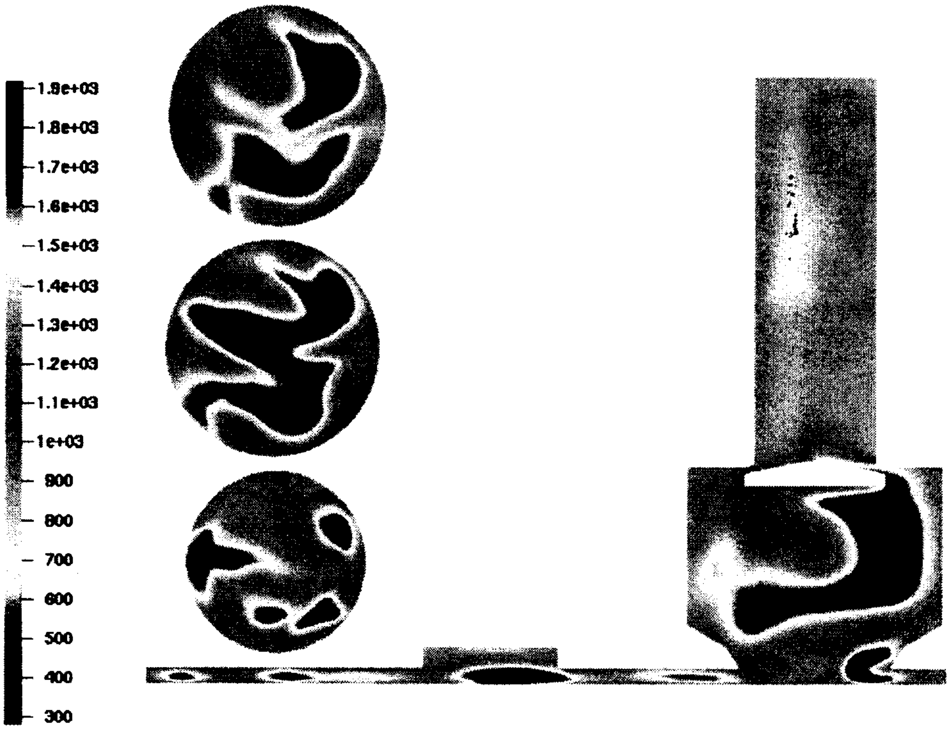

Figure 6.45 (d) 362 CA

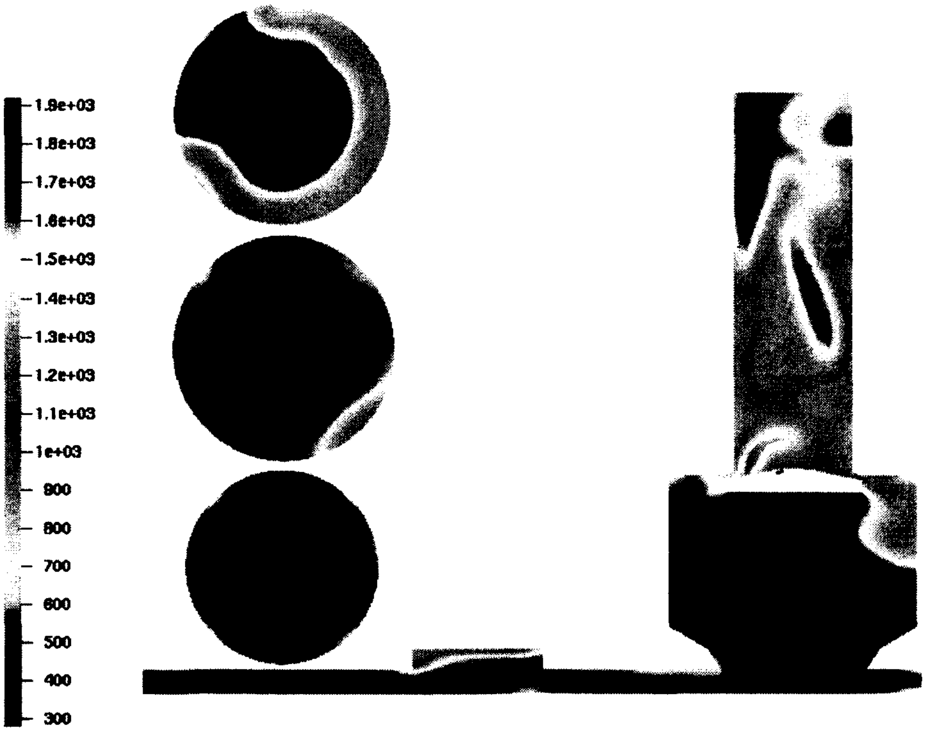

Figure 6.45 (e) 370 CA

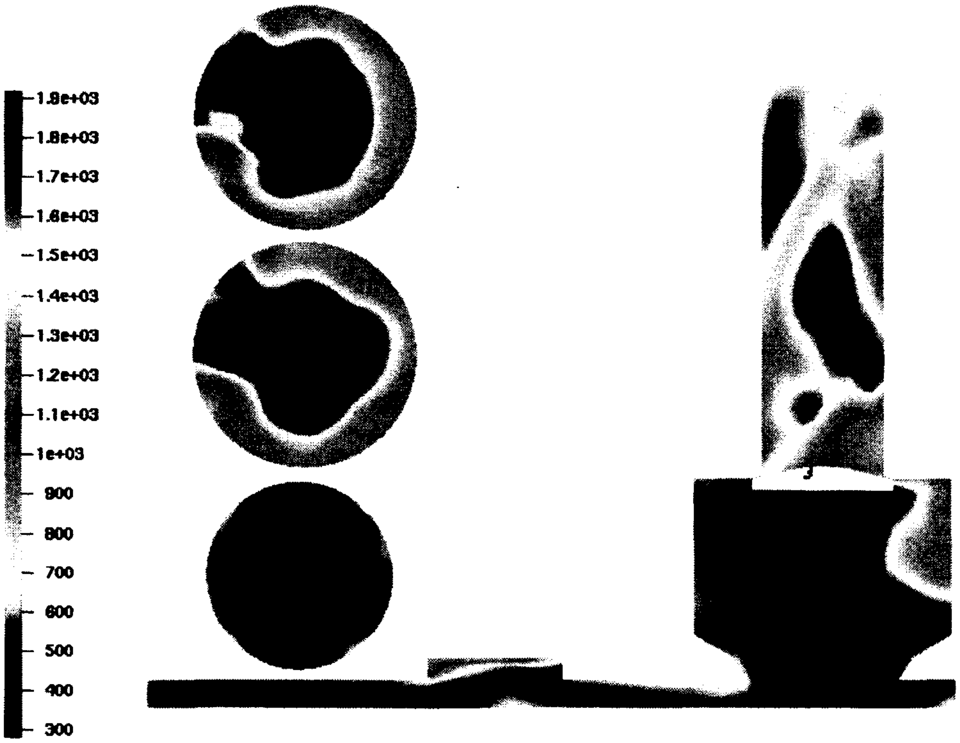

Figure 6.45 (f) 372 CA

Figure 6.45 Temperature contours in XY plane and XZ planes for crank angle (a) 352 CA, (b) 356 CA, (c) 360 CA, (d) 362 CA, (e) 370 CA, and (f) 372 CA.

Species molar fraction contours are plotted to understand the combustion process within the IMR chamber and the production and consumption of some of the species. Figure 6.46 shows the fuel molar fraction contours at different crank angles. These contours indicate the consumption of fuel within the in-cylinder and IMR chamber. The fuel injected into the IMR chamber mixes with the in-cylinder charge when the valve was opened and some of the fuel stays on to the walls surrounding the valve.

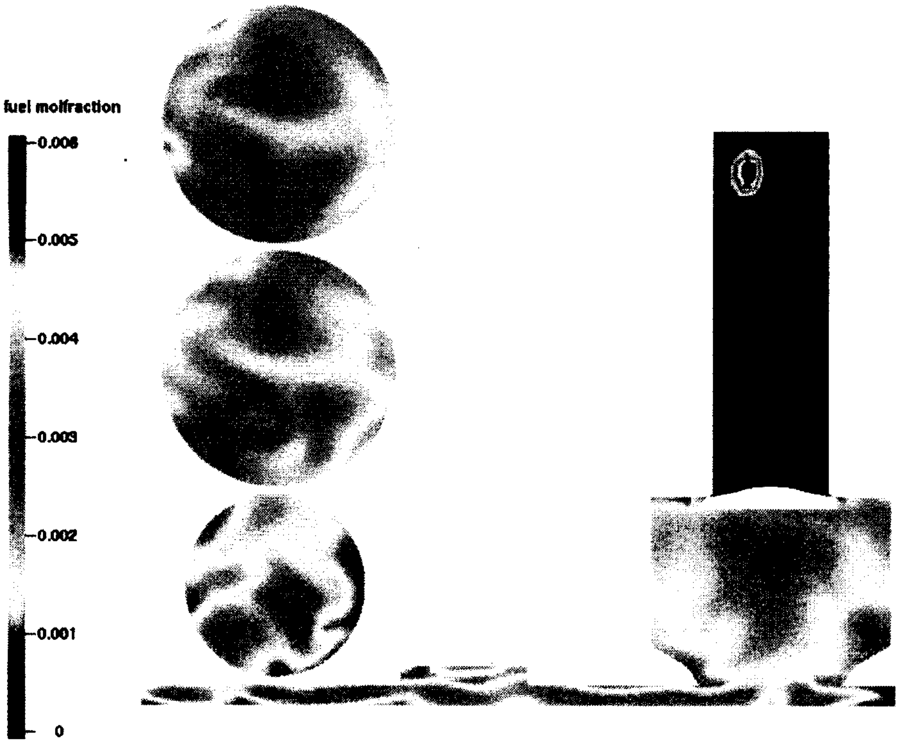

Figure 6.46 (a) 352 CA

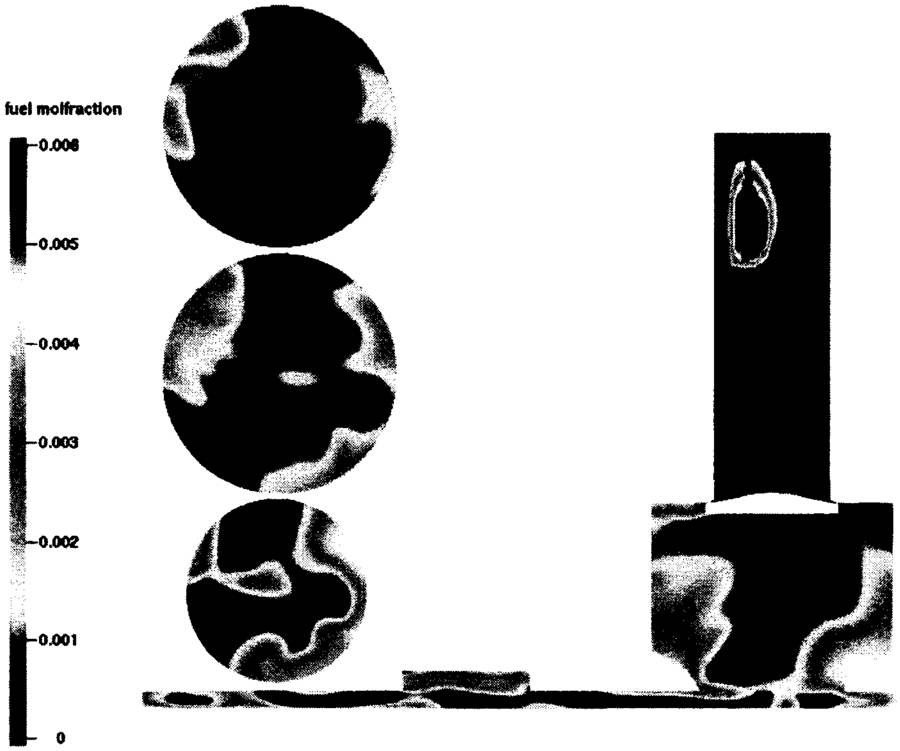
fuel molfraction
0.006
0.005
0.004
0.003
0.002
0.001
0

Figure 6.46 (b) 356 CA

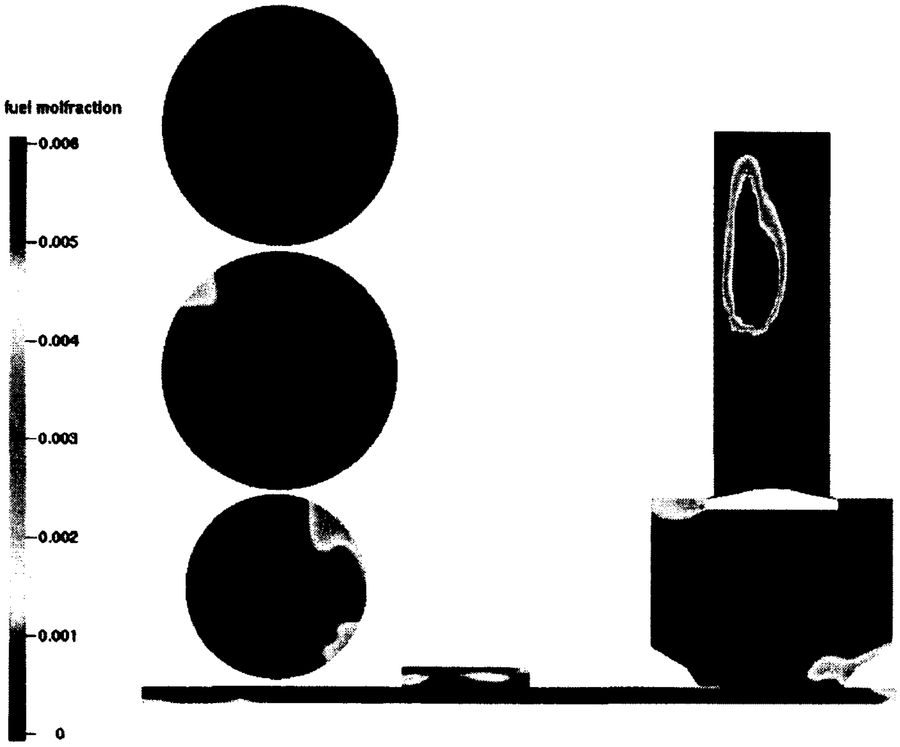
fuel molfraction
0.006
0.005
0.004
0.003
0.002
0.001
0

Figure 6.46 (c) 360 CA

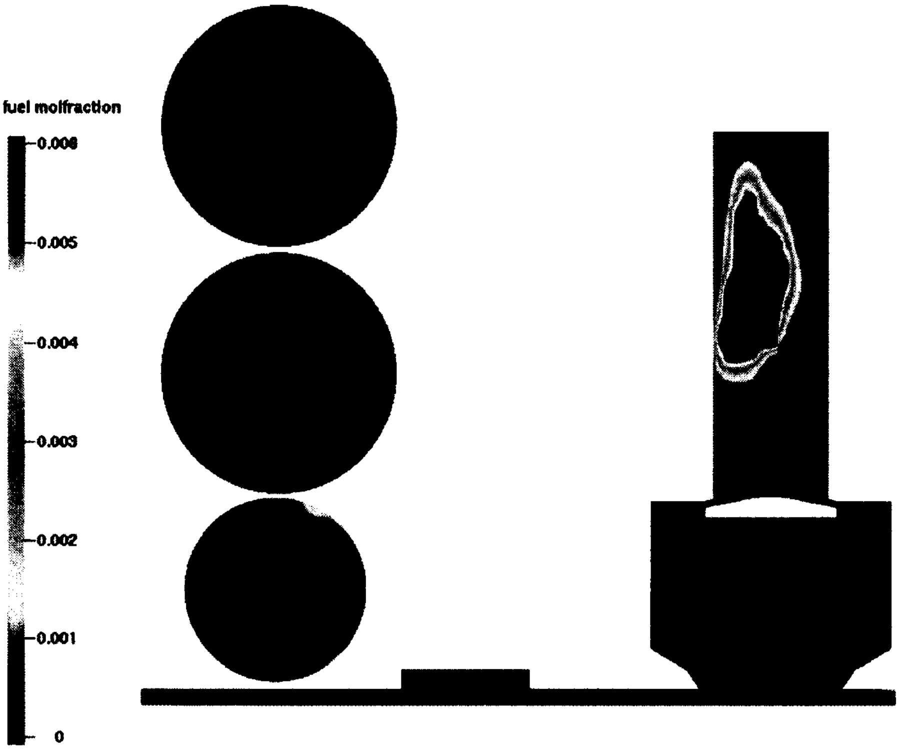

Figure 6.46 (d) 362 CA

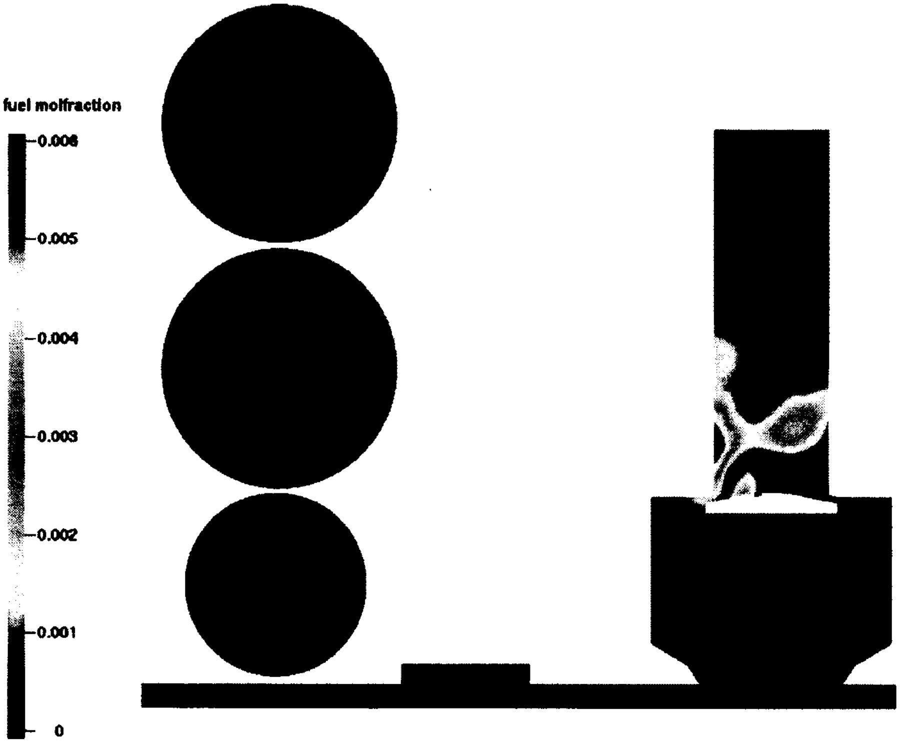

Figure 6.46 (e) 370 CA

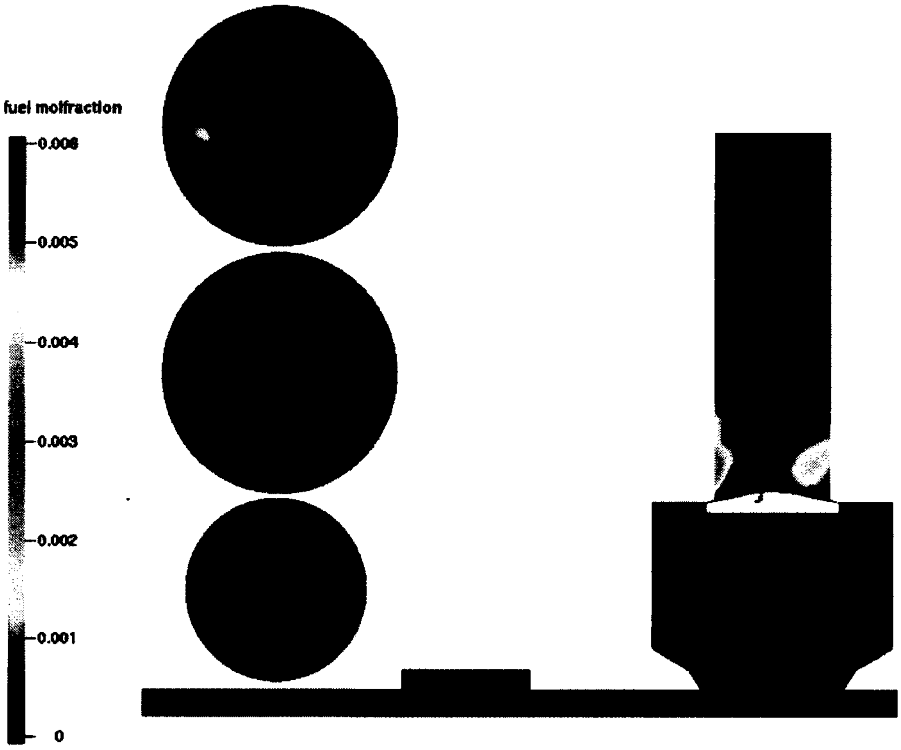

Figure 6.46 (f) 372 CA

Figure 6.46 Fuel molar fraction contours in XY planes and XZ plane at crank angle (a) 352 CA, (b) 356 CA, (c) 360 CA, (d) 362 CA, (e) 370 CA, and (f) 372 CA.

Figure 6.47 shows the consumption of oxygen which indicates the combustion process carried in the pre-chamber and then in the IMR chamber. The O_2 contours in IMR chamber indicate the consumption of O_2 after the valve closure. Figure 6.48 show the N_2 molar fraction contours for various crank angles. Figures 6.48 to 6.54 show the production and consumption of some of the important species to understand the mixing process happening within the IMR chamber and to visualize the species production within the IMR chamber. Figures 6.49 to 6.54 show molar fractions of species CO_2, H_2O, CO, H_2, OH, and NO at various crank angles respectively. These contours indicate the production of CO and H_2 within the IMR chamber and combustion process carried in the pre-chamber from crank angle 352 CA to 372 CA. The results show that the IMR chamber was able to produce reformation products due to internal mixing and fuel injection. The plots indicate high levels of CO_2 and H_2O within the IMR chamber before chamber valve opens from the previous cycle. CO and H_2 are produced in the IMR chamber after 366 CA. Due to high temperature within the IMR chamber, CO and H_2 produced within the IMR chamber are consumed within the same cycle.

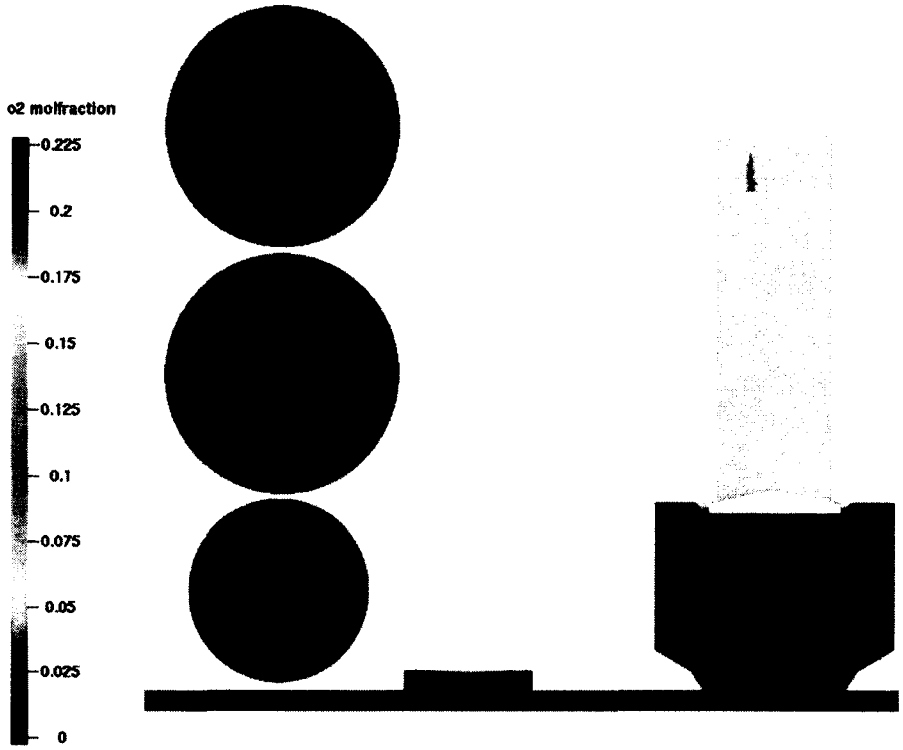

Figure 6.47 (a) 352 CA

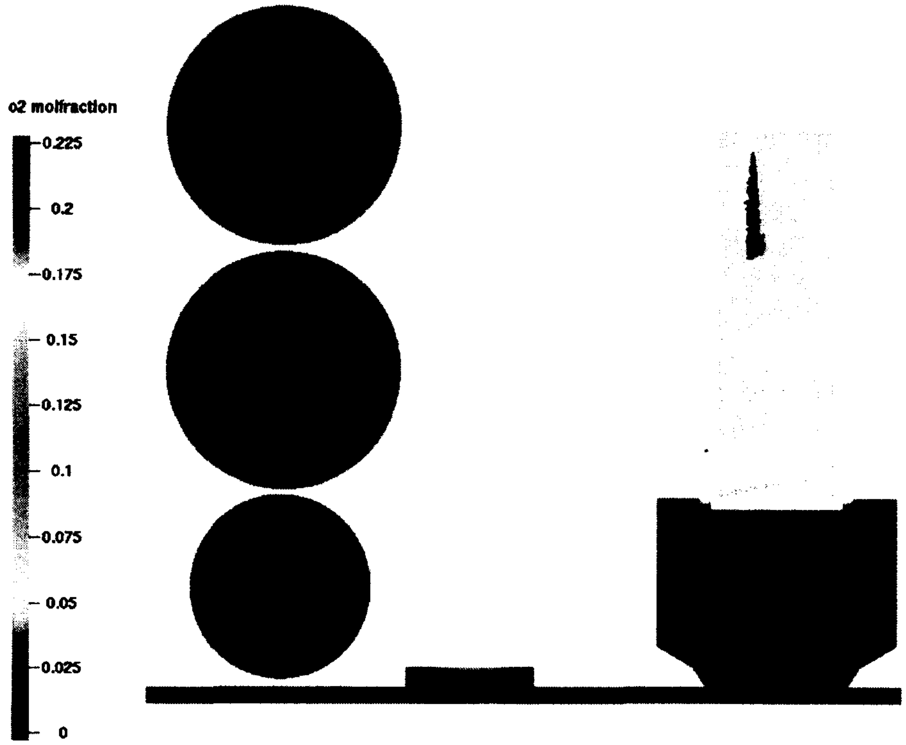

Figure 6.47 (b) 356 CA

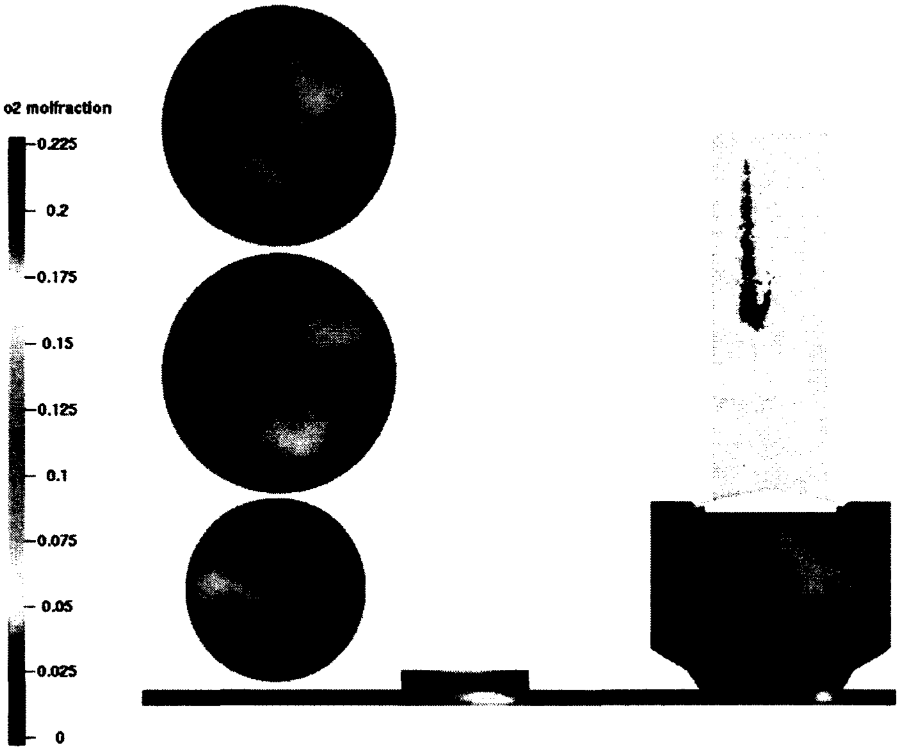

Figure 6.47 (c) 360 CA

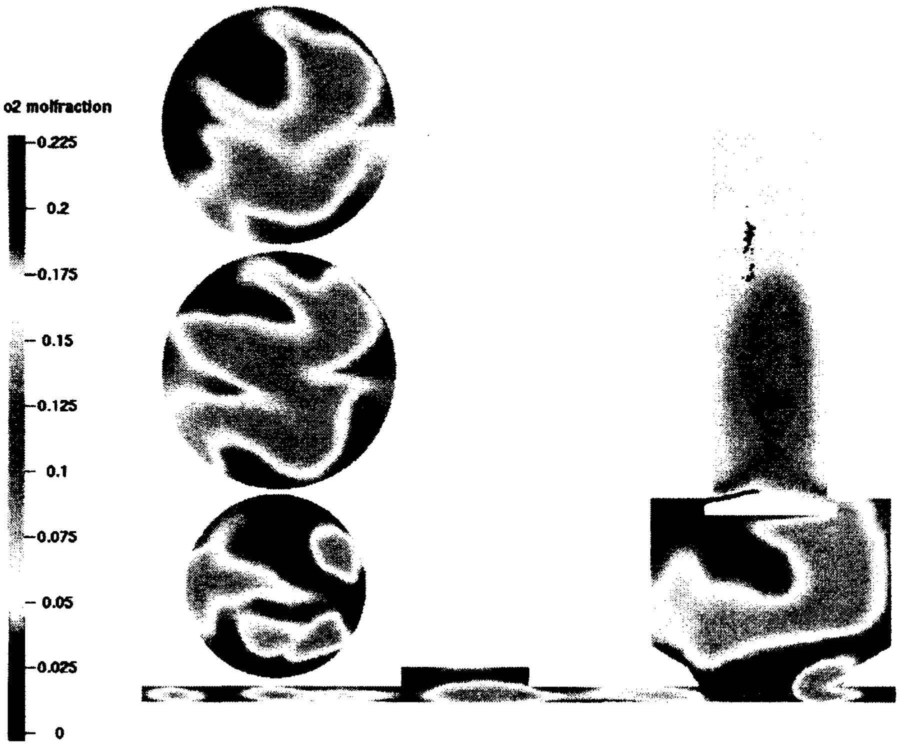

Figure 6.47 (d) 362 CA

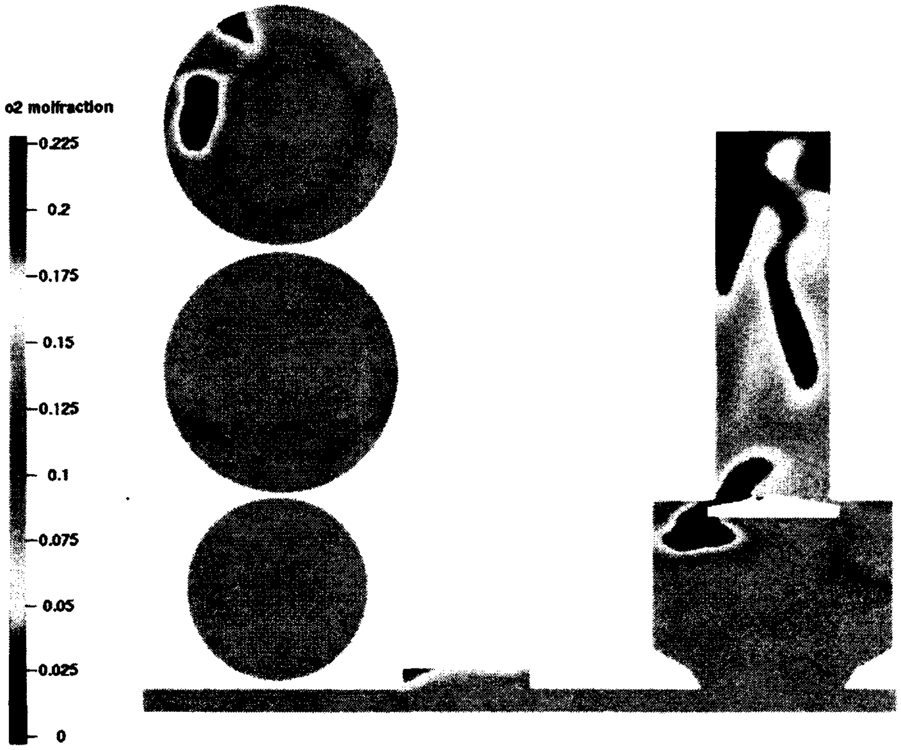

Figure 6.47 (e) 370 CA

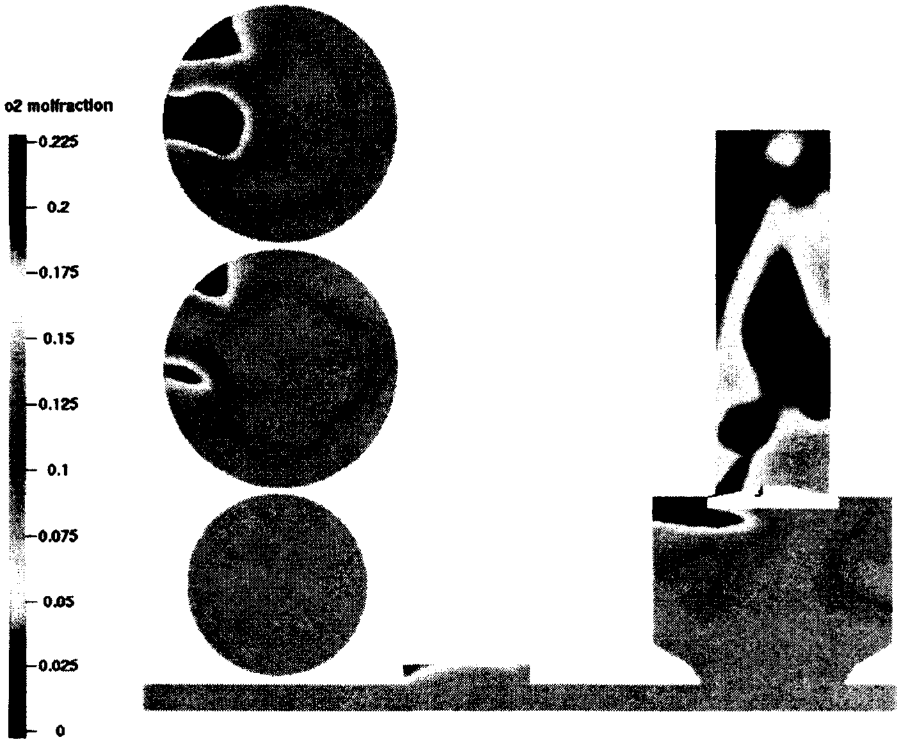

Figure 6.47 (f) 372 CA

Figure 6.47 O_2 molar fraction contours in XY planes and XZ plane at crank angle (a) 352 CA, (b) 356 CA, (c) 360 CA, (d) 362 CA, (e) 370 CA, and (f) 372 CA.

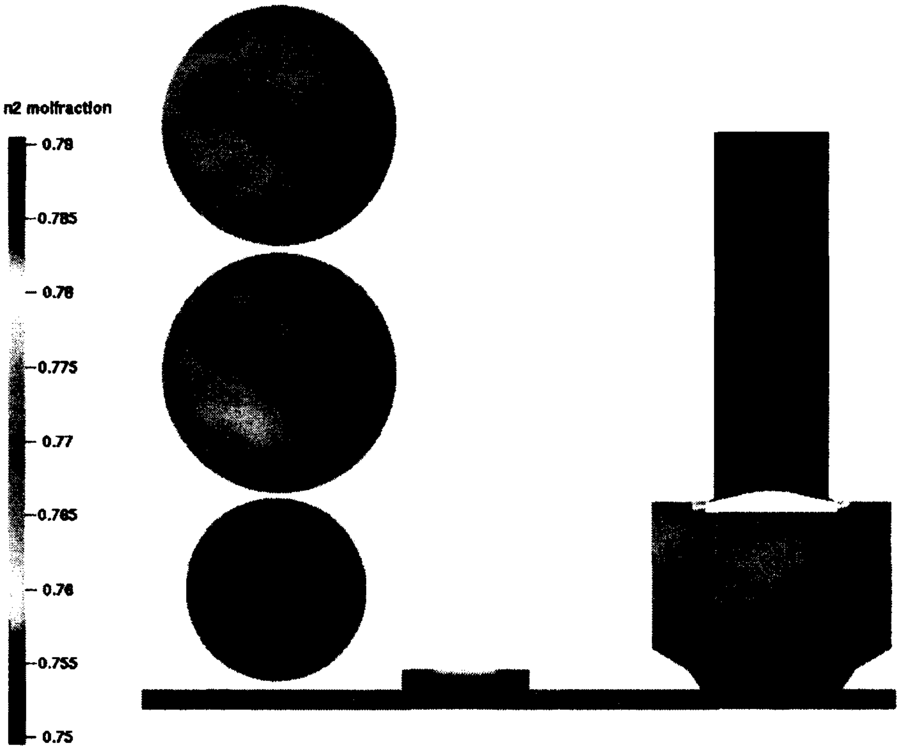

Figure 6.48 (a) 352 CA

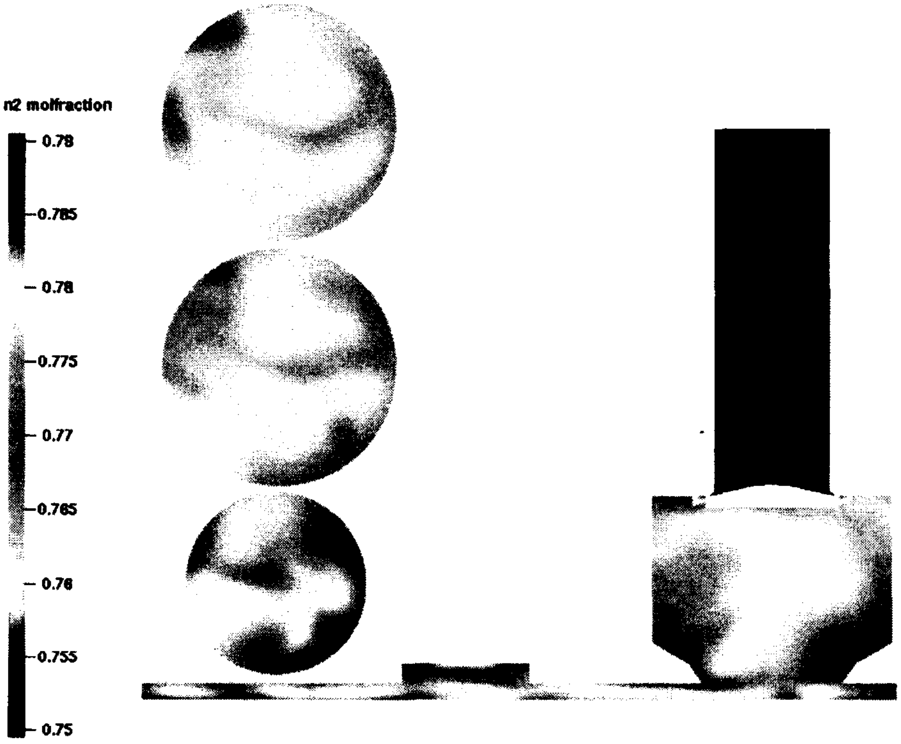

Figure 6.48 (b) 356 CA

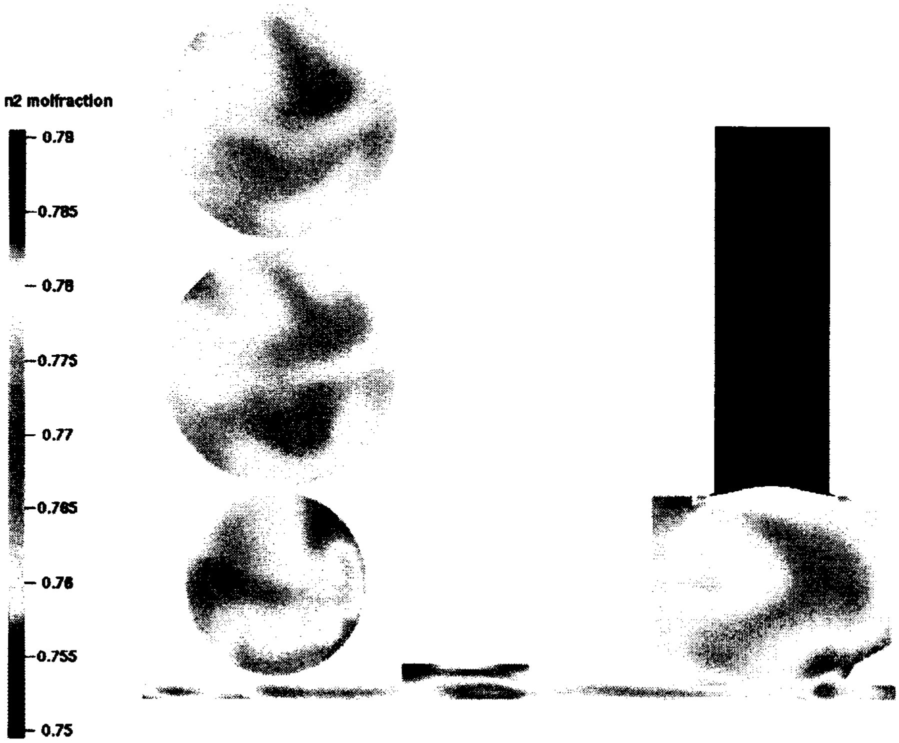

Figure 6.48 (c) 360 CA

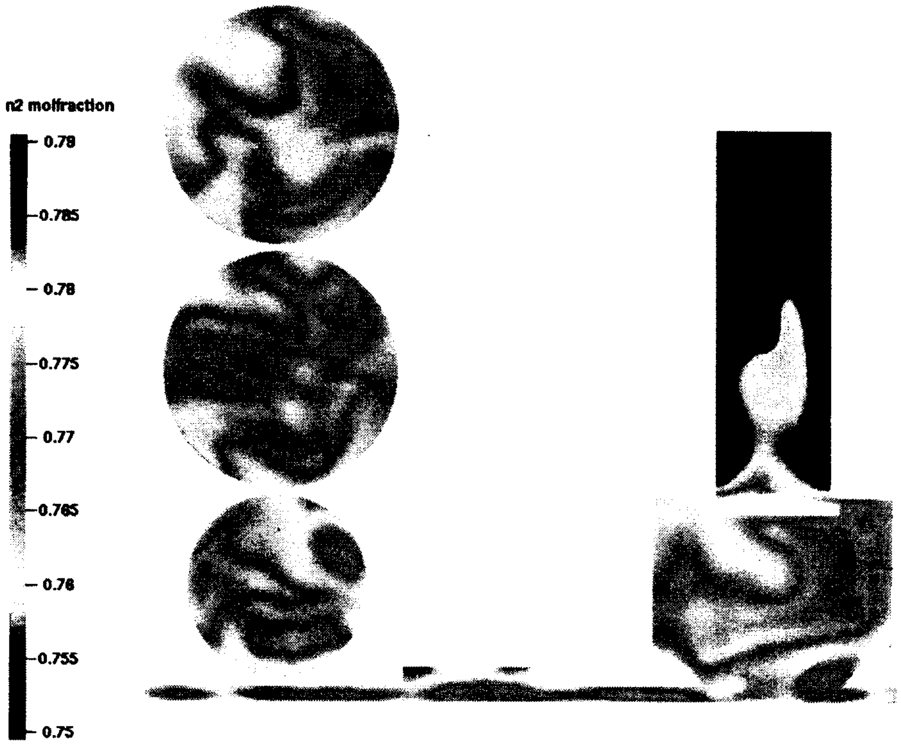

Figure 6.48 (d) 362 CA

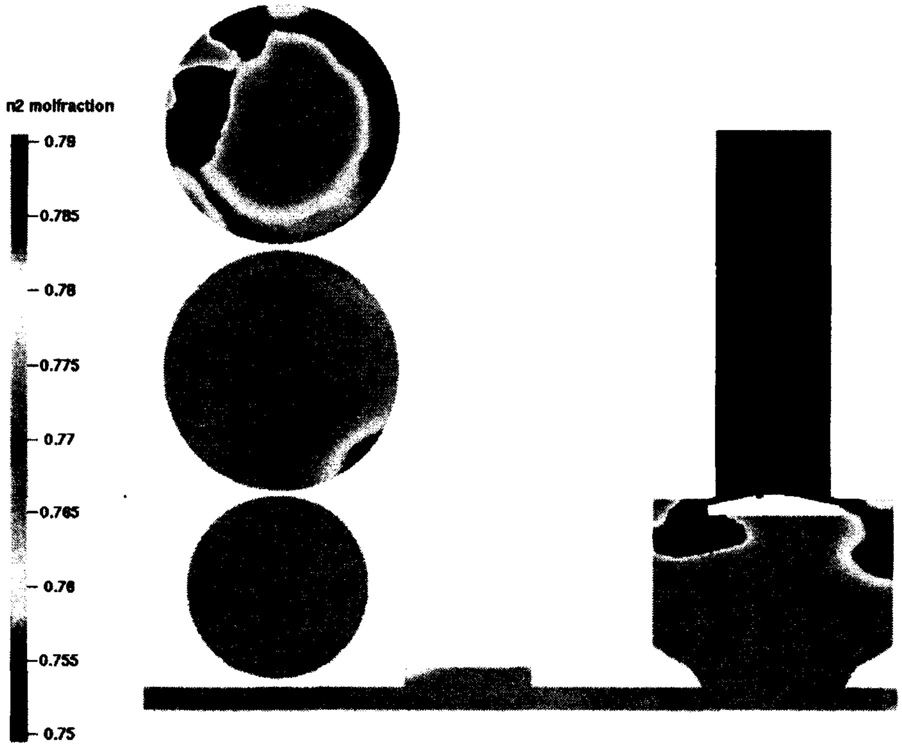

Figure 6.48 (e) 370 CA

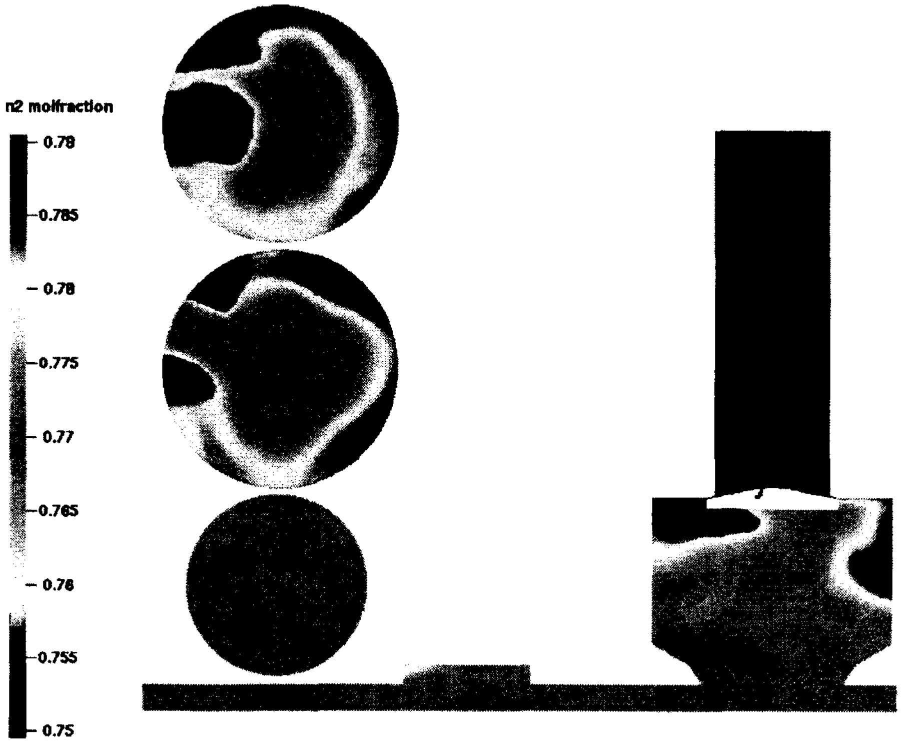

Figure 6.48 (f) 372 CA

Figure 6.48 N_2 molar fraction contours in XY planes and XZ plane at crank angle (a) 352 CA, (b) 356 CA, (c) 360 CA, (d) 362 CA, (e) 370 CA, and (f) 372 CA.

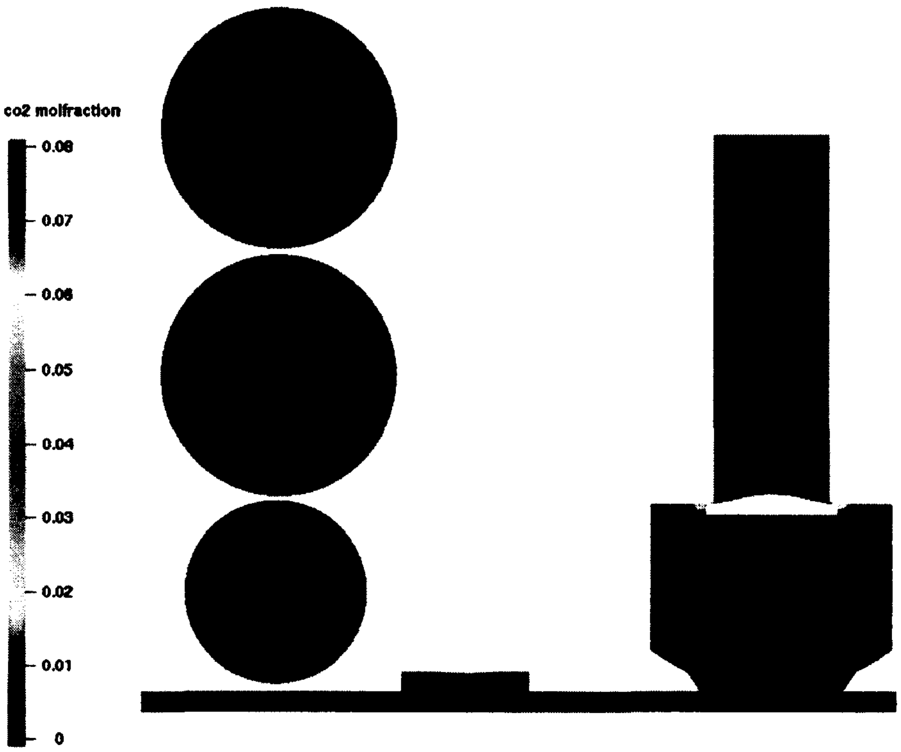

Figure 6.49 (a) 352 CA

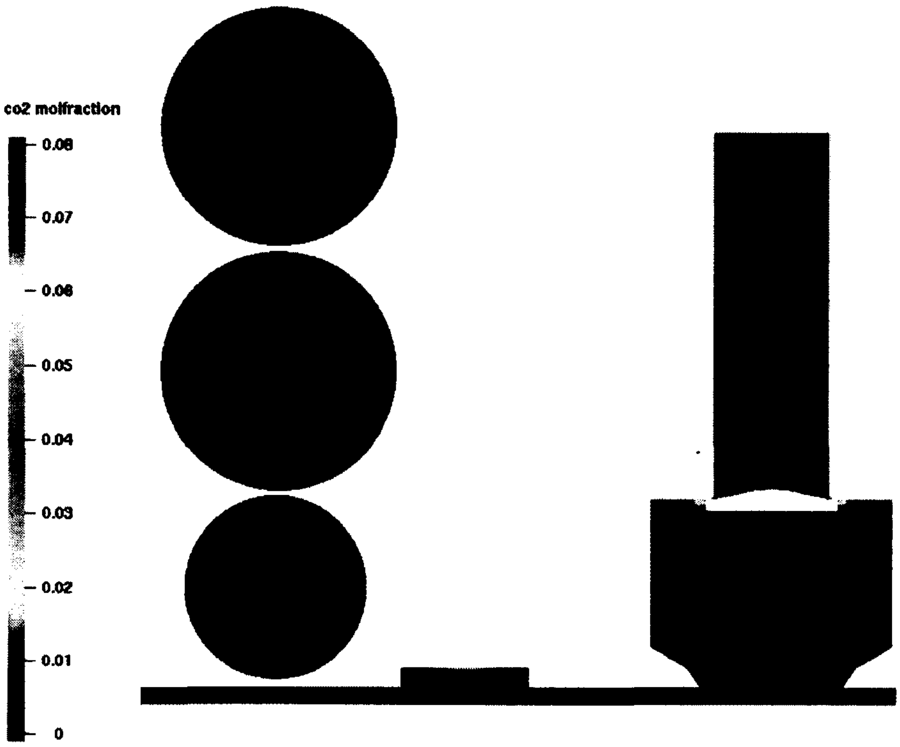

Figure 6.49 (b) 356 CA

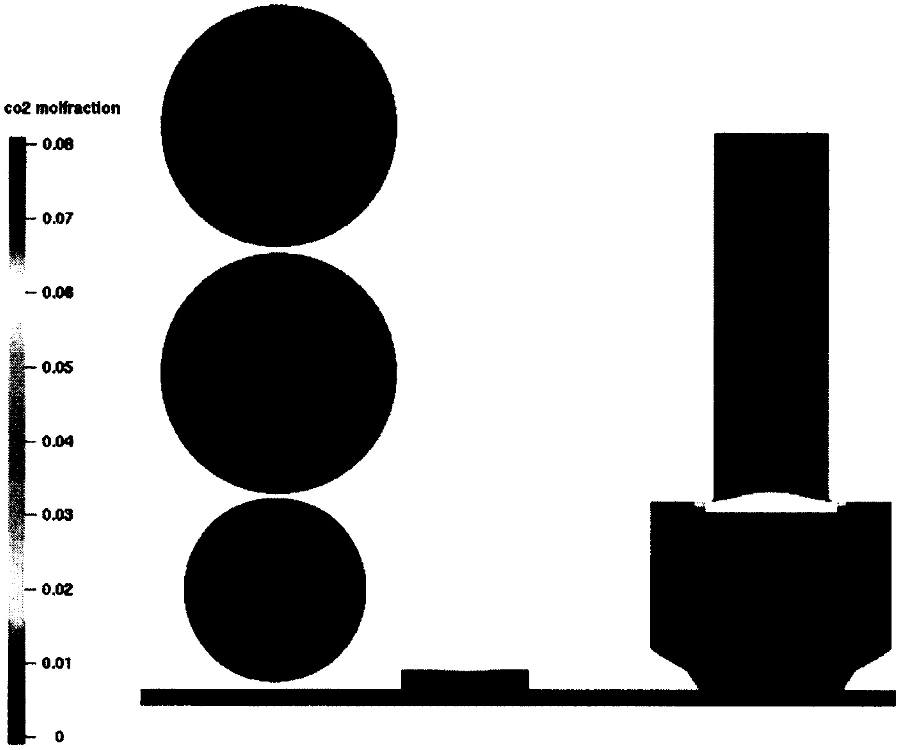

Figure 6.49 (c) 360 CA

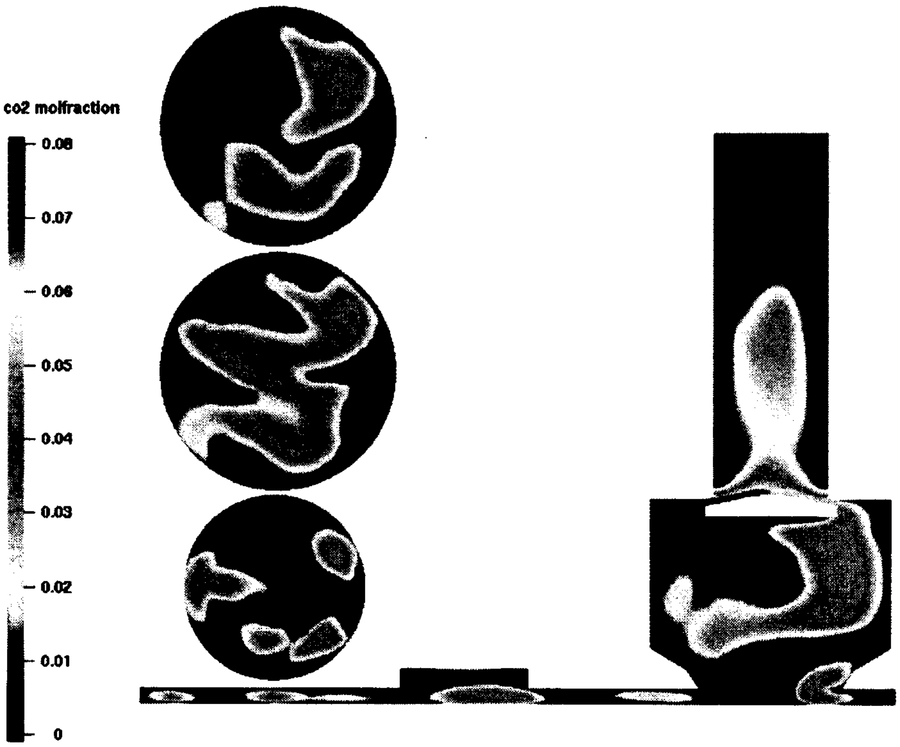

Figure 6.49 (d) 362 CA

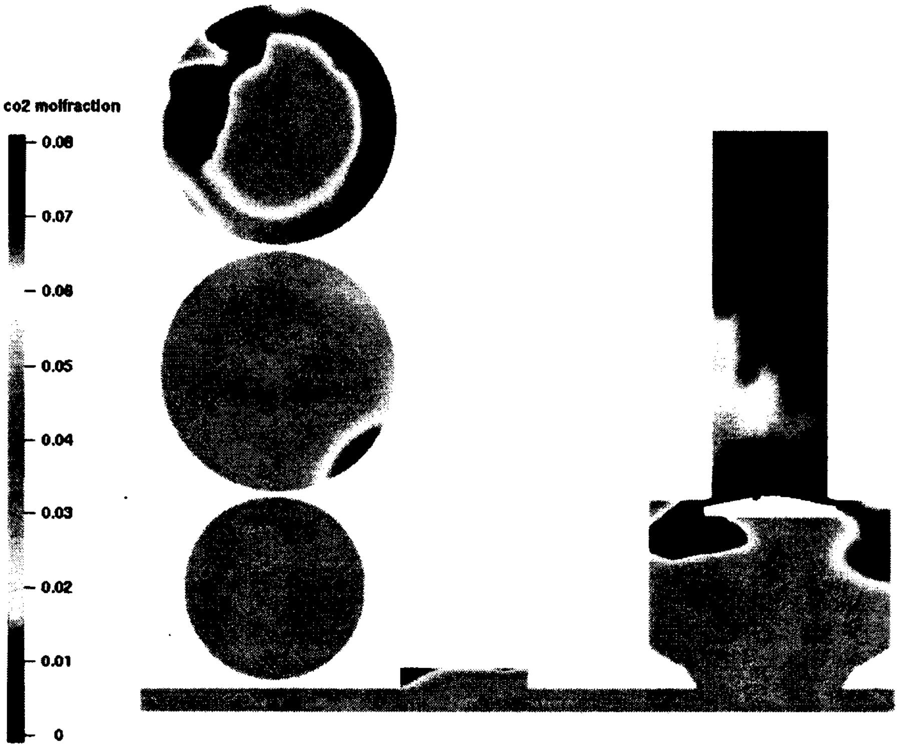

Figure 6.49 (e) 370 CA

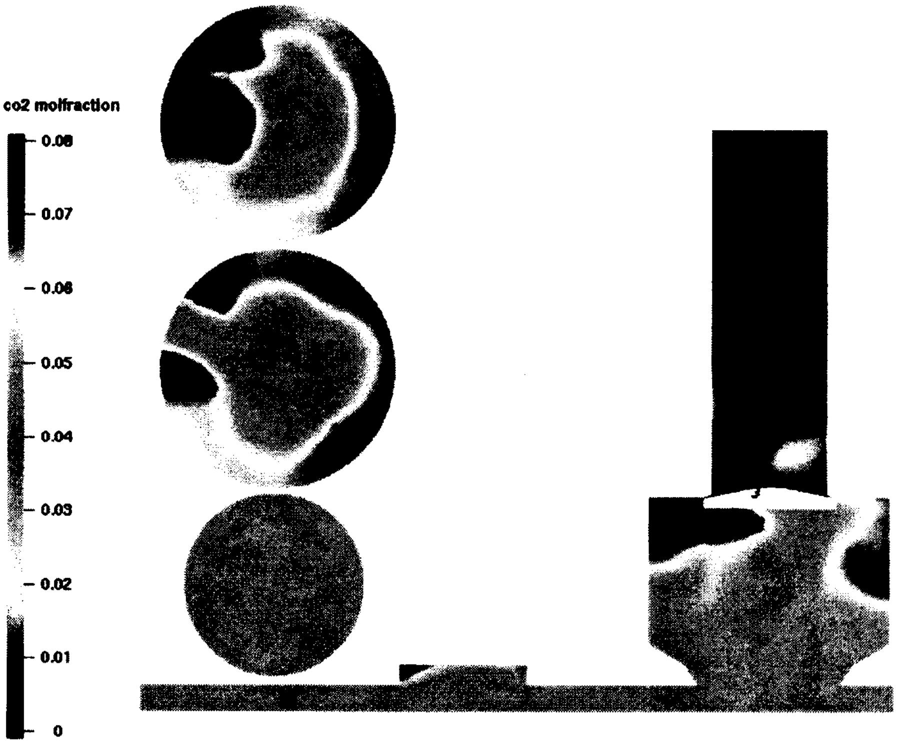

Figure 6.49 (f) 372 CA

Figure 6.49 CO_2 molar fraction contours in XY planes and XZ plane at crank angle (a) 352 CA, (b) 356 CA, (c) 360 CA, (d) 362 CA, (e) 370 CA, and (f) 372 CA.

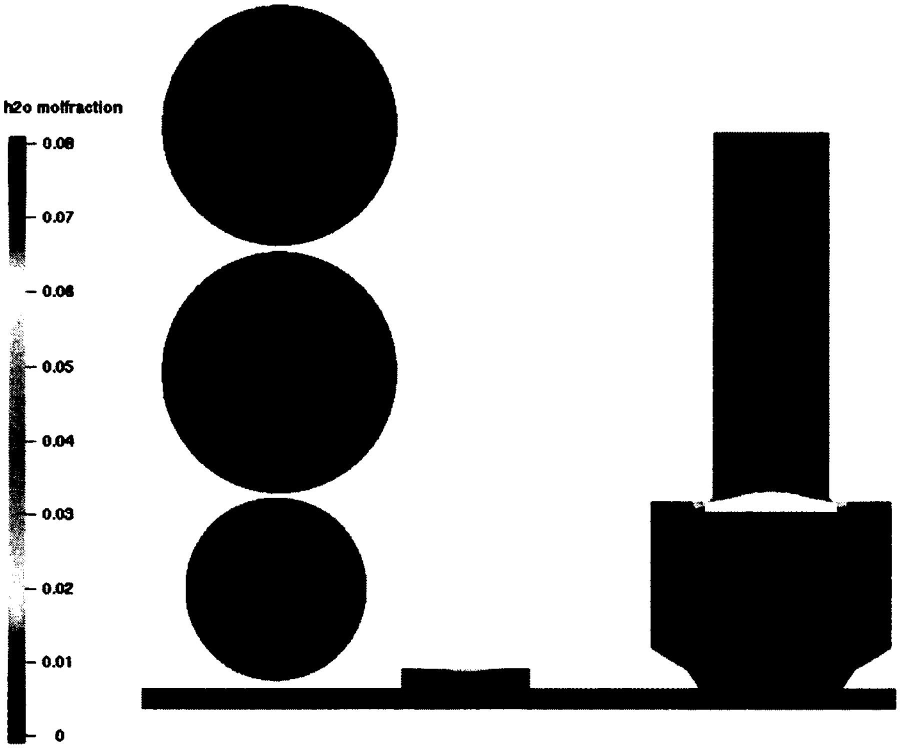

Figure 6.50 (a) 352 CA

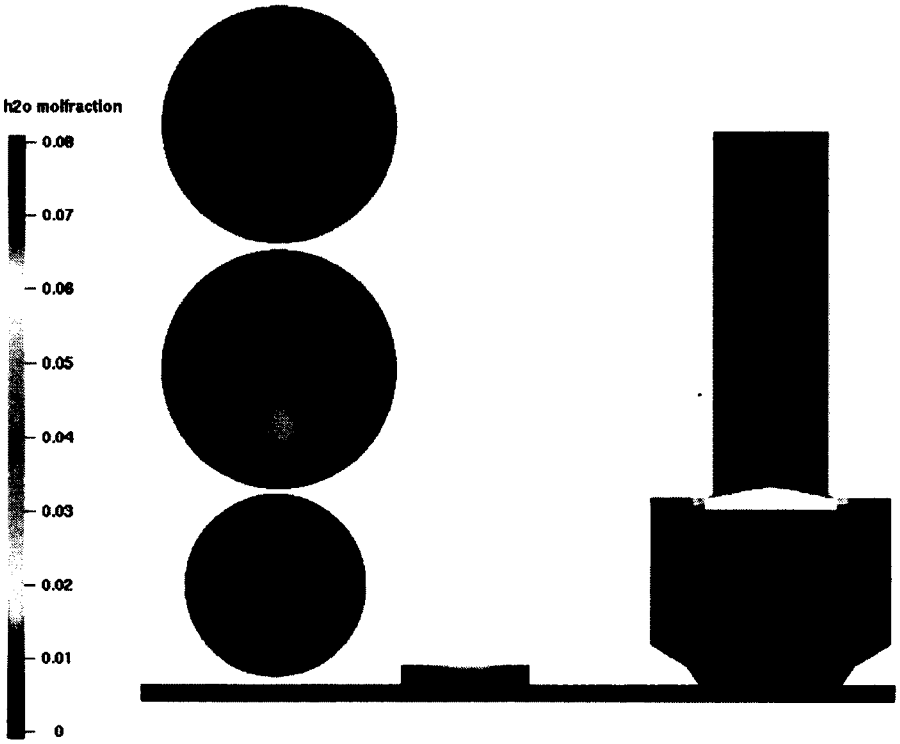

Figure 6.50 (b) 356 CA

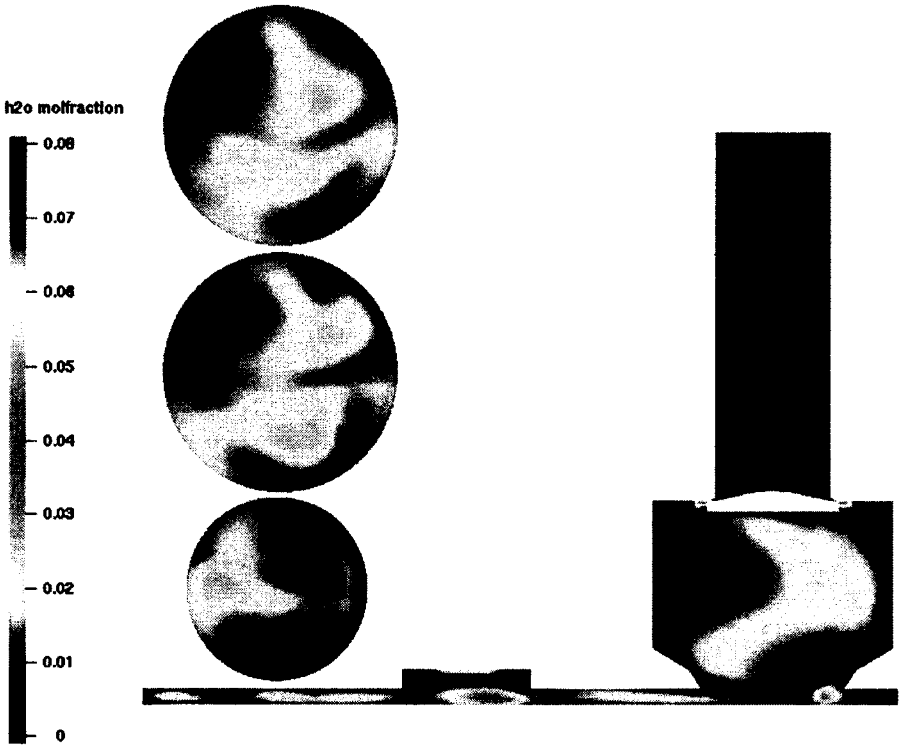

Figure 6.50 (c) 360 CA

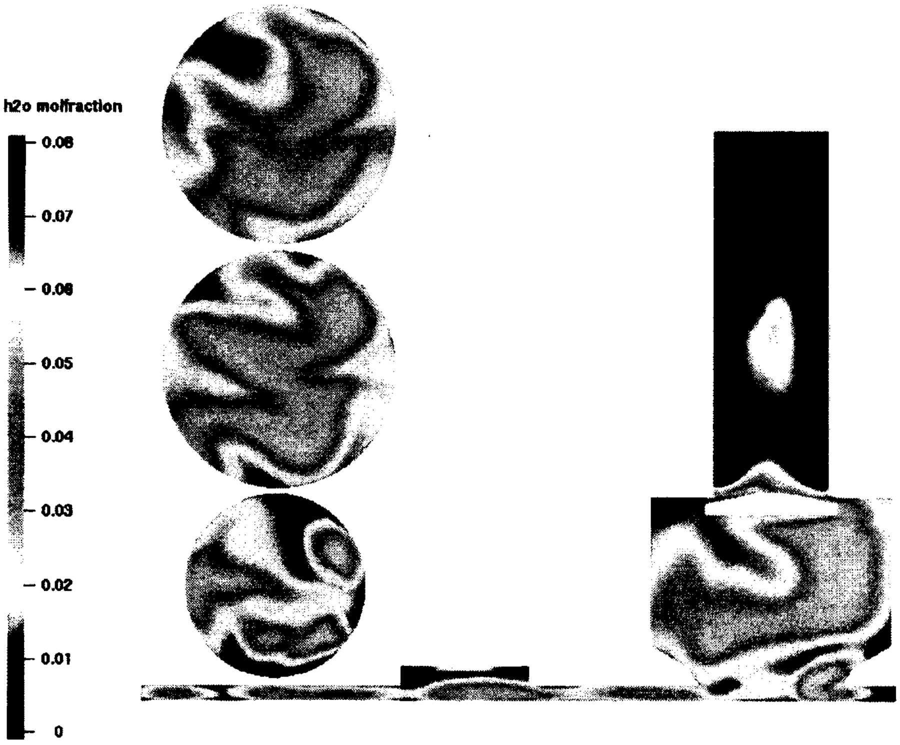

Figure 6.50 (d) 362 CA

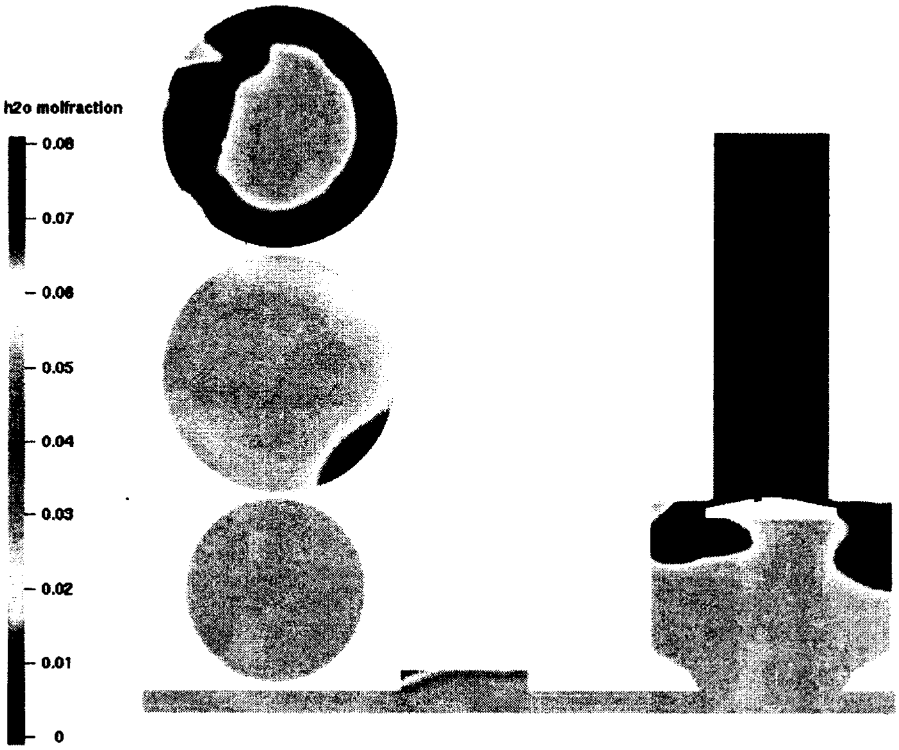

Figure 6.50 (e) 370 CA

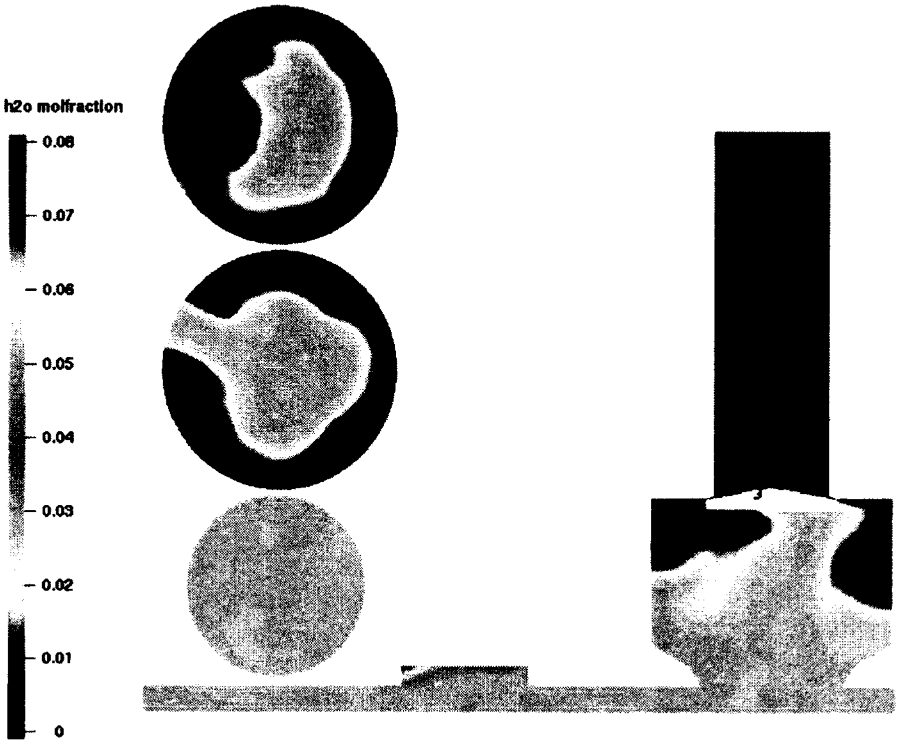

Figure 6.50 (f) 372 CA

Figure 6.50 H_2O molar fraction contours in XY planes and XZ plane at crank angle (a) 352 CA, (b) 356 CA, (c) 360 CA, (d) 362 CA, (e) 370 CA, and (f) 372 CA.

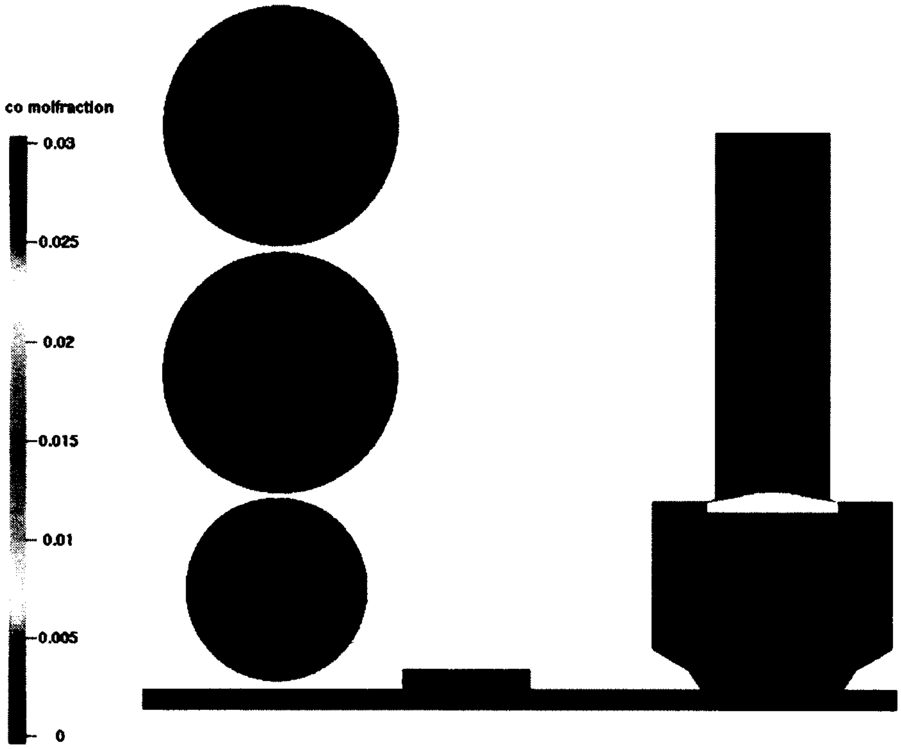

Figure 6.51 (a) 352 CA

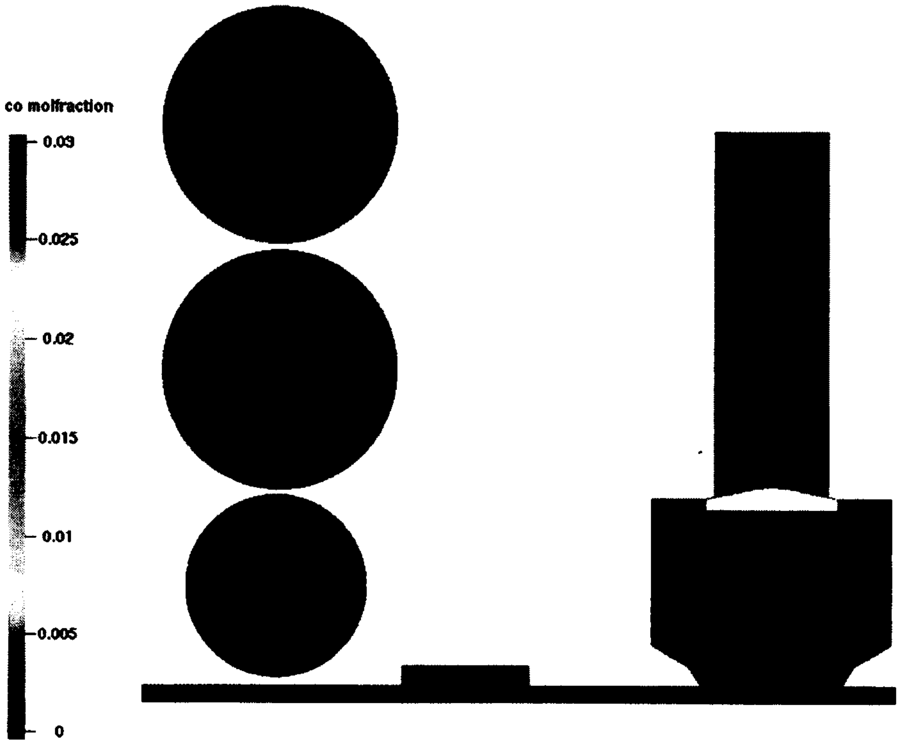

Figure 6.51 (b) 356 CA

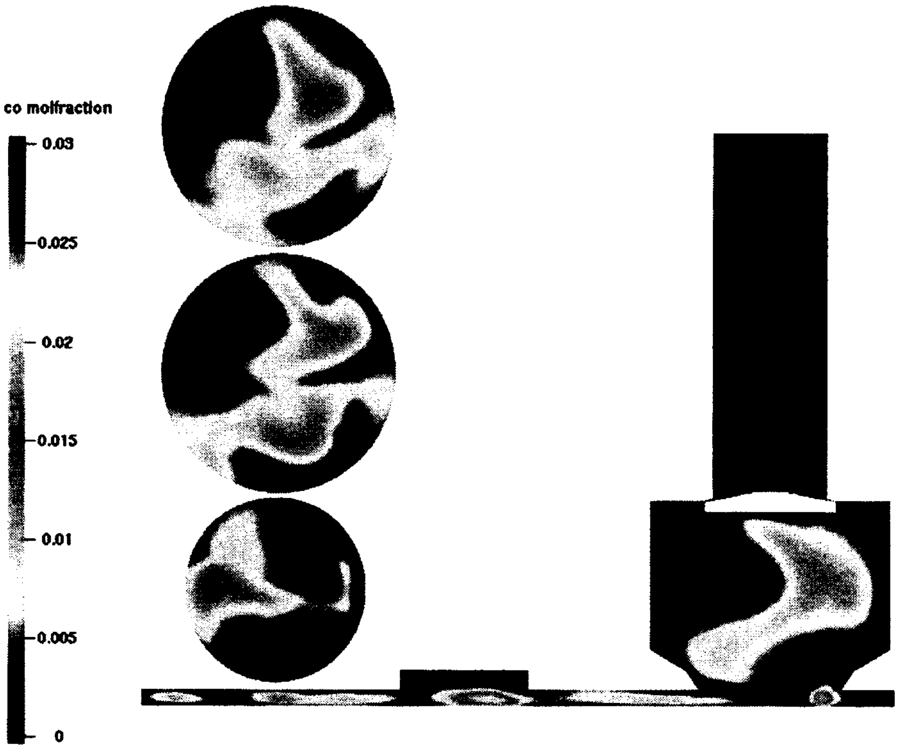

Figure 6.51 (c) 360 CA

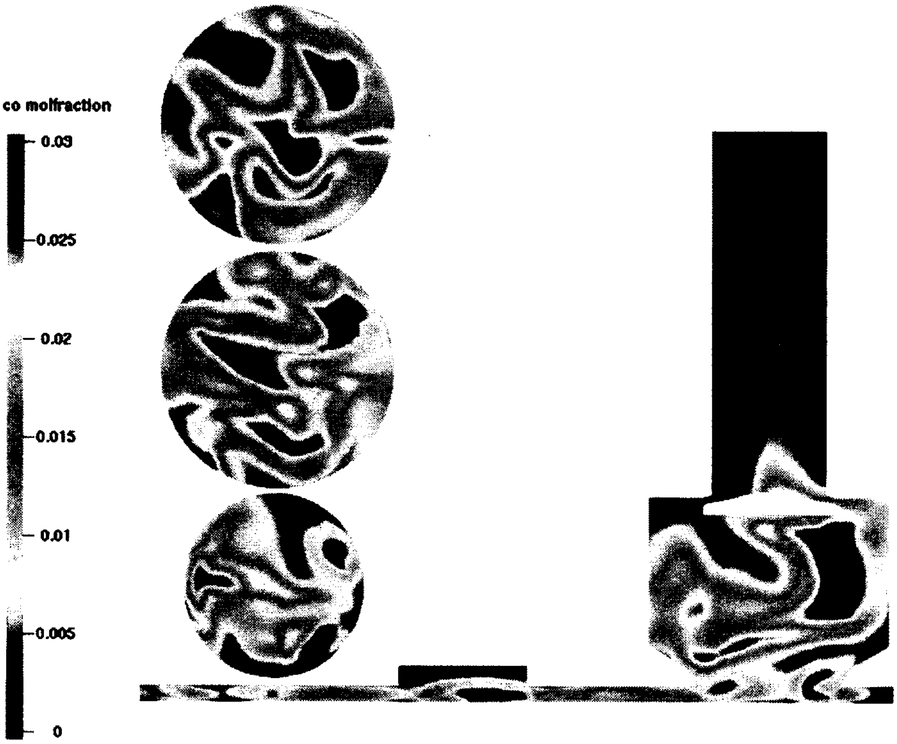

Figure 6.51 (d) 362 CA

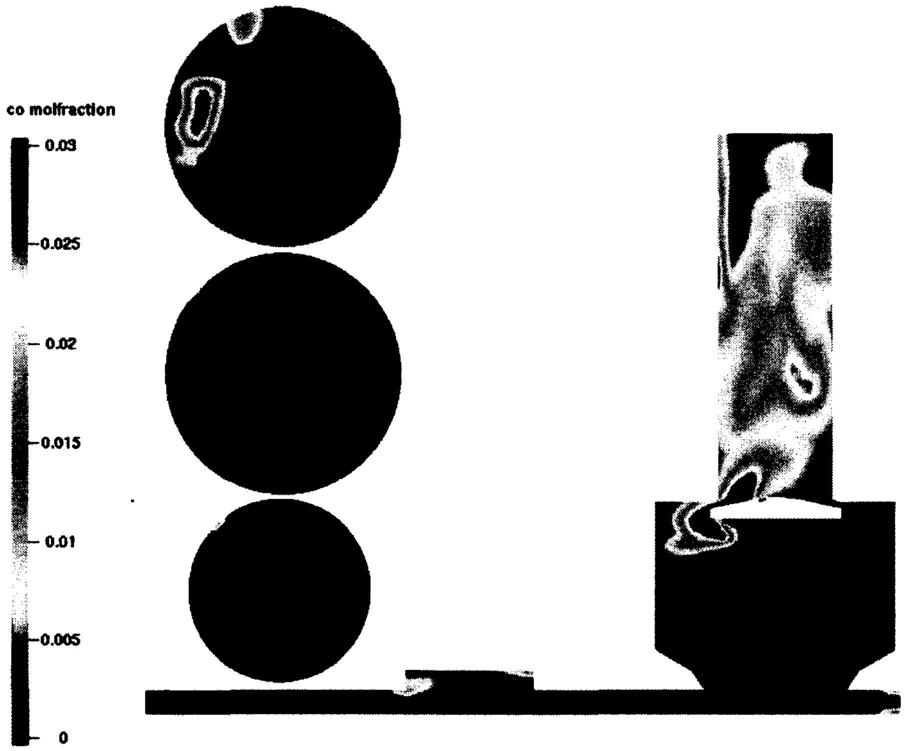

Figure 6.51 (e) 370 CA

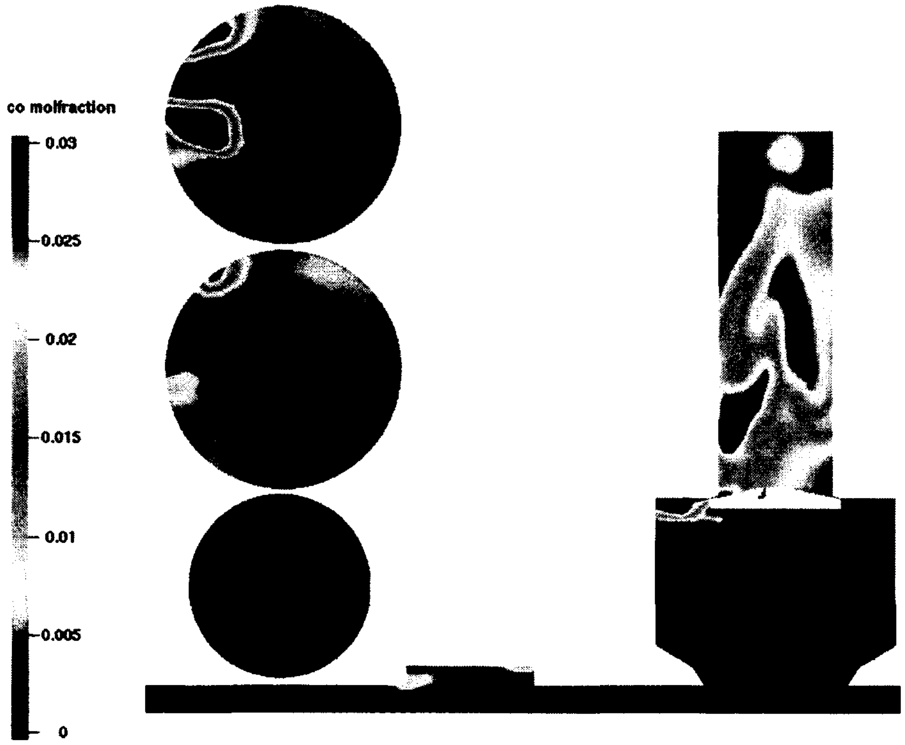

Figure 6.51 (f) 372 CA

Figure 6.51 CO molar fraction contours in XY planes and XZ plane at crank angle (a) 352 CA, (b) 356 CA, (c) 360 CA, (d) 362 CA, (e) 370 CA, and (f) 372 CA.

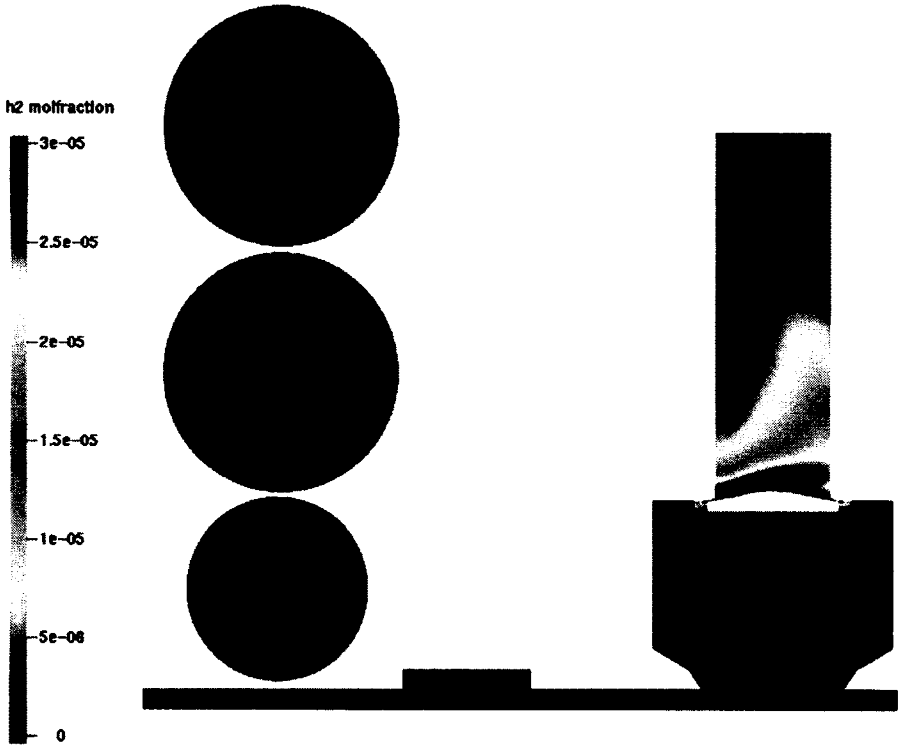

Figure 6.52 (a) 352 CA

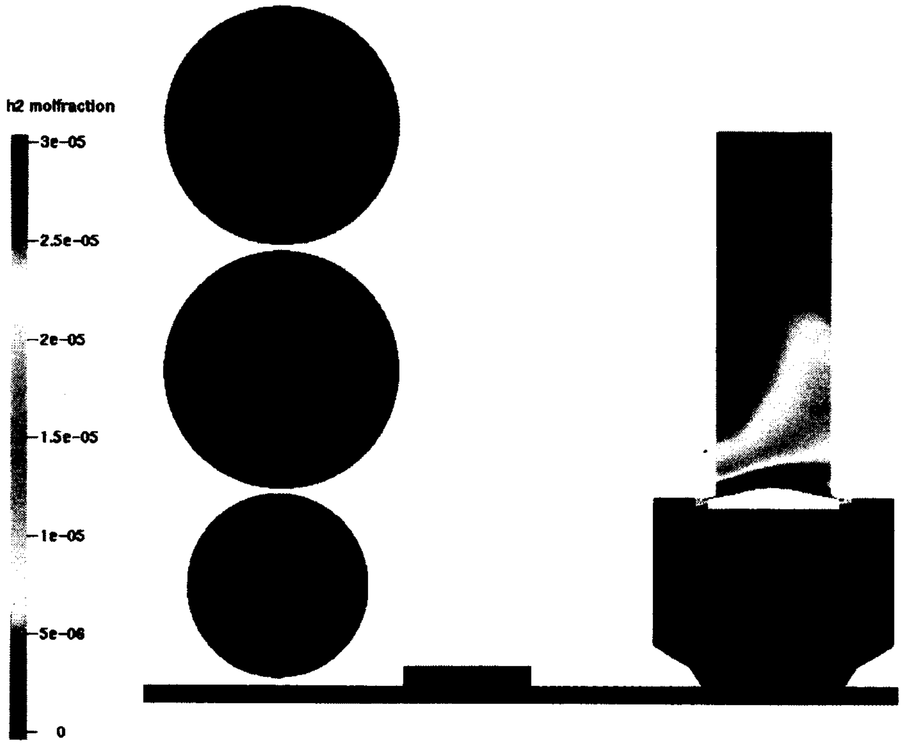

Figure 6.52 (b) 356 CA

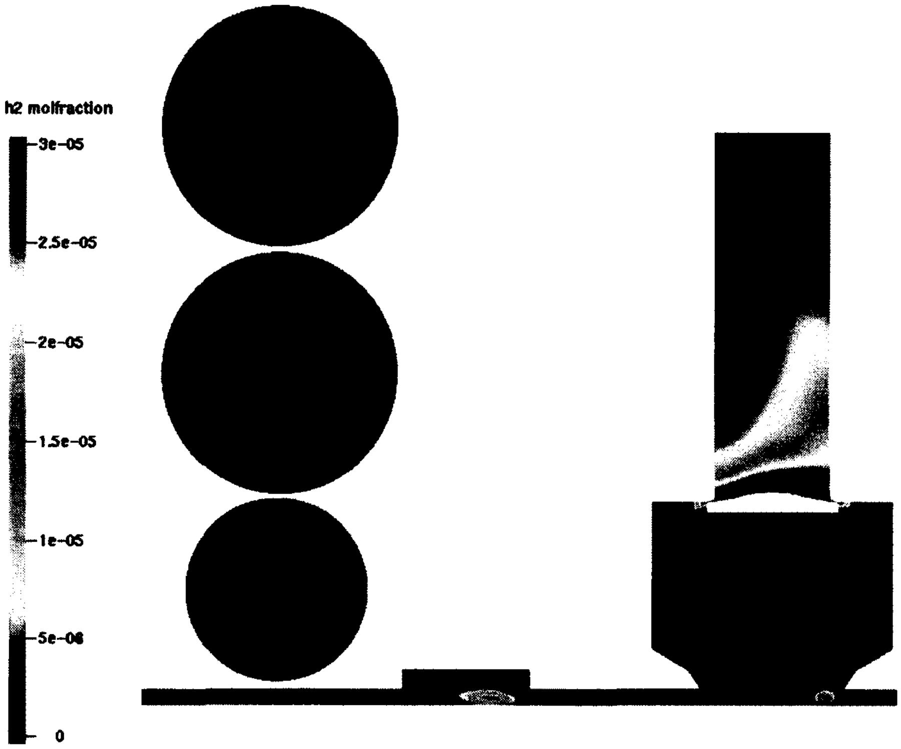

Figure 6.52 (c) 360 CA

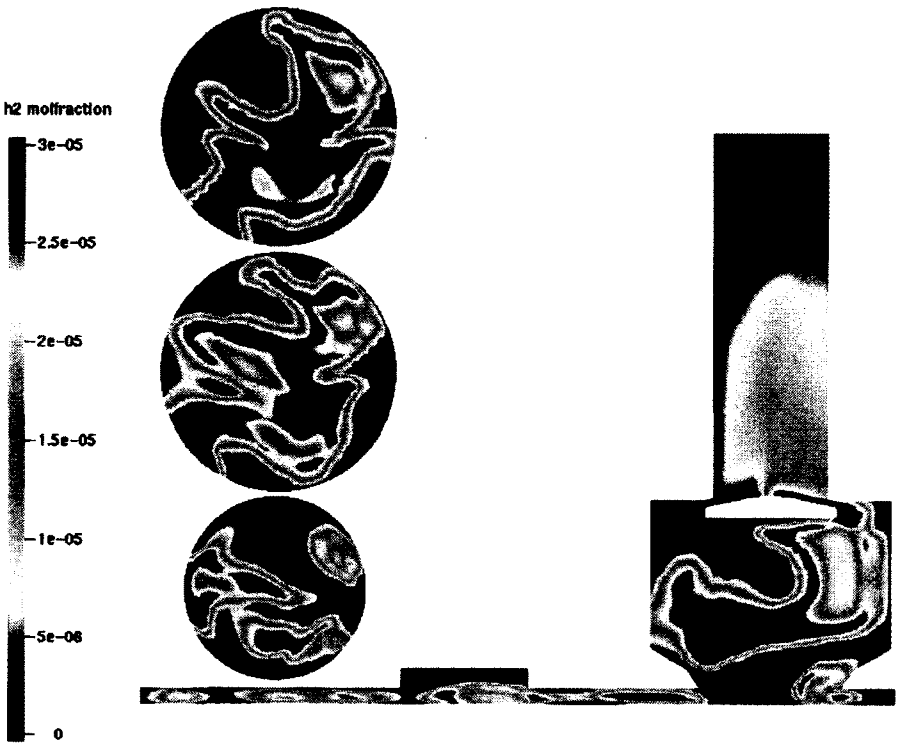

Figure 6.52 (d) 362 CA

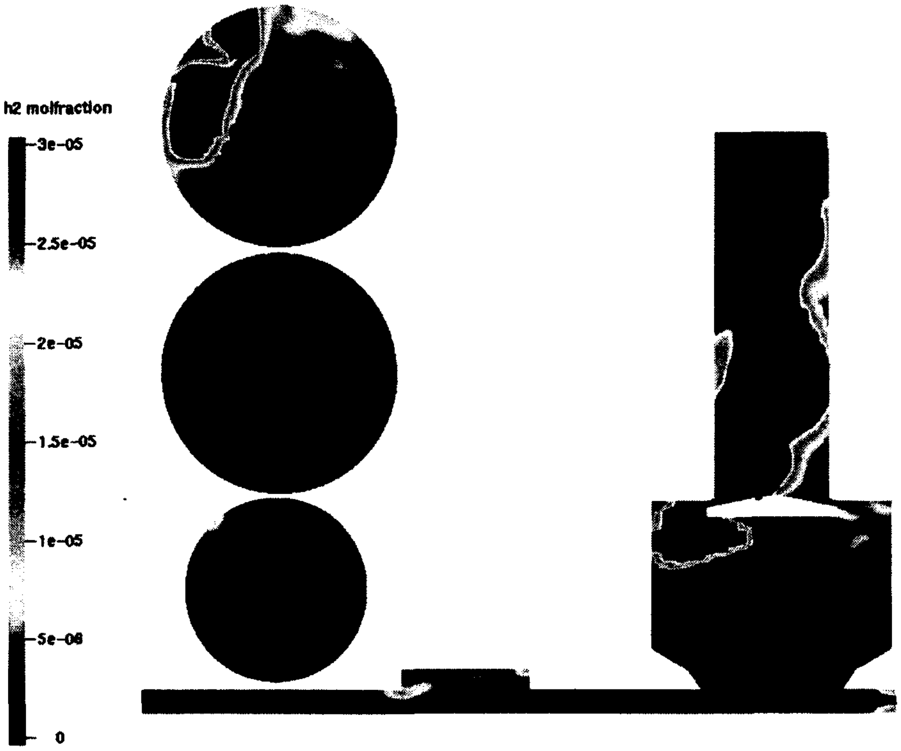

Figure 6.52 (e) 370 CA

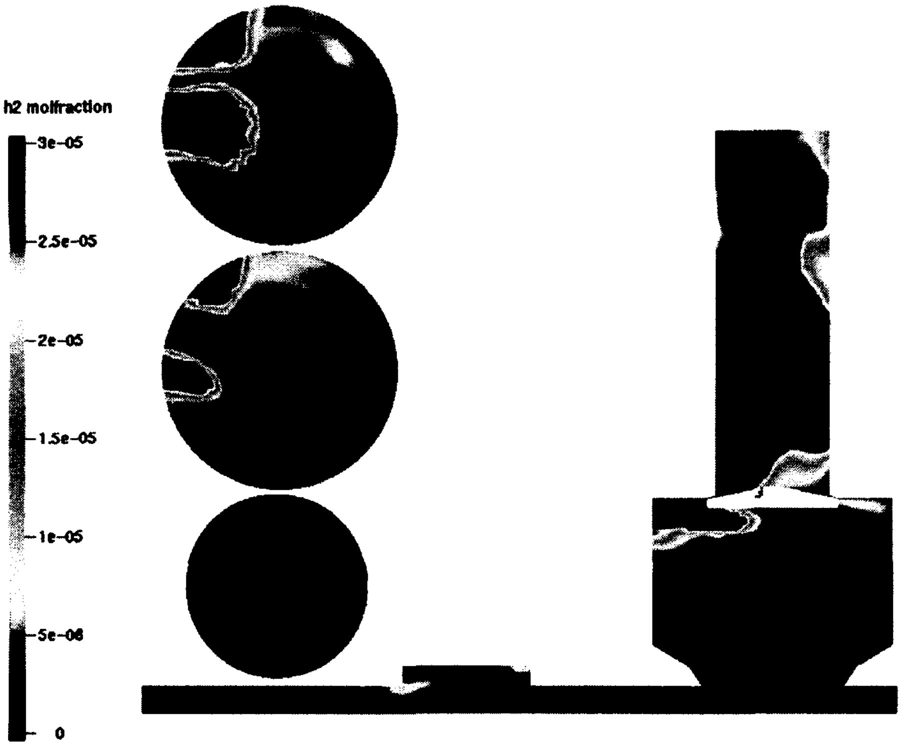

Figure 6.52 (f) 372 CA

Figure 6.52 H_2 molar fraction contours in XY planes and XZ plane at crank angle (a) 352 CA, (b) 356 CA, (c) 360 CA, (d) 362 CA, (e) 370 CA, and (f) 372 CA.

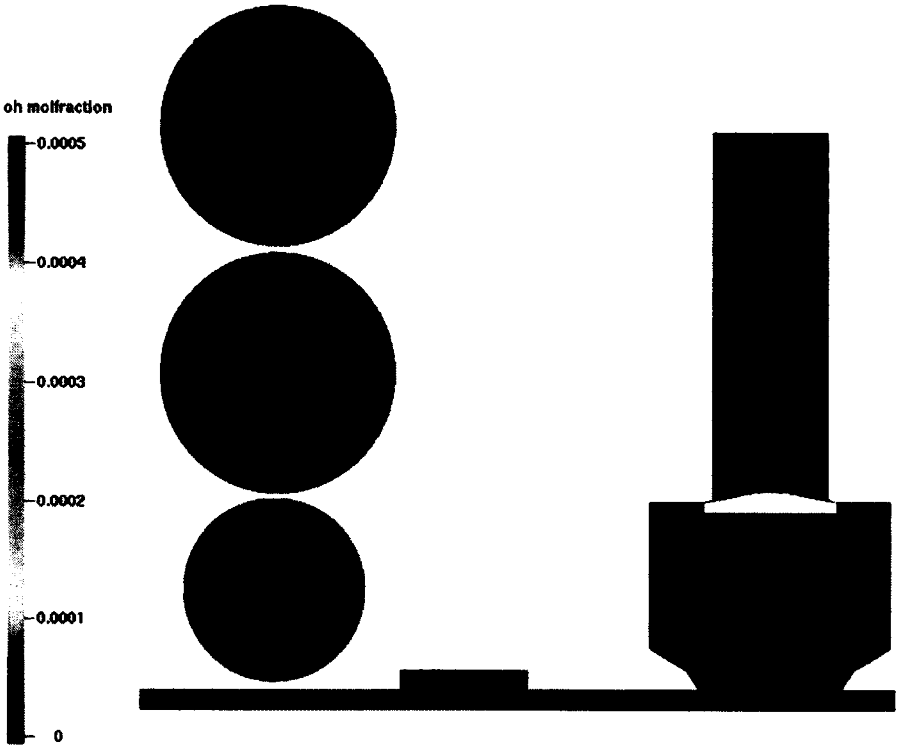
oh molfraction
0.0005
0.0004
0.0003
0.0002
0.0001
0

Figure 6.53 (a) 352 CA

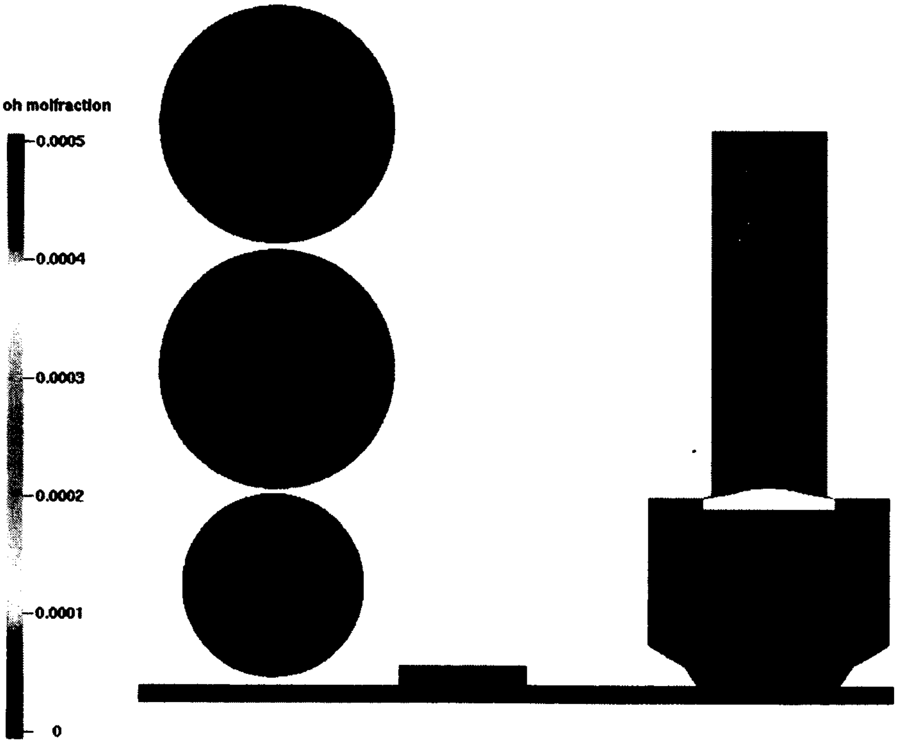
oh molfraction
0.0005
0.0004
0.0003
0.0002
0.0001
0

Figure 6.53 (b) 356 CA

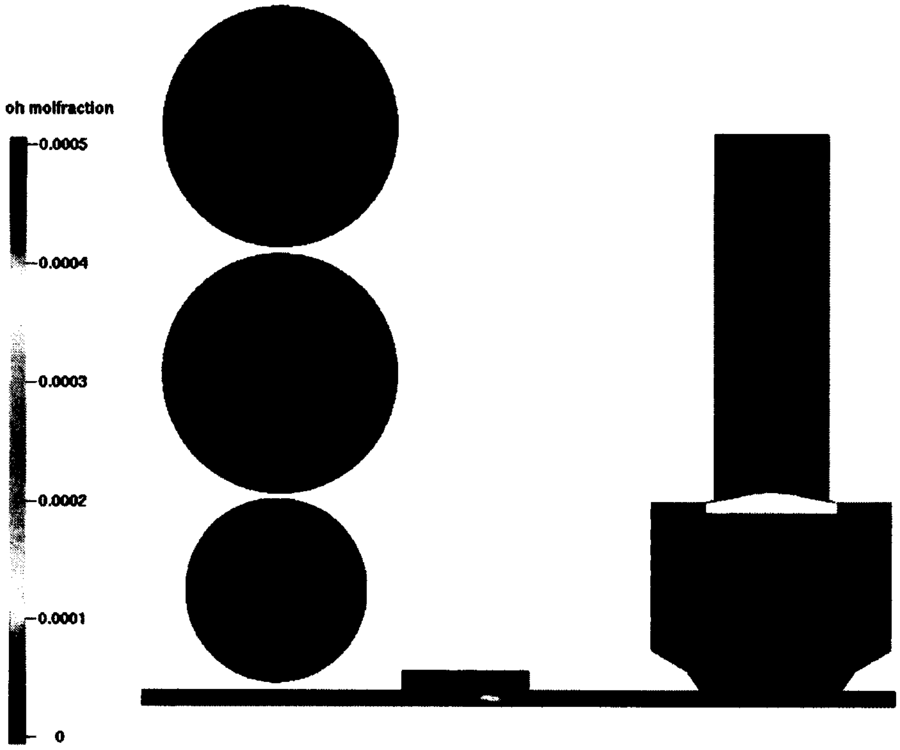

Figure 6.53 (c) 360 CA

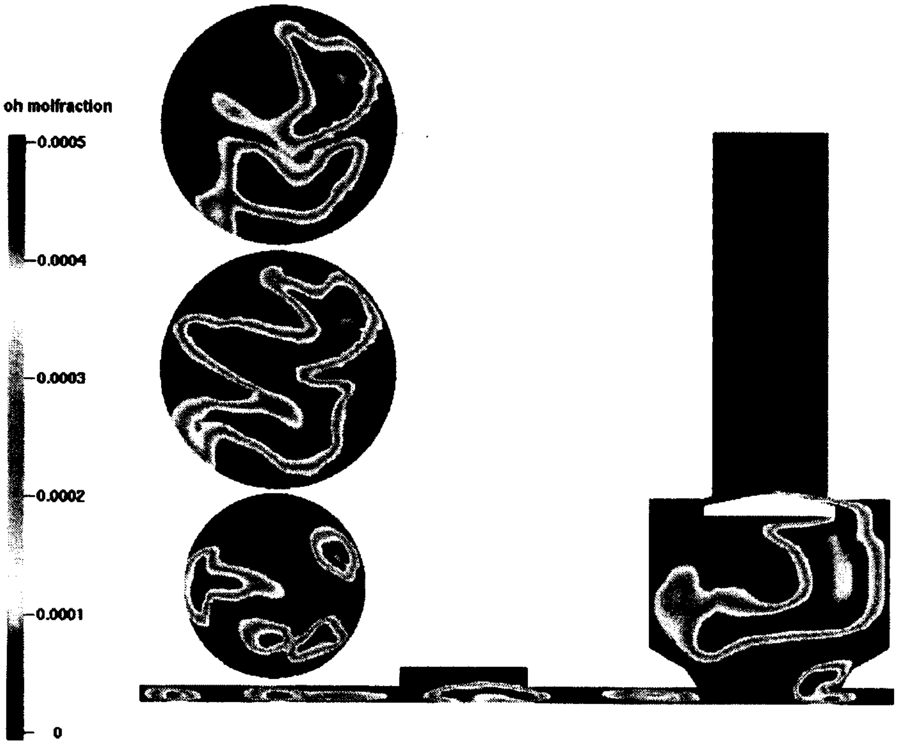

Figure 6.53 (d) 362 CA

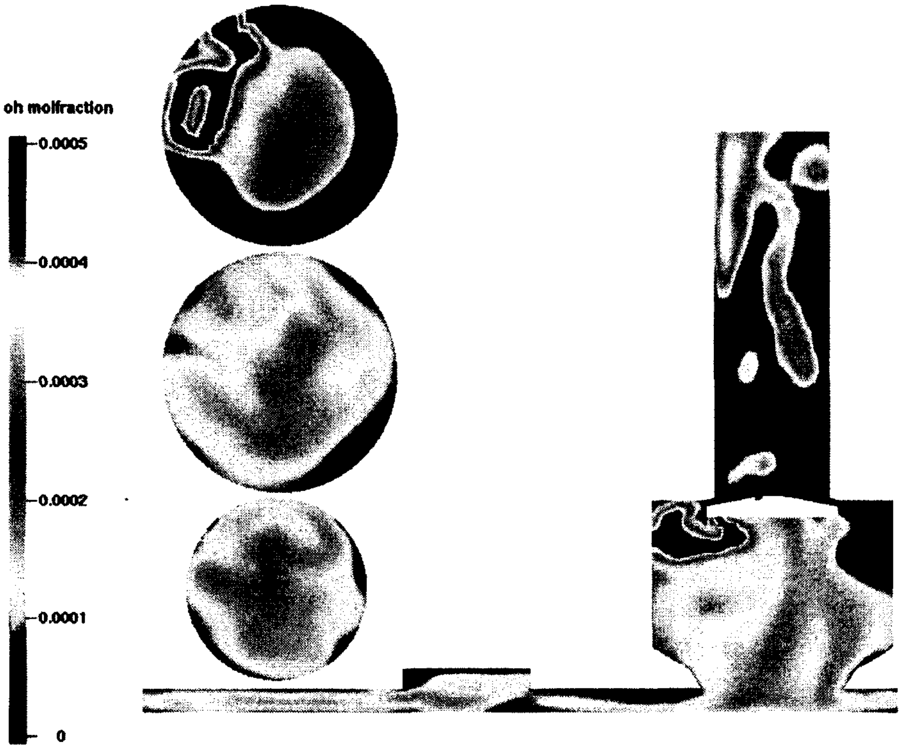

Figure 6.53 (e) 370 CA

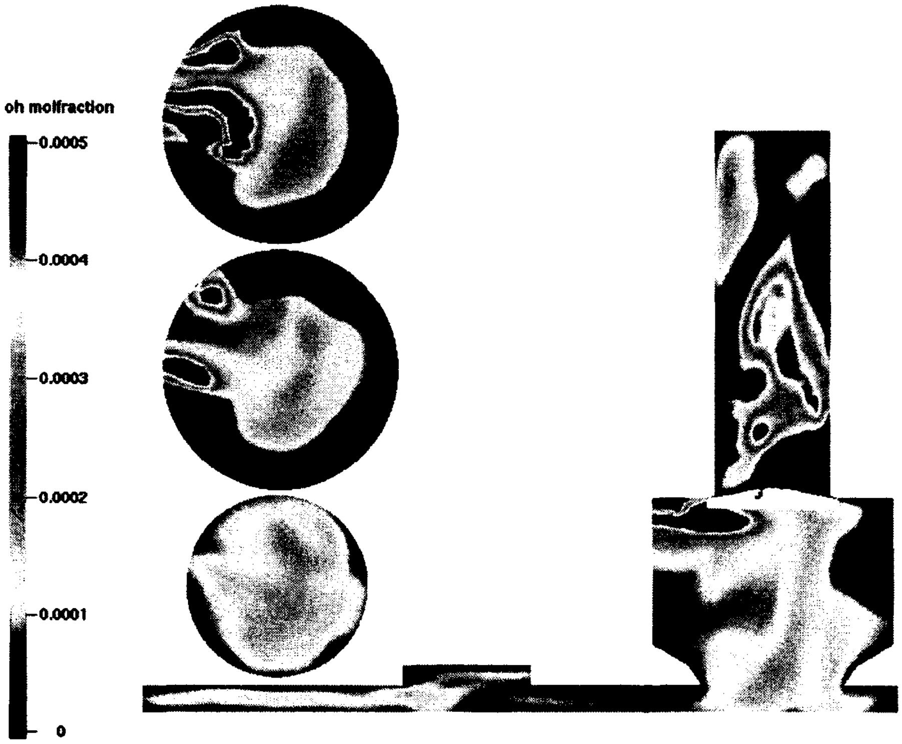

Figure 6.53 (f) 372 CA

Figure 6.53 OH molar fraction contours in XY planes and XZ plane at crank angle (a) 352 CA, (b) 356 CA, (c) 360 CA, (d) 362 CA, (e) 370 CA, and (f) 372 CA.

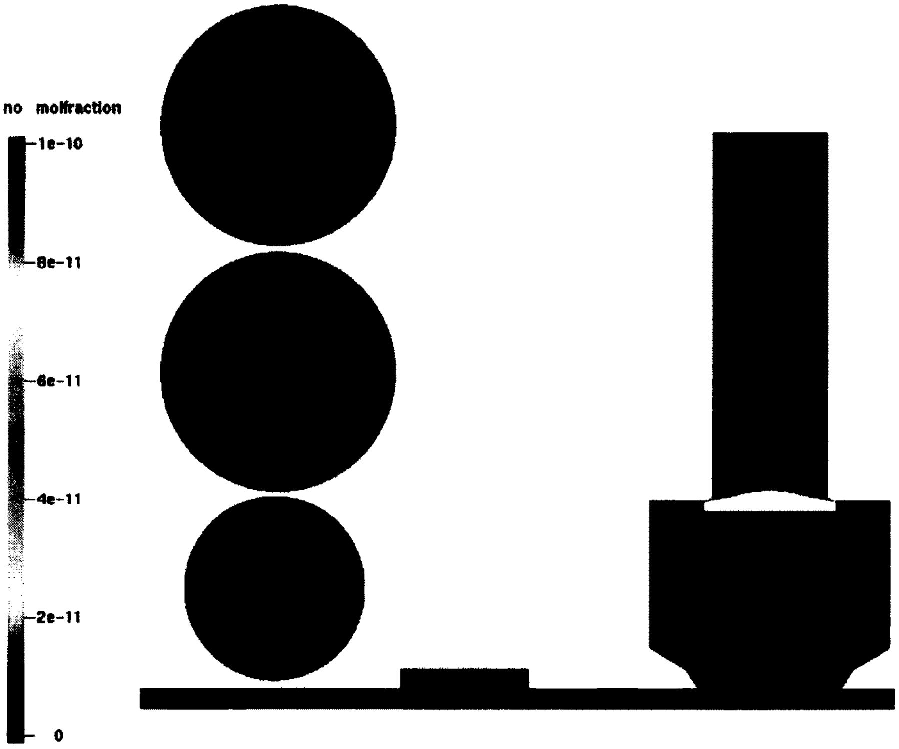

Figure 6.54 (a) 352 CA

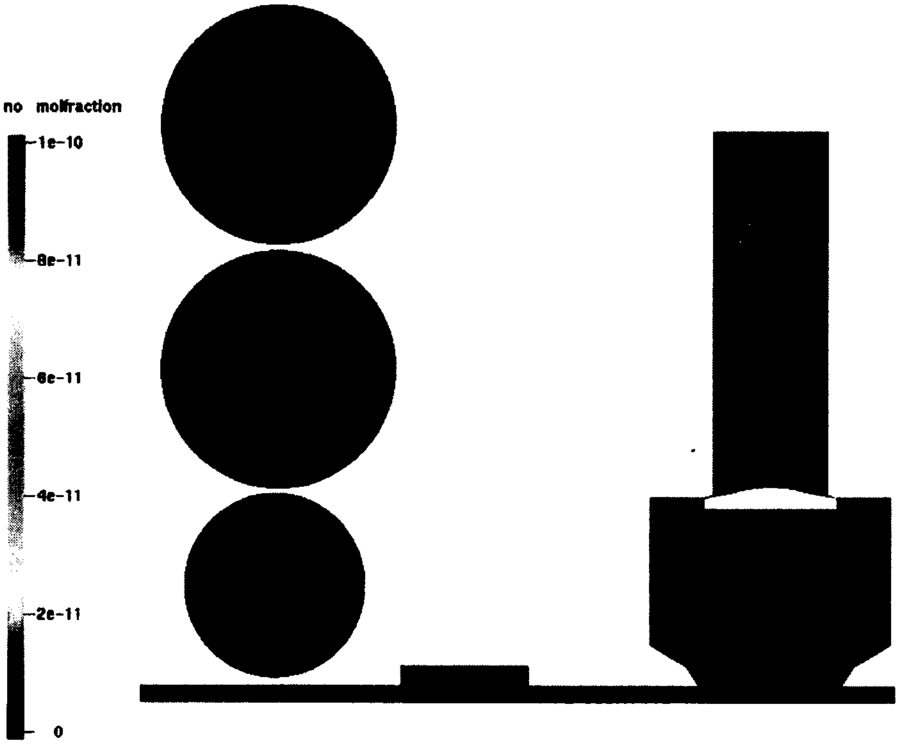

Figure 6.54 (b) 356 CA

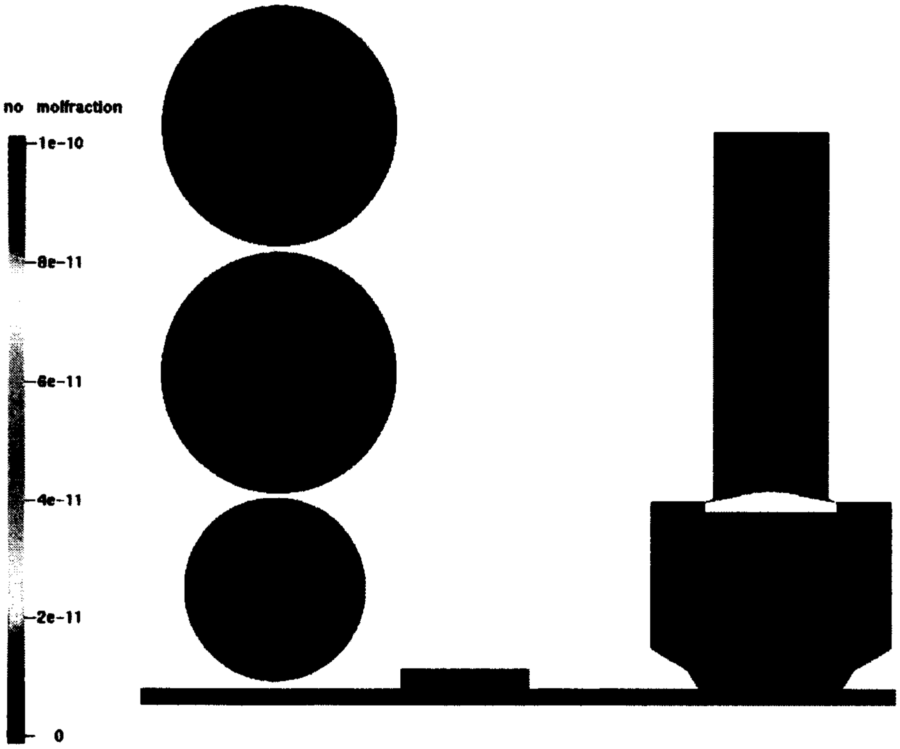

Figure 6.54 (c) 360 CA

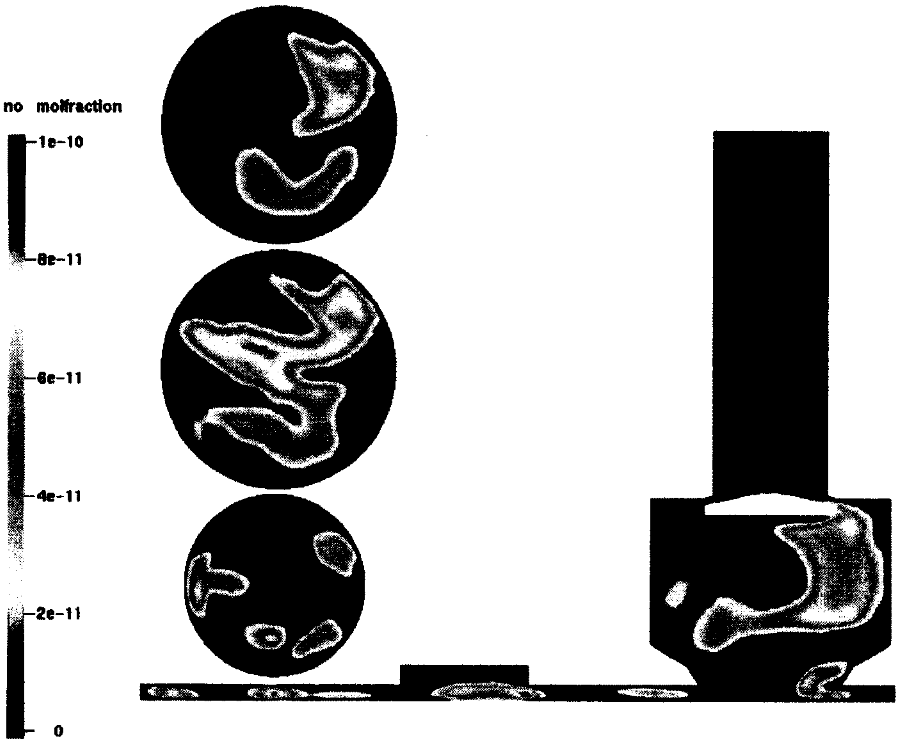

Figure 6.54 (d) 362 CA

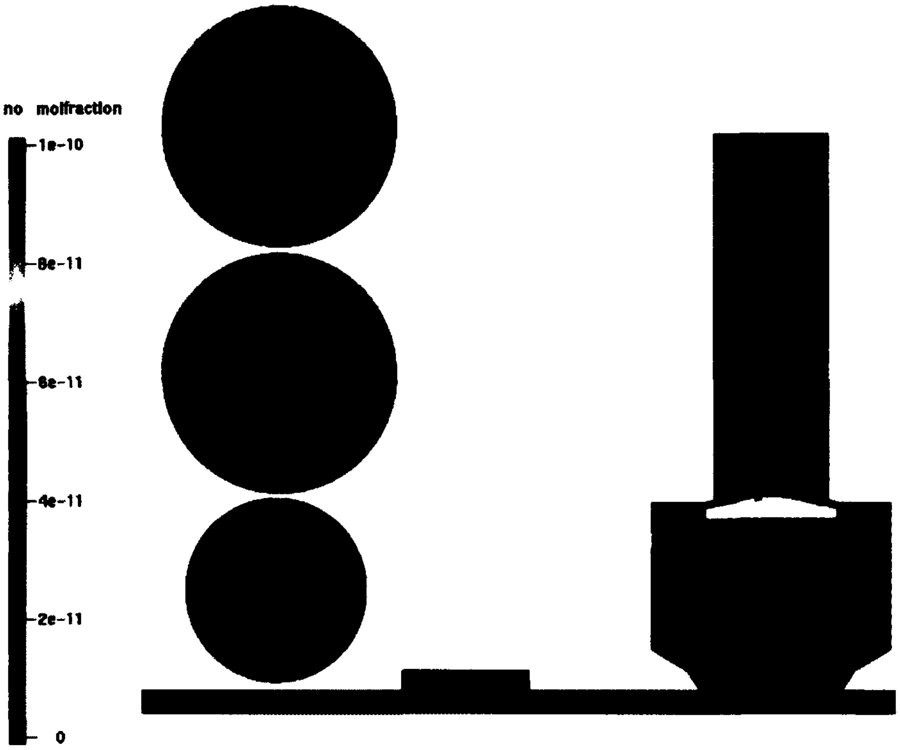

Figure 6.54 (e) 370 CA

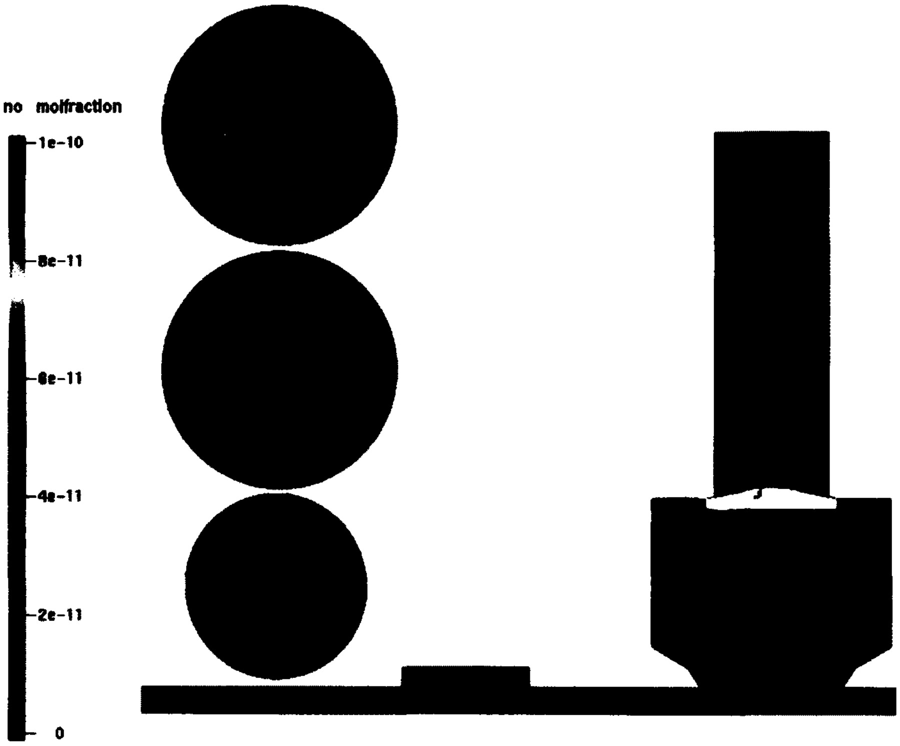

Figure 6.54 (f) 372 CA

Figure 6.54 NO molar fraction contours in XY planes and XZ plane at crank angle (a) 352 CA, (b) 356 CA, (c) 360 CA, (d) 362 CA, (e) 370 CA, and (f) 372 CA.

Effect of IMR chamber fuel injection timing

The effects of varying the IMR chamber fuel injection timing on the HCCI combustion is discussed in terms of IMEP, ISFC, and emissions. Cases 3 and 6 mentioned in Table 6.2 are discussed here. For these two cases, the IMR chamber valve timing is fixed (valve opening at 360 CA and closing at 372 CA). The fuel injection timing is advanced by 10 CA for case 6. Figure 6.55 shows the IMEP obtained for these cases. The results showed that IMEP is increased by 19.9% between Case 3 and 6. By advancing the fuel injection timing before piston reaches the top dead centre, the time required for the fuel to vaporize and mix with the combustion products is increased. For case 6, the fuel injection starts at 350 CA and finishes at 360 CA, therefore the fuel injected has sufficient time to evaporate and mix with IMR chamber gases before the piston reaches the TDC. This allows us to produce higher IMEP compared with case 3 where the injection starts at 360 CA and finishes at 370 CA.

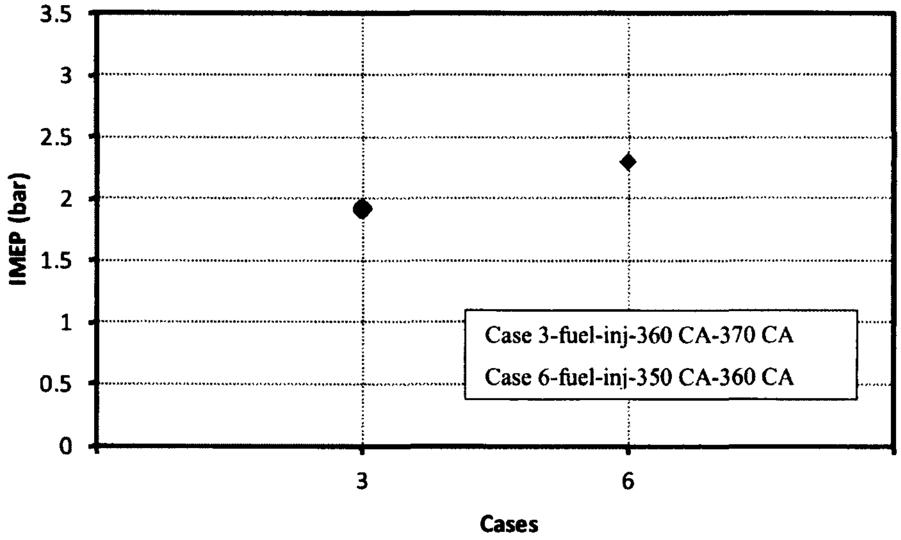

Figure 6.55 IMEP for cases 3 and 6 with constant IMR valve timing and varied fuel injection timing.

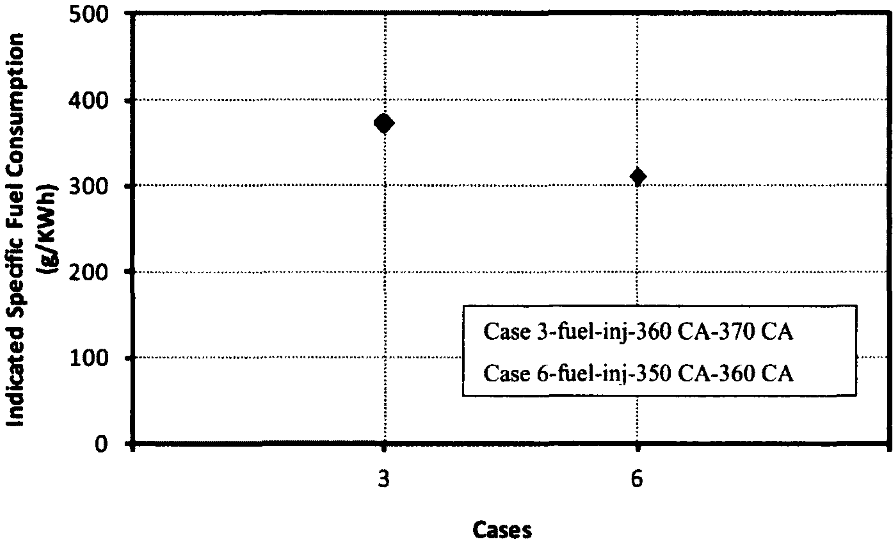

Figure 6.56 ISFC for cases 3 and 6 with constant IMR valve timing and varied fuel injection timing.

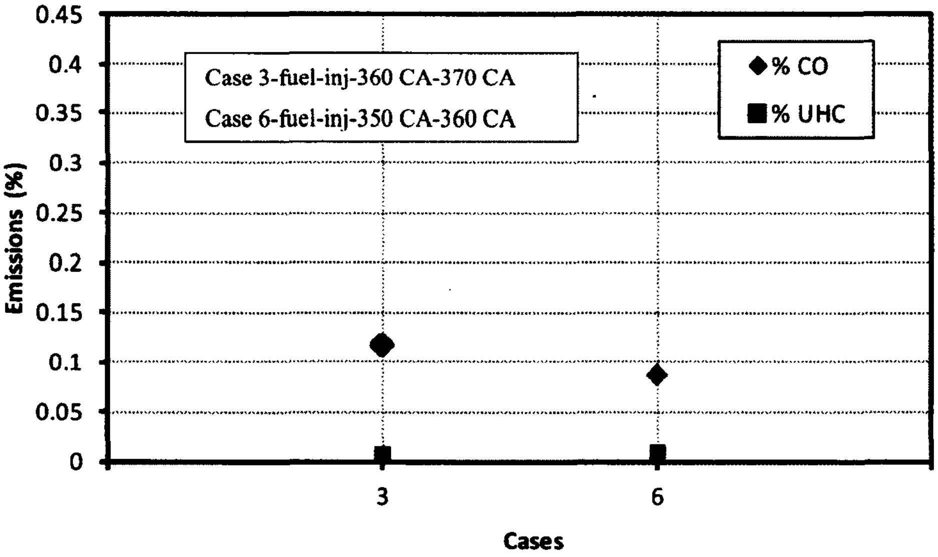

Figure 6.57 Emissions for cases 3 and 6 with constant IMR valve timing and varied fuel injection timing.

Figure 6.56 shows the fuel consumption per unit power produced for cases 3 and 6. Figure 6.57 shows the emissions of CO and UHC for cases 3 and 6. The trends suggest that case 6 produces more power with less fuel consumption and less emissions compared to case 3. This suggests that by advancing the fuel injection timing by 10 CA while keeping valve timing unchanged better performance can be achieved.

Effect of IMR chamber valve timing

Cases 3 and 4 are analyzed to understand the effect of valve timing with keeping the fuel injection timing unchanged. Figure 6.58 shows the IMEP variation between cases 3 and 4. The valve open timing is 360 CA and closing time is 372 CA for case 3 and the valve open timing is 360 CA and closing time is 405 CA for case 4.

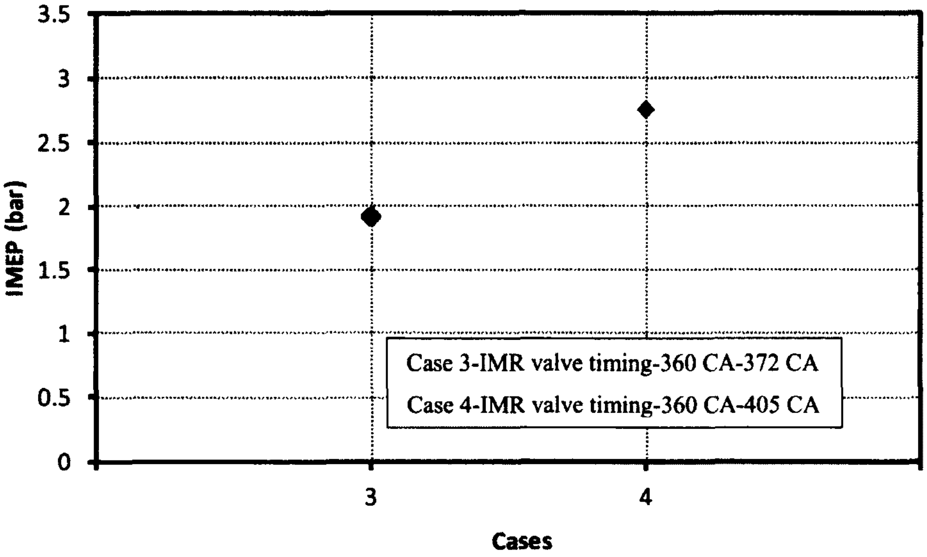

Figure 6.58 IMEP for cases 3 and 4 with constant IMR fuel injection timing and varied valve timing.

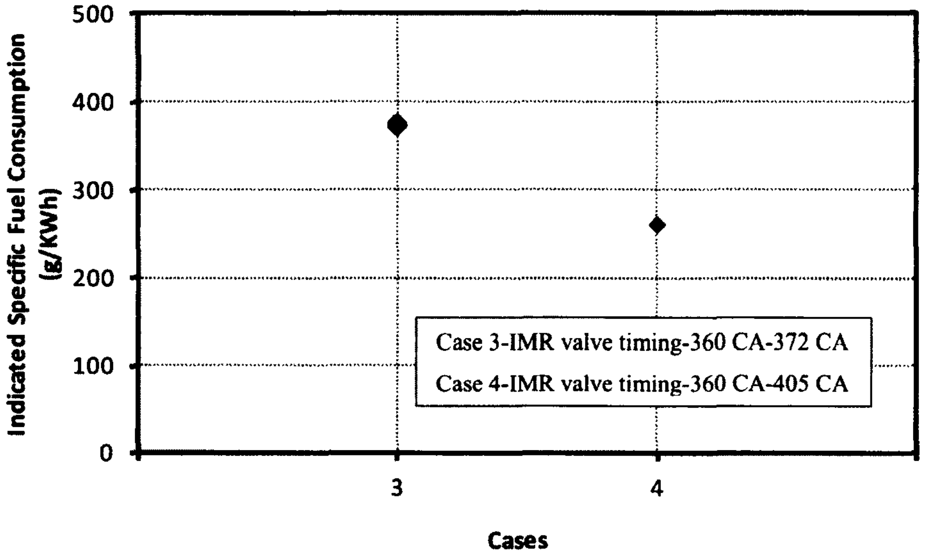

Figure 6.59 ISFC for cases 3 and 4 with constant IMR fuel injection timing and varied valve timing.

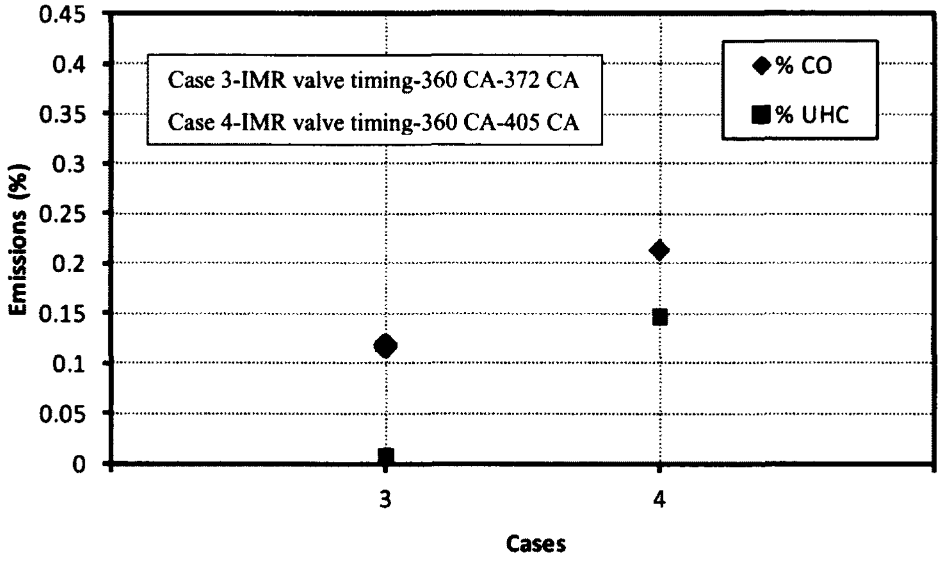

Figure 6.60 Emissions for cases 3 and 4 with constant IMR fuel injection timing and varied valve timing.

The trends for IMEP (Figure 6.58), ISFC (Figure 6.59) and emissions (Figure 6.60) indicate that, by delaying the valve timing, higher IMEP and lower fuel consumption can be obtained although more emissions could be produced. The CO emissions increase by 80% from case 3 to case 4. This indicates that the delay in closing the IMR chamber causes the partially oxidized gaseous products in the IMR chamber to flow into the main cylinder due to the piston movement and come out as exhaust without completely being burnt in case 4, while in case 3 because the valve closes just after the fuel injection finishes and thus the major amount of fuel and the partially oxidized gaseous products would remain inside the IMR chamber without causing emissions for the current cycle. Therefore the valve timing has to be optimized in order to obtain higher IMEP and lower emissions on the same time.

6.3 Summary

In this chapter, the function of the IMR chamber has been demonstrated by comparing the cases with and without this chamber. Also, the effects of the fuel and valve timings for this IMR chamber on the combustion performance has been studied by comparing different cases with different combinations of the fuel and valve timings.

The results show that:

1) the IMR chamber can successfully capture the combustion products whenever needed, which is fundamentally important for controlling the combustion process.

2) the IMR chamber can reform the fuel injected into it to form CO and H_2.

3) the liquid fuel injected into the IMR chamber requires sufficient time to vaporize, mix with the combustion products and partially oxidize to form reformation products. By reducing the time taken for this process, using gaseous fuel, or premixed charge at higher temperature, time required to form reformation products can be greatly reduced.

4) by delaying the valve closing time by 30 CA, the IMEP is increased by 37% for cases 4 and 5 compared to case 3.

5) by advancing the fuel injection timing, IMEP is increased by 12% for case 6 compared to case 3.

6) by advancing the fuel injection timing, ISFC is decreased by 20% for case 6.

4) by optimizing the timings for the valve and fuel injection, it is possible to achieve better control of the combustion process.

Chapter 7

Conclusions

7.1 Contributions and Conclusions

In this work, HCCI combustion strategies have been studied by investigating the details of turbulent flow structures and the details of combustion chemistry inside the HCCI engines.

The contributions and conclusions can be summarized as follows:

1) This study has successfully formulated the CKL solver to investigate the details of turbulence and combustion, by integrating the original KIVA-3V solver with the Large Eddy Simulation technique for turbulence and with CHEMKIN for detailed chemical kinetics.

2) This study has successfully validated the CKL solver by comparing the numerical results with corresponding experiment results and it can be concluded that this solver can be employed in practical combustion engineering applications with reasonable accuracy, e.g., 1-7.5% for peak pressure and 5-10% for IMEP.

3) This study has proposed a new HCCI combustion strategy with an IMR chamber and has investigated the IMR function by using the CKL solver in terms of how to control the combustion process. The results show that this IMR chamber can significantly affect the HCCI combustion process, e.g., by advancing the fuel injecting timing of 10 CA, the IMEP can be improved by 19.9%, and the ISFC and CO emissions can be reduced by 16.6% and 25% respectively; by delaying the IMR valve timing of 33 CA, the IMEP and CO emissions can be increased by 44.2%, and 80% respectively while the ISFC can be reduced by 30.6%.

7.2 Recommendations for future work

1. Further simulations are required to demonstrate the capabilities of IMR chamber on engine performance.

2. Further optimization of the CKL solver to reduce the overall computational time should be done, e.g., the CHEMKIN solver can be parallelized to significantly improve the computational performance.

3. The engine cycle-to-cycle variations can be investigated by using the CKL solver for a better understanding of the HCCI combustion process.

Appendix A

Jia-Xie mechanism for iso-octane

Jia-Xie mechanism output from CHEMKIN solver is shown.

```
CHEMKIN INTERPRETER OUTPUT: CHEMKIN-II Version 3.9  Aug. 1994
                                 DOUBLE PRECISION

                         --------------------
                         ELEMENTS     ATOMIC
                         CONSIDERED   WEIGHT
                         --------------------
                          1. h        1.00797
                          2. c        12.0112
                          3. o        15.9994
                          4. n        14.0067
                         --------------------
-------------------------------------------------------------------
                       C
                    P  H
                    H  A
                    A  R
SPECIES             S  G  MOLECULAR  TEMPERATURE  ELEMENT COUNT
CONSIDERED          E  E  WEIGHT     LOW    HIGH  h  c  o  n
-------------------------------------------------------------------
  1. ic8h18         G  0  114.23266   300   5000  18  8  0  0
  2. o2             G  0   31.99880   300   5000   0  0  2  0
  3. n2             G  0   28.01340   300   5000   0  0  0  2
  4. co2            G  0   44.00995   300   5000   0  1  2  0
  5. h2o            G  0   18.01534   300   5000   2  0  1  0
  6. co             G  0   28.01055   300   5000   0  1  1  0
  7. h2             G  0    2.01594   300   5000   2  0  0  0
  8. h              G  0    1.00797   300   5000   1  0  0  0
  9. o              G  0   15.99940   300   5000   0  0  1  0
 10. oh             G  0   17.00737   300   5000   1  0  1  0
 11. ho2            G  0   33.00677   300   5000   1  0  2  0
 12. h2o2           G  0   34.01474   300   5000   2  0  2  0
 13. ch3o           G  0   31.03446   300   3000   3  1  1  0
 14. ch2o           G  0   30.02649   300   5000   2  1  1  0
 15. hco            G  0   29.01852   300   5000   1  1  1  0
 16. ch2            G  0   14.02709   250   4000   2  1  0  0
 17. ch3            G  0   15.03506   300   5000   3  1  0  0
 18. ch4            G  0   16.04303   300   5000   4  1  0  0
 19. c2h3           G  0   27.04621   300   5000   3  2  0  0
 20. c2h4           G  0   28.05418   300   5000   4  2  0  0
 21. c2h5           G  0   29.06215   300   5000   5  2  0  0
 22. c3h4           G  0   40.06533   300   4000   4  3  0  0
 23. c3h5           G  0   41.07330   300   5000   5  3  0  0
 24. c3h6           G  0   42.08127   300   5000   6  3  0  0
```

```
  25. c3h7           G  0   43.08924   300    5000   7  3  0  0
  26. c4h8           G  0   56.10836   300    5000   8  4  0  0
  27. c8h17          G  0  113.22469   300    5000  17  8  0  0
  28. c8h16          G  0  112.21672   300    5000  16  8  0  0
  29. c8h17oo        G  0  145.22349   300    5000  17  8  2  0
  30. c8h16ooh       G  0  145.22349   300    5000  17  8  2  0
  31. ooc8h16ooh     G  0  177.22229   300    5000  17  8  4  0
  32. oc8h15ooh      G  0  160.21492   300    5000  16  8  3  0
  33. oc8h15o        G  0  143.20755   300    5000  15  8  2  0
  34. n              G  0   14.00670   200    6000   0  0  0  1
  35. n2o            G  0   44.01280   200    6000   0  0  1  2
  36. no             G  0   30.00610   200    6000   0  0  1  1
  37. no2            G  0   46.00550   200    6000   0  0  2  1
-----------------------------------------------------------------
          (k = A T**b exp(-E/RT))
REACTIONS CONSIDERED                          A        b        E

1. ic8h18+o2<=>c8h17+ho2                 1.00E+16    0.0    46000.0
Reverse Arrhenius coefficients:          1.00E+12    0.0        0.0
2. c8h17+o2<=>c8h17oo                    1.00E+12    0.0        0.0
Reverse Arrhenius coefficients:          2.51E+13    0.0    27400.0
3. c8h17oo<=>c8h16oo                     1.14E+11    0.0    22400.0
Reverse Arrhenius coefficients:          1.00E+11    0.0    11000.0
4. c8h16ooh+o2<=>ooc8h16ooh              3.16E+11    0.0        0.0
Reverse Arrhenius coefficients:          2.51E+13    0.0    27400.0
5. ooc8h16ooh=>oc8h15ooh                 8.91E+10    0.0    17000.0
6. ic8h18+oh=>c8h17+h2o                  1.00E+13    0.0     3000.0
7. c8h17+o2<=>c8h16+ho2                  3.16E+11    0.0     6000.0
Reverse Arrhenius coefficients:          3.16E+11    0.0    19500.0
8. oc8h15ooh=>oc8h15o+oh                 3.98E+15    0.0    43000.0
9. oc8h15o+o2<=>c2h3+2ch2o+c3h4+ch3+ho22.45E+13    0.0    32000.0
10. c8h17=c4h8+c3h6+ch3                  1.28E+12    0.0    49000.0
11. c8h16=c4h8+c3h5+ch3                  1.92E+12    0.0    48000.0
12. c4h8+o2=c2h3+c2h4+ho2                2.00E+14    0.0    35900.0
13. c3h7=c2h4+ch3                        9.60E+13    0.0    35900.0
14. c3h7=c3h6+h                          1.25E+14    0.0    36900.0
15. c3h6+ch3=c3h5+ch4                    9.00E+12    0.0     8480.0
16. c3h5+o2=c3h4+ho2                     6.00E+11    0.0    10000.0
17. c3h4+oh=c2h3+ch2o                    1.00E+12    0.0        0.0
18. c3h4+oh=c2h4+hco                     1.00E+12    0.0        0.0
19. ch3+ho2=ch3o+oh                      5.00E+13    0.0        0.0
20. ch3+oh=ch2+h2o                       7.50E+06    2.0     5000.0
21. ch2+oh=ch2o+h                        2.50E+13    0.0        0.0
22. ch2+o2=hco+oh                        4.30E+10    0.0     -500.0
23. ch2+o2=co2+h2                        6.90E+11    0.0      500.0
24. ch2+o2=co+h2o                        2.00E+10    0.0    -1000.0
25. ch2+o2=ch2o+o                        5.00E+13    0.0     9000.0
26. ch2+o2=co2+h+h                       1.60E+12    0.0     1000.0
27. ch2+o2=co+oh+h                       8.60E+10    0.0     -500.0
28. co+oh=co2+h                          5.99E+07    1.3     5232.9
29. oh+ch3o=h2o+ch2o                     5.00E+12    0.0        0.0
30. o+ch3o=oh+ch2o                       1.00E+13    0.0        0.0
```

```
31. o+oh=o2+h                          4.00E+14   -0.5        0.0
32. h+ho2=oh+oh                        1.70E+14    0.0      875.0
33. oh+oh=o+h2o                        6.00E+08    1.3        0.0
34. h+o2+m=ho2+m                       3.60E+17   -0.7        0.0
h2o              Enhanced by    2.100E+01
co2              Enhanced by    5.000E+00
h2               Enhanced by    3.300E+00
co               Enhanced by    2.000E+00
35. h2o2+m=oh+oh+m                     1.00E+17    0.0    45500.0
h2o              Enhanced by    2.100E+01
co2              Enhanced by    5.000E+00
h2               Enhanced by    3.300E+00
co               Enhanced by    2.000E+00
36. h2+oh=h2o+h                        1.17E+09    1.3     3626.0
37. ho2+ho2=h2o2+o2                    3.00E+12    0.0        0.0
38. ch2o+oh=hco+h2o                    5.56E+10    1.1      -76.5
39. ch2o+ho2=hco+h2o2                  3.00E+12    0.0     8000.0
40. hco+o2=ho2+co                      3.30E+13   -0.4        0.0
41. hco+m=h+co+m                       1.59E+18    0.9    56712.3
42. ch3+ch3o=ch4+ch2o                  4.30E+14    0.0        0.0
43. c2h4+oh=ch2o+ch3                   6.00E+13    0.0      960.0
44. c2h4+oh=c2h3+h2o                   8.02E+13    0.0     5955.0
45. c2h3+o2=ch2o+hco                   4.00E+12    0.0     -250.0
46. c2h3+hco=c2h4+co                   6.03E+13    0.0        0.0
47. c2h5+o2=c2h4+ho2                   2.00E+10    0.0    -2200.0
48. ch4+o2=ch3+ho2                     7.90E+13    0.0    56000.0
49. oh+ho2=h2o+o2                      7.50E+12    0.0        0.0
50. ch3+o2=ch2o+oh                     3.80E+11    0.0     9000.0
51. ch4+h=ch3+h2                       6.60E+08    1.6    10840.0
52. ch4+oh=ch3+h2o                     1.60E+06    2.1     2460.0
53. ch4+o=ch3+oh                       1.02E+09    1.5     8604.0
54. ch4+ho2=ch3+h2o2                   9.00E+11    0.0    18700.0
55. ch4+ch2=ch3+ch3                    4.00E+12    0.0     -570.0
56. c3h6=c2h3+ch3                      3.15E+15    0.0    85500.0
57. n+no<=>n2+o                        3.50E+13    0.0      330.0
58. n+o2<=>no+o                        2.65E+12    0.0     6400.0
59. n+oh<=>no+h                        7.33E+13    0.0     1120.0
60. n+co2=no+co                        1.90E+11    0.0     3400.0
61. n2o+o=n2+o2                        1.40E+12    0.0    10810.0
62. n2o+o=no+no                        2.90E+13    0.0    23150.0
63. n2o+h=n2+oh                        4.40E+14    0.0    18880.0
64. n2o+oh=n2+ho2                      2.00E+12    0.0    21060.0
65. n2o+m=n2+o+m                       1.30E+11    0.0    59620.0
66. no+ho2=no2+oh                      2.11E+12    0.0     -480.0
67. no2+o=no+o2                        3.90E+12    0.0     -240.0
68. no2+h=no+oh                        1.32E+14    0.0      360.0
69. no+o+m=no2+m                       1.06E+20   -1.4        0.0
```

NOTE: A units mole-cm-sec-K, E units cal/mole

References

Aceves, S.M., Flowers, D.L., Martinez-Frias, J., Smith, J.R., Westbrook, C.K., and Pitz, W.J., "A sequential fluid-mechanic chemical-kinetic model of propane HCCI combustion," SAE Paper 2001-01-1027, 2001.

Aceves, S.M., Flowers, D.L., Martinez-Frias, J., Dec, J.E., and Sjoeberg, M., "Spatial analysis of emissions sources for HCCI combustion at low loads using a multi-zone model," SAE Paper 2004-01-1910, 2004.

Agarwal, A., and Assanis, D.N., "Multi-dimensional modeing of natural gas ignition under compression ignition conditions using detailed chemistry," SAE Paper 980136, 1998.

Amsden, A.A., O'Rourke, P.J., and Butler, T.D., "KIVA-II: A computer program for chemically reactive flows with sprays," Technical Report LA-11560-MS, Los Alamos National Laboratory, 1989.Amsden, A.A., "KIVA-3V: A block-structured KIVA program for engines with vertical or canted valves," Technical Report LA-13313-MS, Los Alamos National Laboratory, 1997.

Babajimopoulos, A., Assanis, D.N., and Fiveland, S.B., "An approach for modeling the effects of gas exchange processes on HCCI combustion and its application in evaluating variable valve timing control strategies," SAE Paper 2002-01-2829, 2002.

Celik, I., Yavuz, I., and Smirnov, A., "Large eddy simulations of in-cylinder turbulence for internal combustion engines: a review," International Journal of Engine Research, Vol. 2, No. 2, pp. 119-148, 2001.

CEPA http://www.ec.gc.ca/CEPARegistry/regulations/ , 1999.

Christensen, M., and Johansson, B., "The effect of in-cylinder flow and turbulence on HCCI operation," SAE Paper 2002-01-2864, 2002.

Curran, H.J., Gaffuri, P., Pitz, W.J., and Westbrook, C.K., "A comprehensive modeling study of iso-octane oxidation," Combustion and Flame, Vol. 129, pp. 253-280, 2002.

Dec, J.E., and Sjoeberg, M., "A parametric study of HCCI combustion – the sources of emissions at low loads and the effects of GDI fuel injection," SAE Paper 2003-01-0752, 2003.

Erlebacher, G., Hussaini, M.Y., Speziale, C.G., and Zang, T.A., "Toward the Large-Eddy Simulation of compressible turbulent flows," Journal of Fluid Mechanics, Vol. 238, pp. 155–185, 1992.

Fiveland, S.B., and Assanis, D.N., "A four-stroke homogeneous charge compression ignition engine simulation for combustion and performance studies," SAE Paper 2000-01-0332, 2000.

Fiveland, S.B., and Assanis, D.N., "Development of a two-zone HCCI combustion model accounting for boundary layer effects," SAE Paper 2001-01-102, 2001.

Germano, M., Piomelli, U., Moin, P., and Cabot, W.H., "A dynamic sub-grid-scale eddy viscosity model," Physics of Fluids, Vol.3, No. 7, pp. 1760-1765, 1991.

Gnanam, G., "Homogenous Charge Compression Ignition (HCCI) engine fuelled with ethanol, iso-octane and products of in-cylinder reformation in IDI-type engine," PhD Dissertation, University of Windsor, 2008.

Haraldsson, G., Tunestal, P., and Johannsen, B., "HCCI combustion phasing with closed-loop combustion control using variable compression ratio in a multi-cylinder engine," SAE Paper 2003-01-1830, 2003.

Haworth, D.C., "Large-eddy simulation of in-cylinder flows," Oil and Gas Science and Technology, Vol.54, No. 2, pp.175-185, 1999.

Jhavar, R., and Rutland, C.J., "Using large eddy simulations to study mixing effects in early injection diesel engine combustion," SAE Paper 2006-01-0871, 2006.

Jhavar R., "Using large eddy simulation to study diesel DI-HCCI engine flow structure, mixing and combustion," PhD Dissertation, University of Wisconsin – Madison, 2007.

Jia, M., and Xie M.Z., "A chemical kinetics model of iso-octane oxidation for HCCI engines," Fuel, Vol. 85, Issue 17-18, pp. 2593-2604, 2006.

Kaahaaina, N.B., Simon, A., Caton, A.P., and Edwards, C., "Use of dynamic valving to achieve residual – affected combustion," SAE Paper 2001-01-0549, 2001.

Kamata, S., Nakagawa, H., Hori, T., Senda, J., and Fujimoto, H.G., "Instantaneous and statistical structures of non-evaporative diesel spray," SAE Technical Paper, JSAE 20077193, SAE Paper 2007-01-1899, 2007.

Kee, R.J., Rupley, F.M., Meeks, E., and Miller J.A., "CHEMKIN-III: a Fortran chemical kinetics package for the analysis of gas phase chemical and plasma kinetics," Report No. SAND96-8216, Sandia National Laboratories, 1996.

Kong, S.C., Marriot, C.D., Reitz, R.D., and Christensen, M., "Modeling and experiments of HCCI engine combustion using detailed chemical kinetics with multi-dimensional CFD," SAE Paper 2001-01-1026, 2001.

Kong, S.C., and Reitz, R.D., "Use of detailed chemical kinetics to study HCCI engine combustion with consideration of turbulent mixing effects," J. of Engineering for Gas Turbines and Power, ASME, Vol. 124, pp. 702-707, 2002.

Kong, S.C., Marriott, C.D., Reitz, R.D., and Christensen, M., "Modeling the effects of geometry generated turbulence on HCCI engine combustion," SAE Paper 2003-01-1088, 2003.

Kongsereeparp, P., and Checkel, M.D., "Investigation of reformed fuel blending effects in HCCI engines using a multi-zone model," SAE Paper 2007-01-0205, 2007.

Launder, B.E., and Spalding, D.B., "*Mathematical Models of Turbulence*," Academic Press, New York, 1972.

Law, D., "Controlled combustion in an IC-engine with a fully variable valve train," SAE Paper 2000-01-0251, 2000.

Lee. D., Pomraning, E., and Rutland, C.J., "LES modeling of diesel engines," SAE Paper 2002-01-2779, 2002.

Najt, P.M., and Foster, D.E., "Compression-ignited homogeneous charge combustion," SAE Paper 830264, 1983.

Narayanaswamy, K., and Rutland, C.J., "Cycle simulation diesel HCCI modeling studies and control," SAE Paper 2004-01-2997, 2004.

Ogink, R., "Applications and results of a user-defined, detailed-chemistry HCCI combustion model in the AVL BOOST cycle simulation code," International AVL User Meeting, 14–15 October, Graz, Austria, 2003.

Onishi, S., Jo, S.H., Shoda, K., Jo, P.D., and Kato, S., "Active Thermo Atmosphere Combustion (ATAC) – A new combustion process for internal combustion engines," SAE Paper 790501, 1979.

Patel, A., Kong, S.C., and Reitz, R.D., "Development and validation of reduced reaction mechanism for HCCI engine simulation," SAE Paper 2004-01-0558, 2004.

Pomraning, E., and Rutland, C.J., "A dynamic one-equation non-viscosity LES model," AIAA Journal, Vol. 40, No. 4, pp.689-701. 2002.

Sagaut, P., "*Large eddy simulation for ncompressible flows*," 2nd Edition, Springer 2002.

Shen, Y., King, E., and Pfahl, U., "Influences of intake charge preparations on HCCI combustion in a single cylinder engine with variable valve timing and gasoline direct injection," SAE Paper 2006-01-3274, 2006.

Smagorinsky, J., "General circulation experiments with the primitive equations," Monthly Weather Review, Vol. 91, pp. 99-164, 1963.

Sone, K., Patel, N., and Menon, S., "Large eddy simulation of fuel-air mixing in an internal combustion engine," 39th AIAA Aerospace Sciences Meeting, January 8-11, AIAA 2001-0635, 2001.

Sone, K., and Menon, S., “Effect of sub-grid modeling on the in-cylinder unsteady mixing process in a direct injection engine,” J. Engineering for Gas Turbines and Power, Vol. 125, pp. 435-443, 2003.

Stull, D. R., and Prophet, H. “JANAF Thermochemical Tables, 2nd Edition”, (U. S. Department of Commerce/National Bureau of Standards, NSRDS-NBS 37, June 1971). N.W. Chase et al., J. Phys. Chem. Ref. Data vol.3, 311, 1974.

Tanaka, S., Ayala, F., and Keck, J.C., “A reduced chemical kinetic model for HCCI combustion of primary reference fuels in a rapid compression machine,” Combustion and Flame, Vol. 133, pp. 467-481, 2003.

Thobois, L., Rymer, G., Souleres, T., Poinsot, T., and Ven den Heuvel, B., “Large eddy simulation for the prediction of aerodynamics in IC engines,” International Journal of Vehicle Design, Vol. 39, No. 4, 2005.

Thring, R.H., “Homogeneous Charge Compression Ignition (HCCI) engines,” SAE Paper 892068, 1989.

Xu, H.M., Williams, A., Fu, H.Y., Wallace, S., Richardson, S., and Richardson, M., “Operating characteristics of a homogeneous charge compression ignition engine with cam profile switching-simulation study,” SAE Paper 2003-01-1859, 2003.

Yao, M., Zheng, Z., and Liu, H., “Progress and recent trends in homogeneous charge compression ignition (HCCI) engines,” Progress in Energy and Combustion Science, Vol. 35, pp. 398-437, 2009.

Zhao, F., Assanis, D.N., Najt, P.M., Dec, J.E., Eng, J.A., and Asmus, T.W., “Homogeneous charge compression ignition engines: key research and development issues,” SAE PT-94, 2003.

VITA AUCTORIS

NAME: Srikanth Jonnalagedda

PLACE OF BIRTH: Machilipatnam, Andhra Pradesh, India

YEAR OF BIRTH: 1976

EDUCATION

S.V.L. Polytechnic College, Machilipatnam, India
1990-1995 Diploma (Mechanical Engineering)

S.R.K.R Engineering College, Bhimavaram, A.P, India
1996-1999 B.E (Mechanical Engineering)

IIT Madras, Chennai, India
2000-2004 M.S (Aerospace Engineering)

University of Windsor, Windsor, Ontario, Canada
2006-2010 PhD (Mechanical, Automotive and Materials Engineering)